True Liquid Crystal Templating of Nanoparticle-doped Mesoporous Silica

Stephen Gary Wainwright

A thesis for the degree of
Doctor of Philosophy in Chemistry

The University of York

Department of Chemistry

October 2011

Abstract

Using true liquid crystal templating (TLCT), a one-pot method for preparing mesoporous silicas containing metal nanoparticles is available. The method leads to well-defined systems with possible applications is selective catalysis. Using this approach, a range of metal-doped variants of hexagonal silicas (general MCM-41 family) are prepared and show surface areas >1000 m^2 g^{-1} and pore diameters of *ca* 30 Å. Specifically, palladium doped-MCM-41-like silicas are prepared and are shown to be active in the selective oxidation of crotyl alcohol and the activity of the system has been investigated as a function of both metal loading and the pore length – the latter affecting mass transport and therefore rate of conversion.

Templating on Pluronic P123 leads to doped SBA-15-like materials, but in contrast to the findings with low-concentration templating as commonly reported, TLCT leads to materials with surface areas of about 400 m^2 g^{-1}, which is accounted for by the absence of micropores. Catalytic results from these SBA-15 materials will also be presented.

CONTENTS

List of Figures

CHAPTER ONE – INTRODUCTION

CHAPTER TWO – MCM-41 TYPE MATERIALS

CHAPTER THREE – SBA-15 TYPE MATERIALS

CHAPTER FOUR – PREPARATION OF NANOPARTICLE-DOPED SILICAS USING MICELLE-SOLUBLE METAL COMPLEXES

CHAPTER FIVE – SELECTIVE OXIDATION REACTIONS

List of Tables

CHAPTER ONE – INTRODUCTION

CHAPTER TWO – MCM-41 TYPE MATERIALS

CHAPTER THREE – SBA-15 TYPE MATERIALS

CHAPTER FOUR – PREPARATION OF NANOPARTICLE-DOPED SILICAS USING MICELLE-SOLUBLE METAL COMPLEXES

CHAPTER FIVE – SELECTIVE OXIDATION REACTIONS

Acknowledgements

I would like to begin by thanking my supervisor, Professor Duncan Bruce, for giving me the opportunity to complete this work and all his help and guidance over the last five years. The group has changed significantly over the time I’ve been part of it and I’ve enjoyed my time immensely. I have had the chance to travel a number of times, including a wonderful trip to the IZC-IMMS 2010 conference in Sorrento as well as spending a week at the Trieste synchrotron.

Thanks must also go to our colleagues at Cardiff University; Professor Adam Lee, Dr Karen Wilson and Chris Parlett, who have been invaluable in their assistance with the catalytic testing of the materials I prepared. My trips down to Cardiff were always enjoyable and extremely interesting. Professor Wuzong Zhou and Ross Blackley at the University of St. Andrews deserve a huge thank you for all their work and assistance with the vital TEM work.

I am grateful to everyone who has helped me during my time in the Department of Chemistry at York, especially Dr Graeme McAllister and Dr Phil Helliwell for their CHN analysis, Dr Adrian Whitwood for his assistance with the X-ray diffractometer as well as Chris Mortimer from the Department Workshop for his help with installing gas lines for the porosimeter and tube furnace.

None of this work would have been possible without generous funding from the EPSRC.

Finally, I would like to thank my family and all my friends who have kept me motivated and sane over the last few years. Too many to name, but I would not have gotten this far if not for them.

Thank you.

Declaration

I certify that all material in this thesis which is not my own work has been identified and that no material is included for which a degree has previously been conferred on me by this or any other university.

CHAPTER ONE

INTRODUCTION

1.1 Aims

Catalysts are used daily in many applications, from industrial processes (*e.g.* the Haber process[1]), to catalytic converters found in cars,[2] to smaller-scale use in synthetic routes in research laboratories. This work, a continuation of research conducted previously by Bruce and co-workers, aims to provide easy-to-produce, nanoparticle-doped, nanostructured, silica-based catalysts, by preparing a silica monolith built around lyotropic surfactants, which act as a template. Once the base method has been studied, this research will look at controlling the pore size and morphology, particle size and the metal oxidation state. The ultimate aim is the development of a flexible and robust methodology for preparing a wide range of custom catalysts, according to the needs of the process.

1.2 Surfactants

*Surf*ace-*act*ive *a*ge*nts*[3] are so called because of their tendency to adsorb at the surfaces or at the interface between phases[4] and are more commonly known as surfactants. Surfactants are amphiphilic and usually consist of a hydrophilic head group and a hydrophobic tail (Figure 1.1).

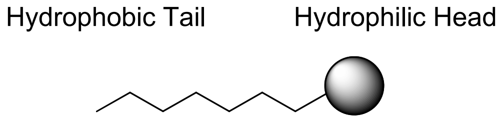

Figure 1.1 Simple schematic of an amphiphile

The head group of a surfactant is a polar species, which gives it a hydrophilic nature. This can vary significantly in design, the four main classes of head-group being cationic, anionic, zwitterionic and non-ionic (Figure 1.2). By comparison, the tail would be a non-polar species and is hydrophobic in nature. Again, the structure of the tail can vary, as can the number of tails, although it is usually a single hydrocarbon, fluorocarbon or dimethylsiloxane chain.

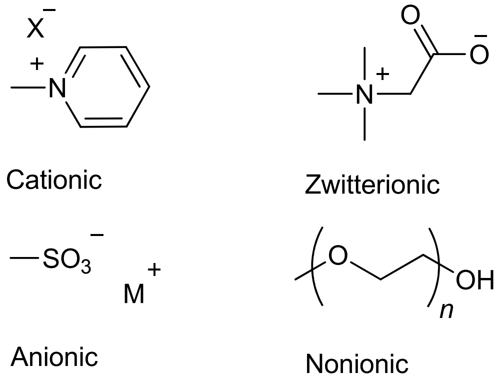

Figure 1.2 Examples of surfactant head groups

When a surfactant is added to a liquid, it typically aggregates at the surface due to the hydrophobic nature of the chains and causes a reduction in the free energy of the surface (the surface tension). Water, the solvent commonly used in a large number of surfactant applications, is held together by a three-dimensional network of hydrogen bonds in its liquid state and it is these bonds that account for its higher-than-expected boiling point. At the interface with air, the water molecules cannot form hydrogen bonds in every direction resulting in an excess of energy on the surface and, as a result, the remaining hydrogen bonds are stronger, minimising the surface area of the interface. This is the phenomenon of surface tension (Figure 1.3). When surfactants are added to the water, they adsorb at the water-air interface and lower the surface tension by allowing the expansion of the surface area without an increase in the surface energy. This effect can be measured quantitatively. The surface tension of a typical air-water interface is 72-73 mN m^{-1} and, after a surfactant is added, the surface tension can be lowered to around 28-30 mN m^{-1}.[5]

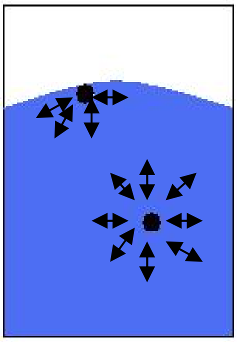

Figure 1.3 Diagram of the forces on a molecule of a liquid

In addition to adsorbing at the surface, if more surfactant is added, free surfactant molecules in the solution aggregate together to form dimers, trimers, oligomers and then micelles. The minimum concentration required for micelle formation is known as the critical micelle concentration, CMC. The appearance of micelles and the CMC can be characterised by a sharp increase in the solubility of the surfactants. Once the CMC is reached and micelles form, all additional surfactant added contributes to the formation of micelles, increasing the micellar concentration. The driving force behind the formation of the micelles, the *hydrophobic effect*, lends to the increased solubility of the surfactant above CMC.

The hydrophobic effect is an entropic effect observed when a hydrophobic substance is placed in a polar solution, *i.e.* surfactant in water. The three-dimensional network of hydrogen bonds in water, described previously, is arranged to give the maximum number of hydrogen bonds; hydrogen bonding minimises enthalpy, overcoming the unfavourable entropy of order. A hydrophobic molecule introduced to the system will disrupt the hydrogen bonding network, increasing the entropy. The more hydrophobic molecules present in the water, the more disruption there is and the higher the entropy gets. The hydrophobic chains become immobile as there is no way for them to escape the water molecules; the water molecules, in turn, form a frozen skin around the chains resulting in a decrease in entropy. As a consequence, the water molecules 'push' the hydrophobic molecules together to give the smallest surface area of disruption. This releases the frozen water molecules, allowing them to re-join the hydrogen bonding network, increasing enthalpy but decreasing entropy. The added mobility allowed to the micelle chains in their oily environment increases the entropy, as does the freedom allowed to the previously frozen water molecules. The enthalpy of micelle formation is very small, arising from the enthalpies of hydrophobic interactions, electrostatic interactions and the hydration of polar groups.[6] The overall entropy change is favourable on the formation of micelles and much larger than the enthalpy changes, resulting in an overall negative free energy, subsequently allowing a spontaneous process.

The critical micelle concentration is sensitive to many factors and, in particular, changes in head group charge and chain length (Table 1.1) can have significant effects. Surfactants with charged headgroups will tend to have a higher CMC value than a non-ionic surfactant. This difference can be accredited to the increased repulsion between charged headgroups which makes micelle formation unfavourable at lower concentrations. Changes to the chain length of the surfactant tend to decrease the CMC with increasing length as aggregation of the micelles becomes more favourable.

Table 1.1 Changes in CMC with alkyl chain length of surfactants[7]

Surfactant	Critical Micelle Concentration / mol dm^{-3} x 10^{-3}
$CH_3(CH_2)_{11}N^+(CH_3)_3\ Br^-$	15.60
$CH_3(CH_2)_{13}N^+(CH_3)_3\ Br^-$	3.76
$CH_3(CH_2)_{15}N^+(CH_3)_3\ Br^-$	0.92

Depending on the head group size, the chain length and chain volume, the micelle usually forms one of the three most common shapes: sphere, rod (cylinder) or disc. The shape the micelle will form can be predicted courtesy of Israelachvilli's ratio:[8]

$$\eta = v / a_o l \tag{1}$$

Where

v = volume occupied by the hydrophobic chain

a_o = cross sectional area of the head group

l = 90% of the length of the fully extended chain

The ratio calculated using this equation gives an approximation of the curvature at the micelle-solvent interface, thereby predicting the shape of the micelle (Table 1.2). Simply speaking, the larger the head group in relation to the tail group, the greater the curvature will be. It should be noted that this does not take into account any particle-particle interactions or external influences, which may affect the formation of the micelles.

Table 1.2. Using Israelachvilli's ratio to predict the shape of the micelle

Israelachvilli's ratio	Shape of the micelle
$\eta < ⅓$	Spherical
$⅓ < \eta < ½$	Rod-like
$½ < \eta < 1$	Disc-like

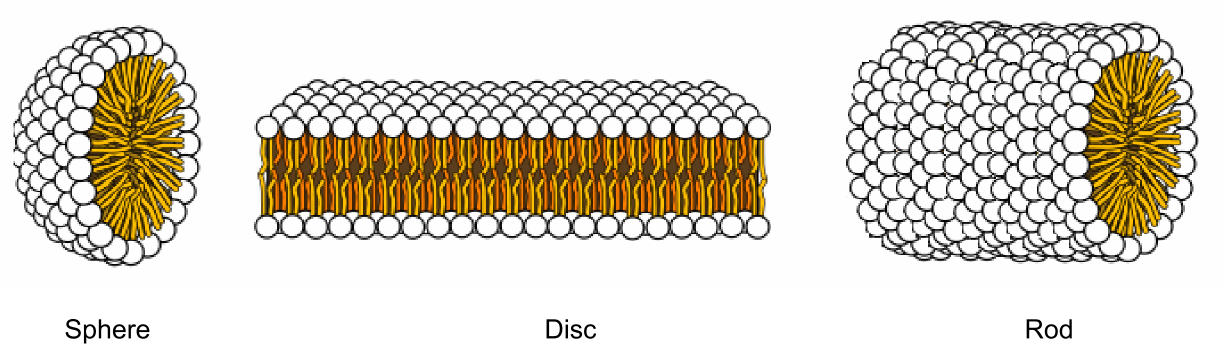

Figure 1.4 Schematic of micelle shapes

Additionally, micelles can be considered as one of two categories: normal or inverse. Normal micelles are those with the polar head groups forming a shell around the oily hydrocarbon core; these are usually found when the micelle forms in polar solvents. Inverse micelles, as the name suggests, are the inverse of this. Inverse micelles form in water when $\eta > 1$, with the polar head-groups in the centre and the hydrocarbon chains forming the protective shell. This occurs when the volume of the tail group is large, usually when there are multiple tails with a small head, resulting in a wedge shape, with the head at the narrow end.

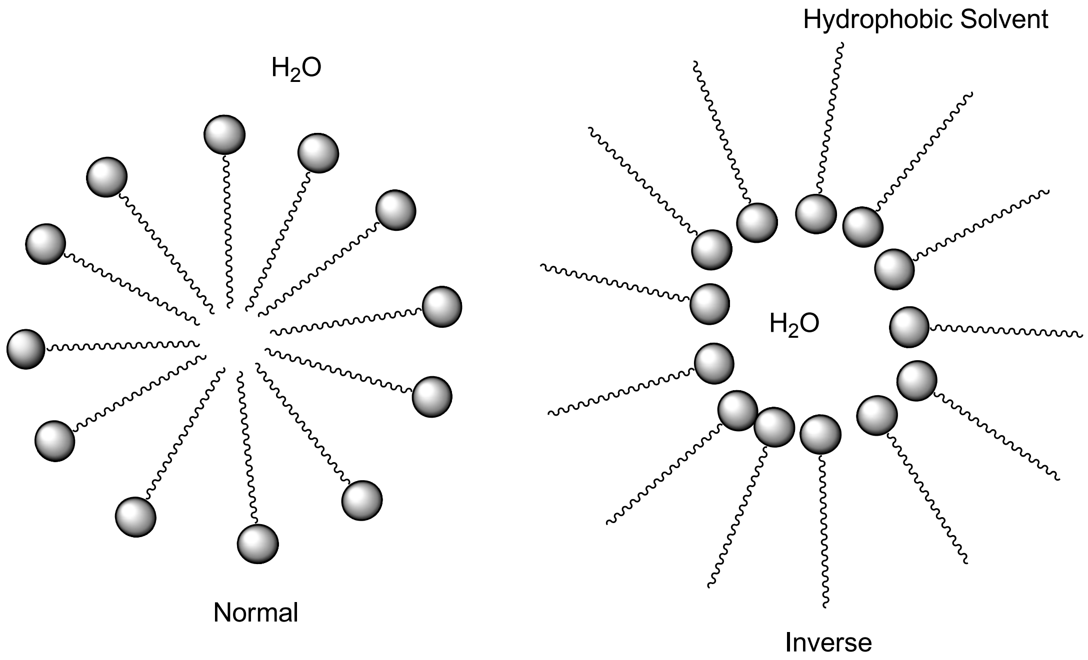

Figure 1.5 Schematic of normal and inverse micelle

1.3 Liquid Crystals

The term 'liquid crystal' is used to describe the fourth state of matter, which exists between the liquid and solid phases. Liquid crystals have properties of both of these states, the long-range orientational order of solids with the fluidity and viscosity of liquids. Liquid crystals are classified as either thermotropic or lyotropic depending on the way in which they are formed. Thermotropic liquid crystals change phase due to temperature changes, whereas lyotropic liquid crystals are formed using solvent (Figure 1.6). The work described here uses lyotropic liquid crystals; therefore, thermotropic materials will not be considered further.

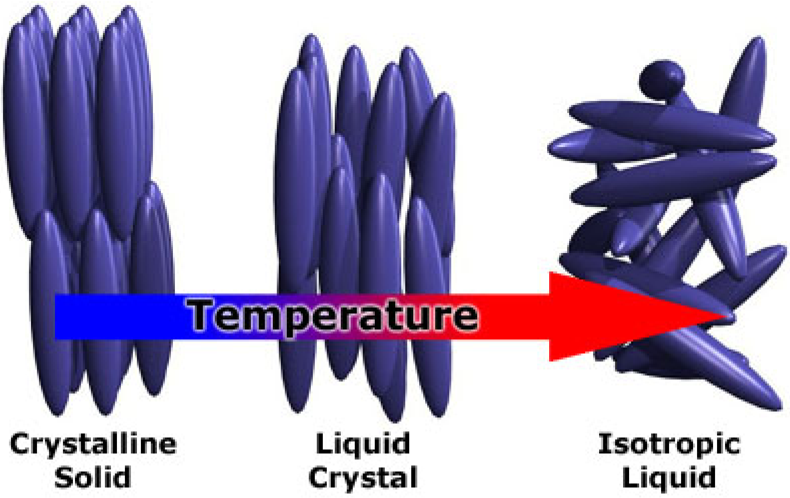

Figure 1.6 The fourth state of matter[9]

Lyotropic mesophases are found in a huge number of applications and systems. Soaps and detergents combined with water form a lyotropic mesophase; biological membranes such as cells and DNA show liquid-crystalline behaviour; even rigid systems such as Kevlar (polyphenyleneterephalamide) have a lyotropic mesophase which is exploited during manufacturing to give Kevlar its high tensile strength. Most surfactants can form lyotropic mesophases, but this is done in a different way to that found with DNA and Kevlar. To consider lyotropic phase formation in surfactants, we can start from micellisation, recalling that all additional surfactant added above the CMC creates new micelles. Thus, micelle concentration increases until a point is reached when micelle concentration is so high that the situation becomes unfavourable energetically and the system reduces its energy by allowing the micelles to organise, forming a liquid crystal phase.

The first mesophase formed in these circumstances is held to depend on the shape of the micelle present before the mesophase forms and so Israelachvilli's ratio can be used to predict the first-observed phase. There are three main types of mesophase, six when both the normal and inverse micelle shapes are taken into account and a seventh mesophase which is neither normal nor inverse (Figure 1.7). Surfactants don't necessarily show all of these phases, but where more than one phase is shown, they will normally exist in the same order on increasing concentration. Each phase is given a letter and a subscript number to identify it; subscript 1 for 'normal' phase and subscript 2 for inverse phase. In addition to these seven mesophases there are also a number of transitional mesophases that can occur, formed using the micelles with shape intermediate between spherical, rod-like and disc like, but these are not so common and are not discussed here.

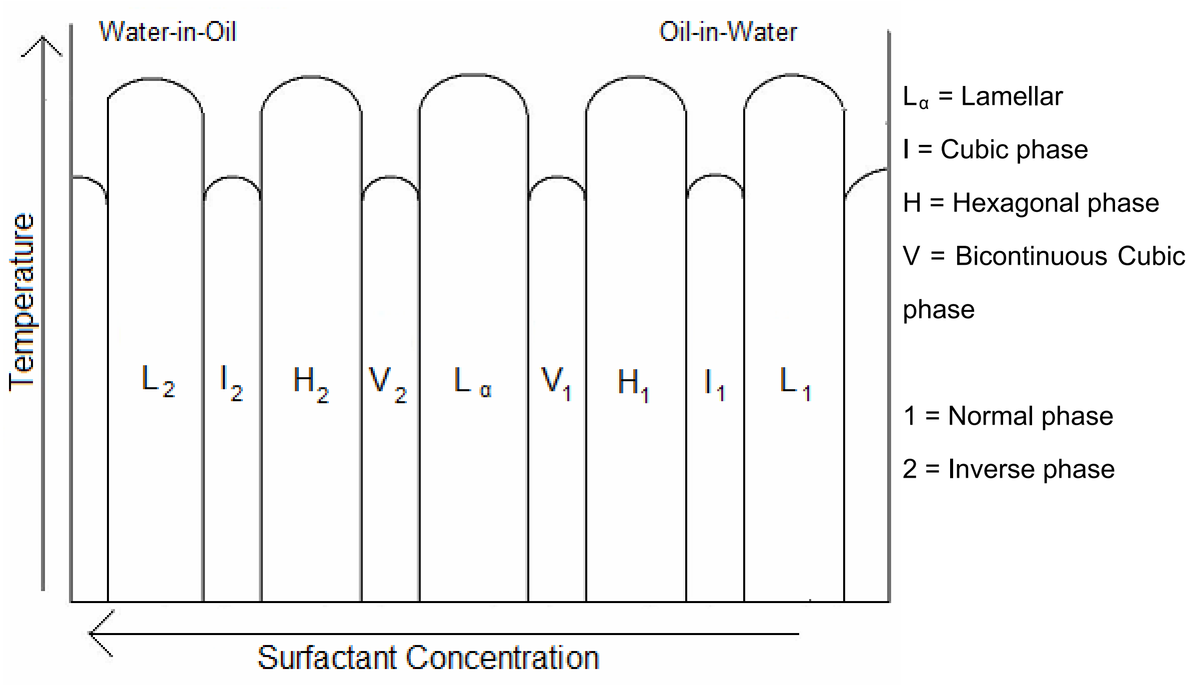

Figure 1.7. Theoretical phase diagram for a surfactant in water

L_α denotes the lamellar phase, where the discs of the micelles have formed layers in the solvent and there are neither normal nor inverse phases. **I** is used to indicate the micellar cubic phase, formed by the ordering of spherical micelles into cubic arrays. The hexagonal phases, $\mathbf{H_1}$ and $\mathbf{H_2}$, are formed from normal and inverse rod like micelles respectively. **V** represents the bicontinuous cubic phases, but, this is not micellar (Figure 1.8).

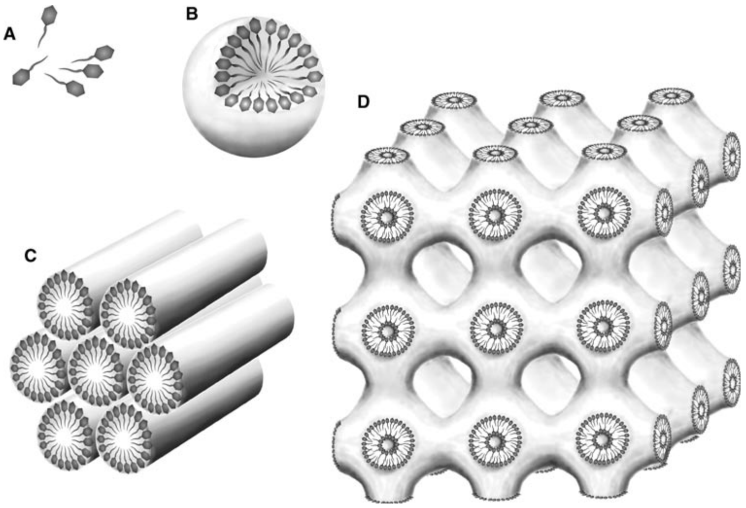

Figure 1.8. A. Monomers, B. Micelle, C. $\mathbf{H}_1$ Hexagonal phase, D. $\mathbf{V}_1$ Bicontinuous cubic phase[10]

The hexagonal phase (Figure 1.9) is a very common form of micelle, comprising of stacks of rod-like micelles ordered into hexagonal arrays. The phase is quite viscous as the rods can only move past each other in one direction, along their long axis. The rods are separated by a continuous water region.

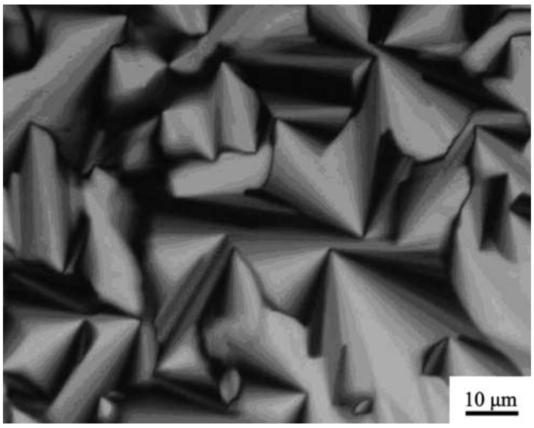

Figure 1.9 Optical texture of the hexagonal (H_1) liquid crystal phase[11]

The cubic phase is more viscous than the hexagonal, with discrete spherical micelles separated by water. The micellar phases may be based on lattices that inhabit the *Pm*3*n*, *Im*3*m* and *Fm*3*m* space groups. Cubic phases may also be bicontinuous and are described as such: the water is divided into two continuous, but separated, regions by a surfactant bilayer.

1.3.1 Characterisation Techniques

1.3.1.1 Polarised Optical Microscopy

Polarised optical microscopy (POM) is the first and most commonly used technique for the characterisation of liquid crystal mesophases. Light passes through a pair of crossed polarisers, between which is placed the sample. If the sample is in the isotropic state, the polarised light passes straight through the sample and is then blocked by the second, crossed, polariser (analyser) allowing nothing to be seen through the eyepiece (Figure 1.10). If the sample is anisotropic, it will split the polarised light into two parts, the ordinary ray and the extraordinary ray, which interfere with one another (plane polarisation is lost) creating an interference pattern or texture. The advantage of characterising liquid crystals this way is due to the fact that most liquid crystal mesophases are anisotropic and show up as visible textures under POM. Due to the different alignment of molecules within different mesophases, it is possible to see a difference in textures between mesophases, even so far as to see it change as the mesophase changes from one to the other. As such POM is an invaluable method of identifying the mesophases exhibited. It should be noted that the lyotropic cubic phases are isotropic and as such do not exhibit any birefringence. This is because they have the same dimensions in all directions; however, they differ from the isotropic phase in being rather viscous and, therefore, identifiable.

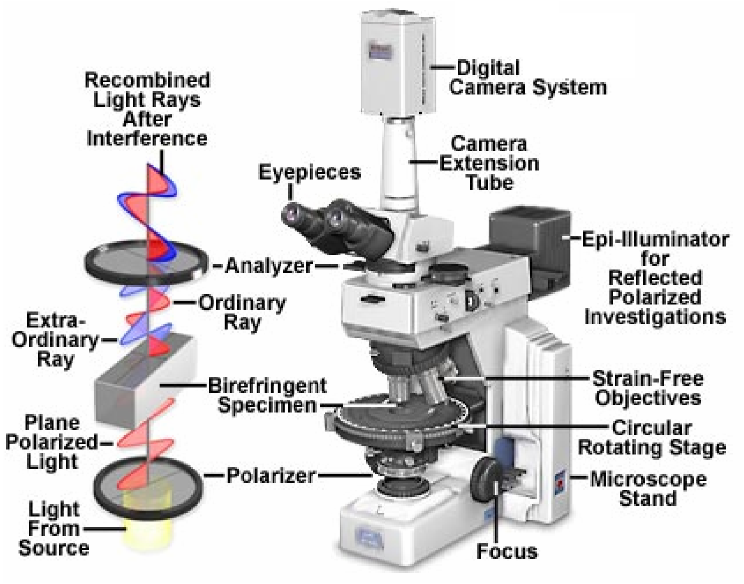

Figure 1.10. Diagram of a polarised optical microscope[12]

1.4 Porous Solids

While porous materials have been formally known for some time, the subject has expanded and received significant interest in recent years,[13] with an ever-increasing range of materials and applications, one of the most significant being in catalysis. Important materials are zeolites,[14] with pore diameters up to 20 Å and, more recently, ordered mesoporous silicas, with pore diameters from 20 to 100 Å. Zeolites are microporous materials made from hydrated aluminosilicate. There are 48 naturally occurring zeolites known and over 150 others have been synthesised. The advantage of zeolites is their open structure, which can accommodate a variety of cations; the disadvantage is the relatively small size of their pores. Zeolites are limited by their pore sizes and industrial demands require large, mesoporous materials. The synthesis of these materials has experienced enormous growth and of particular note is the M41S family.

MCM-41 is the best-known of the mesoporous silicas and is a member of the M41S family, reported by Beck *et al.* in 1992 (Figure 1.11).[15] These materials are synthesised by a method that has become known as *liquid crystal templating* (LCT), which uses a surfactant, such as cetyltrimethyl ammonium bromide (CTAB), which displays a lyotropic mesophase in water. The porous solid is said to form from the base-catalysed condensation of silica from sodium silicate using the surfactant as a template. The surfactant is then removed by calcination to yield silica composed of hexagonally arranged mesopores with a surface area of around 700 m^2 g^{-1} (Figure 1.11). The pores themselves can be tuned in size depending on the surfactant used, ranging from 15 – 100 Å in diameter, the larger pores achievable with the use of a swelling agent to increase the size of the micelles. It should be noted that the concentration of surfactant for this method is above its critical micelle concentration but below the minimum concentration required for mesophase formation.

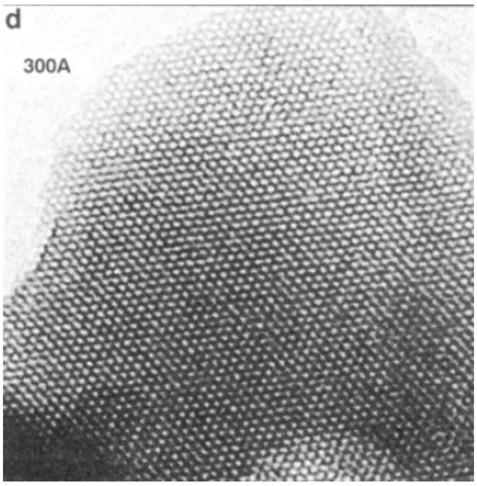

Figure 1.11. TEM image of Beck's MCM-41

The huge number of possible combinations of surfactant and silica source has resulted in a number of sub-families within the MCM-41 type. For example, one could use acid-catalysed condensation instead of base-catalysed, with $Si(OMe)_4$ or $Si(OEt)_4$, as well as any number of different surfactants: anionic, cationic, neutral, Pluronics®[16,17,18] and polymers. To identify these as different from MCM-41, even though they are part of the same family, they often have unique names. For example, SBA-15[19,20], from Santa Barbara, which has a hexagonal structure with both micro- and meso-pores, and TUD-1[21], from Technische Universität Delft. The nomenclature for these materials is very arbitrary, giving little or no details of the material itself unless it is already known what the name represents. MCM-41 and MCM-48 are very different in structure, the former being hexagonal while the latter is bicontinuous cubic; likewise SBA-15 and SBA-16 are hexagonal and bicontinuous cubic respectively.

In 1995, Attard *et al.*[22] adapted the above method, in describing so-called True Liquid Crystal Templating, TLCT. This method, differs from LCT by first forming the lyotropic mesophase of the surfactant, either non-ionic or cationic, prior to the acid-catalysed condensation of $Si(OMe)_4$ (TMOS). The method, originally reported by Attard, mixed the surfactant, octaethylene glycol monododecyl ether ($C_{12}EO_8$, Figure 1.12), with aqueous HCl (pH 2) in a 50:50 wt% ratio. This formed a normal hexagonal (H_1) phase. To this, TMOS was added in a 1:4 ratio with respect to water, so that complete hydrolysis of the TMOS occurred. Attard also stated that during the condensation process, methanol is produced and should be removed immediately by applying a gentle, dynamic vacuum. Once hydrolysis was complete, the surfactant could be removed by either calcination or washing, to leave a mesoporous hexagonal gel monolith. The hexagonal structure was confirmed by TEM and X-ray diffraction, and BET nitrogen adsorption experiments showed the monolith had a specific surface area of 1400 m^2 g^{-1}, which is notably higher than the ~700 m^2 g^{-1} reported for MCM-41 type solids.

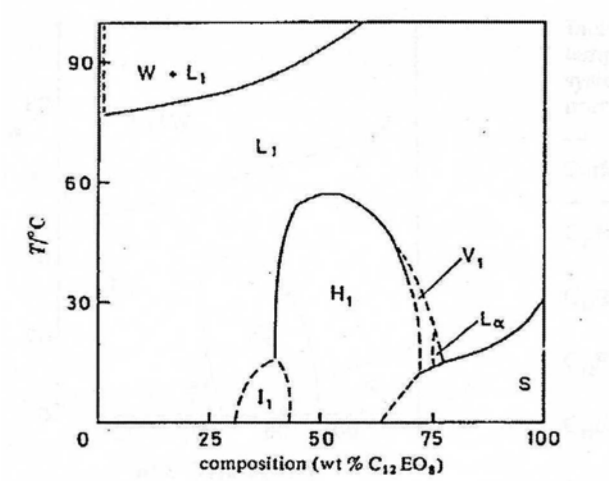

Figure 1.12 Phase diagram of $C_{12}EO_8$[23]

Liquid Crystal Templating was found to be repeatable, but not predictable, whereas True Liquid Crystal Templating is an improvement, as it is found to be both predictable and repeatable.

With a similar hexagonal pore structure to MCM-41 is SBA-15, discovered in 1998, which is traditionally synthesised in highly acidic conditions and low surfactant concentrations. It uses the triblock copolymer Pluronic P123 ($PEO_{20}PPO_{70}PEO_{20}$, Figure 1.13) dissolved in 0.40 mol dm^3 HCl with addition of tetraethoxysilane (TEOS) to form the hexagonally templated silica; using the LCT approach.

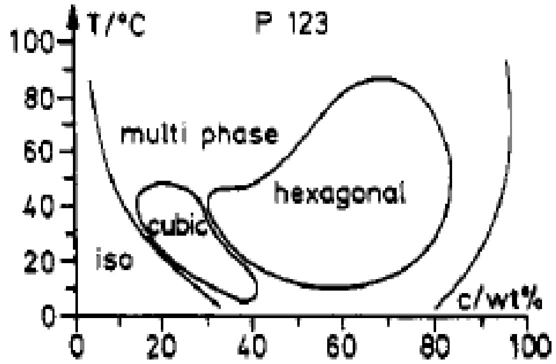

Figure 1.13 Phase diagram of P123, $PEO_{20}PPO_{70}PEO_{20}$[24]

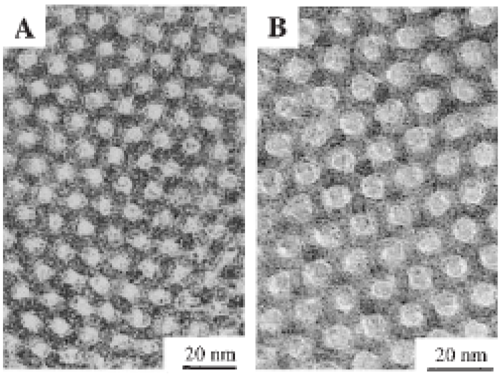

Figure 1.14 TEM image of SBA-15 with different average pore sizes (A) 60 Å (B) 89 Å

SBA-15 has been observed to contain both micropores and mesopores, the mesopores forming the hexagonal structure and the micropores being reported as interconnecting pores between the mesopores.[25] It is suggested that the micropores are formed by 'loose' PEO tail groups of the Pluronic surfactant in one micelle interacting with PEO tails from another micelle to form a channel. The specific surface area of SBA-15 is measured to be about 900 m^2g^{-1}; however, the true mesoporous surface area is much lower than this at around 450 m^2g^{-1}, the difference being accounted for by the micropores. Increasing the synthesis temperature reduces the volume of micropores, until a temperature of 130 ºC is used, reducing the microporosity to almost nothing,[26] while showing an increase in the pore diameter and a reduction in pore-wall thickness and surface area. Alternatively, non-microporous SBA-15 can be synthesised by using surfactant mixtures,[27] post-treatment[28] and microwave-hydrothermal synthesis.[29]

In a method that may be considered to be true liquid crystal templating, evaporation-induced self-assembly (EISA), Stucky *et al.*[30] used a higher concentration of the P123 surfactant (10%) in a volatile polar solvent with weak polarity (ethanol) and added an inorganic precursor with a low polymerisation degree ($SiCl_4$) leaving the resulting sol-gel to hydrolyse and polymerise into a metal oxide network at 40 ºC for 1-7 days. Calcination after this time resulted in a material exhibiting a two-dimensional hexagonal mesostructure observed by low-angle XRD. At the surfactant concentration detailed, a liquid crystal phase forms during the final stage of solvent evaporation in the presence of the inorganic oligomers.

1.4.1 Characterisation Techniques

1.4.1.1 X-Ray Diffraction (XRD)

The long-range order of MCM-41 and the materials studied here give rise to characteristic diffraction patterns in X-ray experiments, which can be used to identify the formation of the mesoporous structure. If the porous solid is considered to be a honeycomb of hollow cylinders packed together hexagonally, the reflections of the X-ray diffraction pattern can be assigned to the (*hk0*) parameters of a two-dimensional hexagonal unit cell (Figure 1.15).

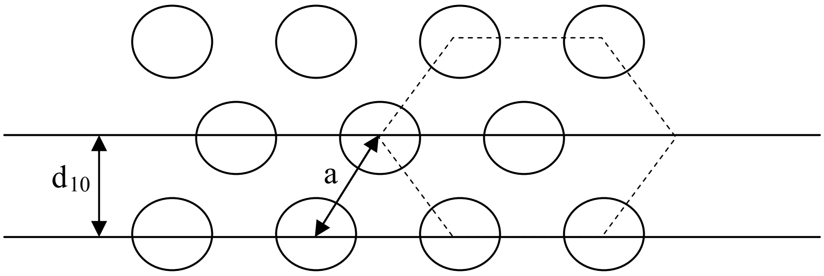

Figure 1.15 Two-dimensional hexagonal unit cell

With the application of Bragg's law (2), the diffraction angle θ, the wavelength of the incident X-rays λ, and an integer n, can be used to calculate the d-spacing, d. With the d-spacing, the repeat distance of the unit cell, or lattice parameter, can be calculated (3).

$$n\lambda = 2d \sin\theta \qquad (2)$$

$$a_0 = 2d_{10} / \sqrt{3} \qquad (3)$$

It should be noted that the silica walls of the solid are amorphous and as such do not diffract the X-rays.

With the application of the Scherrer equation (4),[31] it is possible to calculate the average diameter of particles detected by high-angle XRD:

$$t = 0.9\,\lambda/(B \cos\theta) \qquad (4)$$

where t is the thickness or particle diameter, λ is the wavelength of the incident X-rays, B is the full width at half the maximum height of the diffraction peak (Figure 1.16), and θ is the diffraction angle of the peak maximum. B is corrected for the instrument resolution due to the broadening of the X-ray beam.

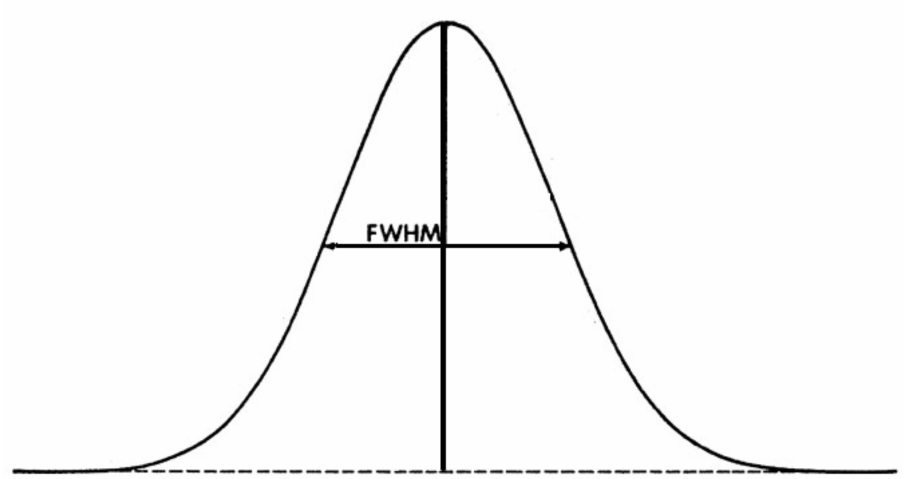

Figure 1.16 Full width at half maximum

1.4.1.2 Nitrogen Adsorption Measurements

Nitrogen (N_2) adsorption is a very commonly used technique to measure the structural properties of porous solids.[32] The technique measures the surface area of the solid by observing the adsorption and desorption of a gas on the surface of the solid. Nitrogen or argon is usually used as the gas, although carbon monoxide and hydrogen can also be used. The gas is added to the free-space above the sample at a series of known pressures and the amount of gas adsorbed onto the surface of the sample is measured. Vacuum is then applied in known stages and the desorption of nitrogen is measured. These pressures are plotted to give an isotherm, which shows characteristic information of the porosity of the material. The surface area, pore diameter and volume can be calculated from the isotherm data.

There are six characteristic forms of isotherms (Figure 1.17), each representing a different type of porous material. Type I isotherms are shown by microporous solids where there are strong interactions between adsorbate and adsorbent, *i.e.* zeolites. Type II isotherms are typically non-porous materials with weak interactions with the gas. Type III isotherms are very uncommon, with weak interactions with the gas; an example is graphitised carbon. Type IV isotherms are the first type that show a hysteresis of the adsorption/desorption curves that are characteristic of mesoporous materials such as MCM-41 and SBA-15; as such, this isotherm will be the most important for this work. Type V isotherms are similar to type IV but have weaker interactions and are shown by either macroporous or mesoporous solids; water vapour adsorption on charcoal would give a type V isotherm. Finally, type VI isotherms are characteristic of well-defined, uniform porous solids.

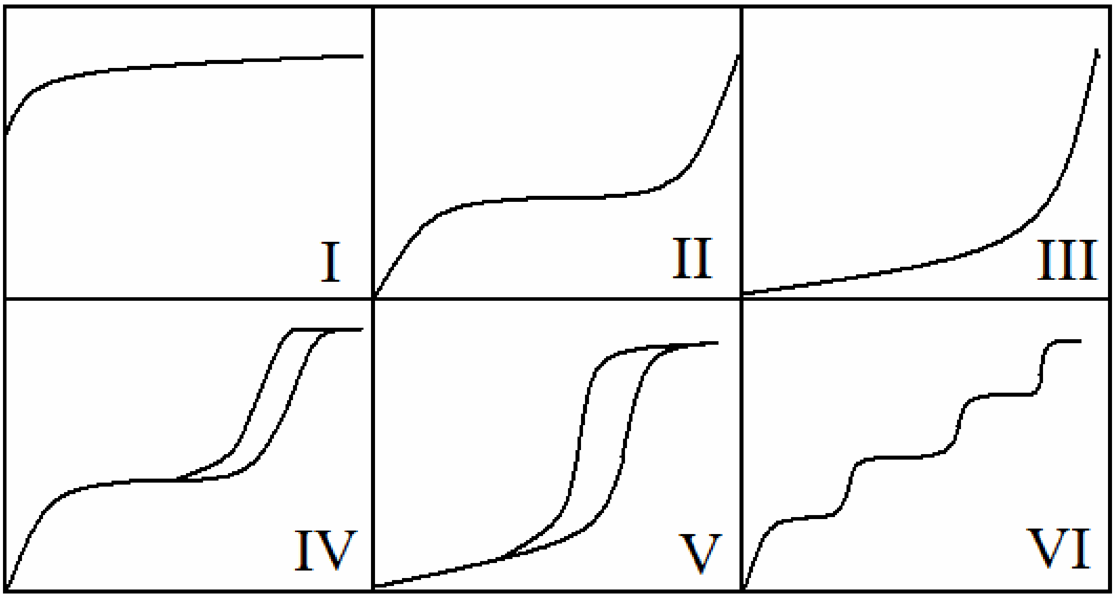

Figure 1.17 The six types of adsorption/desorption isotherm, where the x-axis is relative pressure (P/P_0) and the y-axis is volume adsorbed

The surface area is usually evaluated using the Brunauer, Emmett and Teller (BET) method,[33] which calculates the volume of the monolayer of adsorbed molecules on a given surface, with the surface area being calculated using equation (5):

$$S_{\mathrm{BET}} = n_{\mathrm{m}} A N_{\mathrm{A}} \times 10^{-18} \mathrm{~m}^2 \mathrm{~g}^{-1} \qquad (5)$$

where n_{m} is the number of molecules adsorbed at the monolayer coverage, A is the mean cross-sectional area of the gas molecule, in the case of nitrogen $A = 0.162$ nm^2 and N_{A} is the Avogadro number.

The BET method doesn't distinguish between the meso- or micro-porosity of the material; it is possible to calculate the micropore volume (V_{micro}) by applying the Dubinin-Radushkevich (DR) equation to the adsorption data or either of the α_s- and *t*-methods. The DR equation uses the logarithm of the volume adsorbed ($\log V_{a\text{ds}}$) plotted against the square logarithm of the inverse relative pressure ($\log^2 (P_0/P)$). The central region ($2 < \log^2 (P_0/P) < 15$) is then fitted to obtain a straight line which can be extrapolated to provide the volume of micropores ($\log V_{\text{micro}}$). The α_s-method is based on a comparison of the adsorption isotherm with that of a reference sample. The volume of N_2 adsorped is plotted against the α_s value (6) from the reference isotherm at each relative pressure. The micropore volume (V_{micro}) is established from the y-intercept of the extrapolated linear α_s-plot.

$$\alpha_s = V_a/V_{0.4} \qquad (6)$$

The *t*-method plots the volume of N_2 adsorbed against the multilayer thickness for the adsorption of N_2 on the non-porous reference material *t*. As with the α_s-method, the extrapolation of the linear region of the plot intercepts the *y*-axis and provides the micropore volume (V_{micro}).

The pore volume (V_{total}) of the material is calculated from the amount of N_2 adsorbed at a relative pressure (P/P_0) of around 0.95 – 0.99. The mesoporous pore size distribution is calculated using the Barrett-Joyner-Halenda (BJH) method,[34] which is based on the Kelvin equation, predicting the formation of liquid N_2 in the mesopores of a certain size. Thereby, the relation between P/P_0 and the pore radius can be deduced.

1.4.1.3 Transmission Electron Microscopy (TEM)

Transmission Electron Microscopy (TEM) is a key characterisation technique for porous solids, being a powerful method for determining the structure of the material. TEM generates an image of the structure of the material of interest, from which the pore size, pore wall thickness and lattice parameters can all be measured accurately, and can be used in conjunction with data obtained by other techniques (Figure 1.18).[35]

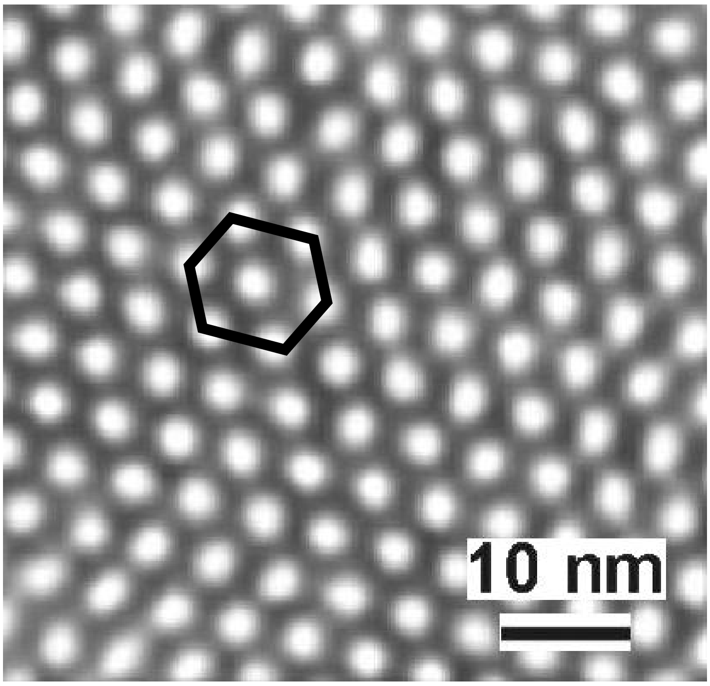

Figure 1.18 TEM image of hexagonal MCM-41[36]

TEM works in a manner similar to conventional light microscopy, the difference being the use of a beam of monochromatic electrons rather than a beam of light. The electrons are shone through the sample and the portion that is transmitted is then projected onto a phosphor screen. Reading the projected image is very intuitive; light areas of the image show areas where the electrons have passed through the sample easily, such as pores, and the darker areas show where the electrons have been slowed down and blocked, such as the silica pore walls (Figure 1.19).

Because electrons are used instead of light, resolution is a few thousand times better than a conventional light microscope, down to the order of a few angstroms (10^{-10} m). The increased resolution is due to the shorter wavelength of the electrons compared with the wavelength of visible light. Maximum resolution can be determined using equation (7):

$$d = \lambda / (2\, n \sin \theta) \qquad (7)$$

where d is the minimum separation that can be resolved by the microscope, λ is the wavelength and n is the refractive index (1 in the vacuum of an electron microscope). Resolution and d are inversely proportional.

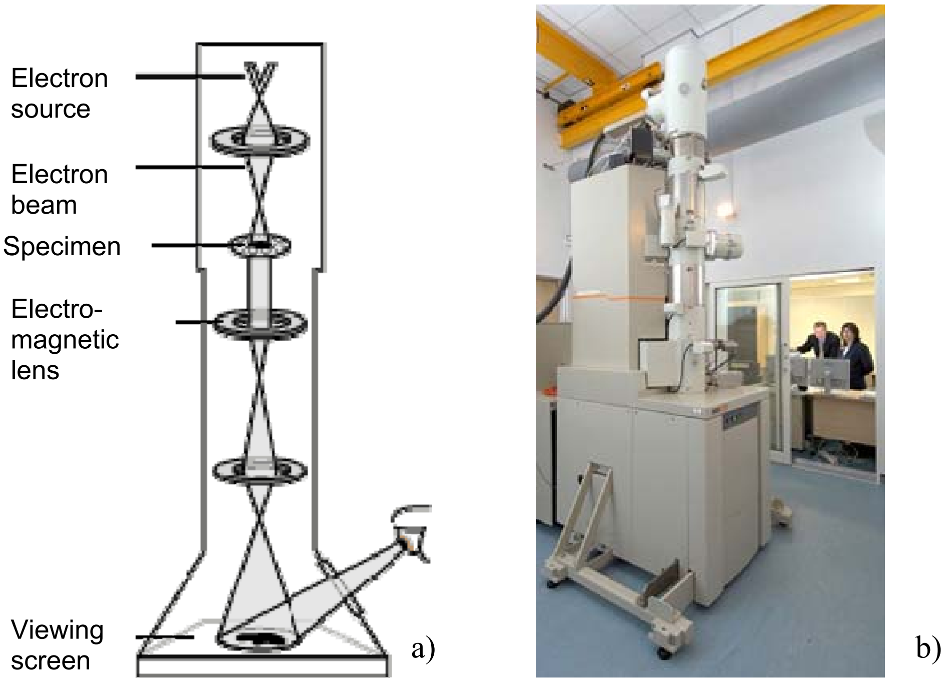

Figure 1.19 a) Diagram of a Transmission Electron Microscope. b) Field Emission Transmission Electron Microscope[37]

1.5 Catalysis

A common use of porous solids is in heterogenous catalysis and of most interest is the introduction of transition metals into the mesoporous silicas. Catalysis is an important and ever expanding area of chemistry, allowing reactions to be more selective and occur with lower energy requirements, becoming more favourable with more and more companies aiming to become ‘green’. Heterogeneous catalysis involves the catalyst being in a different phase to the reaction materials, such as a solid catalyst used in either gaseous or liquid reactions. This has the advantage of easy phase separation once the reaction is complete, usually allowing the catalyst to be recycled and reused.

Mesoporous silicas tend to be catalytically inert and for that reason they are typically doped with an active metal. Normally, there are four general methods for introducing a metal into the silica structure:

1. Primary modifications: direct grafting or impregnation onto the surface using surface silanols of the porous material;
2. Secondary and higher-order modifications: grafting onto a pre-functionalised surface;
3. One-pot synthesis of functionalised silica;
4. Further treatment of materials prepared under methods 1-3 such as heating, evacuation, calcination or reduction.

Mesoporous materials are well suited to catalytic applications due to their advantageous physical properties, primarily their high surface area is favourable for high catalytic activity. Additionally, they tend to have a large pore size as well as having the structural strength not to degrade during reactions. Secondary considerations when discussing the advantages of using mesoporous materials as catalysts are the ease of catalyst recovery, recyclability, minimising metal leaching and providing a catalyst where environmentally damaging reagents or materials are not necessary.[38]

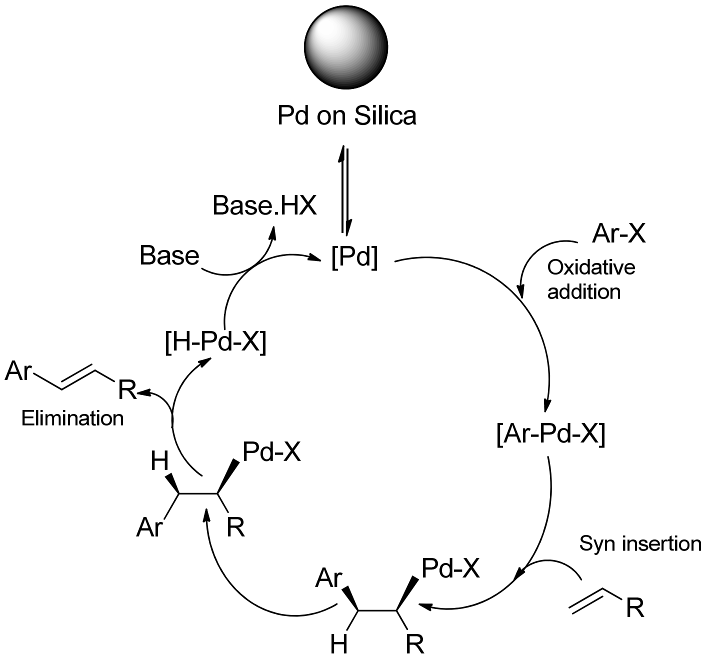

Figure 1.20 Mechanism of the Heck reaction over silica-supported Pd catalysts[39]

Palladium has been extensively reported as being supported on silica for a variety of catalytic reactions.[40] The Heck reaction is a significant example,[41] which allows the arylation, alkylation or vinylation of alkenes by carbon-carbon bond formation of the alkene with aryl halides. A wide range of different palladium complexes have been supported on silica and found to be excellent catalysts for the Heck reaction (Figure 1.20) with negligible metal leaching: Pd^{II}-pincer complexes[42], Pd^{II}-schiff base complexes[43], Pd^{II}-carbometallated palladacycle complexes[44], Pd^{II}-non-symmetrical salen-type coordination complexes[45], Pd^{II}-thiol and Os-cinchona alkaloid complexes,[46] as well as functionalised silica-Pd, Pd nanoparticles in silica[47] and ionic liquid-coated Pd in silica.[48] Silica-supported palladium catalysts have also proven to be an effective catalyst for other carbon-carbon cross-coupling reactions, such as the Sonogashira[49], Suzuki-Miyaura[50] and Stille[51] reactions, as well as hydrogenation reactions and the selective oxidation of alcohols.

1.5.1 Selective Oxidation of Alcohols

The selective oxidation of alcohols to aldehydes is one such process which can be catalysed by heterogeneous catalysts and there are a wide range of catalysts available to oxidise primary alcohols, secondary alcohols, diols and polyols.

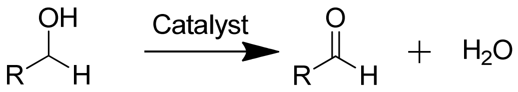

Figure 1.21 The selective oxidation of an alcohol to its aldehyde

The common problem in the oxidation of alcohols is in selectivity, where unwanted side reactions or over oxidation can occur, therefore, this requires the careful choice of the catalyst used and can often require the use of a promoter.[52] There has been extensive work using platinum, ruthenium, palladium and gold catalysts for the selective oxidation reaction, with most studies employing platinum and palladium due to their high activity and selectivity. Of interest here is the reaction using palladium catalysts. Palladium clusters have shown outstanding activity and selectivity towards a range of primary alcohols but are limited by rapid deactivation.[53] Investigations by Lee *et al.*[54] have found evidence that catalyst deactivation is caused by the formation of metallic palladium and that a surface layer of palladium oxide over the clusters is essential for maintaining highly selective oxidation activity. The reaction mechanism has been described as a dehydrogenation of an allylic alcohol coordinated to a cationic palladium species, followed by oxidation of the surface hydride.[55]

1.6 References

1. R. Schlogl, *Angew. Chem. Int. Ed.,* 2003, **42,** 2004.
2. http://www.chemheritage.org/discover/chemistry-in-history/themes/petrochemistry-and-synthetic-polymers/petrochemistry/houdry.aspx, 05/01/2011.
3. C. E. Fairhurst, S. Fuller, J. Gray, M. C. Holmes and G. J. T. Tiddy, in *The Handbook of Liquid Crystals,* G. W. Gray, J. Goodby, D. Demus, H. W. Spies, V. Vill, Wiley-VCH, Weinheim, 1998.
4. B. Jonsson, B. Lindman, K. Holmberg and B. Kronberg, *Surfactants and Polymers in Aqueous Solution,*Wiley, Chichester, 1998.
5. G. T. Barnes and I. R. Gentle, *Interfacial Science,* Oxford University Press, Oxford, 2005.
6. K. S. Birdi, *Coll. Poly. Sci.,* 1983, **261,** 45.
7. D. Lopez and M. M. Velazquez, *J. Chem. Educ.,* 2007, **12**, 327.
8. J. N. Israelachvilli, D. N. Mitchell and B. W. Ninham, *J. Chem. Soc. Faraday Trans. II,*1976, **72,** 1525.
9. http://barrett-group.mcgill.ca/teaching/liquid_crystal/LC02.htm, 04/08/2011.
10. T. Arnold and D. Linke, *Curr. Protocols in Protein Sci.*, 2008, **53,** 48.
11. W. Zhou, J. Zhang, T. Xue, D. Zhao and H. Li, *J. Mater. Chem.,* 2008, **18,** 905.
12. http://www.microscopyu.com/articles/polarized/polarizedintro.html, 05/01/2011.
13. Y. Yamauchi and K. Kuroda, *Chem. Asian J.,* 2008, **3,** 664.
14. D. E. De Vos, M. Dams, B. F. Sels and P. A. Jacobs, *Chem. Rev.,* 2002, **102,** 3615.
15. J. S. Beck, J. C. Vartuli, W. J. Roth, M. E. Leonowicz, C. T. Kresge, K. D. Schmitt, C. T. W. Chu, D. H. Olson, E. W. Sheppard, S. B. McCullen, J. B. Higgins and J. L. Schlenker, *J. Am. Chem. Soc.,* 1992, **114,** 10834.
16. The Pluronic® types are block copolymers from BASF, http://www.basf.co.uk.
17. H. M. Hao and C. L. Chen, *Angew. Chem. Int. Ed.,* 2004, **43,** 980.
18. M. Mesa, L. Sierra and J. L. Guth, *Micropor. Mesopor. Mater.,* 2008, **112,** 338.
19. D. Y. Zhao, J. Feng, Q. Hua, N. Melosh, G. H. Frederickson, B. F. Chmelka and G. D. Stucky, *Science,* 1998, **279,** 548.
20. A. Vinu, J. Justus, D. P. Sawant, K. Ariga, T. Mori, P. Srinivasu, V. V. Balasubramanian, S. Velmathi and S. Alam, *Micropor. Mesopor. Mater.,* 2008, **116,** 108.

---

21. J. Wang, J. C. Groen, W. Yue, W. Zhou and M. O. Coppens, *Chem. Commun.,* 2007, 4653.
22. G. S. Attard, J. C. Glyde and C. G. Göltner, *Nature,* 1995, **378,** 366.
23. D. J. Mitchell, G. J. T. Tiddy, L. Waring, T. Bostock and M. P. McDonald, *J. Chem. Soc., Faraday Trans. I,* 1983, **79,** 975.
24. G. Wanka, H. Hoffmann and W. Ulbricht, *Macromolecules,* 1994, **27,** 4145.
25. A. Galarneau, H. Cambon, F. Di Renzo and F. Fajula, *Langmuir,* 2001, **17,** 8328.
26. K. Miyazawa and S. Inagaki, *Chem. Commun.,* 2000, 2121.
27. D. Li, X. Guan, J. Song, Y. Di, D. Zhang, X. Ge, L. Zhao and F. Xiao, *Colloid. Surface. A,* 2006, **272,** 194.
28. R. Ryoo, C. H. Ko, M. Kruk, V. Antochshuk and M. Jaroniec, *J. Phys. Chem. B,* 2000, **104,** 11465.
29. B. L. Newalkar and S. Komarneni, *Chem. Mater.,* 2001, **13,** 4573.
30. P. D. Yang, D. Y. Zhao, D. I. Margolese, B. D. Chmelka and G. D. Stucky, *Nature,* 1998, **396,** 152
31. P. Scherrer, Nachr. Ges. Wiss. Göttingen, *Math.-Physik. Klasse,* 1918, **2**, 98.
32. S. J. Gregg and K. S. W. Sing, *Adsorption, Surface Area and Porosity,* Academic Press, London, 1982.
33. S. Brunauer, P. H. Emmett and E. Teller, *J. Am. Chem. Soc.,* 1938, **60,** 309.
34. E. P. Barrett, L. G. Joyner and P. P. Halenda, *J. Am. Chem. Soc.,* 1951, **73,** 373.
35. http://nobelprize.org/educational_games/physics/microscopes/tem/index.html, 17/08/10.
36. http://www.princeton.edu/~cml/html/research/templated_ceramics.html, 17/08/10.
37. http://www.york.ac.uk/res/nanocentre/facilities/fetem.htm, 17/08/10.
38. D. J. Macquarrie, *Plat. Met. Rev.,* 2001, **45,** 102.
39. V. Polshettiwar, C. Len and A. Fihri, *Coord. Chem. Revs.,* 2009, **253,** 2599.
40. L. Yin and J. Liebscher, *Chem. Rev.,* 2007, **107,** 133.
41. V. Polshettiwar and A. Molnar, *Tetrahedron,* 2007, **63**, 6949.
42. K. Yu, W. Sommer, J.M. Richardson, M.Weck and C.W. Jones, *Adv. Synth. Catal.,* 2005, **347,** 161.
43. C. Gonzalez-Arellano, A. Corma, M. Iglesias and F. Sanchez, *Adv. Synth. Catal.,* 2004, **346,** 1758.

44. C. Venkatesan and A.P. Singh, *J. Catal.,* 2004, **227**, 148.
45. N.T.S. Phan, D.H. Brown, H. Adams, S.E. Spey and P. Styring, *Dalton Trans.,* **2004**, 1348.
46. B.M. Choudary, N.S. Chowdari, K. Jyothi, N.S. Kumar and M.L. Kantam, *Chem. Commun.*, **2002,** 586.
47. R. B. Bedford, U. G. Singh, R. I. Walton, R. T. Williams and S. A. Davis, *Chem. Mater.,* 2005, **17,** 701.
48. H. A. Kalviri and F. M. Kerton, *Green Chem.,* 2011, **13,** 681.
49. P. –H. Li and L. Wang, *Adv. Synth. Catal.,* 2006, **348,** 681.
50. E. B. Mubofu, J. H. Clark and D. J. Macquarrie, *Green Chem.,* 2001, **3,** 23.
51. N. Kim, M. S. Kwon, C. M. Park and J. Park, *Tetrahedron Lett.,* 2004, **45,** 7057.
52. G. J. Hutchings, *Chem. Commun.*, **2008,** 1148.
53. C. Keresszegi, T. Burgi, T. Mallet and A. Baiker, *J. Catal.*, 2002, **211,** 244.
54. A. F. Lee and K. Wilson, *Green Chem.,* 2004, **6,** 37.
55. T. Mallat and A. Baiker, *Chem. Rev.,* 2004, **104,** 3037.

CHAPTER TWO

MCM-41 TYPE MATERIALS

2.1 Introduction

The true liquid crystal templating (TLCT) approach developed by Attard *et al.*[1] was discussed in detail in the previous chapter and is of interest to this work as a basis to develop a methodology for a one-pot synthesis of nanoparticle-doped mesoporous silica using off-the-shelf reagents.

As mentioned in Chapter 1, liquid crystal templating (LCT) was found to be a repeatable, but not a predictable, methodology, whereas TLCT is an improvement as it is found to be both predictable and repeatable. TLCT utilises the surfactant at the concentration where a known mesophase occurs, whereas LCT occurs at a much lower surfactant concentration, below the critical micelle concentration. This is important when it comes to preparing materials with different surfactants; if a new surfactant exhibits an hexagonal mesophase it will template a material with hexagonal pores by TLCT but not necessarily by the LCT method.

Methods that allow a material to be designed reliably with pre-determined properties are highly desirable and TLCT has sparked an explosion of interest and the approach is still widely examined.[2] For example, it has been shown by El-Safty *et al.*[3] that the TLCT approach is a reliable method for preparing large, translucent, crack-free monoliths with control of the shape and structural morophology. Attard[4] continued his work to prepare porous metals for use as electrodes in batteries and sensors by templating platinum salts around the surfactant to produce platinum films with well-defined long-ranged porous nanostructure. Dag *et al.*[5] have prepared silica films and monoliths doped with Ag, Au and Pt nanoparticles in a one-pot synthesis utilising Attard's TLCT method by the addition of Ag^+, $[AuCl_4]^-$ and $[PtCl_6]^-$ salts into the surfactant/water mixture. They showed that the metal/complex ions are distributed within the mesoporous channels and can be reduced into metal nanoparticles by either chemical or thermal reduction, observing particles of 2 – 6 mn with platinum and silver and 5 – 30 nm with gold. A proposed schematic of the metal particles distributed within the mesoporous silica is shown in Figure 2.1.

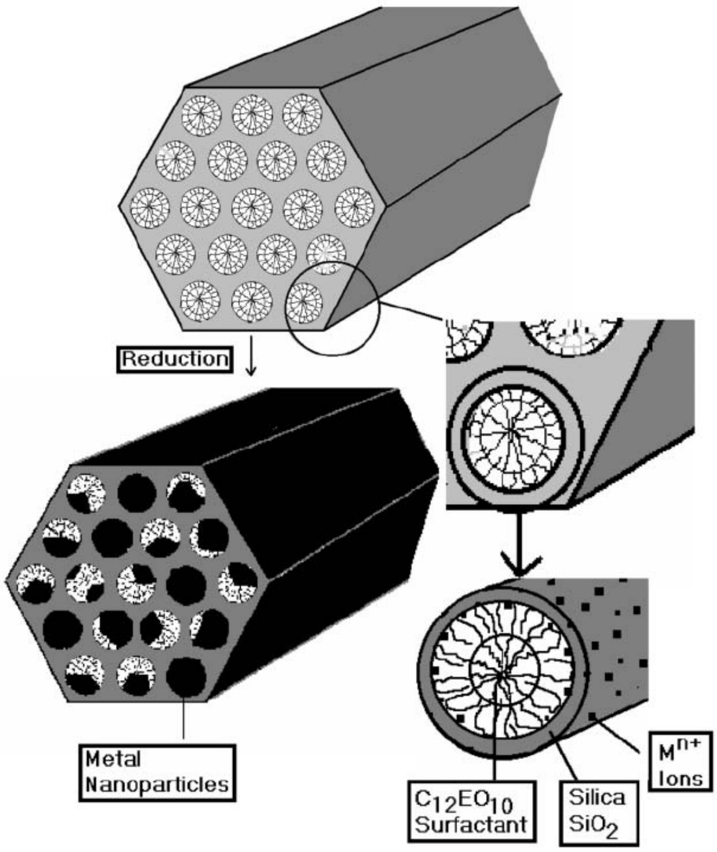

Figure 2.1 Schematic representation of a hexagonal mesoporous silica material before and after reduction of metal or complex ion

Mesoporous silica is catalytically inert and, for that reason, is typically doped with a metal, usually in the form of either metal particles or metal complexes. Normally there are four general methods for introducing a metal into the silicate structure:

1. Primary modifications; *i.e.* direct grafting of metal complexes or impregnation of metal particles into the structure using the surface silanols of the porous material;
2. Secondary and higher-order modifications; grafting complexes into a pre-functionalised surface;
3. One-pot synthesis of functionalised silica;
4. Further treatment of materials prepared under methods 1-3 such as heating, calcination or reduction.

Functionalisation can be introduced by subsequently modifying the inner surfaces of mesostructured silica with organic groups, or grafting. Typically this process is performed by reacting the free silanol groups of the pore surface with organosilanes,

$(R`O)_3SiR$, chlorosilanes, $ClSiR_3$, or silazanes, $HN(SiR_3)_3$. The functionalisation arises from the nature of the R group, which can vary significantly. Grafting has the advantage that the synthetic conditions used usually leave the mesostructure of the silica unchanged. However, lining the pore walls with organic material will reduce the porosity of the material; larger organic groups will result in a larger change.[6] Mal *et al.*[7] utilised grafting to prepare organic functionalised silica for a photochemically controlled system for compound uptake. They grafted coumarin to the pore openings of MCM-41 by performing the grafting step before removing the templating surfactant, a long-chain alkyltrimethylammonium halide, so preventing the coumarin from entering the pore structure. The template was then removed by extraction, not calcination, allowing active compounds such as cholestane derivatives to be inserted into the pores. The samples were then irradiated with UV light ($\lambda > 310$ nm) which dimerised the coumarin and sealed the pore openings. A second irradiation ($\lambda \sim 250$ nm) cleaved the dimers allowing diffusion-controlled release of the compounds.

Alternatively, impregnation is used to introduce metal particles into the porous structure after the silica has been fully prepared. Typically a metal salt solution is added to the silica, just enough to make the material ‘wet’, filling all the pores with the solution. The mixture will be well mixed to ensure good dispersion and the solvent allowed to evaporate before the silica is calcinced to form the metal particles from the salts, ideally well dispersed; this method is known as incipient wetness. A key factor to impregnation by incipient wetness is to control the metal particle size and dispersion. Thermodynamic control tends to lead to the formation of large metal particles, while kinetics leads to multinucleation and smaller metal particles.[8]

Introducing functionalisation by either grafting or impregnation involves, at minimum, a two-step synthesis to prepare the silica and then to functionalise it; this is, at best, time consuming and can be costly. To counter this problem, previous work in the group[9, 10, 11] proposed to introduce the metal particles during the silica preparation. Thus, surfactants were prepared which incorporated the metal precursor within the head group. The idea was that the metal precursor for the catalysts would already be contained within the surfactant and, when the material was calcined and the surfactant removed after templating, metal nanoparticles would remain within the pores of the silica. This was successfully demonstrated by preparing a surfactant containing a ruthenium head group[12]

(Figure 2.2) to be used with the true liquid crystal templating method, yielding a hexagonal MCM-41-like catalyst for use in hydrogenation[13] and oxidation.[14]

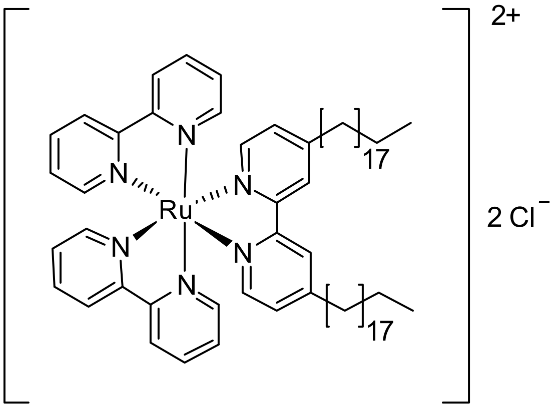

Figure 2.2 Ruthenium surfactant

Unfortunately attempts to repeat this method using other metals proved very difficult and a new method was required. Danks *et al.*[15] successfully prepared a cobalt containing surfactant with a tetradentate amine ligand (triethylenetetramine) and an alkylated bipyridine (Figure 2.3) at a range of chain lengths (12 < *n* < 19). The surfactants showed lyotropic liquid-crystal behaviour in water up to 100 °C exhibiting the micellar cubic and hexagonal phases. However, attempts to use these surfactants to prepare cobalt-doped mesoporous silica were unsuccessful as the surfactant precipitated out of solution on the addition of the silica source (TMOS).

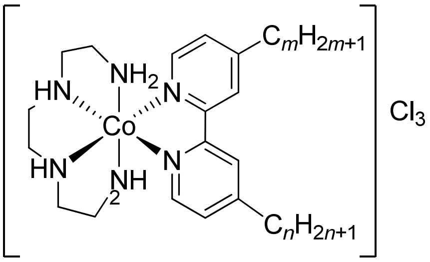

Figure 2.3 Cobalt surfactant

It is desirable to develop a method that allows the ability to predict the pore morphology as well as metal particle dispersion and size to allow flexibility in preparing a catalyst. Following the success with ruthenium, the group then began work towards this goal by incorporating simple metal salt precursors with non-ionic surfactants to prepare porous silicas containing metal nanoparticles.

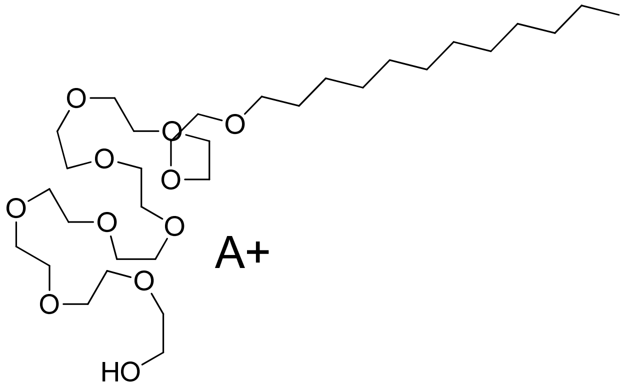

Figure 2.4 Complexation of metal salts with $C_{12}EO_{10}$

Attard's TLCT method, used the surfactant $C_{12}EO_{10}$ in a 50:50 ratio with water, to which ~5 wt% of a metal salt is added to the mixture before the addition of the silica source, tetramethoxylsilane (TMOS). The head group of the surfactant acts in the same manner to that of a linear crown-ether, interacting with the counter ion of a metal salt (Figure 2.4). The head group is thought to 'capture' the cation of the metal complex while the metal containing anion is dissolved in the aqueous region of the mesophase, next to the head group. As it is the aqueous region that the silica condenses and as pore walls are formed, it could be considered that the metal complex would be found at the surfactant/silica boundary. Once the material is calcined, the surfactant will be removed, condensation of the silica framework increases and the metal is free to form particles within the pores. Preparing MCM-41-like hexagonal materials using the true liquid crystal templating method proved successful for non-first row, right-hand-side, transition metals using simple salts such as $K_2[PdCl_4]$, $K[AuCl_4]$ and $K_2[PtCl_4]$.[16] These types of salts were not suitable for the first-row transition metals, as they were found to be too labile and hydrolysed readily to form the cationic metal aqua complex which resulted in them being unsuitable for templating. Therefore, a change in ligand was used. First, the oxalate ligand $K_3[M(C_2O_4)_3]$ was used, which proved successful for chromium(III), iron(III) and vanadium(III); however, when nickel and cobalt were attempted, the metals precipitated out of solution forming insoluble NiC_2O_4 and CoC_2O_4. EDTA was then used and found to be much more versatile, Na[Fe(EDTA)] and $Na_2[Ni(EDTA)]$ among the successful metal precursors used.

The synthesis of porous materials containing mixed-metal particles is also of interest and was investigated by the group.[17] They prepared MCM-41 type materials doped with bimetallic particles, namely Pd/Au from $K_2[PdCl_4]$ and $K[AuCl_4]$, Pt/Co from $K_2[PtCl_4]$ and $Na_2[Co\{EDTA\}]$, and Pd/Ru from $K_2[PdCl_4]$ and $Na_3[Ru\{EDTA\}]$. EDX analysis of the Pt/Co particles gave an average atomic ratio of 45 : 55 (Co : Pt), very close to the calculated predicted ratio. However, examination of individual particles showed the Co : Pt ratio varied from 44 : 56 to 97 : 3, suggesting that the different metal salts were not mixing well during preparation leaving particles with different metal ratios.

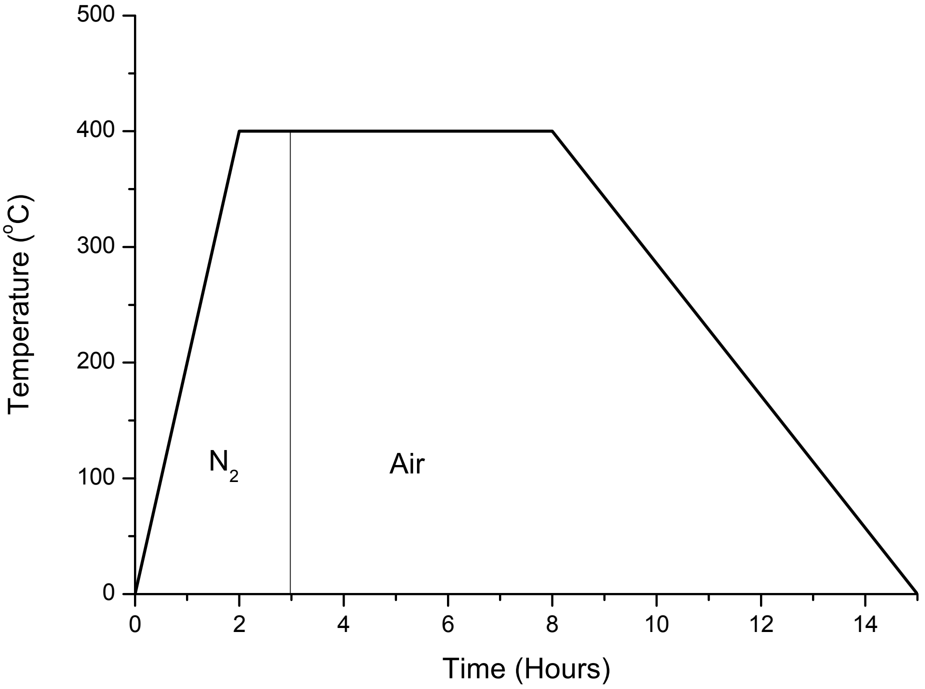

Figure 2.5 Temperature profile of the standard calcination method

In addition to preparing materials doped with a range of metal particles, the group also studied the effect of calcination temperature on the silica structure, finding that increasing the temperature above 700 °C has a detrimental effect on the material; indeed the surface area was too small to measure when calcination was carried out at 800 °C. The optimal temperature was found to be 400 °C, heated at a ramp rate of 3 °C min^{-1} under a flow of nitrogen and holding for 6 hours at that temperature, changing to a flow of lab air after the first hour (Figure 2.5).

A ruthenium doped MCM-41 prepared by King, using $Na_3[Ru\{EDTA\}]$ as precursor, was tested in the hydrogenation of 1-hexene and activity was compared with the Ru-silica prepared using the ruthenium-containing surfactant discussed previously (Figure 2.2). While both were found to be active, the catalyst prepared by the ruthenium-containing surfactant achieved five times higher conversion. The reduced activity is suspected to be caused by the metal particles forming larger than the silica pores reducing the effectiveness of the material as a catalyst. This will be discussed in more detail later in the chapter.

This work will investigate the preparation of nanoparticle-doped mesoporous materials in a methodical manner, beginning with non-doped materials before introducing the metal salts to the mixture to generate nanoparticles. The materials prepared by TLCT for this work were typically synthesised in batches of approximately 0.5 g, enough to perform characterisations. All materials were prepared in duplicate, at a minimum, to ensure repeatability and reliability of the results, and were characterised by BET porosimetry and X-ray diffraction with a selection imaged by transmission electron microscopy. Ultimately, the materials will be used in catalysis and those results will be discussed in Chapter 5.

2.2 Undoped MCM-41

In this work an MCM-41 derivative was prepared by the TLCT method using the $C_{12}EO_{10}$ surfactant (Figure 2.6) as a cheaper alternative to the $C_{12}EO_8$ surfactant used by Attard *et al.* $C_{12}EO_{10}$ was found to exhibit a hexagonal mesophase (Figure 2.7), observed by polarised optical microscopy (POM), when added to acidified water (pH 2) in a surfactant to water ratio of 3:2 (Figure 2.8A). TMOS was added to the mixture in a 4:1 water to TMOS ratio, to ensure all the water was used during the hydrolysis of the silica precursor. This generated a free-flowing mixture that exhibited no mesophase by POM. Evolved methanol was removed by dynamic vacuum (ensuring care was taken not to remove the water) until a viscous gel remained. When observed by POM the hexagonal mesophase was present once again (Figure 2.8B) and the material can be left on the open bench for 24 hours to ensure complete hydrolysis, resulting in a hard monolith ready to be calcined to remove the organic surfactant.

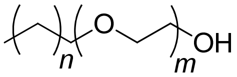

Figure 2.6 $C_{12}EO_{10}$ surfactant; $n = 11$, $m = 10$

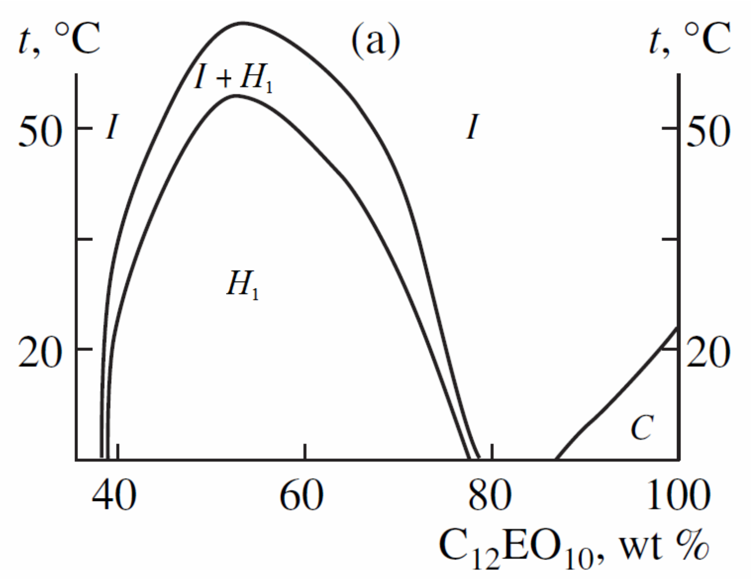

Figure 2.7 Phase diagram of the surfactant $C_{12}EO_{10}$ in water.[18] H_1 = Hexagonal, I = Isotropic liquid

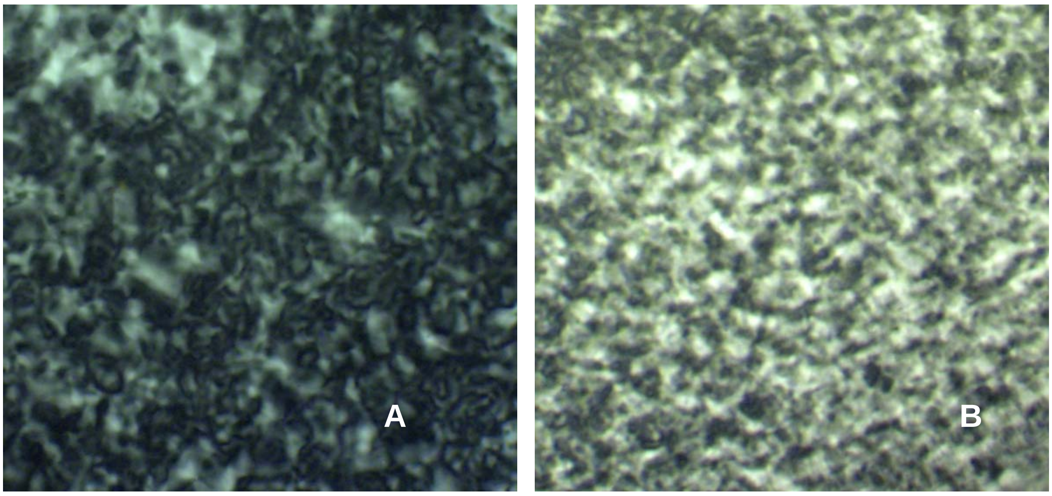

Figure 2.8 A) H_1 mesophase of the $C_{12}EO_{10}$ surfactant in water displaying a typical non-geometric texture; B) H_1 mesophase of the $C_{12}EO_{10}$ surfactant in water and TMOS, after hydrolysis and removal of methanol, also displaying the typical texture, although not as clearly.

The Brunauer-Emmett-Teller (BET) nitrogen adsorption isotherm is shown in Figure 2.9 along with a summary of the results obtained (Table 2.1). The surface area and pore diameters for the material are calculated from the BET analysis, while the *d*-spacing and lattice parameter are calculated using the XRD data. Pore wall thickness is the difference between the lattice parameter and the pore diameter. The isotherm is typical of the type IV isotherm associated with mesoporous materials and the lack of hysteresis is indicative of a narrow pore size distribution. The TEM images (Figure 2.10) show long, straight pores with a pore diameter of 35 Å, as well as the hexagonal structure in the end-on image (Figure 2.10B).

Table 2.1 Structural data for undoped MCM-41-like silica prepared by TLCT

Surface Area / $m^2\,g^{-1}$	Pore Diameter / Å	d-spacing d / Å	Lattice Parameter, a / Å	Pore Wall Thickness / Å
1103	34.6	41.9	48.4	13.8

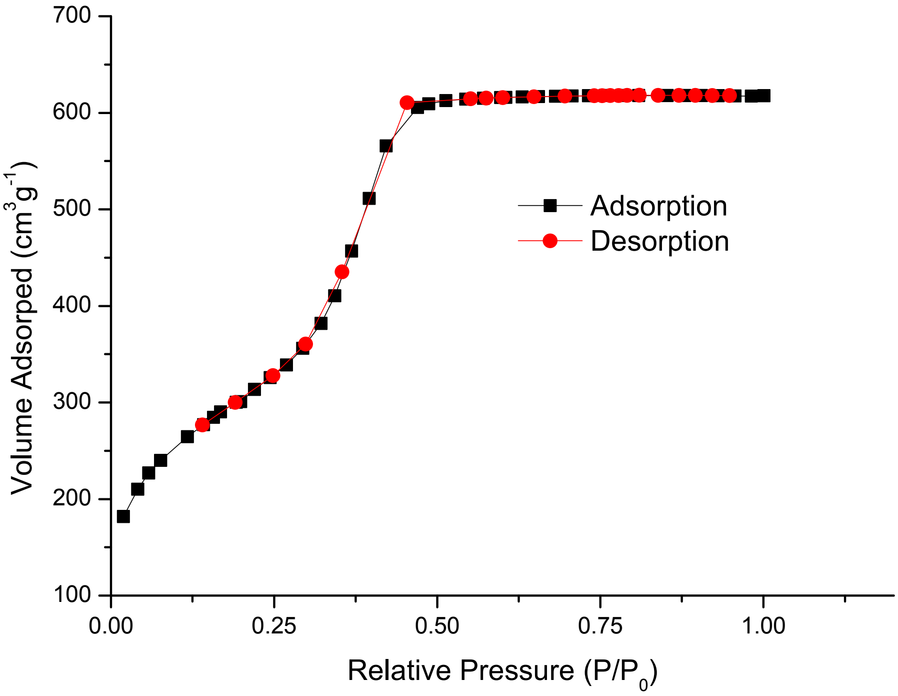

Figure 2.9 Adsorption-desorption isotherm of undoped MCM-41-like silica prepared by TLCT

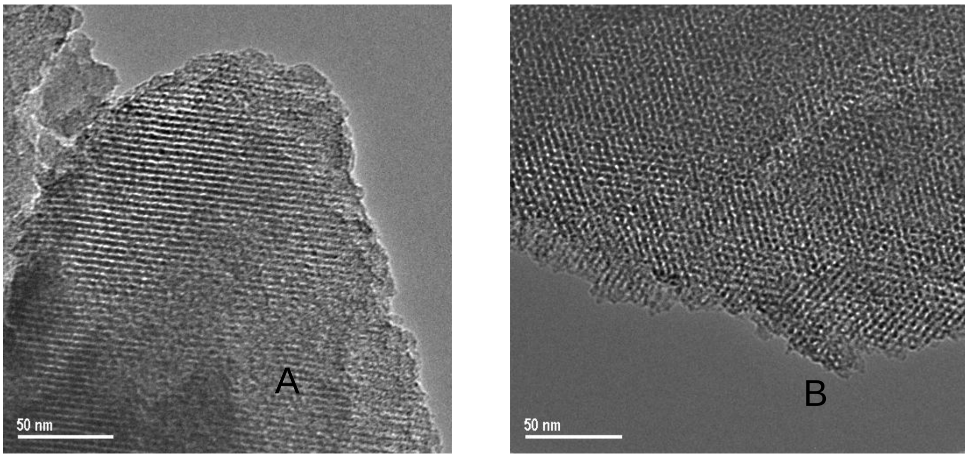

Figure 2.10 TEM images of undoped MCM-41-like silica prepared by TLCT; A) side-on view of pores B) end-on view of pores

The X-ray diffraction pattern (Figure 2.11) also confirms the presence of the hexagonal pore structure with the presence of the d_{10}, d_{11} and d_{20} reflections, representing the 2D symmetry of the structure. Due to the nature of liquid crystals, long-range order is present; as such the d_{11} and d_{20} reflections are observed, but they can be rather weak and can, on occasion, be difficult to identify. However, for a hexagonal unit cell, the relative peak positions can be calculated and thereby confirm the presence of the hexagonal structure using equation (1).

$$1/d_{hk}^2 = 4/3\ (h^2 + k^2 + hk)\ /\ a^2 \tag{1}$$

Table 2.2 Relative peak positions for the reflections of a 2D hexagonal lattice

Relative values of 1/d	*hkl*
1	(10)
√3	(11)
√4	(20)
√7	(21)
√9	(22)

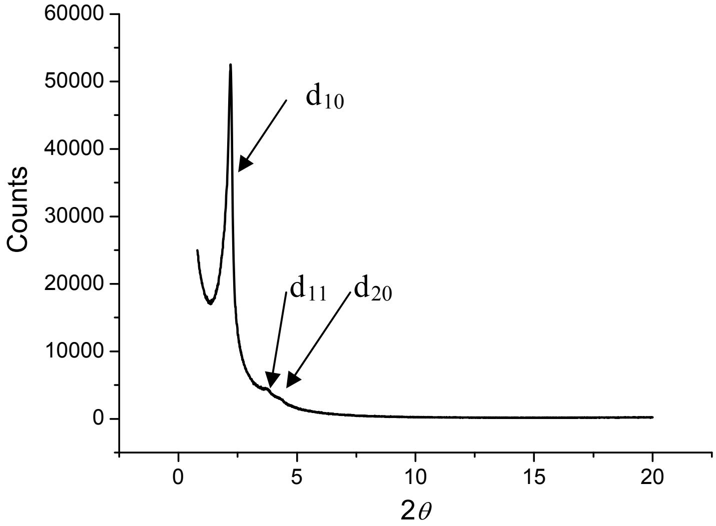

Figure 2.11 X-ray diffraction pattern of undoped MCM-41-like silica prepared by TLCT

Table 2.3 Identification of hexagonal pore structure using relative peak positions

	d_{10} / θ	d_{11} / θ	d_{20} / θ
Observed	2.10	3.68	4.21
Calculated	-	3.64	4.21

Several attempts were made to scale up the preparation to prepare large quantities but each was unsuccessful. For example, an attempt was made to prepare a 5 g batch of material, scaling up each reagent and using a larger flask to accommodate the mixture. While the porosimetry results were found to be as expected with a surface area of 1006 m^2g^{-1} and pore diameter of 33.5 Å, low-angle XRD (Figure 2.12) showed no evidence of hexagonal pore structure and, as such, d-spacing, the lattice parameter and pore wall thickness could not be calculated. It appeared that the methanol produced by such an increased volume of mixture was too difficult to remove fully and interfered with mesophase formation.

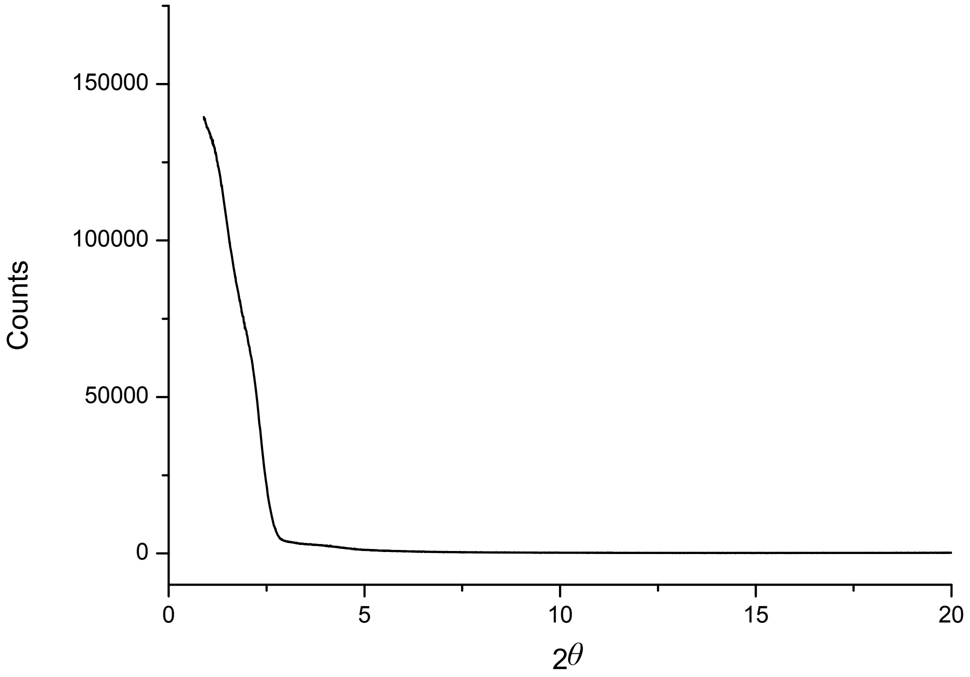

Figure 2.12 X-ray diffraction pattern of a large batch of undoped MCM-41-like silica prepared by TLCT

2.3 Palladium-doped MCM-41

Palladium was used initially in this work to ensure reproducibility of previous work and to further understand the effects of change on the system with a known material before moving onto different metals.

The palladium nanoparticles were introduced into the mesoporous structure of MCM-41 by introducing the metal salt into the sol-gel mixture before the addition of TMOS using the same method used previously by King. Thus 5 wt% of $K_2[PdCl_4]$ (with respect to the surfactant) was fully dissolved in the acidified water (pH 2) before the $C_{12}EO_{10}$ surfactant was added and thoroughly mixed. The mesophase of the sol-gel mixture is checked to ensure the presence of the hexagonal phase to show that the metal salt does not interfere with the liquid-crystalline properties of the mixture. To this, TMOS is then added and allowed to hydrolyse as described above, followed by the same calcination method to form the palladium-doped silica.

The prepared materials were characterised by porosimetry and X-ray diffraction and the results compared with those found previously by King (Table 2.4). Taking into account the experimental error for the apparatus (±5 % for the surface area measurement) there is little difference between the materials. Comparing the materials with the non-doped TLCT-MCM-41 described above shows a slight decrease in surface area and pore diameter, while the pore walls are found to be thicker; this difference in surface area is consistent with the palladium oxide particles filling some of the pores. The oxidation state and size of the palladium particles as well as the effect the cation has on material preparation is to be discussed in more detail in the course of this chapter.

Table 2.4 Structural data for Pd-doped MCM-41-like silica prepared by TLCT from the $K_2[PdCl_4]$ precursor

Source	Surface Area / $m^2 g^{-1}$	Pore Diameter / Å	d-spacing d / Å	Lattice Parameter / Å	Pore Wall Thickness / Å
Undoped	1103	34.6	41.9	48.4	13.7
King	908	27.5	39.8	46.0	18.5
This work	995	24.6	37.2	42.9	18.3

In 2009, Venezia *et al.*[19] prepared a palladium-doped MCM-41 catalyst *via* the incipient wetness technique. Nitrogen adsorption measurements determined the surface area of the support (prior to impregnation) to be 810 m^2g^{-1} with an average pore diameter of 26 Å, which was then loading with 1 wt% palladium, confirmed by X-ray fluorescence analyses. They identified the palladium to be palladium oxide from the X-ray diffraction patterns; however, the peaks were too small and broad to be used to calculate particle size using the Scherrer equation and, rather, they determined that the particles were at the edge of the detection limits (< 3 nm) which would imply the particles would be found within the pore structure.

These initial results demonstrate the reproducibility of the TLCT method to prepare palladium-doped MCM-41 materials as well as a clear comparison with traditional techniques such as incipient wetness impregnation.

2.3.1 Effect of the cation

It was noted that on calcination of the silica prepared using $K_2[PdCl_4]$, palladium oxide particles were formed; however, potassium particles will likely remain. Potassium will potentially affect the activity of the catalyst and should be removed to eliminate any effect it has. As such, the ammonium analogue of the salt was used, $(NH_4)_2[PdCl_4]$, as the ammonium cation will decompose to give NO_2 and H_2O and will be removed along with the surfactant during calcination, leaving just particles of palladium oxide within the silica. Therefore, preparations were carried out under identical conditions to compare $K_2[PdCl_4]$ and $(NH_4)_2[PdCl_4]$ to see if there is any effect using the different cations (Table 2.5). X-Ray diffraction patterns support the formation of the hexagonal structure for both materials (Figure 2.13).

Table 2.5 Structural data for Pd-doped MCM-41-like silica prepared by TLCT

Precursor	Surface Area / m^2 g^{-1}	Pore Diameter / Å	d-spacing d / Å	Lattice Parameter / Å	Pore Wall Thickness / Å
Undoped	1103	34.6	41.9	48.4	13.7
$K_2[PdCl_4]$	995	24.6	37.2	42.9	18.3
$(NH_4)_2[PdCl_4]$	1157	30.2	42.4	49.0	18.8

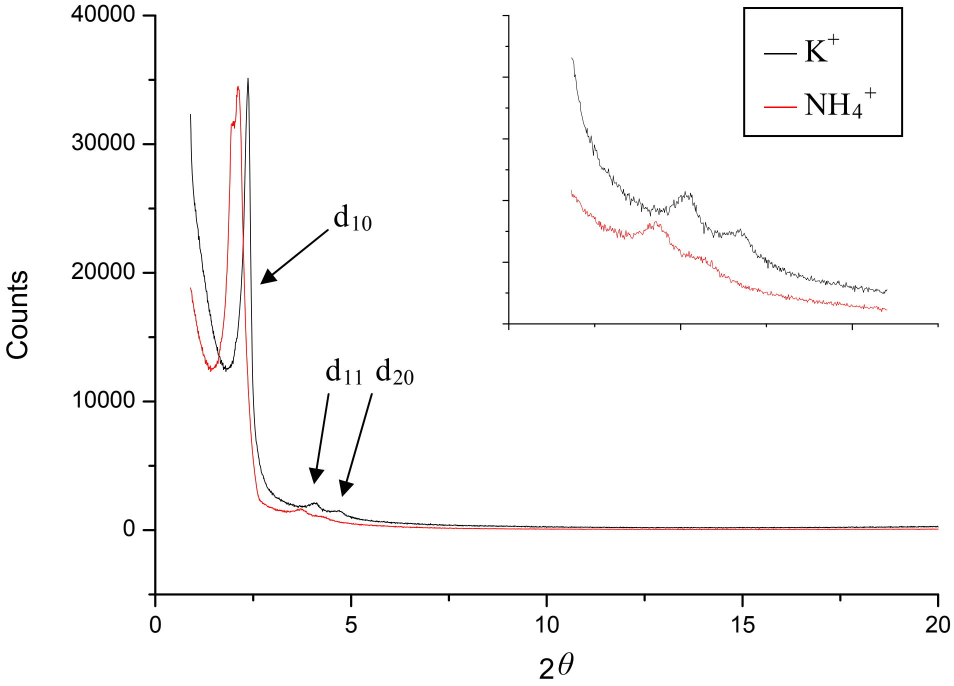

Figure 2.13 X-ray diffraction pattern of Pd-doped MCM-41-like silica prepared by TLCT using a) $K_2[PdCl_4]$ b) $(NH_4)_2[PdCl_4]$

Calculations from the XRD results and porosimetry analysis of the materials show that the ammonium cation appeared to have caused some pore swelling, increasing the surface area with a larger pore size and, therefore, a larger lattice parameter. Both materials show the same Type IV isotherm shape (Figure 2.14) expected of a mesoporous material.

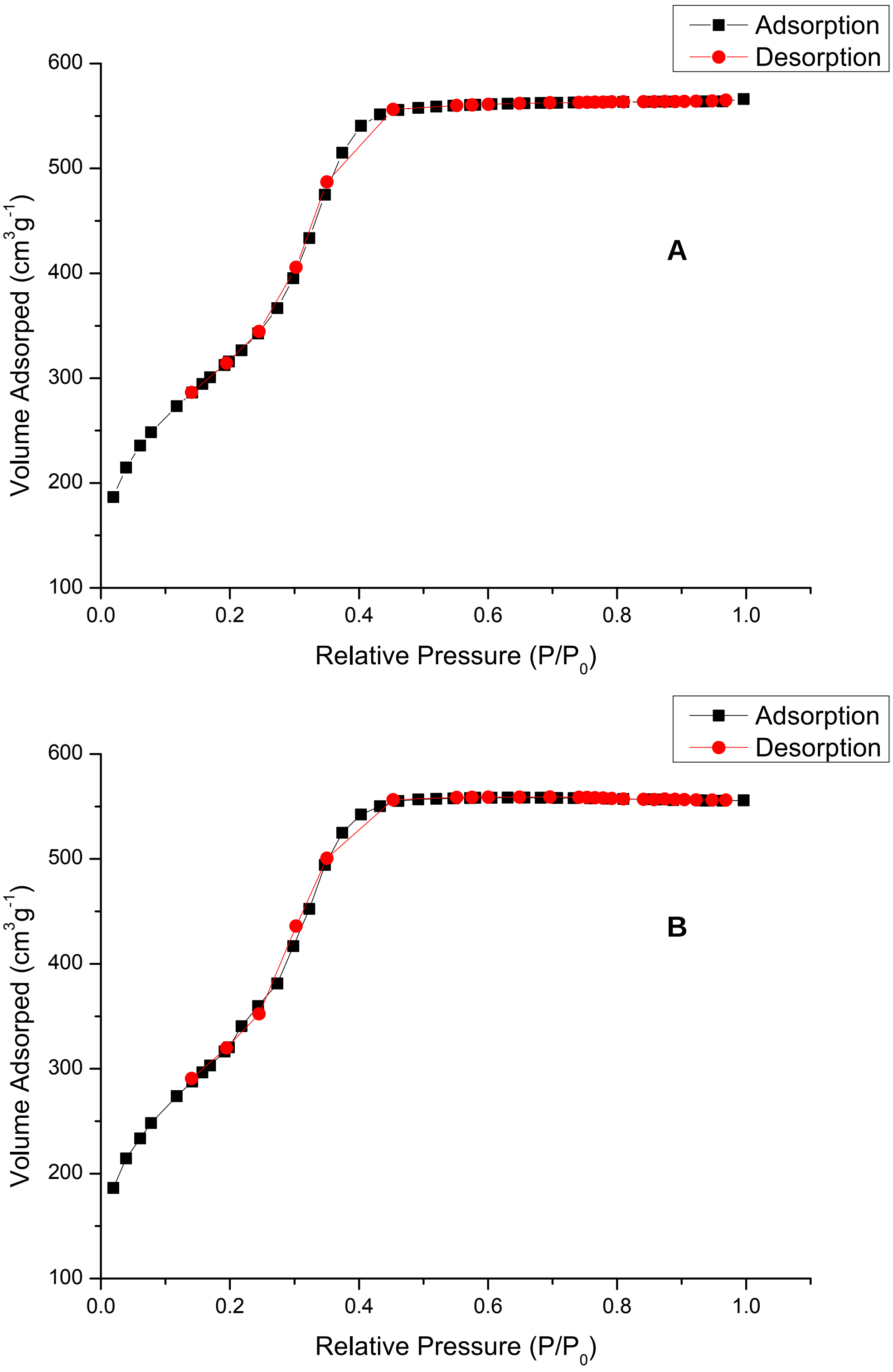

Figure 2.14 Adsorption-desorption isotherm of Pd-doped MCM-41-like silica prepared by TLCT using a) $(NH_4)_2[PdCl_4]$ b) $K_2[PdCl_4]$

While not a significant difference, it is clear that the change in cation has had an effect on the surface area and pore structure. This is possibly caused by the different temperatures at which the salts decompose.

The effect does not appear to be significant or detrimental to the formation of the desired material; therefore, $(NH_4)_2[PdCl_4]$ was continued to be used in preparation of palladium doped silicas.

2.3.2 Particle size

The size and location of the metal particles is an important factor to control. It is important for catalytic activity that the particles are small, well dispersed and contained within the pore network. Previous work in the group found that TLCT-MCM-41 doped with iridium or platinum showed small, well-dispersed particles, while gold and palladium formed larger particles that extended through pore walls occupying multiple pores. It was suggested that this was as a result of the stability of the metal source, with Pd and Au chlorometallates decomposing readily during calcination, while the other salts are more stable. This would suggest that by altering the calcination method or conditions it would be possible to prepare smaller particles contained within the pores. Small particles are desirable to make the best use of available material for catalytic reactions; small particles would yield a higher active surface area compared with the same quantity of metal in fewer, larger particles as more of the metal will be situated in the bulk of the particle and inaccessible for reaction (Figure 2.15).

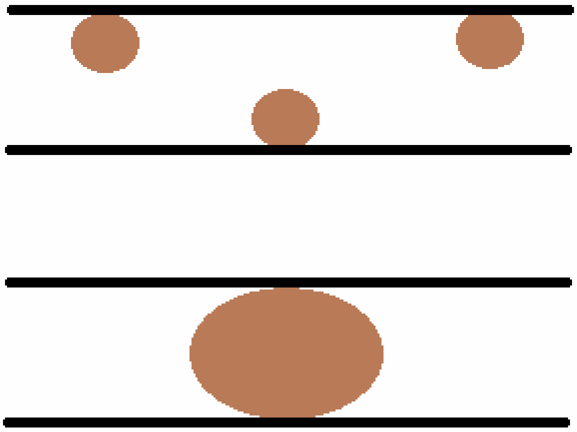

Figure 2.15 Schematic of particle size vs. surface area

TEM images (Figure 2.16) of the palladium-doped MCM-41 prepared using $(NH_4)_2[PdCl_4]$ show the metal particles, identified by the darker areas in the image, are significantly larger than the pores and have not been contained within even two or three pores as observed by King. The particles within the sample shown in Figure 2.16 have an average diameter of 21.2 nm, calculated from XRD patterns (Figure 2.17) using the Scherrer equation and a measured diameter of 24 nm from the TEM image. Likewise, material prepared with $K_2[PdCl_4]$ as the precursor, the Scherrer equation determined the average particle size to be 28.6 nm. It could be assumed that the palladium particles are beginning to aggregate before the silica walls are fully formed and hardened; therefore, they can easily force through the walls, becoming bigger than the pores as the palladium aggregates. If the silica walls are given the time and opportunity to harden before the palladium particles form, they may be solid enough to prevent the aggregation and keep the particles small and within each pore.

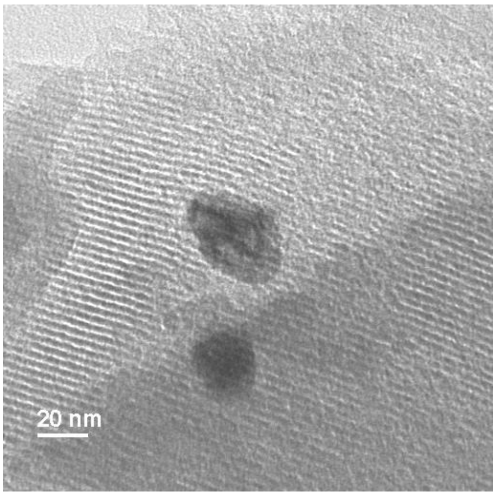

Figure 2.16 TEM image of Pd-doped MCM-41-like silica prepared by TLCT

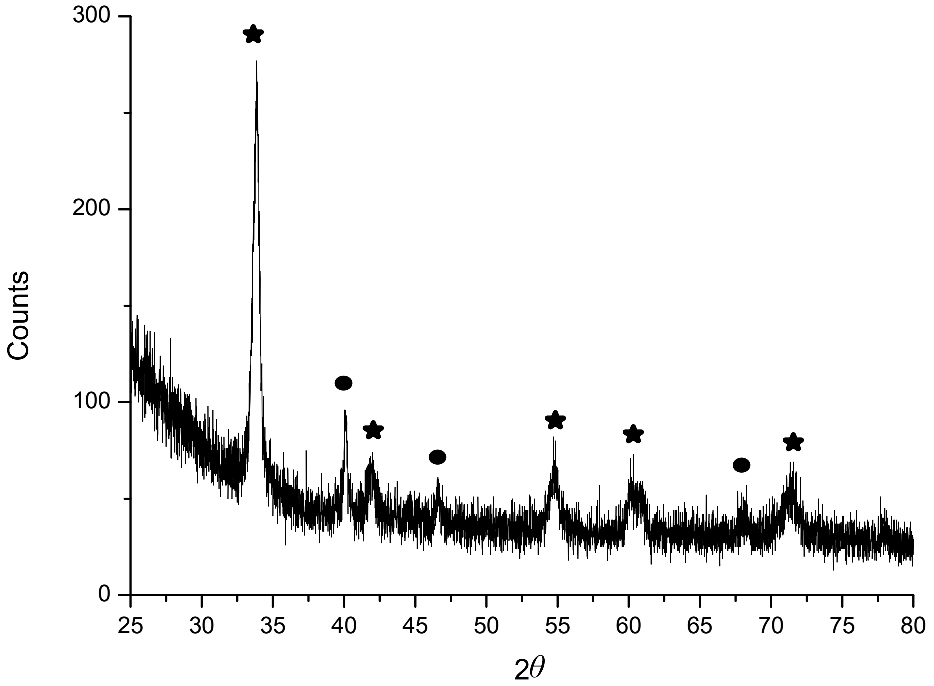

Figure 2.17 Wide-angle X-ray diffraction pattern of Pd-doped MCM-41-like silica prepared by TLCT, (★) peak positions of PdO, (●) peak positions of Pd metal

Thus, in an effort to confine the particles to within the pores, the calcination method was adjusted for a selection of samples. The standard method for calcination involves heating the as-synthesised samples to 400 °C at a rate of 3 °C per minute, all under nitrogen. This temperature is then held for one hour in nitrogen and a further 5 hours in air before cooling slowly. To allow the silica walls time to harden, the samples were given an extra drying period by heating to 100 °C at a rate of 1 °C per minute and holding for 24 hours under nitrogen before cooling back down to room temperature, they were then calcined fully by the same method as before. However, this did not appear to have any effect on the particle size, with particles of 18.9 nm, calculated from high-angle XRD using the Scherrer equation. Porosimetry and XRD characterisation (Table 2.6 and Figure 2.18) show that the modified calcination method had no adverse effect on the structure. It is clear that a more significant alteration needs to be made to the methodology to contain the palladium particles within the pore structure; this will be discussed in Chapter 4.

Table 2.6 Structural data for a Pd-doped MCM-41-like silica prepared by TLCT using modified calcination method

Surface Area / m^2 g^{-1}	Pore Diameter / Å	d-spacing d / Å	Lattice Parameter / Å	Pore Wall Thickness / Å
1196	32.5	42.6	49.2	16.7

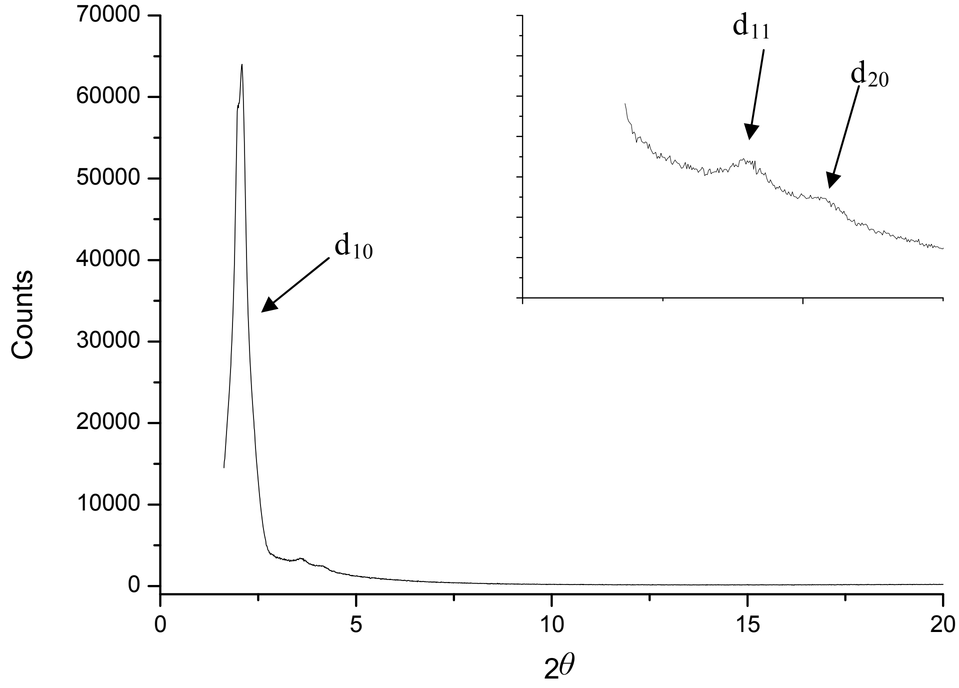

Figure 2.18 X-ray diffraction pattern of a Pd-doped MCM-41-like silica prepared by TLCT

In 2008, Domínquez-Domínquez *et al.,*[20] prepared palladium-doped MCM-41 using two different methods, simultaneous synthesis, where palladium nanoparticles dispersed in water were added to the CTAB solution during the synthesis of MCM-41, and incipient wetness. Nitrogen adsorption measurements determined the surface area of the two materials to be 875 m^2 g^{-1} and 970 m^2 g^{-1}, respectively, with average pore diameters of 27 Å and 39 Å. The first was comparable with other impregnation results, as expected; however, the latter is more comparable to the materials prepared here by TLCT. Interestingly, they observed palladium particles that appeared to be contained within the pores with incipient wetness, measuring 24.6 Å by TEM and 28.1 Å by CO chemisorption, and larger particles using the simultaneous synthesis method, 68.2 Å by TEM and 112.5 Å by CO chemisorption, which is consistent with the effect seen here.

From these results and those observed by Domínquez-Domínquez it is clear that a more stable precursor is required to control the particle size of palladium nanoparticles when using one-pot methods. Incipient wetness impregnation does not suffer the same problems as the pores are already fully formed before the palladium is introduced.

2.3.3 Oxidation state of the particles

In order to determine the oxidation state of the palladium particles within the silica, extended X-ray absorption fine structure (EXAFS) measurements were taken of a sample in three stages of preparation; as-synthesised, calcined and reduced by hydrogen. The data for the as-synthesised samples were taken prior to calcination, where silica hydrolysis had fully completed, the pores would have formed but the surfactant would still be present. The data for the calcined sample were taken after calcination, where the surfactant would have been removed, and the reduced sample were taken after a portion of the calcined sample was heated to 400 °C, under hydrogen, for 2 hours.

Table 2.7 Oxidation state of Pd

Sample preparation	Palladium Species	Oxidation state
As-synthesised	$K_2[PdCl_4]$	Pd^{II}
Calcined	PdO	Pd^{II}
Reduced	Pd Metal	Pd^0

The observed oxidation states, fitted from the EXAFS results (Table 2.7 and Figure 2.19) show the evolution of the palladium as it is calcined and reduced. It has been shown that a surface layer of palladium oxide is crucial for high activity in the selective oxidation reaction, while palladium metal rapidly deactivates.[21] This would suggest that the calcined Pd/silica would be the ideal state for the selective oxidation reaction. However, palladium catalysts would usually be reduced before being used in this reaction as it is expected that after reduction, the surface palladium metal will oxidise to give a thin layer of palladium oxide covering the palladium particles.

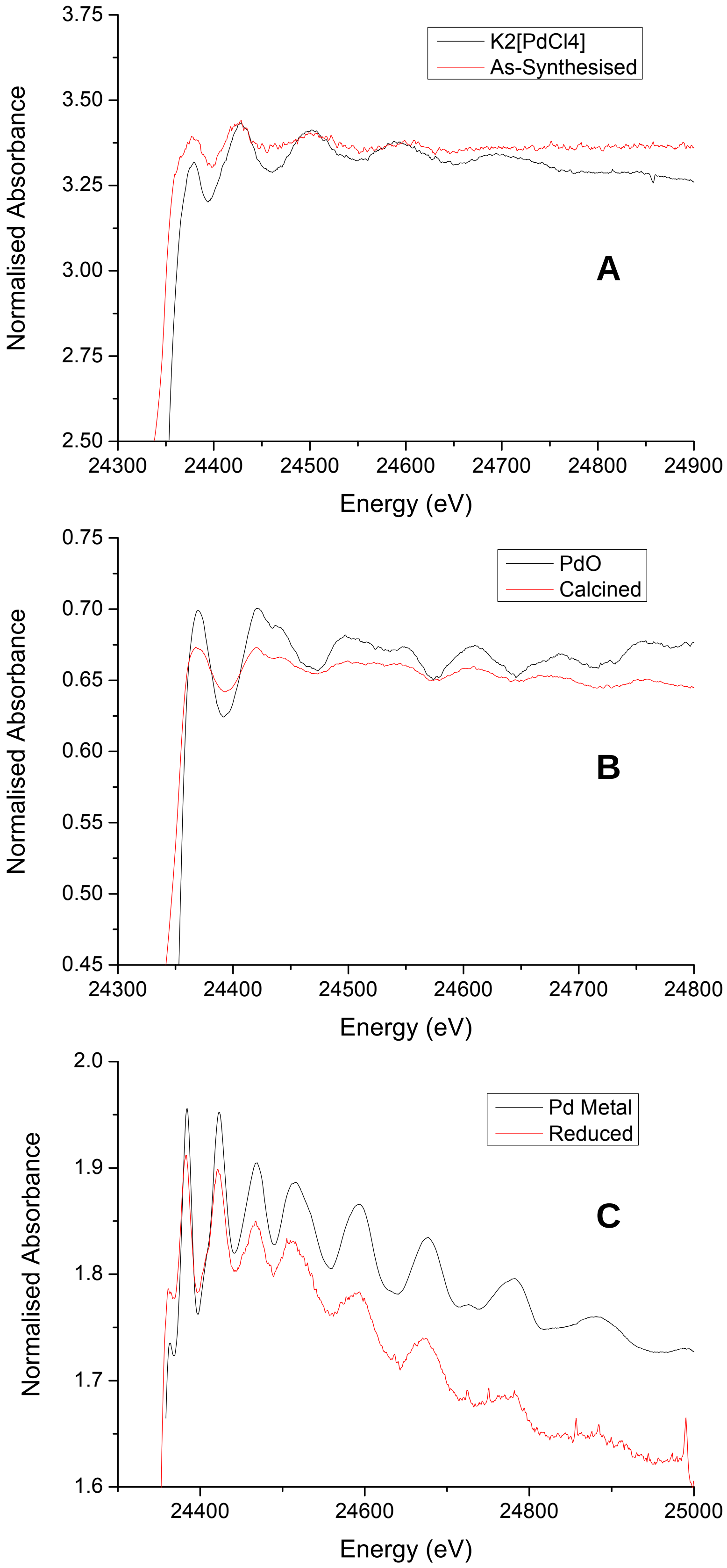

Figure 2.19 EXAFS results A) As-synthesised material with $K_2[PdCl_4]$ B) Calcined material with PdO standard C) Reduced material with Pd metal standard

The presence of $K_2[PdCl_4]$ within the as-synthesised sample is an assumption; the metal complex will have been added to acidified water and been present during the silica hydrolysis; it is expected to be still $K_2[PdCl_4]$ as the sample matches well with the EXAFS analysis of $K_2[PdCl_4]$.

In addition of EXAFS, wide-angle XRD is a useful technique for identifying the oxidation state of the metal particles; however, it is a weaker and more limited technique due to the lower energies used and, as such, smaller particles (< ~3 nm) will not be detected. Peak positions of the Pd-doped MCM-41-like silica prepared by TLCT can be identified and compared with known peak positions (Figure 2.20)

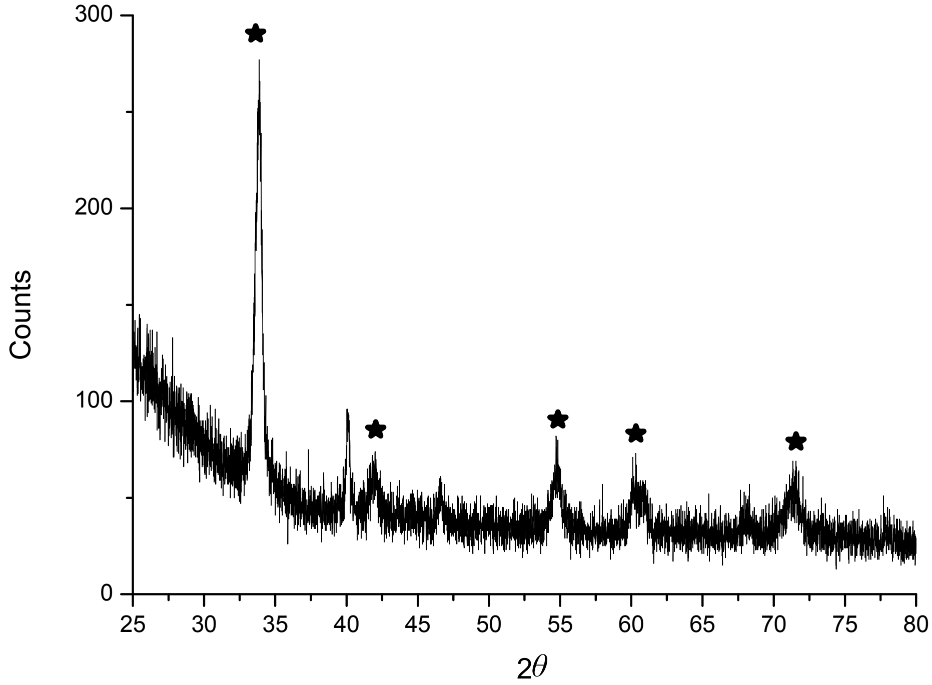

Figure 2.20 Wide-angle X-ray diffraction pattern of Pd-doped MCM-41-like silica prepared by TLCT, (★) peak positions of PdO

The standard calcination method used for all materials was described previously as a 6 hour heating at 400 °C with the first hour under a flow of nitrogen and then 5 hours under a flow of lab air; this yields a material containing palladium oxide particles as identified by EXAFS and wide-angle XRD. Interestingly, altering the method to keep the flow of nitrogen throughout the whole process (heating, at temperature and cooling) yields a material that contains palladium metal, without the need for a reduction step under hydrogen (Figure 2.21). Scherrer equation calculations show that the palladium metal particles form slightly larger at 22.0 nm compared to the 14.1 nm of palladium oxide.

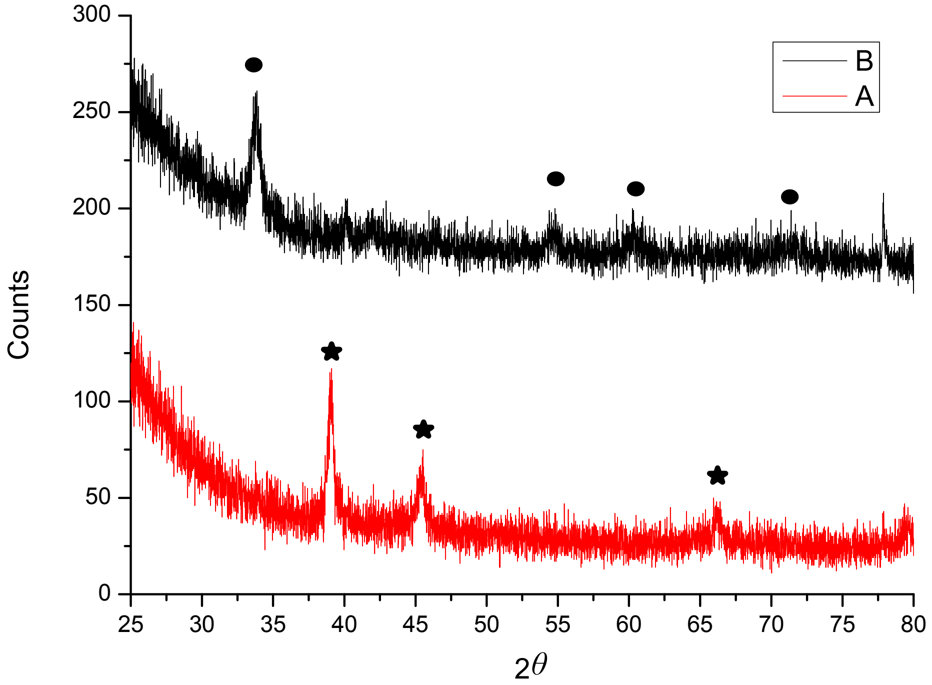

Figure 2.21 Low angle XRD of Pd-doped MCM-41-like silica prepared by TLCT with differing calcination methods A) Nitrogen only; (★) peak positions of Pd metal B) Standard calcination nitrogen/air; (●) peak positions of PdO

The desired palladium metal particles required for selective oxidation catalysis (Chapter 5) has been identified by EXAFS after reduction and by wide-angle XRD after a modified calcination method was tested. Should the activity of the two materials prove to be comparable, the modified calcination method will be much more favourable as it removes the need for a reduction step which is costly in time and energy.

2.3.4 Metal loading

The majority of the palladium-doped TLCT-MCM-41 materials thus far have contained a palladium loading of ~5 wt%. Lee *et al.*[22] showed that when a lower metal loading is used in incipient wetness impregnation, smaller particles are observed with improved dispersion within the pores and, therefore, improved catalytic activity is observed.

Therefore, a series of materials were prepared using increasing loadings of palladium metal from 0.01 wt% to 2.50 wt%, first of all to examine any change the amount of metal salt introduced to the sol-gel mixture might have on the mesoporous structure, as well as to prepare a range of materials for catalytic testing. The structural characterisation results are displayed in Table 2.8.

Table 2.8 Structural data for Pd-doped MCM-41-like silica prepared by TLCT

Metal loading	Surface Area / $m^2\ g^{-1}$	Pore Diameter / Å	d-spacing d / Å	Lattice Parameter / Å	Pore Wall Thickness / Å
0.00 wt%	1103	34.6	41.9	48.4	13.7
0.01 wt%	1101	34.1	41.9	48.4	14.2
0.05 wt%	1132	33.0	41.2	47.5	14.5
0.10 wt%	1158	38.0	45.9	53.0	14.9
0.50 wt%	1070	40.2	41.9	48.4	11.6
1.00 wt%	1207	35.3	41.7	48.2	12.5
2.50 wt%	1146	33.7	41.9	48.4	14.6

Increasing the palladium loading from 0.01 wt% to 2.50 wt% has no significant effect on the material. While the values observed for surface area for all samples were within the experimental error of the porosimeter, there does appear to be an inconsistency with larger pore diameters and lattice parameter of the 0.1 and 0.5 wt% samples. Both these materials were prepared in duplicate with consistent characterisation results; the reason for their difference is unknown as there doesn't appear to be any trend caused by the different metal loadings.

It should be noted that preparing materials in the quantities used here is difficult at the lower loadings as only 0.08 mg of $(NH_4)_2[PdCl_4]$ is required for a loading of 0.01 wt%, which is difficult to weigh out precisely.

These results show that there can be confidence that the addition of the palladium salt does not detrimentally affect the mesophase of the surfactant or the condensation of the silica, allowing MCM-41 like mesoporous silica containing palladium nanoparticles to be prepared by a one-pot synthesis.

2.4 Other transition metals in MCM-41

2.4.1 Platinum

It was previously noted that King observed larger particles for palladium-doped silica and smaller particles, contained within the pores, for platinum-doped silica. It is the intention to repeat this effect and determine the cause for the difference. Initially a direct repeat of her preparation will be performed using $K_2[PtCl_4]$, however as was discussed previously, $(NH_4)_2[PtCl_4]$ will then be used in preference to remove the potassium from the equation.

The BET nitrogen adsorption results (Table 2.9) for platinum-doped silica compares well with those prepared by King and are similar in magnitude to the Pd silica shown previously. Likewise, materials prepared with the ammonium salt show an increased surface area.

Table 2.9 Structural data for Pt-doped MCM-41-like silica prepared by TLCT

Precursor	Surface Area / $m^2\ g^{-1}$	Pore Diameter / Å	d-spacing d / Å	Lattice Parameter / Å	Pore Wall Thickness / Å
Undoped	1103	34.6	41.9	48.4	13.7
$K_2[PtCl_4]$	977	27.1	37.8	43.6	16.5
$K_2[PtCl_4]$*	838	26.5	39.8	45.9	19.4
$(NH_4)_2[PtCl_4]$	1163	25.0	39.2	45.2	20.2

*Result from King's work

The TEM images (Figure 2.22) show the clear pore structure with long straight pores; however, it is clear the particles formed were larger than the pores. While the particle size is much smaller than those seen in palladium-doped silica, the platinum particles are still larger than those measured by King (8.6 nm diameter from TEM and 13.5 nm using the Scherrer equation), forming larger than the pores (3.9 nm diameter) and, on average, filling 2 – 3 separate pores. These measurements were repeated and found to be consistent, which would suggest a key limitation to relying on TEM images for material characterisation; while the images collected may show good pore structure and metal nanoparticles, they are only isolated snap-shots of the bulk material and small particles contained within pores in one region may not be representative of the whole.

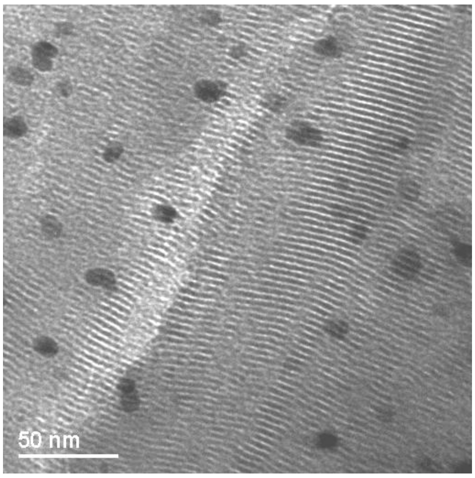

Figure 2.22 TEM image of Pt-doped MCM-41-like silica prepared by TLCT

Yao *et al.*[23] characterised platinum-doped MCM-41 impregnated by three different methods; equilibrium adsorption (EA), ion exchange (IE) and vacuum evaporation impregnation (VEI). VEI was a new preparation method where the aqueous platinum precursor and MCM-41 were stirred and heated in a round-bottom flask with the outlet connected to a distillation chamber and a vacuum applied. While each method was successful in producing the desired material (Table 2.10) they demonstrated that the MCM-41 structure collapsed when exposed to an aqueous medium at high pH, suggesting an attack of the hydroxide groups on the Si atoms of MCM-41 which leads to the cleavage of Si-O bonds. This is consistent with the method used by Shi *et al.*[24] to remove the silica template in the synthesis of self-supported mesoporous cobalt and chromium nitrides.

Table 2.10 Structural data for Yao's Pt-doped MCM-41 silica

Precursor	Method	Surface Area / $m^2\ g^{-1}$	Pore Diameter / Å	Loading / wt%
$Pt(acac)_2$	EA	1130	24.65	0.39
$[Pt(NH_3)_4]^{2+}$	IE	897	28.07	0.29
$[Pt(NH_3)_4]^{2+}$	VEI	897	28.07	1.26

Sobczak *et al.*[25] carried out a study in 2007 which included a comparison of platinum doped MCM-41 with the parent, undoped MCM-41 (Table 2.11). They used the standard methodology for preparing the MCM-41[26]; however, the observed pore wall thickness is thinner than usually observed; no explanation for this difference was given. With a platinum loading of 1 wt%, they observed very little change in the structural characterisation, with the slight decrease in surface area and pore volume being accounted for by the platinum particles occupying the pores. Using time-of-flight secondary mass spectrometry (TOF-SIMS) investigations, they identified the presence of Pt^-, PtO^- and PtO_2^- ions in abundance as well as lower amounts of $PtCl^-$ and $PtClO^-$ species, providing evidence that calcination at 450 °C is not sufficient to remove all of the chlorine from the material. Additionally, they identified the presence of a small amount of chlorine in the parent MCM-41, originating from the template used during synthesis. This should be taken into account for any applications where chlorine could poison the catalytic activity.

Table 2.11 Structural data for Sobczak's Pt-doped MCM-41 silica

Precursor	Surface Area / $m^2\,g^{-1}$	Pore Diameter / Å	Pore volume / cm^3g^{-1}	Pore Wall Thickness / Å
None	990	36	0.89	9
$H_2[PtCl_6]$	970	36	0.87	9

2.4.2 Gold

It has only been relatively recently that gold has been strongly considered as a catalyst, reviews in 1972[27] and 1985[28] observed a lack of activity with gold as a catalyst "Although the catalytic properties of gold are surpassed by those of Group VIII metals, especially palladium and platinum, possible applications of gold in catalytic processes have been widely studied" and "In spite of its low intrinsic activity, gold can influence the activity and selectivity of Group VIII metals." However, gold began to show its true nature in 1982 when Hutchings[29] discovered that gold was active for acetylene hydrochlorination. Hashmi and Hutchings[30] recently wrote a review of gold and its catalytic properties, discussing its use in hydrogenation, selective oxidation, nucleophilic addition and reactions involving carbon monoxide, stating that "gold has proven to be an effective catalyst for many reactions in which a catalyst had not been previously identified, and many new discoveries are still expected." The most notable discovery for the field of gold catalysis was the realisation that gold was effective for carbon monoxide oxidation reactions under mild conditions.

Due to the capacity for gold to oxidise carbon monoxide at low temperatures it has been proposed to use gold catalysts in the fuel cells for uses such as electric cars. Landon *et al.*[31] reported an Au/Fe_2O_3 catalyst for potential application in a combined polymer electrolyte fuel cell with a catalytic reformer. They prepared a stable gold catalyst that selectively oxidises carbon monoxide in the presence of excess H_2, H_2O and CO_2 within the environment of a fuel cell system.

Along with palladium, gold nanoparticles doped onto silica are another area of interest for selective oxidation catalysis.[32] Catalytic activity of gold is strongly related to the size of the metallic gold particles. Indeed, in the case of low temperature oxidation reactions, only small particles (< 5 nm) are found to be active at all.[33] As such it would be desirable to prepare materials for catalysis containing gold nanoparticles using the one-pot TLCT method.

In addition to their work with platinum, Sobczak *et al.*[34] prepared MCM-41 materials doped with gold nanoparticles. They used both incipient wetness impregnation and co-precipitation, where $H[AuCl_4]$ was added directly to the synthesis of conventional MCM-41, and compared their characterisations with each other and the parent MCM-41, as they did with platinum. In both materials they observed Au^0 particles and identified the hexagonal pore structure from the high- and low-angle XRD patterns, respectively. Doping the silica by incipient wetness impregnation showed little change in the surface measurements of the material, surface area reduced from 1076 m^2g^{-1} to 1049 m^2g^{-1}, which is within the experimental error, with the addition of gold, while the average pore diameter remained 39 Å and gold particle size was too small to be measured accurately (< 3 nm). However, co-precipitation reduced the surface area and pore diameter to 886 m^2g^{-1} and 29 Å and gold particles were observed to range from 3 – 18 nm by TEM, clearly larger than the pores. Additionally, they also observed that co-precipitation led to the formation of two forms of gold, metallic gold and $AuCl^-$, while incipient wetness impregnation formed only metallic gold.

Using $(NH_4)[AuCl_4]$ as precursor in exactly the same manner as with palladium and platinum previously, an Au-doped MCM-41 was prepared and characterised (Table 2.12). Low-angle XRD (Figure 2.23) confirmed the presence of the hexagonal pore structure with the characteristic d_{11} and d_{20} reflections and porosimetry results were consistent with previous materials prepared. High-angle XRD (Figure 2.24) was used to identify the oxidation state of the gold particles and calculate the average particle size, finding the peak positions to match with those of metallic gold. Using the Scherrer equation the average particle size was found to be 49.8 nm.

Table 2.12 Structural data for Au-doped MCM-41-like silica prepared by TLCT

Precursor	Surface Area / m^2 g^{-1}	Pore Diameter / Å	d-spacing d / Å	Lattice Parameter / Å	Pore Wall Thickness / Å
Undoped	1103	34.6	41.9	48.4	13.7
$(NH_4)[AuCl_4]$	1133	33.3	41.2	47.5	14.2

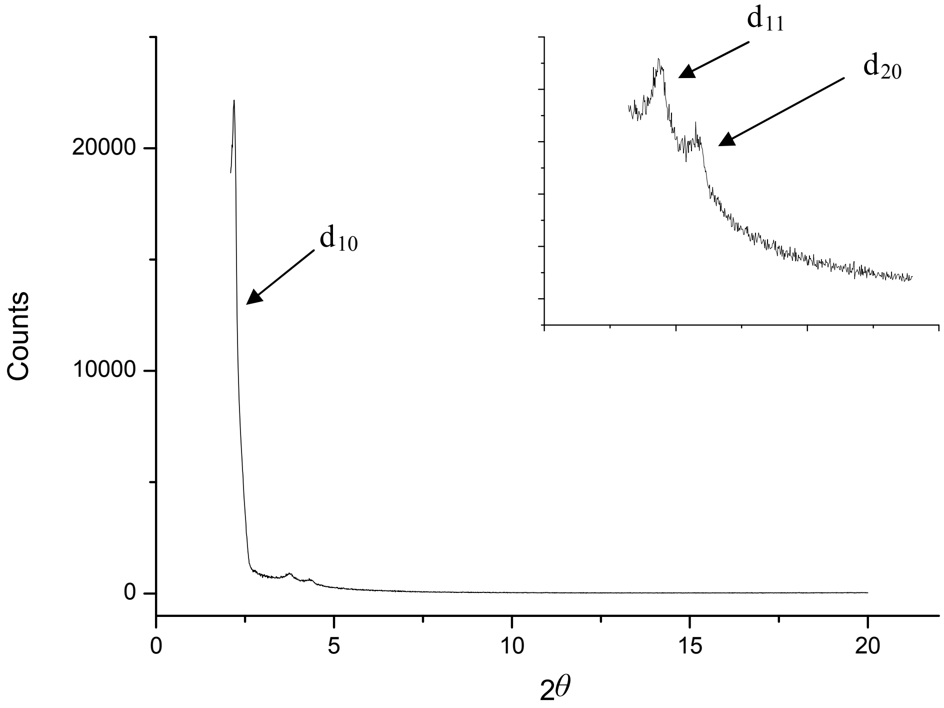

Figure 2.23 X-ray diffraction pattern of an Au-doped MCM-41-like silica prepared by TLCT

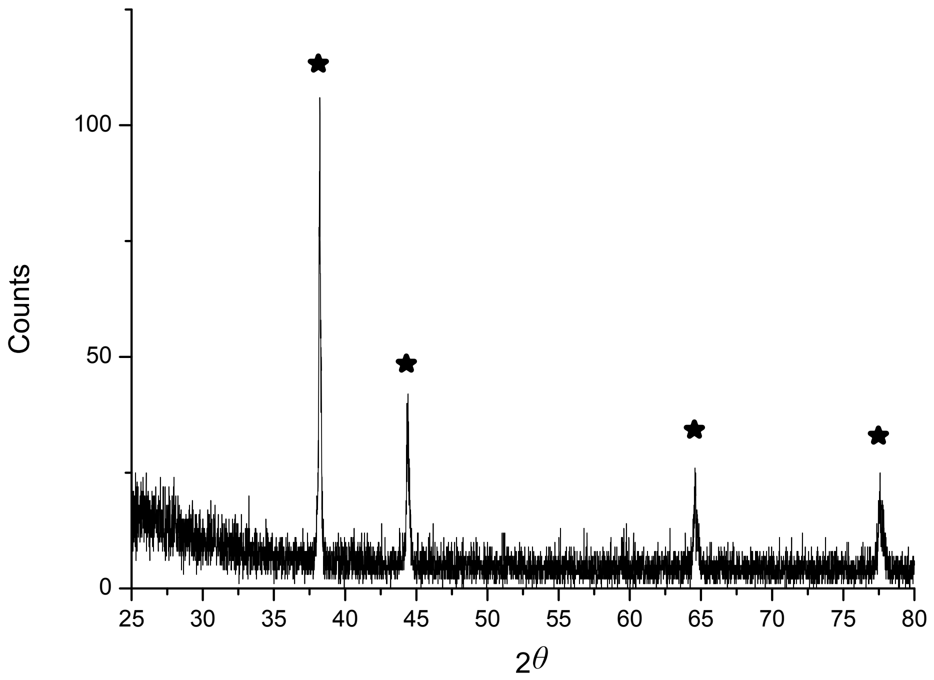

Figure 2.24 Wide-angle X-ray diffraction pattern of Au-doped MCM-41-like silica prepared by TLCT, (★) peak positions of Au metal

As with the palladium-doped silicas, a series of materials were prepared at different metal loadings from 0.01 wt% to 2.50 wt% for later catalytic testing (Chapter 5). The structural data (Table 2.13) shows a slight increase in surface area as the series progresses; however, this is not a significant effect and is within the experimental error of the equipment.

Table 2.13 Structural data for Au-doped MCM-41-like silica prepared by TLCT

Metal loading	Surface Area / $m^2 g^{-1}$	Pore Diameter / Å	d-spacing d / Å	Lattice Parameter / Å	Pore Wall Thickness / Å
0.01 wt%	933	29.6	43.6	50.4	20.7
0.05 wt%	987	33.1	48.5	56.0	22.8
0.10 wt%	1009	30.6	40.0	46.2	15.5
0.50 wt%	1086	34.4	44.0	50.8	16.4
1.00 wt%	1069	30.8	40.3	46.5	15.7
2.50 wt%	1109	32.2	41.3	47.8	15.5

As can be seen in the TEM image of the 2.5 wt% material (Figure 2.25) the metal particles are once again aggregating, becoming much larger than intended and are not contained within the pores. The average particle size, calculated from the Scherrer equation, was found to be 40.6 nm for this material. It was not possible to identify particles using either high-angle XRD or TEM for the lower loading materials, probably due to the lower limits of both detection methods, suggesting well dispersed, small particles, although this could not be confirmed.

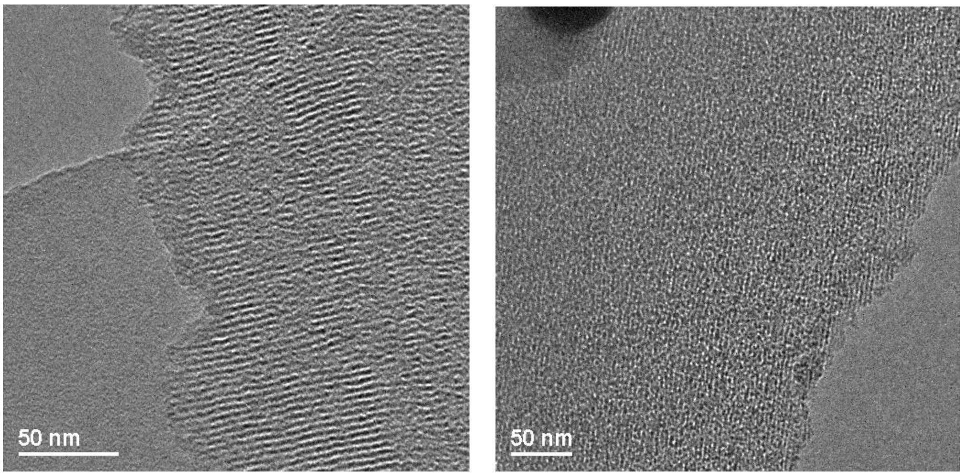

Figure 2.25 TEM images of Au-doped MCM-41-like silica prepared by TLCT

The addition of the gold precursor into the preparation has not adversely affected the structure of the silica, with evidence of long, straight, hexagonal pores. However it is clear that the gold precursor is unfavourable for preparing small particles, also shown by Sobczak's[34] work. Whether this can be corrected by using a different, more stable, precursor is worthy of investigation and will be discussed further in Chapter 4.

2.4.3 Bimetallic MCM-41

Catalysts commonly have to be promoted with additional metals to prevent or limit deactivation or to improve selectivity. For instance, cobalt-based catalysts supported on MCM-41 can be used in the hydrodesulfurisation of thiophene; however, the catalyst is deactivated by coke formation during the reaction. Venezia *et al.*[35] studied the possibility of adding palladium and gold to the cobalt catalyst to reduce the coking. By co-impregnation of cobalt and gold over palladium modified silica, they observed an increase in Co_3O_4 particle dispersion and increased cobalt reducibility which led to an increase in catalytic activity.

Surowiec *et al.*[36] prepared an MCM-41 material impregnated with FeCo nanoparticles by incipient wetness impregnation. They prepared a 5 wt% solution containing both metal ions and used this to impregnate the MCM-41. After calcination they identified ferromagnetic Fe nanoparticles stabilised with Co to form a nanocomposite.

King *et al.* synthesised an MCM-41 material using the TLCT method doped with platinum and cobalt metal precursors to form PtCo bimetallic particles. Initial EDX analysis found the ratio of metal within the material to be 45 : 55 (Co : Pt), close to the calculated value; however, closer analysis found that the ratio within specific particles ranged from 44: 56 to 97 : 3, suggesting the precursors had not mixed fully to yield particles of the correct mixture. They observed that the particles had magnetic properties similar to true PtCo bimetallic materials in spite of the range of compositions observed in the material.

As discussed previously, King prepared TLCT-MCM-41 materials doped with bimetallic nanoparticles; of interest here is the material prepared using the $K_2[PdCl_4]$ and $K[AuCl_4]$ precursors. A material was prepared using the $(NH_4)_2[PdCl_4]$ and $(NH_4)[AuCl_4]$ precursors for comparison (Table 2.14). King observed a reduction in surface area and pore diameter, presumably due to the bimetallic particles blocking some of the pores and leaving some of the pore structure inaccessible during porosimetry. However, the material prepared here shows very little difference from the parent, undoped TLCT-MCM-41.

Table 2.14 Structural data for Pd/Au-doped MCM-41-like silica prepared by TLCT

Source	Surface Area / $m^2 g^{-1}$	Pore Diameter / Å	d-spacing d / Å	Lattice Parameter / Å	Pore Wall Thickness / Å
Undoped	1103	34.6	41.9	48.4	13.7
This work	1164	33.3	41.9	48.4	15.1
King	849	28.1	39.2	45.3	17.2

Low-angle XRD was used to identify the presence of the hexagonal pore structure (Figure 2.26) with the predictable reflections of d_{10}, d_{11} and d_{20} and using high-angle XRD the metal particles were identified (Figure 2.27). Peak matching palladium oxide and metallic gold were all assigned and the average particle size calculated using the Scherrer equation, finding palladium oxide particles to be 13.7 nm and gold particles to be 23.1 nm in size. This would suggest that the two metals have not mixed well to form truly bimetallic particles; rather they have formed separate palladium oxide and gold particles.

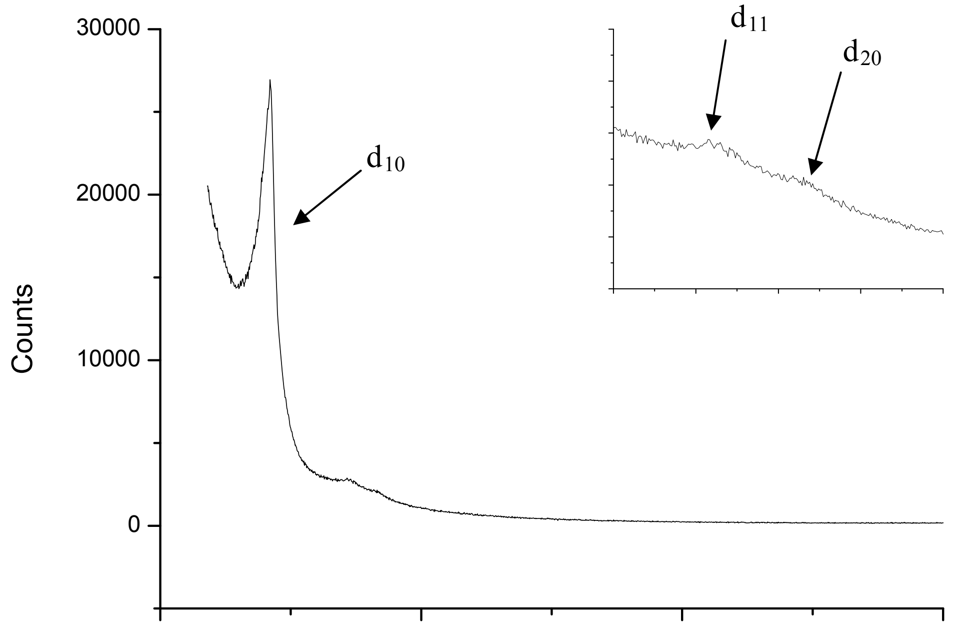

Figure 2.26 X-ray diffraction pattern of a Pd/Au-doped MCM-41-like silica prepared by TLCT

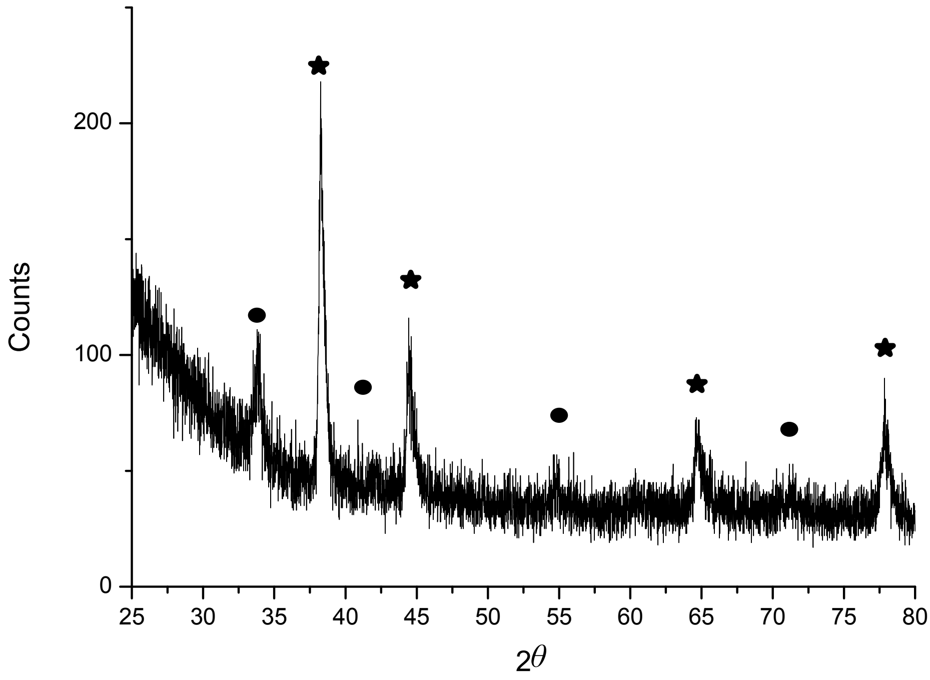

Figure 2.27 Wide-angle X-ray diffraction pattern of Pd/Au-doped MCM-41-like silica prepared by TLCT, (★) peak positions of Au metal and (●) peak positions of PdO

TEM images were taken of the Pd/Au-doped TLCT-MCM-41 (Figure 2.28) clearly showing the long, straight, pores as expected with well dispersed particles of a uniform size. The particles are clearly larger than the pores, occupying multiple pores, and were measured to be approximately 8.5 nm in diameter, close in size to the calculated size of the palladium oxide particles.

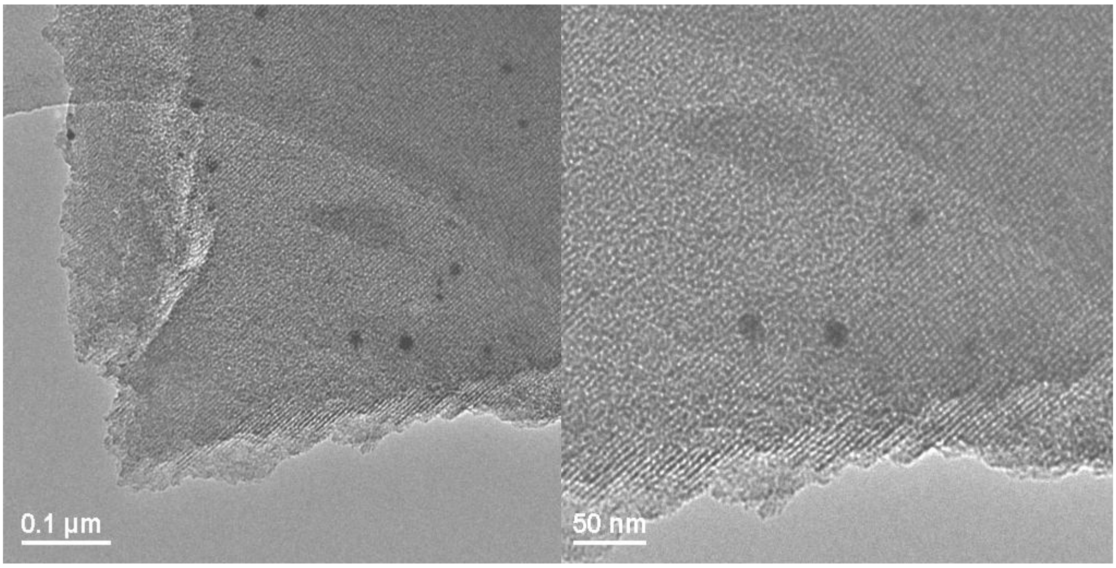

Figure 2.28 TEM images of Pd/Au-doped MCM-41-like silica prepared by TLCT

While it has been demonstrated to be possible to introduce two different metals into the preparation of TLCT-MCM-41, control of the particle size and composition still needs to be addressed. Control of the particle size should be more manageable with monometallic systems in the first instance (Chapter 4) before applying the same changes to bimetallic materials. It is expected that the limitation in preparing particles with predictable metal compositions (*i.e.* 50/50 mixtures) is a matter of achieving homogeneous mixing of the two precursors prior to calcination. Other work within the group has looked at preparing a precursor which contains the two metals, bound covalently to eliminate the need for mixing.[37]

2.5 Lanthanide-doped MCM-41

The later portion of the study into doped MCM-41 prepared by TLCT considered the preparation of lanthanide-doped silica. Lanthanides were chosen primarily because the lanthanide series offers a variety of different physical and chemical properties.

Chemically, lanthanides are known to exhibit a number of features, differentiating them from *d*-block metals:[38]

1. A wide range of coordination numbers;
2. Coordination geometries determined by ligand steric factors rather than crystal field effects;
3. They generally form labile, ionic complexes that undergo facile exchange of ligand, however when multidentate complexing agents are used, higher stability constants are observed;
4. The 4*f* orbitals in the Ln^{3+} ion do not participate directly in bonding. Therefore, their spectroscopic and magnetic properties are largely uninfluenced by the ligand;
5. They readily form hydrated complexes on account of the high hydration energy of the small Ln^{3+} ion.

Lanthanides have exhibited magnetic properties of interest such as the magnetic susceptibility of phoshoro-azo derivatives of europium(III) and terbium(III) measured by Borzechowska *et al.*[39] and the ferromagnetic spin-spin coupling of a copper(II)-gadolinium(III) complex observed by Sasaki *et al.*[40] Several trivalent lanthanide ions have shown luminescence in the visible or near-infrared spectral regions with irradiation with ultraviolet light. Lathanides rely on the antenna effect for luminescence, where the ligand absorbs a suitable wavelength of radiation and transfers the energy to the lanthanide which is excited to the emissive state (Figure 2.29).[41] The different ions emit differently coloured light; europium(III) emits red, terbium(III) emits green, thulium(III) emits blue, while ytterbium(III), neodymium(III) and erbium(III) emit in the near-infrared.[42] Light emission of lanthanides is known as luminescence rather than fluorescence or phosphorescence due to the mechanism of the emission. Fluorescence is singlet-to-singlet emission and phosphorescence is a singlet-to-triplet emission, while lanthanides utilise an intraconfigurational *f-f* transition.

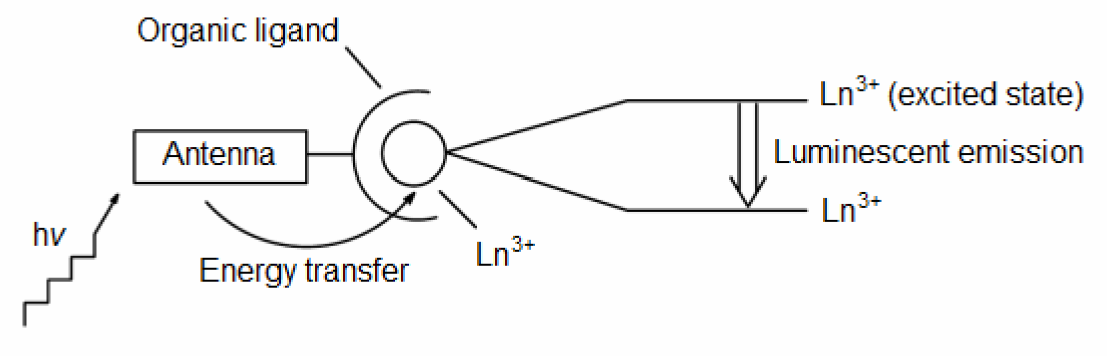

Figure 2.29 Schematic of the Antenna effect

Lanthanides have found a use as optically emissive materials when doped onto silica-based glasses. For instance, using nanoscale particles doped with lanthanide(III) luminescent centres, allows the physical and electronic properties of the particles to be modulated by varying shape and size, for the design of microlasers, thin-film devices or luminescent nanosensors.[43] The key factor in synthesis of these materials is control of the particle size, which is largely dependent on the preparation method. Patra *et al.*[44] doped nanoparticles (20 – 30 nm) of europium and terbium onto submicron spheres of silica and alumina and observed luminescence intensities comparable or higher than commercial phosphors.

Gadolinium(III) is used as an MRI contrast agent owing to its suitable isotropic magnetic properties and large number of unpaired electrons. Its relatively long electron-spin relaxation time ($\sim 10^{-9}$ s) makes it more suitable than other paramagnetic ions of, for example, dysprosium(III), europium(III) or ytterbium(III). However, free gadolinium(III) is toxic at a lower concentration than the required imaging dose; therefore, the ion is complexed with a ligand to form a complex *in vivo*. Gadolinium(III) was found to form a stable complex with EDTA, $[Gd(EDTA)(H_2O)_n]^{2-}$ (n = 2-3); however, when it came to use as an MRI imaging agent animal studies found it to have a poor stability. To replace this, complexes with DTPA (Figure 2.30A) were used as the ligand to form $[Gd(DTPA)(H_2O)]^{2-}$ which was found to be more stable.[45] A range of different complexes are currently used as MRI contrast agents; for instance, in the US, the Food and Drug Administration approve the use of gadodiamide (Omniscan), gadoversetamide (Optimark), gadoteridol (Prohance) and gadobenate dimeglumine (Multihance) (Figure 2.31).[46]

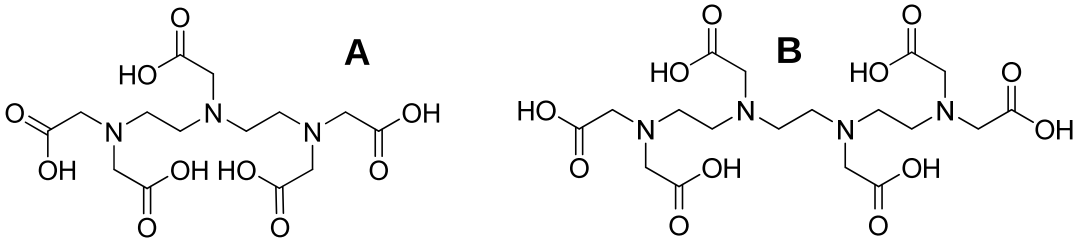

Figure 2.30 A) DTPA ligand[47]; B) TTHA ligand.[48]

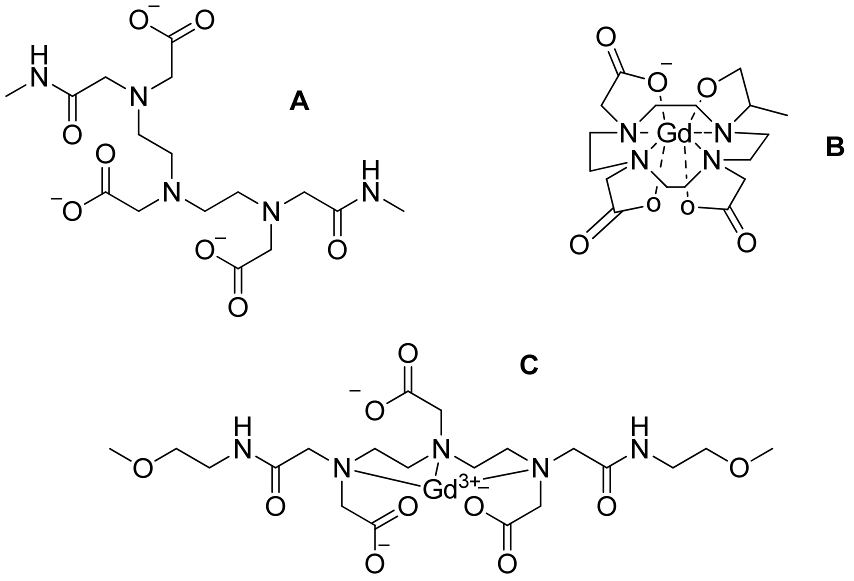

Figure 2.31 A) Gadodiamide; B) Gadoversetamide; C) Gadoteridol

A stable, water-soluble lanthanide complex was required to include in the TLCT method. Initially, EDTA and DTPA complexes of lanthanum(III) were prepared; however, these were both found to be insoluble at the concentrations in water involved in the templating method, namely 30 mg of complex in 0.4 cm^3 water. From this, the next ligand of this type in increasing size, TTHA (Figure 2.30B), was used and was found to dissolve and to work well with the templating method.

Wang *et al.*[49] prepared $(NH_4)_3[Eu(TTHA)]\cdot 5H_2O$ and compared its structure with $(NH_4)[Eu(EDTA)(H_2O)_3]\cdot H_2O$. They observed that in the EDTA complex, the Eu^{3+} ion was coordinated to two N atoms and four O atoms from the EDTA ligand, while the other 3 coordination sites were occupied by O atoms from the H_2O anion molecules. In comparison to this, the TTHA complex showed the Eu^{3+} ion coordinated to four N atoms and five O atoms, all from the TTHA ligand (Figures 2.32 and 2.33)

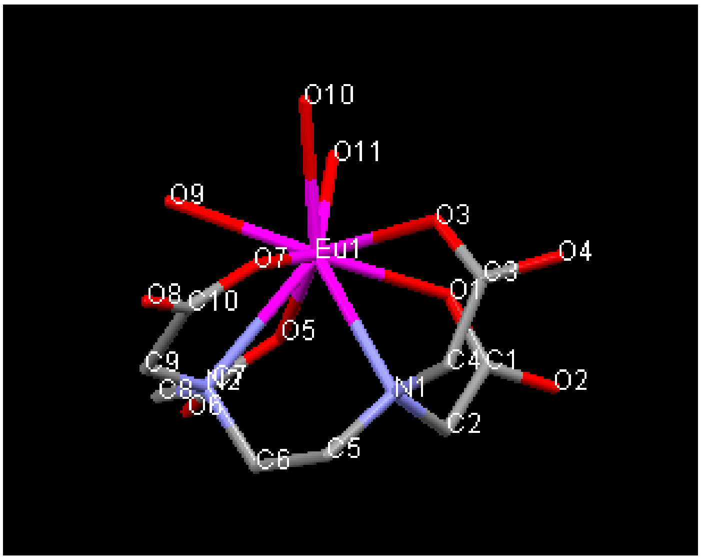

Figure 2.32 Molecular structure of $[Eu^{III}(EDTA)(H_2O)_3]^-$ determined by Wang[49]

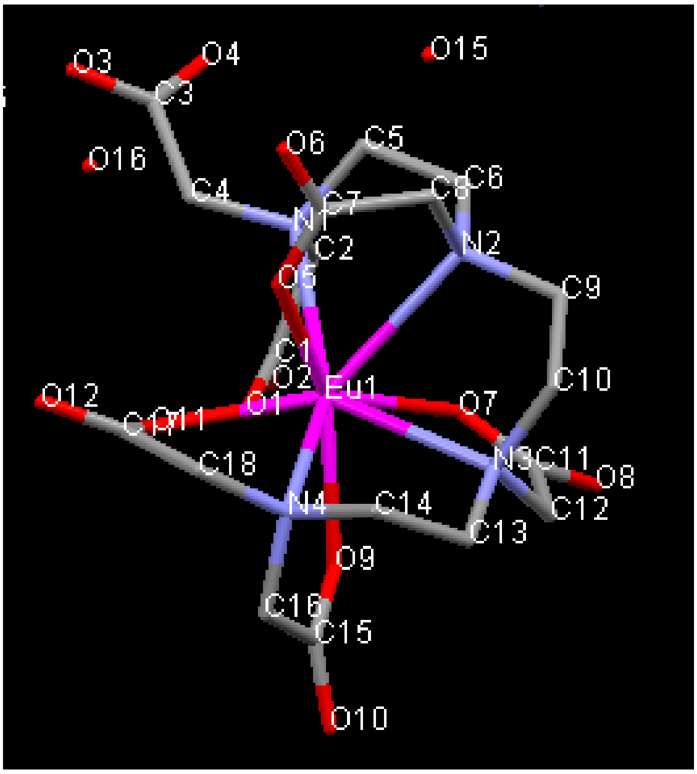

Figure 2.33 Molecular structure of $[Eu^{III}(TTHA)]^{3-}$ determined by Wang

A range of lanthanide metals were chosen to explore the series; lanthanum, europium, dysprosium, holmium, erbium and lutetium. Each was prepared as a TTHA salt with an ammonium cation, as described by Wang, and used in the TLCT methodology as described previously. Each of these complexes is very hygroscopic due to the high hydration energies, which led to inaccuracies in the CHN measurements of the complexes. Excess water would be expected to be removed by calcination along with the organic ligand and ammonium counter ion; therefore, this wasn't considered to be a concern; however, it should be noted that the water molecules will affect the predicted metal loading as the exact water content is not taken into consideration during these calculations. Each of the lanthanide complexes were used to prepare lanthanide doped TLCT-MCM-41 (Table 2.15).

Table 2.15 Structural data for Ln-doped MCM-41-like silica prepared by TLCT

Metal Precursor	Surface Area / $m^2\ g^{-1}$	Pore Diameter / Å	d-spacing d / Å	Lattice Parameter / Å	Pore Wall Thickness / Å
None	1103	34.6	41.9	48.4	13.7
$(NH_4)_3$[La(TTHA)]	1228	35.8	44.0	50.8	15.0
$(NH_4)_3$[Eu(TTHA)]	1204	42.2	45.7	52.8	10.6
$(NH_4)_3$[Ho(TTHA)]	1296	33.2	43.6	50.3	17.1
$(NH_4)_3$[Dy(TTHA)]	1332	33.1	44.6	51.5	18.3
$(NH_4)_3$[Er(TTHA)]	1380	34.8	43.0	49.7	14.8
$(NH_4)_3$[Lu(TTHA)]	1270	33.8	43.8	50.6	16.7

Low-angle XRD (Figure 2.34) shows very well defined peaks for d_{10}, d_{11} and d_{20} suggesting a well ordered hexagonal pore structure. The larger TTHA ligand appears to have caused an increase in the material surface area and all, apart from the europium-doped material which has a larger pore diameter, exhibit thicker pore walls than standard. This effect is counter-intuitive in that thicker pore walls would usually be indicative of smaller pores. This suggests that the micelle size hasn't changed, keeping the pores sizes the same and, instead, the micelles appear not to be packing as closely together as would be expected. The TTHA ligand could be acting as a swelling agent within the aqueous phase of the sol-gel mixture. To ensure the increased surface area was genuine, the materials were all prepared a number of times; results for the lanthanum MCM-41 are shown in Table 2.16. Repeating the synthesis showed very little difference in the porosity or structure of the materials, confirming the observed surface area increase.

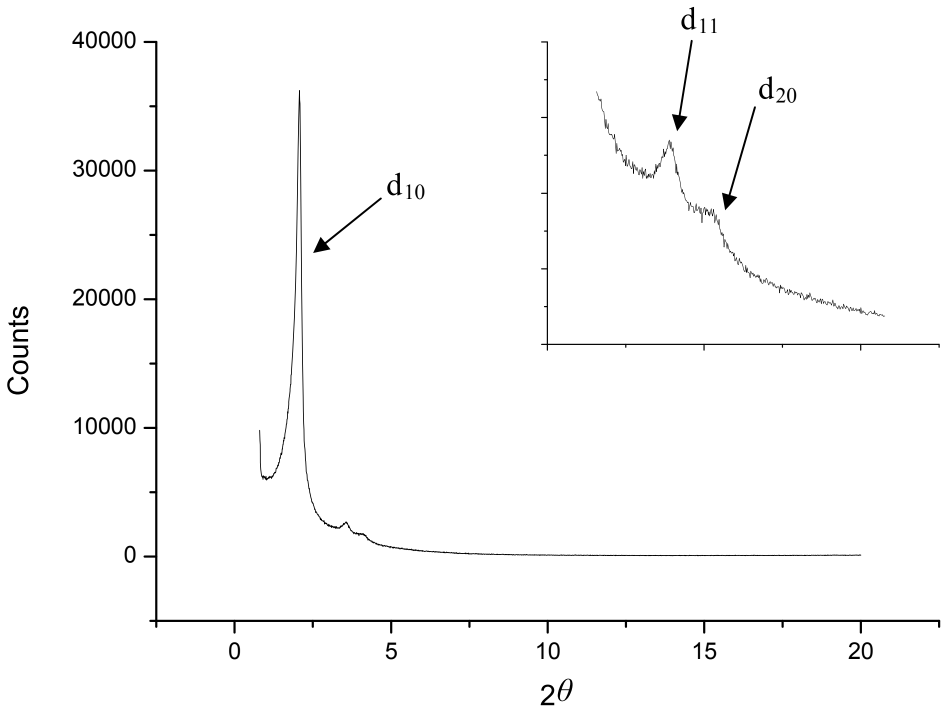

Figure 2.34 X-ray diffraction pattern of a La-doped MCM-41-like silica prepared by TLCT

Table 2.16 Structural data for La-doped MCM-41-like silica prepared by TLCT using $(NH_4)_3[La(TTHA)]$

Sample	Surface Area / $m^2\ g^{-1}$	Pore Diameter / Å	d-spacing d / Å	Lattice Parameter / Å	Pore Wall Thickness / Å
1	1228	35.8	44.0	50.8	15.0
2	1146	32.8	42.3	48.8	15.9
3	1178	31.7	42.6	49.2	17.5
4	1155	35.9	42.6	49.2	13.2

In 2008, Ikeue *et al.*[50] reported a series of lanthanide-doped mesoporous silicas, incorporating lanthanum, cerium and praseodymium into FSM-16[51] by incipient wetness impregnation and co-precipitation. FSM-16 is a well ordered, mesoporous hexagonal silica similar to MCM-41; however, the synthetic procedure is very different. FSM-16 is formed by surfactant micelles forcing layered kanemite (silicate sheets) to fold in such a way to yield a hexagonal structure. The co-precipitation method used is detailed below in Figure 2.35.

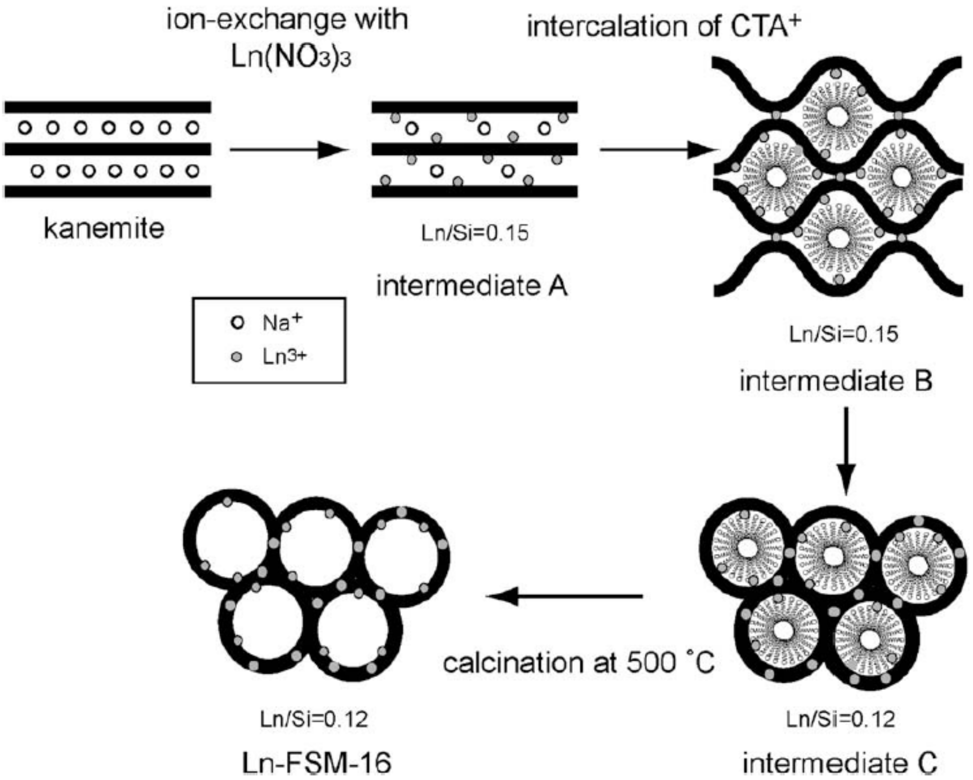

Figure 2.35 Schematic mechanism for incorporation of Ln species into FSM-16 framework

Table 2.17 Structural data for Ikeue's Ln-FSM-16

Sample	Impregnation method	Surface Area / $m^2 g^{-1}$	Pore Diameter / Å	Ln/Si ratio by XRF
FSM-16	None	1100	25.2	-
La-FSM-16	Co-precipitation	754	25.2	0.12
La-FSM-16	Incipient wetness	348	19.0	0.10
Ce-FSM-16	Co-precipitation	698	25.2	0.12
Ce-FSM-16	Incipient wetness	641	23.2	0.15
Pr-FSM-16	Co-precipitation	750	25.2	0.12
Pr-FSM-16	Incipient wetness	322	19.0	0.09

By each method Ikeue observed a significant decrease in surface area of the materials compared with the parent material (Table 2.17) and in the case of incipient wetness impregnation the pore diameter also decreased. By EXAFS analysis, they observed that use of the co-precipitation method resulted in lanthanide species were highly dispersed and isolated tetrahedrally within the silica framework of the FSM-16 with the lack of Ln-oxide species and the atomic distance of Ln-O being shorter than expected in a bulk oxide, suggesting it was incorporated into SiO_4 sites.

The TEM image of the lanthanum-doped TLCT-MCM-41 materis shown in Figure 2.36 shows the well-formed hexagonal pore structure suggested by low-angle XRD, although no lanthanum particles were identified in either the TEM images or wide-angle XRD. A scanning electron microscope with energy-dispersive X-ray spectroscopy (SEM-EDX) confirmed the presence of the lanthanide metals (Table 2.18) within the materials, although at a much lower loading that expected. This difference is likely due to the SEM-EDX only penetrating the material surface to a small degree, leaving most of the metal unaccounted for. With the presence of the lanthanides confirmed, while they are not observed by XRD or TEM, suggests that they were either too small to be detected (< 2 nm) or the metals have been incorporated within the silica structure itself during hydrolysis. It should be possible to differentiate between the two using EXAFS in the same way that Ikeue determined that the lanthanides were within the silica framework of their materials.

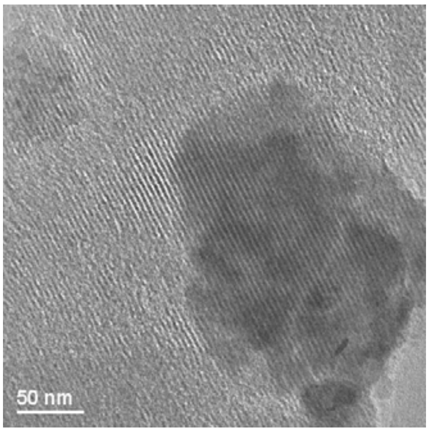

Figure 2.36 TEM image of La-doped MCM-41-like silica prepared by TLCT

Table 2.18 SEM-EDX metal loadings

Metal Precursor	Metal loading / wt %	Expected metal loading / wt %
$(NH_4)_3[Eu(TTHA)]$	0.60 ± 0.05	3.14
$(NH_4)_3[Ho(TTHA)]$	0.74 ± 0.07	2.29
$(NH_4)_3[Dy(TTHA)]$	0.70 ± 0.07	3.28
$(NH_4)_3[Er(TTHA)]$	0.91 ± 0.11	3.01

In order to assess the compatibility of preparing a bimetallic doped MCM-41 using very different metal precursors, a Pd/Ce-doped TLCT-MCM-41 was synthesised using $(NH_4)_2[PdCl_4]$ and $(NH_4)_3[CeTTHA]$. Porosity and structure (Table 2.19) appears unchanged by the two precursors with very little difference between the doped material and the undoped parent. In the same way as with the palladium/gold-doped MCM-41 prepared previously, high-angle XRD (Figure 2.37) was used to identify the separate metal particles as cerium oxide (CeO_2) with an average particle size of 68.6 nm and palladium metal with an average particle size of 18.1 nm.

Table 2.19 Structural data for Pd/Ce-doped MCM-41-like silica prepared by TLCT

Precursor	Surface Area / $m^2\,g^{-1}$	Pore Diameter / Å	d-spacing d / Å	Lattice Parameter / Å	Pore Wall Thickness / Å
None	1103	34.6	41.9	48.4	13.7
$(NH_4)_2[PdCl_4]$ $(NH_4)_3[CeTTHA]$	1120	33.8	42.8	49.5	15.6

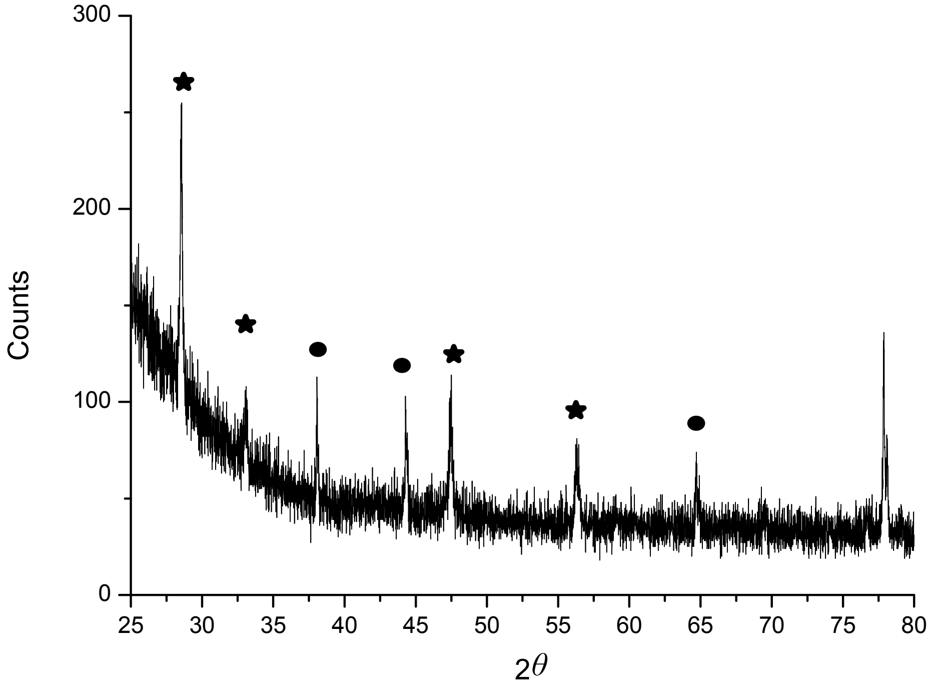

Figure 2.37 Wide-angle X-ray diffraction pattern of Pd/Ce-doped MCM-41-like silica prepared by TLCT, (★) peak positions of CeO_2 and (●) peak positions of Pd metal

While the use of different precursors does not inhibit the preparation of the bimetallic-doped MCM-41, the material suffers from the same limitations in mixing and particle sizes being much larger than the pores.

2.6 Summary

King demonstrated that it is possible to prepare an MCM-41-like material using the $C_{12}EO_{10}$ surfactant with the addition of a metal salt $A_m[MCl_n]$ where A = Na, Li or K and M is a precious metal; Pt, Pd, Au, Ir, Rh or Re. The observations above have extended the series to include A = NH_4 to eliminate any unwanted metals from the material. Palladium-, platinum- and gold- doped silicas have been studied in more detail and continue to produce large particles that are not contained within the pore structure. The palladium- and gold-doped materials prepared for catalysis are likely to show low activity due to the large particle sizes observed in these materials. This all emphasises the need to find a more suitable precursor that will be more favourable to forming smaller, well-dispersed particles within the pore network. It could be assumed that the metal precursors are decomposing at a lower temperature than is required by the silica to fully condense, resulting in the aggregation of metal particles before the pore walls are fully developed. Modifying the calcination method showed no improvement on the particle size; therefore, another method must be found. Changing the surfactant to produce larger and more stable pores in an effort to contain the particles is to be considered in Chapter 3, while Chapter 4 will discuss the possibility of organometallic precursors which will be soluble within the surfactant to better restrain the particles within the pores.

A series of new materials has been prepared, incorporating metals from the lanthanide series using the $(NH_4)_3[Ln(TTHA)]$ complex as precursor. While the use of this complex has had an effect on the mesophase, it is only minor, resulting in increased surface area with a good hexagonal pore structure still being observed. The presence of each respective lanthanide has been detected; however, the exact location and size of the lanthanide particles is still to be confirmed and, based on the observations of Ikeue's *et al.,* it is possible the lanthanides have become incorporated into the silica structure. However, the question of why these precursors result in an increase in surface area remains unanswered.

A more thorough and critical conclusion of this work will be made in Chapter 5 to include suitable comparisons with SBA-15.

2.7 Experimental

2.7.1 General Experimental

All reagents and solvents were used as received.

Optical microscopy was performed using an Olympus BX50 microscope at x100 and x200 magnification with a Linkam Scientific LTS 350 heating stage and VWR international 18 x 18 mm borosilicate glass microscope cover slips of a thickness no. 1.

The as-synthesised silica gels were calcined in a Carbolite tube furnace using a type 3216 temperature controller. Unless otherwise stated, silicas prepared with $C_{12}EO_{10}$ were degassed for 20 minutes with nitrogen followed by heating at 3 K min^{-1} to 673 K. This temperature was held for one hour under nitrogen and a further 5 hours under a flow of air before cooling to room temperature.

Low-angle X-ray diffraction patterns were recorded using a Bruker D8 diffractometer with CuK_{α} radiation (wavelength 1.54 Å). Surface areas, average pore diameters and average pore volumes were determined using BET adsorption-desorption measurements on a Micromeritics Tristar 3000 surface analyser, using nitrogen at 77 K as the adsorbing gas.

TEM and SEM images were courtesy of Professor Wuzong Zhou, Ross Blackley and Dr Zixue Su at the University of St Andrews.

2.7.2 Synthesis

$(NH_4)_3[La(TTHA)]$ [52]

H_6TTHA (1.02 g, 2.00 mmol) was dissolved in hot water (100 cm^3) and $La(NO_3)_3.5H_2O$ (0.85 g, 2.0 mmol) was added in batches and heated under reflux for 3 h. Aqueous ammonia (35% solution) was added drop-wise until the pH reached 6. The resulting colourless solution was dried to yield white crystals. Lutetium ($Lu(NO_3)_3.5H_2O$

(0.28 g, 0.7 mmol)), europium ($Eu_2O_3.5H_2O$ (0.36 g, 1.0 mmol)), dysprosium ($Dy(NO_3)_3.5H_2O$ (0.72 g, 2.0 mmol)), holmium ($Ho(NO_3)_3.5H_2O$ (0.88 g, 2.0 mmol)) and erbium ($Er(NO_3)_3.5H_2O$ (0.88 g, 2.0 mmol)) analogues were also prepared by the same method.

Table 2.20 CHN analysis

Metal Precursor	C / % found (calculated)	H / % found (calculated)	N / % found (calculated)
$(NH_4)_3$[La(TTHA)]	23.47 (31.73)	4.75 (5.33)	16.30 (14.39)
$(NH_4)_3$[Eu(TTHA)]	29.41 (28.88)	5.38 (5.66)	12.75 (13.10)
$(NH_4)_3$[Ho(TTHA)]	23.52 (30.56)	4.79 (5.13)	16.04 (13.86)
$(NH_4)_3$[Dy(TTHA)]	21.69 (30.66)	5.12 (5.15)	16.47 (13.91)
$(NH_4)_3$[Er(TTHA)]	18.86 (30.46)	4.48 (5.11)	15.50 (13.81)

2.7.3 Preparation of Silicas

$C_{12}EO_{10}$ templated silicas[53,54,55,56]

$K_2[PdCl_4]$ (0.03 g, 5 wt% with respect to surfactant) was dissolved in water (0.40 g) acidified with HCl to pH 2. Added to this was polyoxyethylene-10-lauryl ether ($C_{12}EO_{10}$, 0.60 g) and the mixture sonicated to aid mixing until a homogeneous, viscous gel was formed. The hexagonal, H_1, phase formed was identified by polarised optical microscopy. Tetramethoxylsilane (0.8 cm^3, 5.35 mmol) was added to the gel and mixed thoroughly to yield a free-flowing liquid. This was placed under a light vacuum (120 mbar) at 40 °C to remove the evolved methanol. When the gel became viscous and the hexagonal mesophase was identified by polarised optical microscopy, the mixture can be left on the open bench for 24 h to complete condensation. A portion (0.91 g) of the as-synthesised material was placed in the tube furnace for calcination to yield a dark brown coloured silicate (0.33 g).

Table 2.21 Range of silicas prepared using $C_{12}EO_{10}$

Metal	Metal Precursor	Mass of Precursor / g	Mass of Metal / g	Wt% of Metal in calcined material$^+$
Pd	$K_2[PdCl_4]$	0.040	0.013	3.5
Pd	$(NH_4)_2[PdCl_4]$	0.042	0.016	4.4
Pt	$K_2[PtCl_4]$	0.033	0.016	5.9
Pt	$(NH_4)_2[PtCl_4]$	0.042	0.022	6.2
Au	$(NH_4)[AuCl_4]$	0.047	0.026	7.5
Pd/Au	$(NH_4)_2[PdCl_4]$	0.018	0.006	2.2
	$(NH_4)[AuCl_4]$	0.011	0.006	1.9
Pd/Ce	$(NH_4)_2[PdCl_4]$	0.015	0.006	1.6
	$(NH_4)_3[Ce(TTHA)]$	0.028	0.006	1.6
La	$(NH_4)_3[La(TTHA)]$	0.030	0.007	2.2
Eu	$(NH_4)_3[Eu(TTHA)]$	0.034	0.007	3.1
Ho	$(NH_4)_3[Ho(TTHA)]$	0.031	0.007	2.3
Dy	$(NH_4)_3[Dy(TTHA)]$	0.034	0.008	3.3
Er	$(NH_4)_3[Er(TTHA)]$	0.035	0.008	2.7
Lu	$(NH_4)_3[Lu(TTHA)]$	0.043	0.010	3.3

$^+$Calculated wt % of metal within the whole sample after calcination

2.8 References

1. G. S. Attard, J. C. Glyde and C. G. Göltner, *Nature,* 1995, **378,** 366.
2. Y. Wan and D. Zhao, *Chem. Rev.,* 2007, **107,** 2821.
3. S. A. El-Safty, T. Hanaoka and F. Mizukami, *Adv. Mater.,* 2005, **17,** 47.
4. G. S. Attard, P. N. Bartlett, N. R. B. Coleman, J. M. Elliott, J. R. Owen and J. H. Wang, *Science,* 1997, **278,** 838.
5. Ö. Dag, O. Samarskaya, N. Coombs and G. A. Ozin, *J. Mater. Chem.,* 2003, **13,** 328.
6. F. Hoffmann, M. Cornelius, J. Morell and M. Fröba, *Angew. Chem. Int. Ed.,* 2006, **45,** 3216.
7. N. K. Mal, M. Fujiwara and Y. Tanaka, *Nature,* 2003, **421,** 350.
8. J. Sun and X. Bao, *Chem. Eur. J.,* 2008, **14,** 7478.
9. N. C. King, *PhD Thesis,* University of Exeter, 2005.
10. K. E. Amos, *PhD Thesis,* University of Exeter, 2005.

11 M. J. Danks, *PhD Thesis,* University of Exeter, 2002.

12. K. E. Amos, N. J. Brooks, N. C. King, S. Xie, J. Canales-Vázquez, M. J. Danks, H. B. Jervis, W. Zhou, J. M. Seddon and D. W. Bruce, *J. Mater. Chem.,* 2008, **18,** 5282.
13. M. J. Danks, H. B. Jervis, M. Nowotny, W. Zhou, T. A. Maschmeyer and D. W. Bruce, *Catal. Lett.,* 2002, **82,**
14. N. C. King, C. Dickinson, W. Zhou and D. W. Bruce, *Dalton Trans.,* 2005, 1027.
15. M. J. Danks, M. E. Light and D. W. Bruce, *Eur. J. Inorg. Chem.,* 2009, **28,** 4232.
16. N. C. King, R. A. Blackley, W. Zhou and D. W. Bruce, *Chem. Commun.,* 2006, 3411.
17. N. C. King, R. A. Blackley, M. L. Wears, D. M. Newman, W. Zhou and D. W. Bruce, *Chem. Commun.,* 2006, 3414.
18. N. M. Selivanova, V. V. Osipova and W. G. Galyametdinov, *Russ. J. Phys. Chem.,* 2006, **80,** 649.
19. A. M. Venezia, R. Murania, G. Pantale, V. La Parola, S. Scirè and G. Deganello, *Appl. Catal. A: General,* 2009, **353,** 296.
20. S. Domínguez-Domínguez, Á. Berenguer-Murcia, Á. Linares-Solano and D. Cazorla-Amorós, *J. Catal.,* 2008, **257,** 87.
21. A. F. Lee and K. Wilson, *Green Chem.,* 2004, **6,** 37.

22. A. F. Lee, S. F. J. Hackett, J. S. J. Hargreaves and K. Wilson, *Green Chem.,* 2006, **8,** 549.
23. N. Yao, C. Pinckney, S. Lim, C. Pak and G. L. Haller, *Micro. Meso. Mater.,* 2001, **44,** 377.
24. Y. Shi, Y. Wan, R. Zhang and D. Zhao, *Adv. Funct. Mater.,* 2008, **18,** 2436.
25. I. Sobczak, J. Grams and M. Ziolek, *Micro. Meso. Mater.,* 2007, **99,** 345.
26. J. S. Beck, J. C. Vartuli, W. J. Roth, M. E. Leonowicz, C. T. Kresge, K. D. Schmitt, C. T. W. Chu, D. H. Olson, E. W. Sheppard, S. B. McCullen, J. B. Higgins and J. L. Schlenker, *J. Am. Chem. Soc.,* 1992, **114,** 10834.
27. G. C. Bond, *Gold Bull.,* 1972, **5,** 11.
28. J. Schwank, *Gold Bull.,* 1985, **18,** 1.
29. G. J. Hutchings, *J. Catal.,* 1985, **96,** 292.
30. A. S. K. Hashmi and G. J. Hutchings, *Angew. Chem. Int. Ed.,* 2006, **45,** 7896.
31. P. Landon, J. Ferguson, B. E. Solsona, T. Garcia, A. F. Carley, A. A. Herzing, C. J. Kiely, S. E. Golunski and G. J. Hutchings, *Chem. Commun.,* 2005, 3385.
32. C. D. Pina, E. Falletta, L. Prati and M. Rossi, *Chem. Soc. Rev.,* 2008, **37,** 2077.
33. G. C. Bond and D. T. Thompson, *Catal. Rev.-Sci. Eng.,* 1999, **41,** 319.
34. I. Sobczak, A. Kusior, J. Grams and M. Ziolek, *J. Catal.,* 2007, **245,** 259.
35. A. M. Venezia, R. Murania, G. Pantale, V. La Parola, S. Scirè and G. Deganello, *Appl. Catal. A: General,* 2009, **353,** 296.
36. Z. Surowiec, M. Wiertel, B. Bierska-Piech and M. Budzyńsky, *J. Phys.: Conference Series,* 2010, **217,** 12113.
37. N. Seti and D. W. Bruce, *Unpublished work,* 2011.
38. S. Cotton, in *Comprehensive Coordination Chemistry II, Vol 3,* J. A. McClevertym and T. J. Meyer, Vol. Ed. G. F. R. Parkin, Elsevier, Oxford, 2004.
39. M. Borzechowska, V. Trush, I. Turowska-Tyrk, W. Amirkhaniv and J. Legendziewicz, *J. Alloys Compds.,* 2002, **341,** 98.
40. M. Sasaki, K. Manseki, H. Horiuchi, M. Kumagai, M. Sakamoto, H. Sakiyama, Y. Nishida, M. Saki, Y. Sadaoka, M. Ohba and H. Okawa, *J. Chem. Soc., Dalton Trans.,* 2000, **3,** 259.
41. S. Cotton, *Lanthanide and Actinide Chemistry,* John Wiley & Sons Ltd, Chichester, 2006.

42. K. Binnemans, in *Handbook on the Physics and Chemistry of Rare Earths, Vol. 35, Chapter 225,* K. A. Gschneidner, J. -C. G. Bünzli and V. K. Percharsky, Elsevier B. V., Amsterdam, 2005.
43. S. Comby and J. -C. G. Bünzli, in *Handbook on the Physics and Chemistry of Rare Earths, Vol. 37, Chapter 235,* K. A. Gschneidner, J. -C. G. Bünzli and V. K. Percharsky, Elsevier B. V., Amsterdam, 2007.
44. A. Patra, E. Sominska, S. Ramesh, Y. Koltypin, Z. Zhong, H. Minti, R. Reisfeld and A. Gedanken, *J. Phys. Chem. B,* 1999, **103,** 3361.
45. H. -J. Weinmann, R. C. Brasch, W. -R. Press and G. E. Wesbey, *J. Am. Roentgenology,* 1984, **142,** 619.
46. http://www.fda.gov/Drugs/DrugSafety/PostmarketDrugSafetyInformationforPatientsandProviders/ucm142882.htm, 22/04/2011.
47. H. R. Maecke, A. Riesen and W. Ritter, *J. Nucl. Med.,* 1989, **30,** 1235.
48. I. Lukes, J. Kotek, P. Vojtisek and P. Hermann, *Coord. Chem. Rev.,* 2001, **216,** 287.
49. J. Wang, X. D. Zhang, W. G. Jia, Y. Zhang and Z. R. Liu, *Russian J. Coord. Chem.,* 2004, **30,** 130.
50. K. Ikeue, T. Tanaka, N. Miyoshi and M. Machida, *Solid State Sci.,* 2008, **10,** 1584.
51. S. Inagaki, A. Koiwai, N. Suzuki, Y. Fukushima and K. Kuroda, *Bull. Chem. Soc. Jpn.,* 1996, **69,** 1449.
52. J. Wang, X. D. Zhang, W. G. Jia, Y. Zhang and Z. R. Liu, *Russian J. Coord. Chem.,* 2004, **30,** 130.
53. Y. Huang, W. Qin, X. Huo and Y. Dai, *Coll. Surf. A: Physicochem. Eng. Aspects,* 2006, **276,** 228.
54. K. S. Sharma and A. K. Rakshit, *Bull. Chem. Soc. Jap.,* 2005, **78,** 771.
55. S. B. Sulthana, P. V. C. Rao, S. G. T. Bhat, T. Y. Nakano, G. Sugihara and A. K. Rakshit, *Langmuir,* 2000, **16,** 980.
56. D. J. Mitchell, *J. Chem. Soc., Faraday Trans. I,* 1983, **79,** 975.

CHAPTER THREE

SBA-15 TYPE MATERIALS

3.1 Introduction

Following on from the work on MCM-41, it is clear that it is advantageous to have control over the design of the catalysts prepared by TLCT; one such design parameter is pore morphology. Primarily, the aim is to utilise a larger pore diameter to better contain the size of metal particles to prevent the large particles observed in Chapter 2 from aggregating. Secondly, but also important, is matters of mass transport during catalysis.[1] Larger pores allow larger reagents access to the active sites and are less diffusion limited by pores blocking with material during the reaction. It was described previously in Chapter 1 that using different surfactants as templates generates different pore networks; as such it is intended to adapt the TLCT method to utilise other surfactants with the intention to prepare the desired material.

SBA-15 has received much attention since its discovery in 1998.[2] Due to its high surface area (>700 m^2 g^{-1}), ordered hexagonal structure and tunable pore size (20 – 300 Å), SBA-15 makes a good catalytic support and is an ideal candidate for progressing this work. Traditionally, SBA-15 is synthesised, using the LCT approach, in highly acidic conditions and low micelle concentrations, using the triblock copolymer Pluronic P123 ($PEO_{20}PPO_{70}PEO_{20}$, Figure 3.1) dissolved in 0.40 mol dm^3 HCl and tetraethoxysilane (TEOS) to form the hexagonally templated silica. It is also known that SBA-15 contains both micro- and meso-pores within its structure.[3] The micropores account for roughly half the surface area of the SBA-15 material so, while the surface area may appear to be ~900 m^2 g^{-1} in a given material for catalysis, only half of this may be accessible to the reactants. This may cause problems, especially if the active metal has been introduced into the micropores during impregnation rather than the larger mesopores, resulting in it being completely inaccessible for reaction.

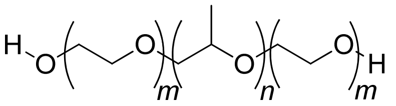

Figure 3.1 P123 surfactant *m* = 20, *n* = 70

P123 is one of a family of surfactants known as Pluronics® and P123 is a block co-polymer comprising of two polyethylene oxide blocks with a polypropylene oxide block in the centre (PEO-PPO-PEO), with an average molecule weight of ~5,800 g mol^{-1}.

Hartmann and Vinu[4] examined the structural stability of SBA-15 by assessing the material by powder XRD, nitrogen-, benzene- and *n*-heptane- adsorption, and mercury porosimetry. They found that it was less mechanically stable than other mesoporous materials such as MCM-41 and MCM-48, due to an unfavourable ratio between pore diameter and the pore wall thickness; MCM-41 has a much more favourable ratio, despite its thinner walls. The low mechanical stability could present a disadvantage for industrial applications as a pressure of 260 MPa was found to cause a 40% decrease in pore volume as a fraction of the pores were irreversibly destroyed.

In 2008, Chytil *et al.*,[5] expanded on the work of Hartmann and Vinu and also found a reduction in N_2 sorption measurements at a pressure of 191 MPa (40% decrease); however, they also determined that the micropore volume remained constant throughout the experiment, suggesting it was the mesopores being affected by the pressure as well as no additional micropores being formed in the process.

SBA-15 was suggested as a drug delivery system by Halamová *et al.,*[6] in 2010, using the porous network to load and release the drug naproxen, (*S*)-6-methoxy-α-methyl-2-napthalenacetic acid, a non-steroidal anti-inflammatory drug.[7] They loaded the naproxen into normal SBA-15 and SBA-15 modified by grafting aminopropyl groups onto the surface. They observed a significant decrease in the surface areas of the two samples after loading, from 794 $m^2\ g^{-1}$ to 167 $m^2\ g^{-1}$ for SBA-15 and 327 $m^2\ g^{-1}$ to 76 $m^2\ g^{-1}$ for the modified SBA-15 as well as a reduction in pore volume and diameter, suggesting successful loading of the naproxen into the pore structure. When it came to drug release, the unmodified SBA-15 was observed to release more in the first hours, resulting in a higher overall release rate and quantity of naproxen released.

3.2 Non-doped SBA-15

SBA-15 was prepared using a True Liquid Crystal Templating method following a similar method used to prepare TLCT-MCM-41, with the $C_{12}EO_{10}$ surfactant being replaced by P123. It was found to be easier to use a 50:50 mix of P123:water as the surfactant is significantly more viscous than $C_{12}EO_{10}$. As such, 0.5 g of P123 was mixed with 0.5 g of water which had been acidified to pH 2 by the addition of HCl. The mixture was sonicated at 40 °C until a homogeneous gel was observed. The sol-gel was predicted to exhibit a hexagonal mesophase by the phase diagram[8] (Figure 3.2), which was confirmed by polarised optical microscopy (Figure 3.3). Tetramethoxysilane (TMOS) was added to the sol-gel in 4:1 mole ratio with the water to ensure full hydrolysis occurred and, once fully mixed, any evolved methanol was removed by dynamic vacuum until a gel like substance remained, which was left on the open bench for 24 hours before calcination. The material was calcined at 500 °C for 6 hours under a flow of air to remove the organic surfactant.

It should be noted that recent work has found the phase diagram used below to be inaccurate for P123, however this doesn't affect the amounts used in this method; the hexagonal phase is indeed found at the 50:50 mixture.[9]

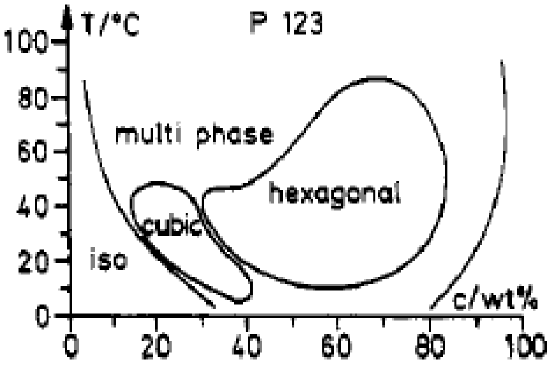

Figure 3.2 Phase diagram of P123, $PEO_{20}PPO_{70}PEO_{20}$[8]

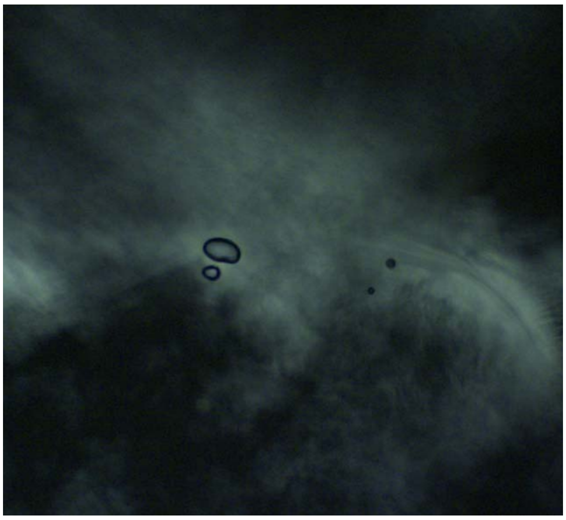

Figure 3.3 H_1 mesophase of the P123 surfactant in water

Literature values[10] for the surface area of SBA-15 range from 690 – 1040 $m^2\ g^{-1}$ and pore diameters from 46 – 300 Å, which can all be prepared by altering the preparation conditions. While the total surface area is recorded to be ~1000 $m^2\ g^{-1}$, the mesoporous surface area of SBA-15 materials is actually around 500 $m^2\ g^{-1}$, while the remaining surface area observed is attributed to the micropores between the hexagonal pore networks which can be observed by porosimetry. However, the silicas prepared using P123 by the TLCT method yields a material with a surface area of 600 $m^2\ g^{-1}$. Using nitrogen t-plot analysis it is possible to identify the limit between microporous and mesoporous material. In the material synthesised by TLCT, only 180 $m^2\ g^{-1}$ of the total surface area is accounted for by micropores; a significant drop compared to the ~50:50 mixture seen in standard SBA-15 materials. The TEM image of the non-doped silica is shown below in Figure 3.4 showing the long, straight pores running in parallel.

Table 3.1 Structural data for SBA-15

	Surface Area / $m^2\ g^{-1}$	Pore Diameter / Å	Pore Volume / cm^3g^{-1}	Micropore volume / cm^3g^{-1}	Micropore area / m^2g^{-1}
LCT SBA-15	949	63.2	0.94	0.12	457
TLCT SBA-15	600	51.5	0.78	0.07	178

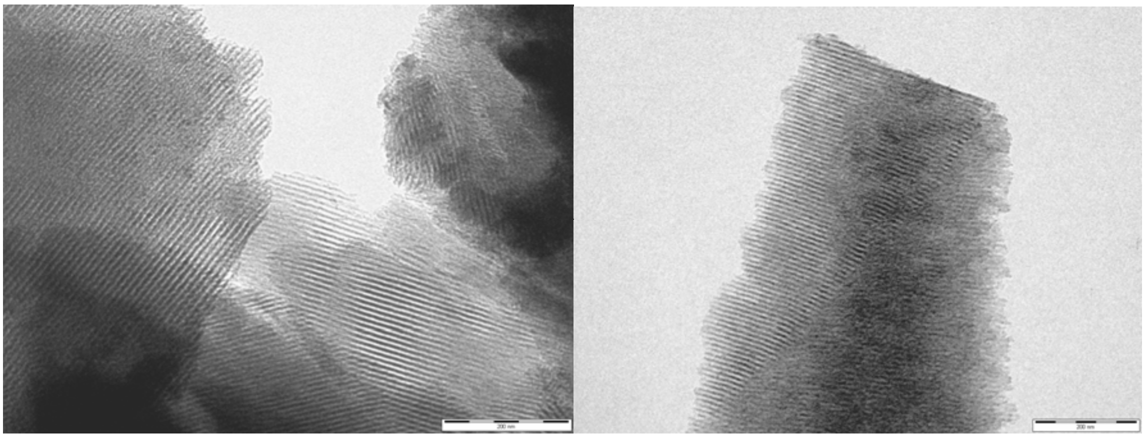

Figure 3.4 TEM images of undoped SBA-15-like silica prepared by TLCT; scale bar = 200 nm

The nitrogen sorption isotherm (Figure 3.5) shows the characteristic hysteresis loop of SBA-15 materials. Figure 3.6 shows the pore size distribution of the TLCT SBA-15 prepared here, clearly identifying the mesopores with a diameter of 5.1 nm and the micropores appearing just on the edge of the detection limit of the equipment with a diameter < 2 nm.

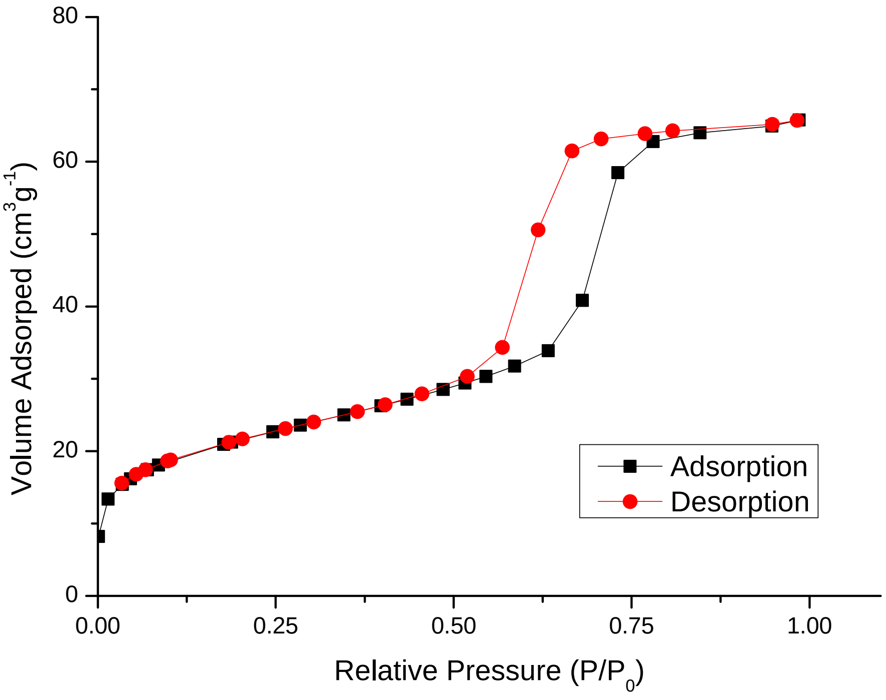

Figure 3.5 Adsorption-desorption isotherm of undoped SBA-15-like silica prepared by TLCT

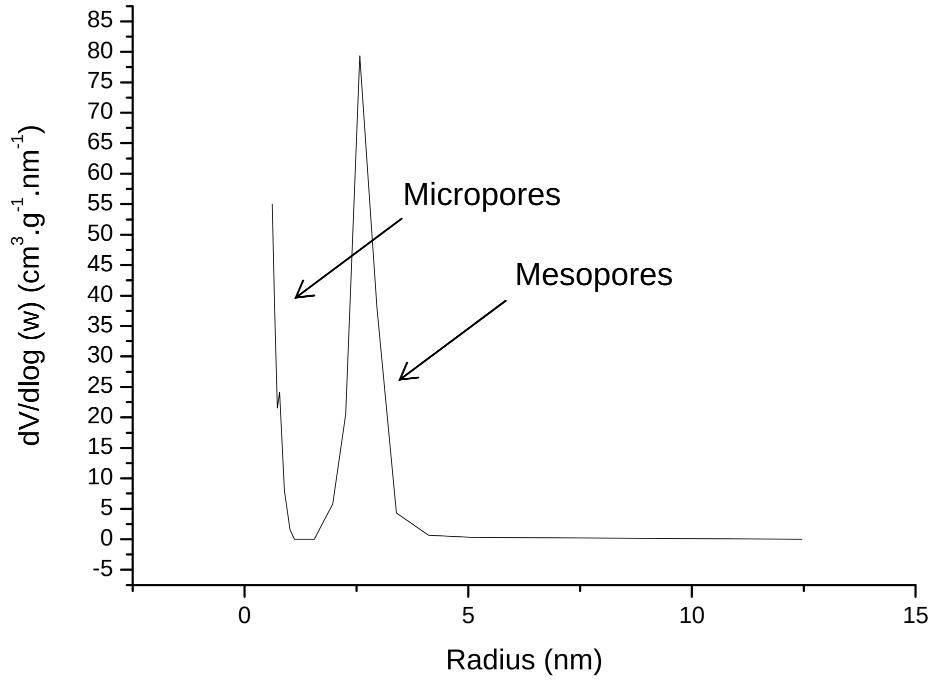

Figure 3.6 Pore size distribution of undoped SBA-15-like silica prepared by TLCT

The hexagonal structure can be verified using low-angle XRD (Figure 3.7) by identifying the characteristic d_{10} and d_{11} reflections; however, the expected d_{20} reflection could not be observed, suggesting the material's long-range ordering is not as clearly defined as with TLC SBA-15. The calculated values of d_{11} and d_{20} were used to confirm the hexagonal structure and are shown in Table 3.2.

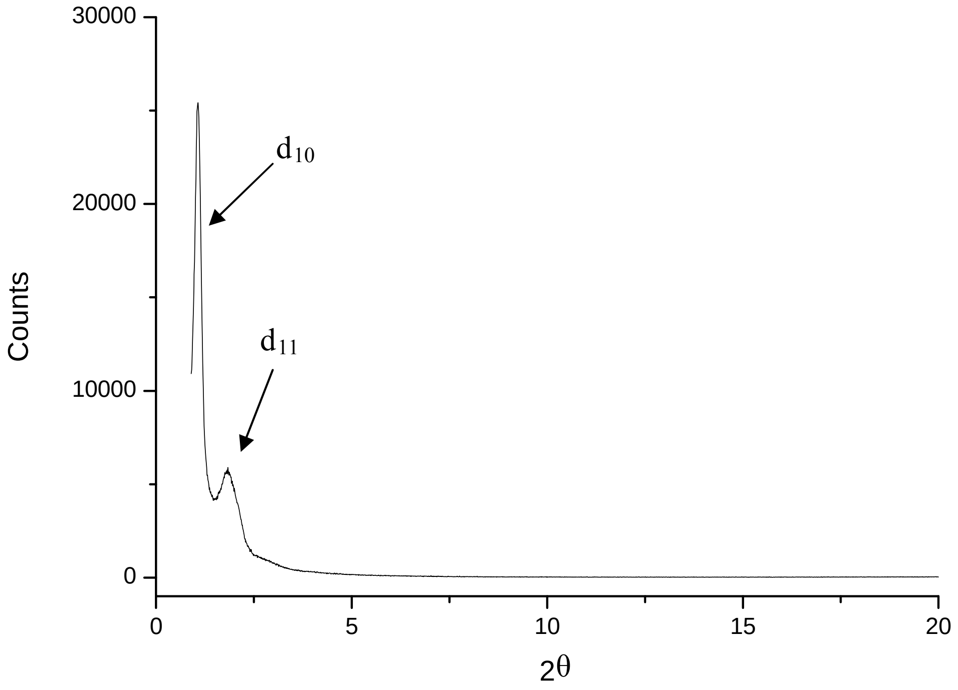

Figure 3.7 X-ray diffraction pattern of undoped SBA-15-like silica prepared by TLCT

Table 3.2 Identification of hexagonal pore structure using relative peak positions

	d_{10}	d_{11}	d_{20}
Observed	1.14	1.83	-
Calculated	-	1.97	2.28

Combining the nitrogen sorption results with the data calculated from the XRD pattern, we obtain the structural data for TLCT SBA-15 shown in Table 3.3.

Table 3.3 Structural data for undoped SBA-15-like silica prepared by TLCT

Surface Area / $m^2 g^{-1}$	Pore Diameter / Å	d-spacing d / Å	Lattice Parameter / Å	Pore Wall Thickness / Å
600	51.5	77.4	89.4	37.9

These data show that it is possible to prepare an SBA-15-like material, with few micropores, using the TLCT method. SBA-15 has been heavily studied since its discovery; however, there are no prior reports of it being prepared in this manner. With the parameters of the parent, undoped material established it was the intention to use the same methodology to prepare metal nanoparticle doped SBA-15 using the same one-pot method as with MCM-41 in Chapter 2.

Traditional methods for controlling micropore content in SBA-15 include increasing the temperature during synthesis, which is found to reduce the volume of micropores, until a temperature of 130 ºC is reached, reducing the microporosity to almost nothing,[11] while showing an increase in the pore diameter and a reduction in pore-wall thickness and surface area. Alternatively, non-microporous SBA-15 can be synthesised by using surfactant mixtures,[12] post-treatment[13] and microwave-hydrothermal synthesis.[14]

3.3 Palladium doped SBA-15

Palladium was the first metal to be studied with the new TLCT-SBA-15 to allow a direct comparison with palladium-doped MCM-41, structurally as well as catalytically (Chapter 5). 0.03 g of $(NH_4)_2[PdCl_4]$, 4 wt%, was dissolved in the acidified water before the P123 surfactant was added and mixed in the same way as TLCT-SBA-15 was prepared previously.

In 2008, Wang *et al.*[15] prepared palladium-doped SBA-15 by incipient wetness impregnation using an aqueous solution of $PdCl_2$. With a palladium loading of 2 wt% they observed a small decrease in surface area from 597 $m^2\ g^{-1}$ to 526 $m^2\ g^{-1}$ and no change to the average pore diameter of 7.7 nm. They calculated the palladium particle size to be 8.5 nm from X-ray data and application of the Scherrer equation, and measured them to be 8.2 nm from TEM images. Both are slightly larger than the average pore size of 7.7 nm, suggesting that the particles have encroached on the pore walls, but have been contained by them in a well dispersed manner. They also observed that increasing the metal loading from 0.5 wt% to 5.0 wt% had little effect on the particle sizes, remaining at ~8.2 nm by TEM.

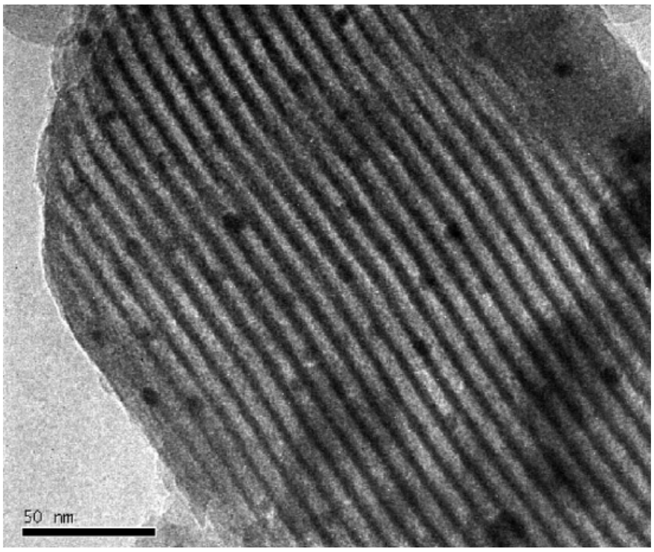

Figure 3.8 TEM image of Wang's Pd-SBA-15

In 2007, Han *et al.*[16] reported a co-precipitation method of preparing SBA-15 doped with palladium nanoparticles. They prepared the SBA-15 using the standard method, adding aqueous $PdCl_2$ to the mixture prior to the addition of tetraethyoxysilane (TEOS). With a palladium loading of 5.7 wt%, they observed an overall surface area of 615 $m^2 g^{-1}$, average pore diameter of 57.8 Å and calculations from the high-angle XRD gave a particle size of 7.6 nm. Once again, with a particle size only slightly larger than the pore size, it is suggested that the particles are well dispersed and confined within the pores, which is confirmed by the TEM images (Figure 3.9). They demonstrated the ease with which palladium loading could be altered; however, they observed that higher loadings (> 10 wt%) resulted in an inferior hexagonal structures (by low-angle XRD). They reported that the prepared materials showed high catalytic activity for both the Suzuki and Heck coupling reactions.

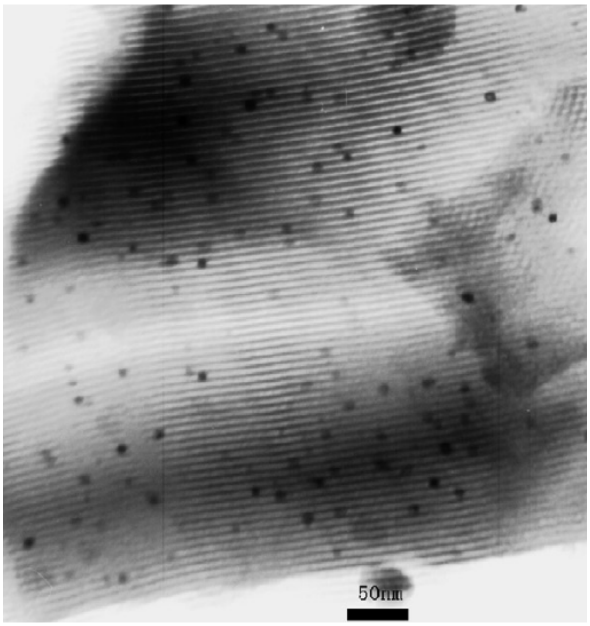

Figure 3.9 TEM image of Han's Pd-SBA-15

The results reported by Wang *et al.* and Han *et al.*[16] suggest that SBA-15 is better suited to controlling and containing palladium particle growth and dispersion than the MCM-41 materials and should be favourable for use in the TLCT method. It is important to note that in Wang's work, the palladium was added to completed pore structures while Han was introducing particles of a specified size, both methods would naturally be favourable towards the desired particle size within SBA-15.

$(NH_4)_2[PdCl_4]$ was added to the TLCT-SBA-15 method described previously at a loading of ~4 wt% and the resultant material characterised fully, Table 3.4. Curiously, once the palladium salt was mixed with the P123/water sol-gel the mixture turned black in colour. This was unusual as previously prepared materials using $C_{12}EO_{10}$ and $(NH_4)_2[PdCl_4]$ had been the same brown colour of the palladium salt. It is thought that the salt may have oxidised in the presence of P123, possibly caused by the large number of ethylene oxide units within the tail group.

Nitrogen sorption measurements again show a lowered surface area of around 600 m^2 g^{-1}, which is consistent with the characteristics observed for non-doped TLCT-SBA-15. A smaller pore diameter was observed along with an increase in pore wall thickness, indicative of palladium within the pores.

Table 3.4 Structural data for Pd-doped SBA-15-like silica prepared by TLCT

Precursor	Surface Area / m^2 g^{-1}	Pore Diameter / Å	d-spacing d / Å	Lattice Parameter / Å	Pore Wall Thickness / Å
$(NH_4)_2[PdCl_4]$	621	34.5	87.3	100.8	66.2

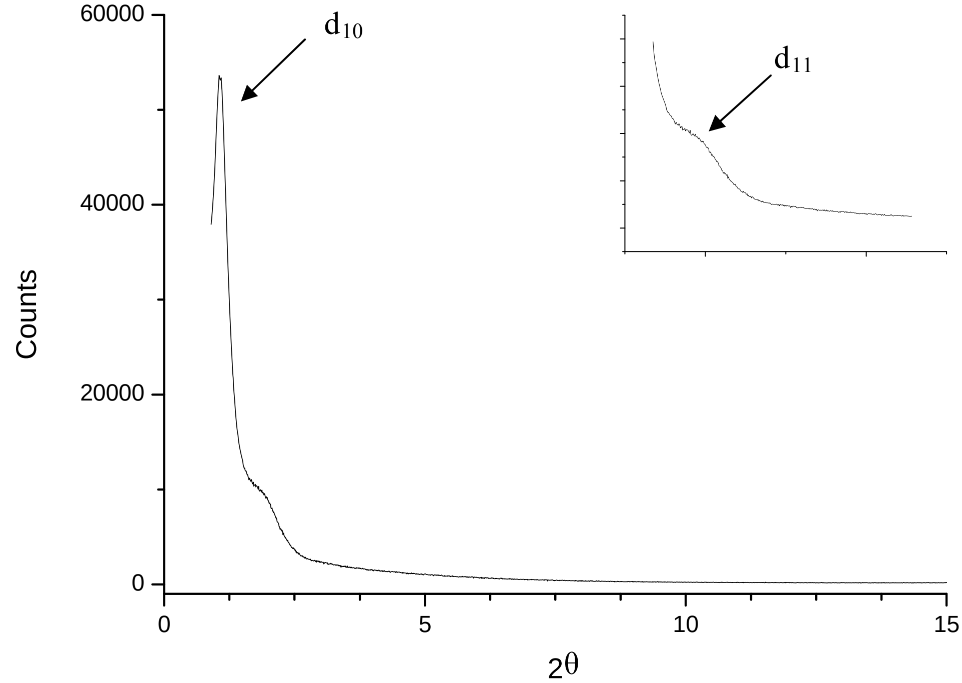

Figure 3.10 X-ray diffraction pattern of Pd-doped SBA-15-like silica prepared by TLCT

Low-angle XRD was used to identify the hexagonal pore structure and, as with the undoped SBA-15, only the d_{10} and d_{11} reflections were visible, again suggesting that while the hexagonal structure is present, it is not as well defined and contains less long-range ordering than the ideal material. This is likely caused by the increased viscosity of the P123 compared with the $C_{12}EO_{10}$ surfactant, making it slower to form the mesophase after the methanol is removed, compared with the rate at which the TMOS hydrolyses.

3.3.1 Particle size

TEM images of the palladium-doped material (Figure 3.11) show the pore structure very clearly, with long, straight pores in excess of 1 μm in length. The repeat distance or lattice parameter (pore wall thickness and pore diameter) was measured to be 10.1 nm by low-angle XRD and 9.8 nm by TEM. The metal particles are clearly visible in three of the images shown, appearing to be well dispersed and of uniform size, a significant improvement to the previous surfactant template, $C_{12}EO_{10}$ (Chapter 2). However, the particles were measured to be 14.8 nm, clearly larger than an individual pore. The particles can be seen occupying multiple pores, although only two, or at most three. A slight ‘bending’ of the pore walls can be seen around the particles within the images, this can be used as in indication that the particles are positioned within the pores themselves and causing the walls to be pushed around them during condensation, rather than the particles being found on the silica surface, outside the pore structure.

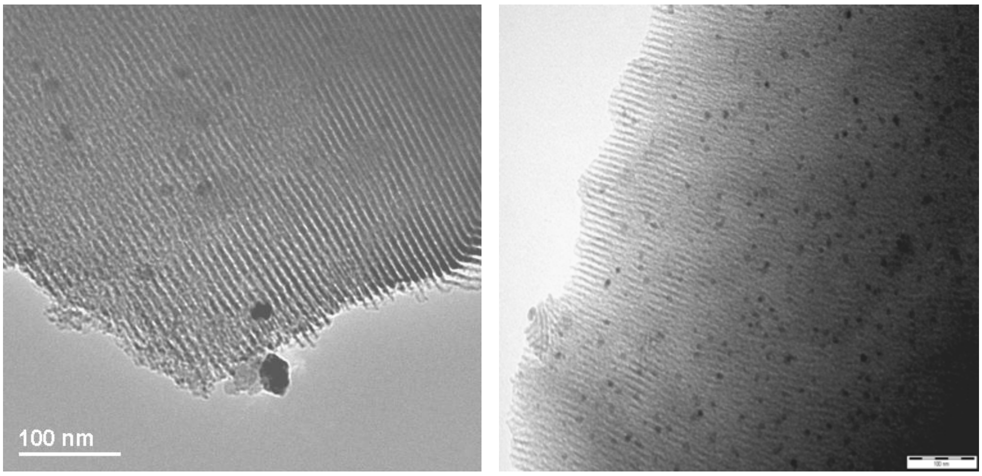

Figure 3.11 TEM images of Pd-doped SBA-15-like silica prepared by TLCT

In addition to measuring with TEM, the average particle size was calculated from the wide-angle XRD (Figure 3.12) using the Scherrer equation and found to be in very good agreement with the TEM images at 15.6 nm. Using the wide-angle XRD it was also possible to identify the oxidation state in the particles, by comparing it with standards, and all five peaks match well with that of palladium (II) oxide.

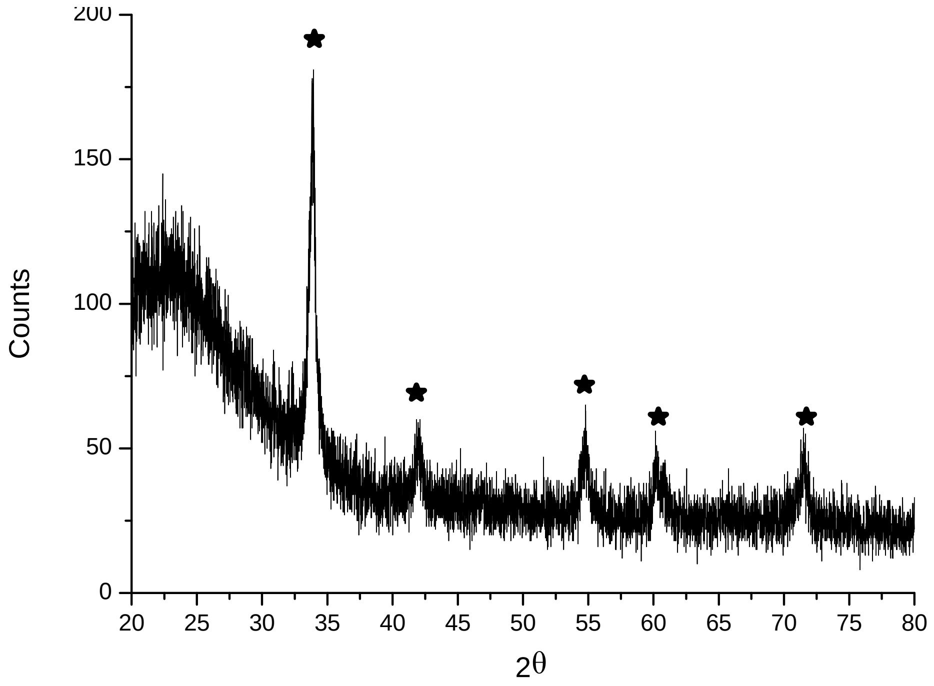

Figure 3.12 Wide-angle X-ray diffraction pattern of Pd-doped SBA-15-like silica prepared by TLCT, (★) peak positions of PdO

As a final method of particle size characterisation, CO pulse chemisorption was carried out by C. Parlett at Cardiff University to determine an average crystallite size of 11.1 nm with a total metal surface area of 22.45 m^2 g^{-1}. Each of these techniques using different methods to arrive at very similar particle size measurements lends confidence in the dispersion and uniformity of the particles within the material.

While the change in surfactant, and pore size, appears to have been favourable in controlling the particle size, it has not completely solved the problem and it is likely that the stability of the precursor and the temperature at which it decomposes is still an issue.

3.3.2 Metal loadings

With the intention of using the prepared materials for catalytic testing, as with the palladium-doped TLCT-MCM-41 in Chapter 2, a series of materials with different palladium loadings were prepared. Using palladium loadings of 0.01, 0.05, 0.1, 0.5, 1.00 and 2.50 wt%, the series was produced and characterised (Table 3.5). The specific surface area varies slightly over the series, but not significantly and it does not appear to have an obvious pattern or trend. However, as the palladium loading increases, the pore diameter decreases from 53 Å to 41 Å and an increase in the pore wall thickness is observed from 41 Å to 71 Å. The increased wall thickness is partly accounted for by the decreasing pore diameter, being filled by the palladium particles; however, this only explains a 12 Å increase; the remaining 18 Å is attributed to an increase in the lattice parameter. The palladium precursor will be situated in the aqueous region prior to silica hydrolysis, presumably as loading increases cause a slight swelling in between the micelles that would form the pores after hydrolysis/calcination.

Table 3.5 Structural data for Pd-doped SBA-15-like silica prepared by TLCT

Metal loading	Surface Area / $m^2\ g^{-1}$	Pore Diameter / Å	d-spacing d / Å	Lattice Parameter / Å	Pore Wall Thickness / Å
0.00 wt%	600	51.5	77.4	89.4	37.9
0.01 wt%	611	52.9	81.4	94.0	41.0
0.05 wt%	647	48.2	83.5	96.4	48.2
0.10 wt%	721	43.4	83.5	96.4	52.9
0.50 wt%	619	48.2	85.7	99.0	47.5
1.00 wt%	518	46.3	87.3	100.8	54.4
2.50 wt%	776	40.7	97.0	112.0	71.2

3.4 Other transition metals in SBA-15

3.4.1 Platinum

By analogy with the MCM-41 materials discussed in Chapter 2, the platinum precursor $(NH_4)_2[PtCl_4]$ was used to dope TLCT-SBA-15 with platinum nanoparticles. We are able to compare this method with incipient wetness impregnation by once again considering the work of Wang *et al.*[17] who observed a material with a surface area of 521 m^2 g^{-1} and a pore diameter of 77 Å for a platinum loading of 2 wt%. By measuring the platinum particles observed in the TEM images (Figure 3.13); they determined the average particle size to be 7.8 nm, almost identical to the pore diameter.

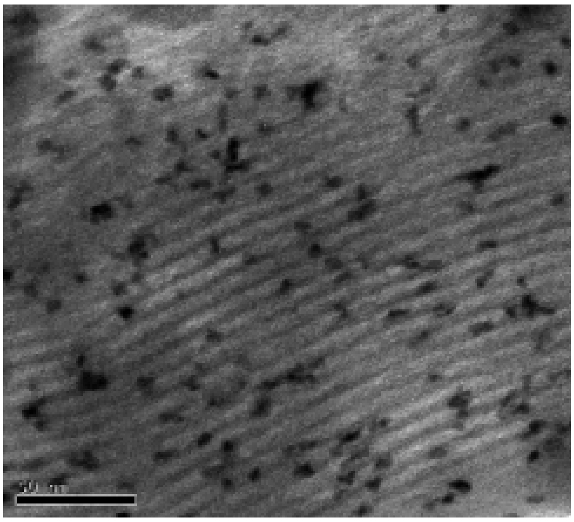

Figure 3.13 TEM image of Wang's Pt-SBA-15

In comparison, Chytil *et al.*[18] prepared platinum doped SBA-15 using a novel route which involved preparing platinum nanoparticles of around 6-10 nm which were then added to the standard SBA-15 method as a platinum sol, rather than just water. They compared the prepared material with platinum doped SBA-15 by incipient wetness impregnation. All three materials prepared, SBA-15, Pt-SBA-15 and Pt_{nano}-SBA-15, showed the presence of a well-ordered, two-dimensional hexagonal pore structure by low angle XRD. They observed that the platinum nanoparticles retained their shape and size during the synthesis of SBA-15; however, chemisorption and catalytic testing suggested that some of the particles were inaccessible, possibly due to incorporation within the bulk silica.

In a similar study, Rioux *et al.*[19] prepared a series of platinum nanoparticles in a range of sizes, from 1.7 – 7.1 nm, each with a narrow size distribution and doped them onto SBA-15 by including a platinum colloidal aqueous solution in the synthesis of SBA-15. They used a method which would yield an SBA-15 material with a pore diameter of 9.0 nm and a high surface area of 700-800 m^2g^{-1} and observed by TEM that the particles were well dispersed within the pores, which could be seen most clearly with the larger 7.1 nm particles (Figure 3.14). They tested the prepared materials as a catalyst for ethylene hydrogenation and ethane hydrogenolysis finding that smaller platinum particles demonstrated a higher activity. They also observed that the materials exhibited good thermal stability during reaction.

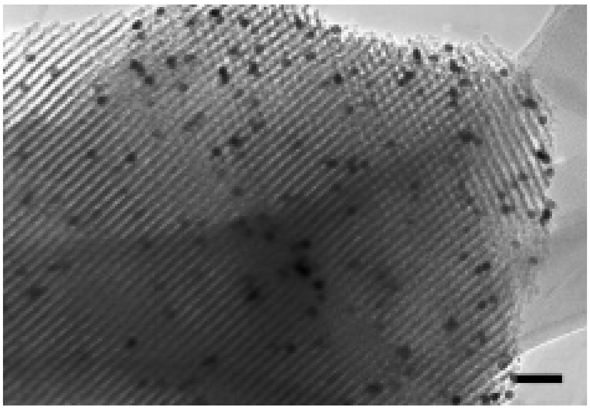

Figure 3.14 TEM image of Rioux's Pt-SBA-15 with 7.1 nm particles

While each of the methods previously discussed was successful in preparing well-dispersed, platinum-doped SBA-15, they all involve a two-step synthesis process. Chen *et al.*[20] reported a one-pot method where 3-mercaptopropyltrimethosysilane (MPTMS) and $H_2[PtCl_6]$ were added to the SBA-15 preparation after 1-3 hours. They identified the hexagonal pore structure by low-angle XRD and measured a surface area of 665 $m^2\ g^{-1}$. The average pore diameter was not reported; however, particle sizes were found to be 2.4 nm (3 wt% loading) and 4.5 nm (7.5 wt% loading) from the wide-angle XRD, which would suggest the particles are within the pores, an inference confirmed by TEM images showing well-dispersed particles.

Platinum-doped TLCT-SBA-15 was prepared using $(NH_4)_2[PtCl_4]$ to a loading of 4.1 wt% using the same method as with the palladium precursor; the structural characterisations were found to be comparable and are shown in Table 3.6. Interestingly, the platinum salt did not turn black when added to the P123 surfactant as with $(NH_4)_2[PdCl_4]$, presumably the salt is unaffected by the surfactant. The hexagonal pore structure was identified by the characteristic d_{10} reflection (Figure 3.15) as well as the barely visible d_{11} and d_{20} reflections which were confirmed as such by calculating the expected peak positions (Table 3.7).

Table 3.6 Structural data for Pt-doped SBA-15-like silica prepared by TLCT

Precursor	Surface Area / $m^2 g^{-1}$	Pore Diameter / Å	d-spacing d / Å	Lattice Parameter / Å	Pore Wall Thickness / Å
$(NH_4)_2[PtCl_4]$	622	42.5	77.4	89.4	46.9

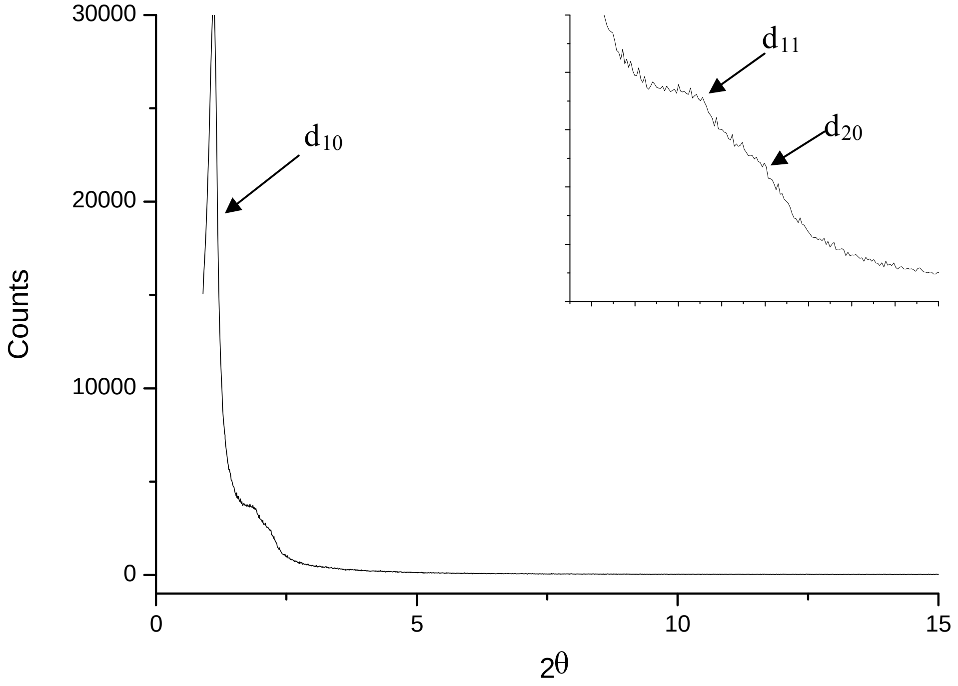

Figure 3.15 X-ray diffraction pattern of Pt-doped SBA-15-like silica prepared by TLCT

Table 3.7 Identification of hexagonal pore structure using relative peak positions

	d_{10}	d_{11}	d_{20}
Observed	1.09	1.75	2.10
Calculated	-	1.89	2.19

Examining the wide-angle XRD pattern of the material prepared (Figure 3.16), it is possible to identify the platinum particles as platinum metal with an average particle size of 22.7 nm, which is significantly larger than the pore diameter of 4.2 nm. As we know, the Scherrer equation gives an average particle size across the sample and does not account for small particles that cannot be detected. However, TEM images (Figure 3.17) show metal particles at a much smaller size, 5.6 nm, which appear to be contained within the pores and well-dispersed. CO chemisorption supports this measurement with an average particle size of 3.8 nm and a metal surface area of 37.04 m^2 g^{-1}. This suggests that while some of the platinum has clearly formed small particles within the pore network in a well dispersed manner, there are also larger particles present which were detected by X-ray diffraction.

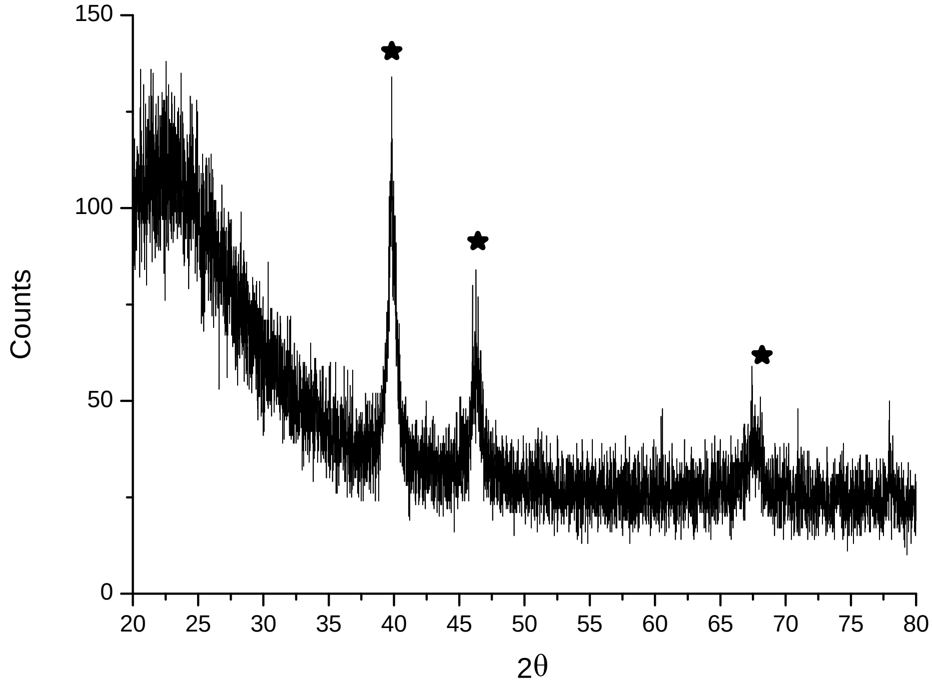

Figure 3.16 Wide-angle X-ray diffraction pattern of Pt-doped SBA-15-like silica prepared by TLCT, (★) peak positions of Pt metal

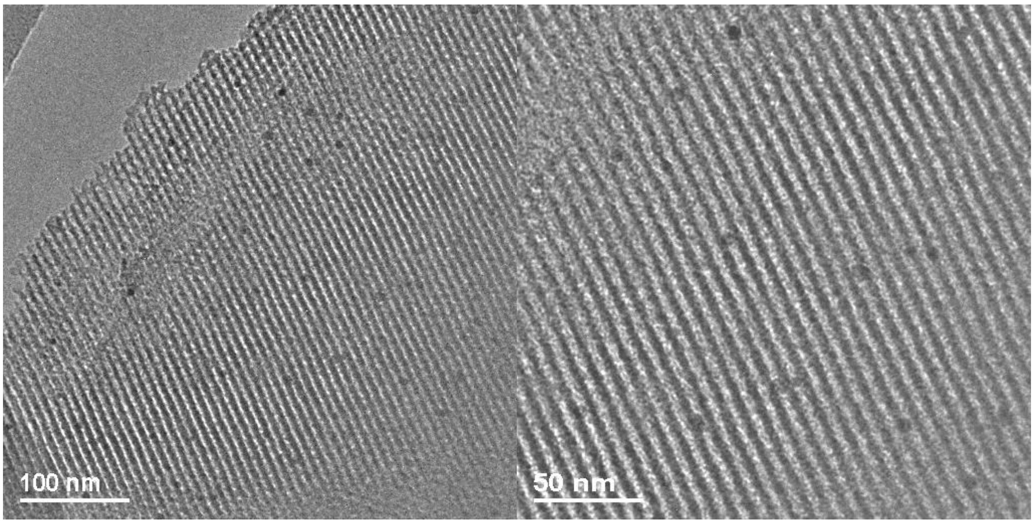

Figure 3.17 TEM images of Pt-doped SBA-15-like silica prepared by TLCT

The $(NH_4)_2[PtCl_4]$ precursor appears to behave in a much more favourable manner with the P123 surfactant, preparing an SBA-15-like silica doped with platinum nanoparticles that are well dispersed and contained within the pore structure.

3.4.2 Gold

Interest in gold nanoparticles was discussed in Chapter 2 and the challenge to prepare small nanoparticles (< 5 nm) continues by attempting to dope gold nanoparticles in the porous network of SBA-15. Jin *et al.*[21] reported gold particles with a size of 1.8 nm contained within a modified SBA-15 in 2008. They prepared a mesporous organosilica incorporated with bridging disulfide-imidazolium units (Figure 3.18), PMO-SBA-15, and utilised the disulfide groups to capture aqueous chloroaurate(III) groups; the chloride ions were then washed away at room temperature to yield Au-PMO-SBA-15. They characterised the material as having a surface area of 450 $m^2\ g^{-1}$ and a pore diameter of 4.8 nm, reduced from 513 $m^2\ g^{-1}$ and 6.5 nm in the undoped PMO-SBA-15. They identified the gold nanoparticles to be 1.8 nm from measurements of the TEM images collected.

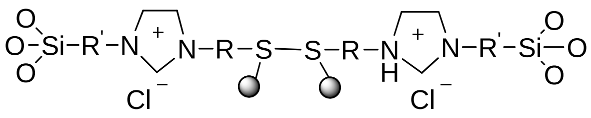

R = $(CH_2)_6$, and R' = $(CH_2)_3$

Figure 3.18 Bridging disulphide-imidazolium unit

Escamilla-Perea *et al.*[22] doped gold onto SBA-15 using the deposition-precipitation method. With a gold loading of 1 wt% they observed a significant drop in surface area from 819 $m^2 g^{-1}$ to 487 $m^2 g^{-1}$. Interestingly, they measured the change in pore volumes of the total porosity and the volume attributed to micropores, with total volume reducing from 0.964 $m^3 g^{-1}$ to 0.718 $m^3 g^{-1}$, of which the micropores accounted for a reduction of 0.096 $m^3 g^{-1}$ to 0.023 $m^3 g^{-1}$. While the gold particles within the micropores are likely to be very small which is favourable, they are also likely to be difficult to access.

Again in 2008, Li *et al.*[23] used gold-doped SBA-15 in a different manner; as a template to prepare gold nanorods. They firstly impregnated gold nanoparticles into SBA-15 modified by the addition of 3-aminopropyltriethoxysilane (APTES), reporting nanoparticle 'seeds' of 3 – 5 nm within the SBA-15 with a surface area of 421 m^2g^{-1} and pore diameter of 4.9 nm. Following this, they used a modified seed-mediated growth method to deposit more gold into the material, which would fill the pore channels, creating nanorods of up to 200 nm in length a with a uniform diameter (Figure 3.19). Li extracted the gold nanorods by dissolving the SBA-15 in 2 wt% HF in ethanol solution containing 1 wt% of 1-dodecanethiol.

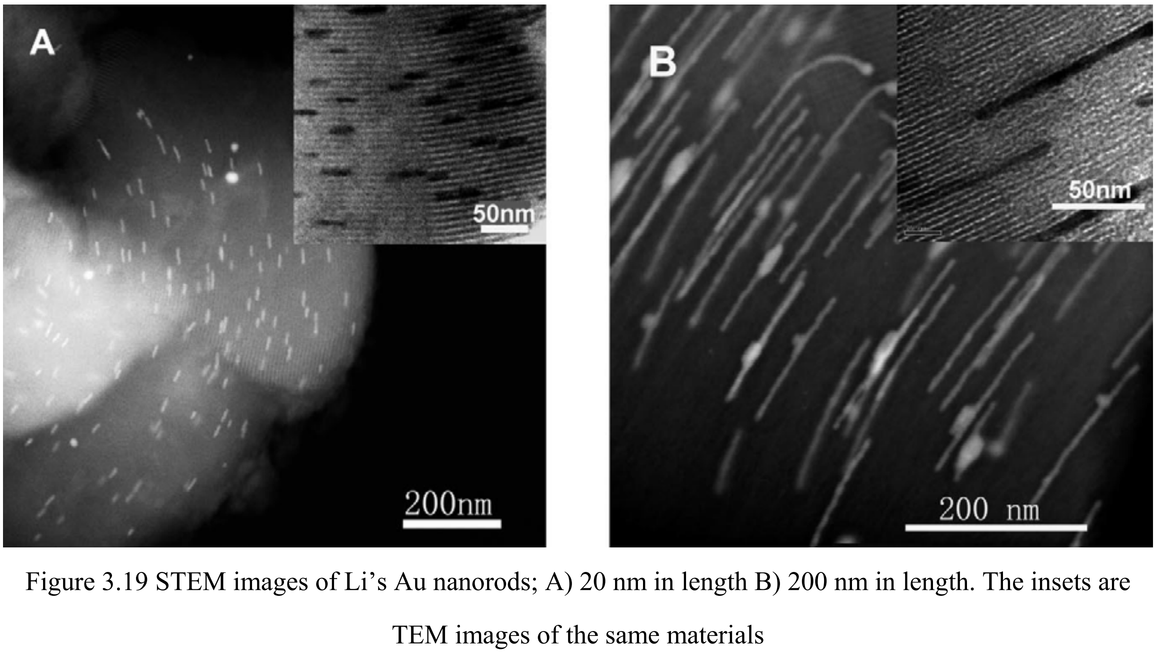

Figure 3.19 STEM images of Li's Au nanorods; A) 20 nm in length B) 200 nm in length. The insets are TEM images of the same materials

In 2009, Lee *et al.*[24] reported their investigation into the importance of the synthesis conditions when preparing gold nanoparticles doped onto a variety of silica hosts. They considered HMS, MCM-41, MCM-48, SBA-15 and SBA-16 as supports for the gold nanoparticles. Prior to loading the gold particles onto the silica material, the silicas were grafted by amine functional groups, either (3-aminopropyl)triethoxysilane (APTS) or N-[3-(trimethoxysilyl)propyl]ethylenediamine (DAPTS) and then the gold precursor, $HAuCl_4$, was introduced by incipient wetness impregnation.

They observed (Table 3.8) that the lower calcination temperature of 200 °C was more favourable for generating smaller gold particles, presuming that the gold sintered with heating, forming larger particles. With a pore size of 6.8 nm, the material prepared using the APTS ligand and water as the solvent was the only one to exhibit particles fully contained within the pore structure (Figure 3.20).

Table 3.8 Lee's investigation into the synthesis conditions

Bifunctional ligand	Solvent used for loading gold	Calcination temperature / °C	Au particle size / nm
APTS	Water	200	2.1 – 3.2
APTS	Water	550	3.2 – 10.3
APTS	Ethanol	200	4.5 – 15.7
APTS	Ethanol	550	3.9 – 19.4
DAPTS	Water	200	5.8 – 8.7
DAPTS	Water	550	3.9 – 11.7
DAPTS	Ethanol	200	4.5 – 18.0
DAPTS	Ethanol	550	3.9 – 23.3

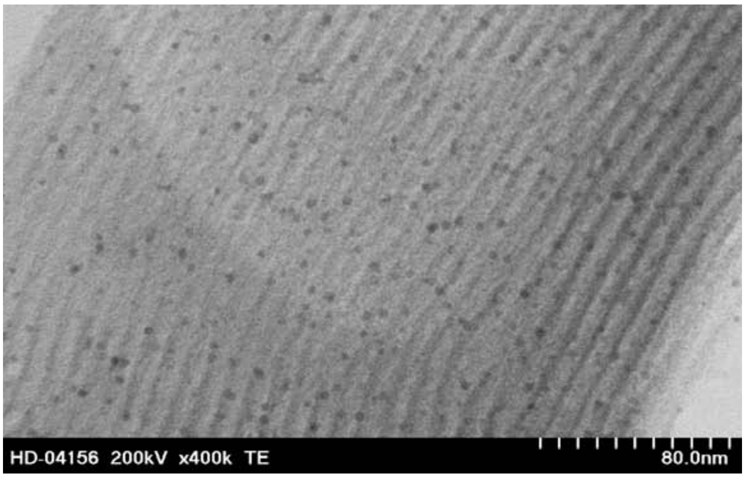

Figure 3.20 Lee's SBA-15 doped with gold nanoparticles, using the APTS ligand, water as solvent and calcination temperature of 200°C

A series of gold nanoparticles doped into TLCT-SBA-15 were prepared using $NH_4[AuCl_4]$ at the same range of metal loadings used previously, 0.01 wt% to 2.50 wt%, with structural results shown in Table 3.9. There is a general trend towards increasing lattice parameter with increasing metal loading, which is consistent with previous observations. The hexagonal pore structure is identified from the low angle XRD (Figure 3.21) and the clear pores can be seen in the TEM images collected (Figure 3.22).

Table 3.9 Structural data for Au-doped SBA-15-like silica prepared by TLCT

Metal loading	Surface Area / $m^2 g^{-1}$	Pore Diameter / Å	d-spacing d / Å	Lattice Parameter / Å	Pore Wall Thickness / Å
0.00 wt%	600	51.5	77.4	89.4	37.9
0.01 wt%	607	49.3	72.7	84.0	34.6
0.05 wt%	627	53.7	75.6	87.3	33.5
0.10 wt%	545	52.6	82.1	94.8	42.1
0.50 wt%	631	59.1	85.0	98.1	39.0
1.00 wt%	839	44.9	85.0	98.1	53.2
2.50 wt%	619	47.2	82.8	95.6	48.3

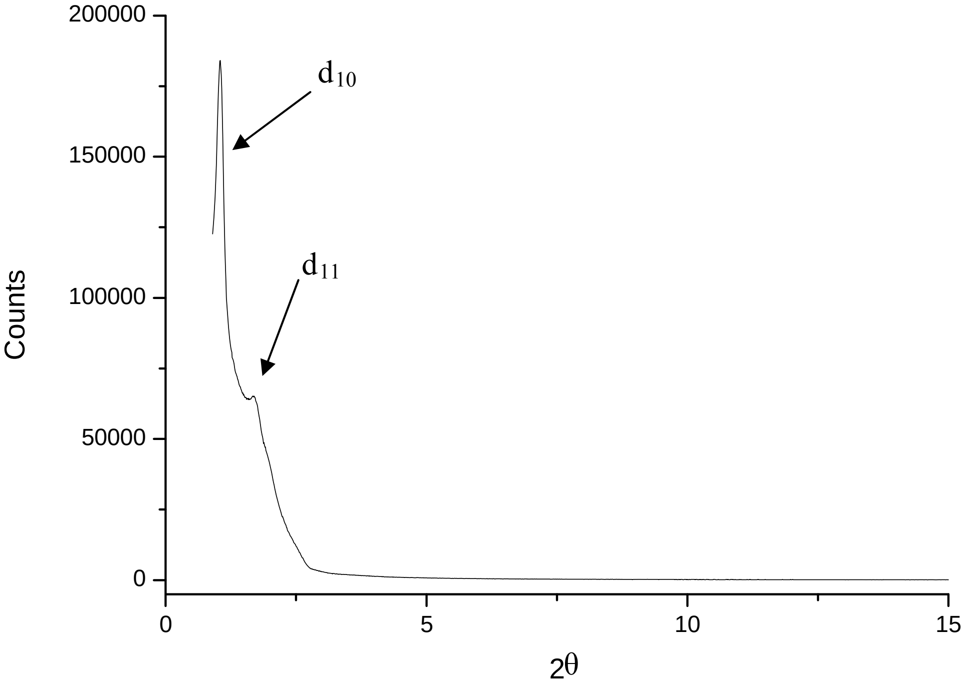

Figure 3.21 X-ray diffraction pattern of Au-doped SBA-15-like silica prepared by TLCT

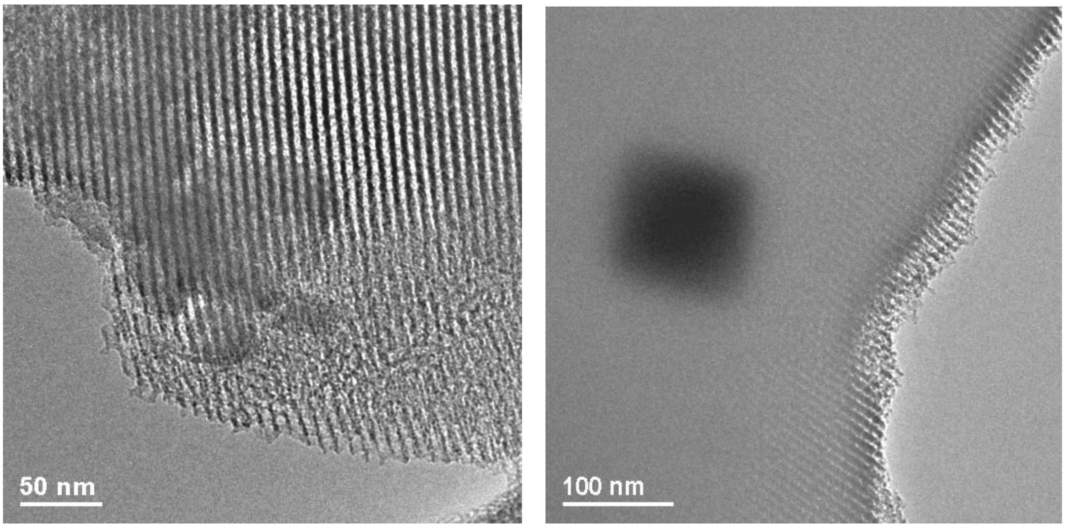

Figure 3.22 TEM images of Au-doped SBA-15-like silica prepared by TLCT

While the TEM images show clear pores of uniform diameter and reasonably long length (> 300 nm), the pores do not appear to contain any gold particles. Instead it appears the gold has agglomerated into larger particles, probably located on the surface of the silica. The peak positions found in the wide-angle X-ray diffraction patterns (Figure 3.23) allow the metal particles to be identified as that of metallic gold and Scherrer equation calculations corroborate the large particles observed in the TEM images with an average particle size of 36.4 nm.

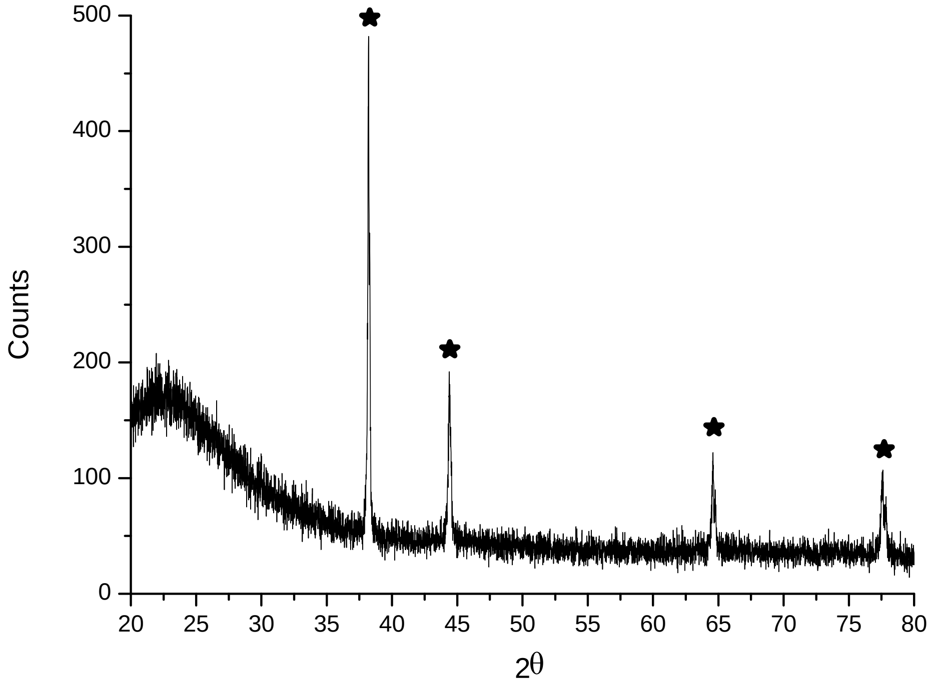

Figure 3.23 Wide-angle X-ray diffraction pattern of Au-doped SBA-15-like silica prepared by TLCT, (★) peak positions of Au metal

Based on the observations here and those made by Lee[24] it appears likely that the gold precursor becomes thermally unstable and sinters at a temperature below that used during calcination, resulting in the agglomeration of the gold particles. It could also be assumed that this sintering occurs below the temperature at which the silica walls harden and become solid enough to contain the particles, as this would have resulted in gold nanotubes like those synthesised by Li.

3.4.3 Bimetallic SBA-15

It is common in catalytic applications for more than one metal to be supported on the silica, to lend properties of both metals to the favourable reaction, to aid in selectivity or to prevent catalyst deactivation. There are a range of bimetallic SBA-15 catalysts reported for a variety of reactions such as Au-Cu in CO oxidation,[25] Ni-Co for H_2 production from cellulose decomposition,[26] Pd-Bi in the oxidation of lactose[27] and Ru-Ni for the hydrogenation of acetonitrile.[28]

Zheng *et al.*[29] prepared Pd-Au doped SBA-15 for the Suzuki-Miyaura coupling reaction by grafting G4-poly (amido-amine) (G4-PAMAM, where G represents the generation) (Figure 3.24) into the pores of the SBA-15 and using this to stabilise the formation of nanoparticles when $K_2[PdCl_4]$ and $H[AuCl_4]$ were added. By TEM they identified that monodisperse nanoparticles had been generated and stabilised within the pore channels. Crucially, they observed that Pd-G4-PAMAM-SBA-15 displayed high catalytic activity for the Suzuki-Miyaura coupling reaction; however, the Pd/Au-G4-PAMAM-SBA-15 exhibited even higher activity.

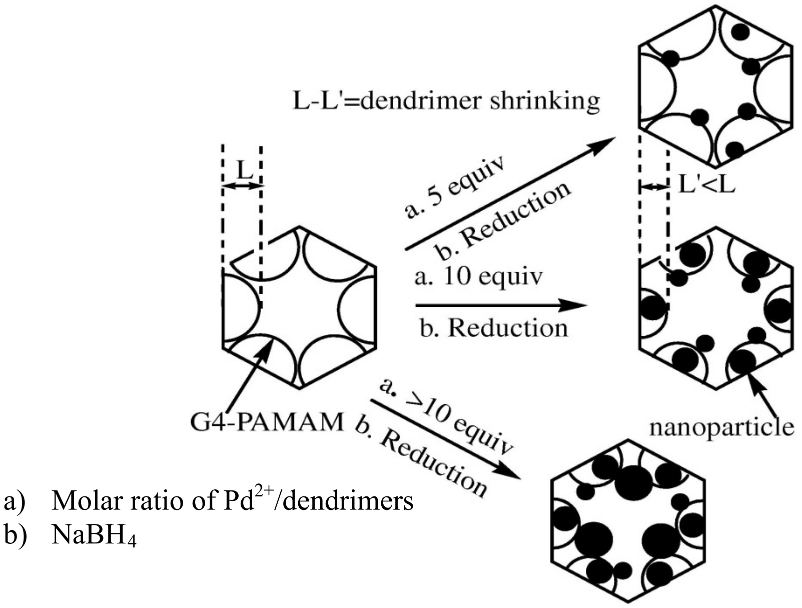

Figure 3.24 Zheng's proposed procedure for the preparation of the catalyst

A comparison between Au-SBA-15 and Pd/Au-SBA-15 was reported by Ma *et al.*[30] using both direct grafting and impregnation methods. They observed that the addition of palladium into the catalyst could decrease the particle size compared with the catalyst containing only gold. The Au-SBA-15 material prepared by direct grafting yielded gold particles of 10 nm; when palladium was added to the synthesis, the particles were found to be 5 nm in size and uniformly dispersed. Additionally, they observed that the palladium did not reduce the selectivity of the catalyst in the oxidation reaction of benzyl alcohol.

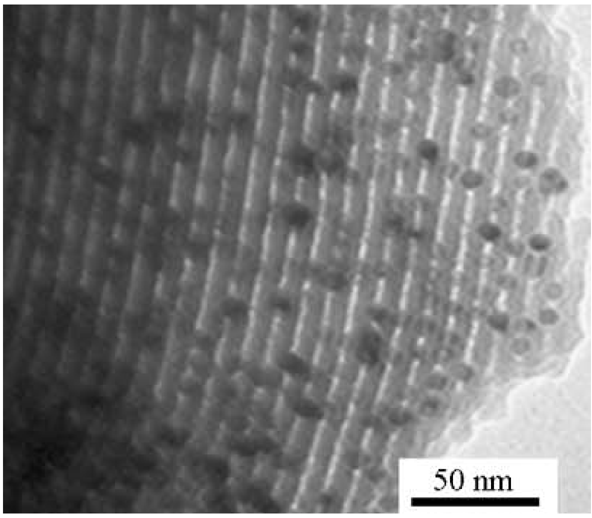

Figure 3.25 TEM image of Ma's direct grafted Au/Pd-SBA-15 with 5 nm particles

Following the same methodology as previous preparations a TLCT-SBA-15 was prepared using both the $(NH_4)_2[PdCl_4]$ and $(NH_4)[AuCl_4]$ precursors. As with the MCM-41 bimetallic materials, the intention was to observe Au/Pd bimetallic nanoparticles within the pores. Comparing the bimetallic material with the two monometallic materials, gold and palladium, the porosimetry results are very similar (Table 3.10) with smaller pores and thicker walls compared with the undoped SBA-15.

Table 3.10 Structural data for Au/Pd-doped SBA-15-like silica prepared by TLCT

Precursor	Surface Area / $m^2\ g^{-1}$	Pore Diameter / Å	d-spacing d / Å	Lattice Parameter / Å	Pore Wall Thickness / Å
None	600	51.5	77.4	89.4	37.9
$(NH_4)_2[PdCl_4]$	621	34.5	87.3	100.8	66.2
$(NH_4)[AuCl_4]$	619	47.9	82.8	95.6	48.3
$(NH_4)_2[PdCl_4]$ $(NH_4)[AuCl_4]$	605	37.7	80.0	92.4	54.9

High-angle XRD (Figure 3.26) identified the particles as containing metallic gold and palladium oxide; however, in the same manner as with the MCM-41 bimetallic materials, once the average particle sizes were calculated it appears that separate particles have formed. The metallic gold was calculated to be 24.0 nm in size and the palladium oxide to be 14.3 nm. These sizes are consistent with the particle sizes calculated for the separate gold and palladium materials (Table 3.11), also suggesting that the precursors have not mixed well and instead formed separate particles within the silica.

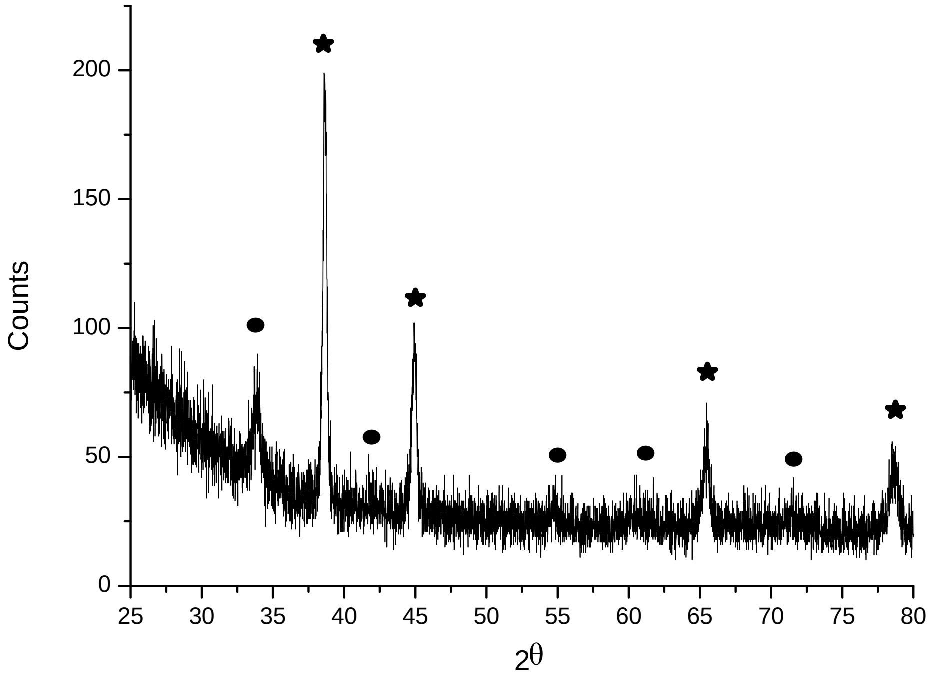

Figure 3.26 Wide-angle X-ray diffraction pattern of Au/Pd-doped SBA-15-like silica prepared by TLCT, (★) peak positions of Au metal and (●) peak positions of PdO

Table 3.11 Particle size measurements using the Scherrer equation

Precursor	Metal Species	Particle Size / nm
$(NH_4)_2[PdCl_4]$	PdO	15.6
$(NH_4)[AuCl_4]$	Au Metal	36.4
$(NH_4)_2[PdCl_4]$/ $(NH_4)[AuCl_4]$	PdO/Au Metal	14.3 / 24.0

Particle sizes observed by TEM (Figure 3.27) are consistent with the calculated measurements of the palladium oxide particles, which appear to be somewhat larger than the individual pores, but look to be contained within them due to the slight pore wall bending around the particle. However, the larger gold particles were not identified within these images, suggesting that the particles may not have formed within the pore structure due to their larger size. Further to the observations made with bimetallic-doped materials prepared on MCM-41 in Chapter 2, this reinforces the requirement for homogeneous mixing of the precursors to achieve particles that could be considered bimetallic. This is likely to only be feasible with a bimetallic precursor rather than two mixed precursors.

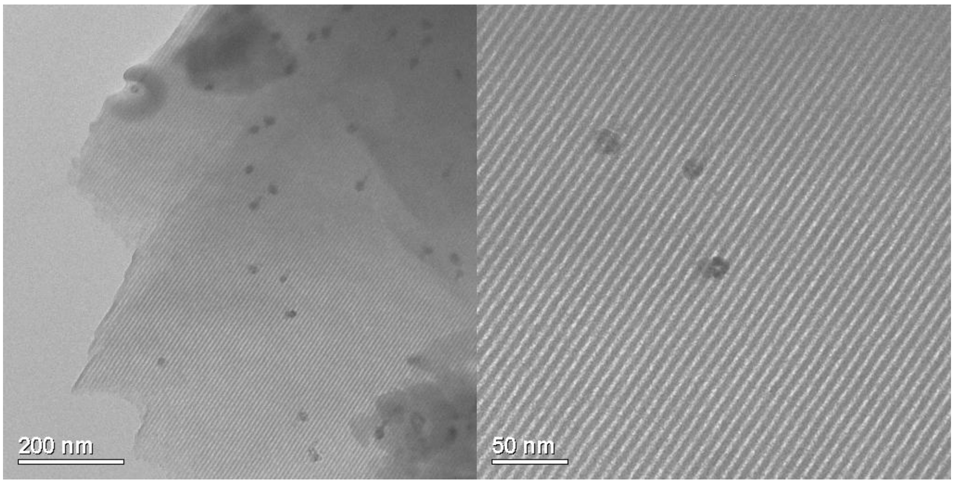

Figure 3.27 TEM images of Au-doped SBA-15-like silica prepared by TLCT.

3.5 Other Pluronics – SBA-16

A potential problem with hexagonal pore networks is blockage and mass transport issues during catalysis. If a pore containing a metal particle blocks, the particle becomes completely inaccessible. This can be overcome by using a different structural pore network; by interconnecting the pores, mass transport becomes less of a problem as there are multiple routes to each metal particle. By changing the template to one that exhibits a bicontinuous cubic phase (Figure 3.28), it is believed that silica can be prepared which would retain the interconnecting pore network exhibited by the surfactant.

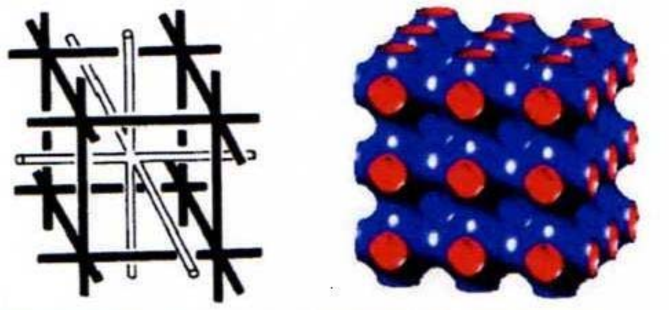

Figure 3.28 The *Im3m* bicontinuous cubic phase

The bicontinuous cubic phase is found between the hexagonal and lamellar regions of the phase diagram and is a very viscous mesophase with an isotropic texture when observed by polarised optical microscopy. It was first characterised and reported by Luzzati *et al.*[31] in 1967 during a crystallographic study of lipid-water systems. The bicontinuous cubic phase is described as having the hydrophobic and hydrophilic domains being separately connected while the amphiphiles form bilayers between the domains.[32] The bilayer is believed to orientate into a single-sheeted three-periodic hyperbolic surface which has a net surface curvature of zero, otherwise known as the infinite periodic minimal surface model.[33]

The Pluronic® F127 (Figure 3.29), has a similar molecular structure to P123; however it exhibits a micellar cubic phase (Figure 3.30). F127 was used in the LCT method to prepare SBA-16 by Zhao *et al.* in 1998 and they reported the silica as having an *Im3m* cubic V_1 structure, identified from the low-angle XRD pattern. Structurally, they found the silica to have a surface area of 740 m^2g^{-1} and an average pore diameter of 5.4 nm.

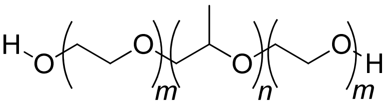

Figure 3.29 F127 surfactant $m = 106$, $n = 70$

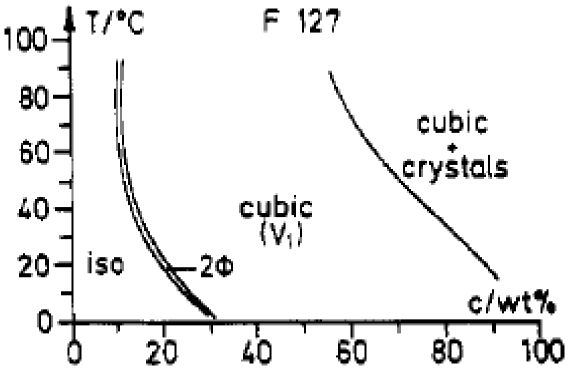

Figure 3.30 Phase diagram of F127

Ma *et al.*[34] prepared SBA-16 in 2010 and modified the surface with 3-aminopropyltriethoxysilane before introducing $[Pd_3(OAc)_6]$ to form palladium nanoparticles within the pore structure. They observed that the addition of the amino groups reduced the surface area of the silica from 763 $m^2\ g^{-1}$ down to 240 $m^2\ g^{-1}$, with a final surface area after the palladium particles were introduced being 163 $m^2\ g^{-1}$, a significant reduction. When tested with the oxidation of benzylic alcohols, 1-phenylethanol and allylic alcohols, the catalyst showed high activity, selectivity and good recovery and recyclability. The recyclability was attributed to the isolated nanocages of SBA-16 which prevented the growth of Pd nanoparticles during the reaction.

It was the intention to use the F127 surfactant as a template to produce an SBA-16 like silica by the TLCT method. However, the bicontinuous cubic phase of F127 is extremely viscous and as such has proven very difficult to use as a template as the phase doesn't appear to form before the hydrolysis of the silica precursor occurs, resulting in amorphous silica once the template is removed. While other surfactants are available that exhibit the same mesophase, this will also be very viscous and as such these were not investigated during this work.

Recent work within the group[35] has provided a more detailed picture of the phase diagram of F127 in water, revealing that, where a cubic phase is observed at room temperature, a much more fluid, isotropic phase is observed at lower temperatures of 4 °C allowing mixing to be achieved between the surfactant, water and the silica source TMOS. It is feasible that exploiting this observation will allow SBA-16 type materials to be prepared using the TLCT methodology.

3.6 Summary

A novel methodology has been demonstrated for preparing SBA-15 silicas, which massively reduces the formation of micropores. This is advantageous over the standard methodology as it requires modification to prepare SBA-15 without micropores and this can be difficult. TLCT-SBA-15 is compatible with the addition of metal salts to prepare nanoparticle doped SBA-15 for palladium, platinum and gold and has proven to be much more favourable towards smaller particles which appear to be contained within the pores in the case of palladium and platinum.

The observation of the gold particles still aggregating and becoming much larger than the pores supports the idea discussed in Chapter 2 that the precursors are decomposing at a low temperature. This is mitigated slightly by the change in surfactant in the case of palladium.

Rather than examining another surfactant, which is not the root cause of the problem, instead it is advisable to consider a change in precursor; this will be examined in Chapter 4.

It is worth noting that while this methodology has proven successful with porosimetry and TEM images to support the formation of the SBA-15 material, low-angle XRD has consistently shown, at best, average results to show the hexagonal structure. A large peak showing the d_{10} reflection with a much smaller d_{11} reflection is observed, but the expected d_{20} is either obscured or simply not present. As discussed, this is an indication that the long-range order is lessened compared with standard SBA-15 materials, which could prove to be disadvantageous.

A more thorough and critical conclusion of this work will be made in Chapter 5 to include suitable comparisons with MCM-41.

3.7 Experimental

3.7.1 General Experimental

The as-synthesised silica gels were calcined in a Carbolite tube furnace using a type 3216 temperature controller. Unless otherwise stated, silicas prepared with P123 were heated at 3 K min^{-1} to 673 K. This temperature was held for six hours under a flow of air before cooling to room temperature.

3.7.2 Preparation of Silicas

P123 templated silicas

$(NH_4)_2[PdCl_4]$ (0.03 g, 5 wt % with respect to surfactant) was dissolved in water (0.50 g) acidified with HCl to pH 2. Added to this was Pluronic® polymer P123 (0.50 g) and the mixture sonicated at 40 °C to aid mixing until a homogeneous, viscous liquid was formed. Tetramethoxylsilane (1.0 cm^3, 6.72 mmol) was added to the gel and mixed thoroughly to yield a free-flowing liquid. This was placed under a light vacuum (120 mbar) at 40 °C to remove the evolved methanol. When the gel becomes viscous and the hexagonal mesophase can be identified by polarised optical microscopy, it can be left on the open bench for 24 h to complete condensation. A portion (0.78 g) of the as-synthesised material was placed in the tube furnace for calcination to yield a dark brown coloured silicate (0.31 g)

Platinum-, gold- and palladium/gold bimetallic-SBA-15 were prepared in the same manner using the metal precursors listed in Table 3.12.

Table 3.12 Range of silicas prepared using P123

Metal	Metal Precursor	Mass of Precursor / g	Mass of Metal / g	Wt% of Metal in calcined material$^+$
Pd	$(NH_4)_2[PdCl_4]$	0.029	0.011	2.9
Pt	$K_2[PtCl_4]$	0.031	0.015	4.1
Au	$(NH_4)[AuCl_4]$	0.014	0.007	2.6
Au/Pd	$(NH_4)_2[PdCl_4]$	0.015	0.006	2.5
	$(NH_4)[AuCl_4]$	0.014	0.008	3.6

$^+$Calculated wt % of metal within the whole sample after calcination

3.8 References

1. C. N. Satterfeild, *Mass Transfer in Heterogeneous Catalysis,* M.I.T Press, 1970.
2. D. Zhao, J. Feng, Q. Huo, N. Melosh, G.H. Frederickson, B.F. Chmelka and G. D. Stucky, *Science*, 1998, **279**, 548.
3. A. Galarneau, H. Cambon, F. Di Renzo and F. Fajula, *Langmuir,* 2001, **17,** 8328.
4. M. Hartmann and A. Vinu, *Langmuir,* 2002, **18,** 8010.
5. S. Chytil, L. Haugland and E. A. Blekkan, *Micro. Meso. Mater.,* 2008, **111,** 134.
6. D. Halamová, M. Badaničová, V. Zeleňák, T. Gondová and U. Vainio, *Appl. Surf. Sci.,* 2010, **256,** 6489.
7. A. Rostom, K. Muir, C. Dube, A. Lanas, E. Jolicoeur and P. Tubwell, *Drug Healthcare Patient Saf.,* 2009, **1,** 47.
8. G. Wanka, H. Hoffmann and W. Ulbricht, *Macromolecules,* 1994, **27,** 4145.
9. G. Zhang, X. Chen, Y. Zhao, F. Ma, B. Jing and H. Qiu, *J. Phys. Chem. B,* 2008, **112,** 6578.
10. D. Zhao, Q. Huo, J. Feng, B. F. Chmelka and G. D. Stucky, *J. Am. Chem. Soc.,* 1998, **120,** 6024.
11. K. Miyazawa, S. Inagaki, *Chem. Commun.,* 2000, 2121.
12. D. Li, X. Guan, J. Song, Y. Di, D. Zhang, X. Ge, L. Zhao and F. Xiao, *Colloids and Surfaces A: Physicochem. Eng. Aspects,* 2006, **272,** 194.
13. R. Ryoo, C. H. Ko, M. Kruk, V. Antochshuk and M. Jaroniec, *J. Phys. Chem. B,* 2000, **104,** 11465.
14. B. L. Newalkar and S. Komarneni, *Chem. Mater.,* 2001, **13,** 4573.
15. Z. Wang, Y. Xie and C. Liu, *J. Phys. Chem. C,* 2008, **112,** 19818.
16. P. Han, X. Wang, X. Qiu, X. Ji and L. Gao, *J. Mol. Catal. A: Chem.,* 2007, **272,** 136.
17. Z. Wang, Y. Xie and C. Liu, *J. Phys. Chem. C,* 2008, **112,** 19818.
18. S. Chytil, W. R. Glomm, E. Vollebekk, K. Bergem, J. Walmsley, J. Sjöblom and E. A. Blekkan, *Micro. Meso. Mater.,* 2005, **86,** 198.
19. R. M. Rioux, H. Song, J. D. Hoefelmeyer, P. Yang and G. A. Somorjai, *J. Phys. Chem. B,* 2005, **190,** 2192.
20. A. Chen, W. Zhang, X. Li, D. Tan, X. Han and X. Bao, *Catal. Lett.,* 2007, **119,** 159.
21. Y. Jin, P. Wang, D. Yin, J. Liu, H. Qiu and N. Yu, *Micro. Meso. Mater.,* 2008, **111,** 569.

---

22. L. Escamilla-Perea, R. Nava, B. Pawelec, M. G. Rosmaninho, C. L. Peza-Ledesma and J. L. G. Fierro, *Appl. Catal. A: Gen.,* 2010, **381,** 42.
23. Z. Li, C. Kübel, V. I. Pârvulescu and R. Richards, *ACS Nano,* 2008, **2,** 1205.
24. B. Lee, Z. Ma, Z. Zhang, C. Park and S. Dai, *Micro. Meso. Mater.,* 2009, **122,** 160.
25. X. Liu, A. Wang, L. Li, T. Zhang, C. Y. Mou and J. F. Lee, *J. Catal.,* 2011, **278,** 288.
26. M. Zhao, T. L. Church and A. T. Harris, *Appl. Catal. B: Environ.,* 2011, **101,** 522.
27. K. Belkacemi and S. Hamoudi, *Ind. Eng. Chem. Res.,* 2010, **49,** 6878.
28. P. Braos-García, C. García-Sancho, A. Infantes-Molina, E. Rodríquez-Castellón and A. Jiménez-López, *Appl. Catal. A: Gen.,* 2010, **381,** 132.
29. Z. Zheng, H. Li, T. Liu and R. Cao, *J. Catal.,* 2010, **270,** 268.
30. C. Y. Ma, B. J. Dou, J. J. Li, J. Cheng, Q. Hu, Z. P. Hao and S. Z. Qiao, *Appl. Catal. B: Environ.,* 2009, **92,** 202.
31. V. Luzzati and P. A. Spegt, *Nature,* 1967, **215,** 701.
32. L. E. Scriven, *Nature,* 1976, **263,** 123.
33. S. T. Hyde, *Curr. Opin. Sol. State Mater. Sci.,* 1996, **1,** 653.
34. Z. Ma, H. Yang, Y. Qin, Y. Hao and G. Li, *J. Mol. Catal. A: Chem.,* 2010, **331,** 78.
35. A. Smirnova and D. W. Bruce, *Unpublished work,* 2011.

CHAPTER FOUR

PREPARATION OF NANOPARTICLE-DOPED SILICAS USING MICELLE-SOLUBLE METAL COMPLEXES

4.1 Micelle-soluble metal complexes

Thus far, this work has shown that MCM-41 and SBA-15 can be prepared using the TLCT method and that, furthermore, metal nanoparticles can be included in the structure through this one-pot method. Materials prepared in this way have shown a clear pore structure by low-angle XRD and TEM, as intended, but on many occasions the metal nanoparticles were found to be large and not contained within a single pore as can be seen in Figure 4.1.

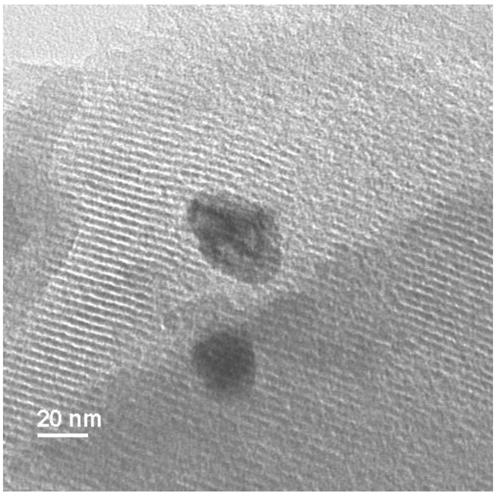

Figure 4.1 TEM image of palladium-doped MCM-41 prepared by TLCT

A significant aim of this work is to prepare a material doped with well-dispersed metal nanoparticles contained within the pores of a mesoporous silica. This is important as larger particles result in the blocking of multiple pores or they escape the pores and are located on the surface. This results in wasted or large surface area material that cannot add to efficiency during a catalytic reaction. Ideally, with particles entirely within single pores, it may be possible also to take advantage of the confined environment provided.[1] As described in Chapter 2, efforts to prevent the particles from aggregating together and breaking through the pore walls in MCM-41 were unsuccessful. It is known that the metal salts (*i.e.* $(NH_4)_2[PdCl_4]$) used thus far are soluble within the aqueous phase of the sol-gel mixture and it is thought that as the TMOS hydrolyses, the metal cations would be complexed by the ethylene oxide groups of the surfactant retaining a homogeneous distribution (Figure 4.2A)[2] and that during calcination the particles would aggregate within the pores, as suggested in Figure 4.2 C.[3]

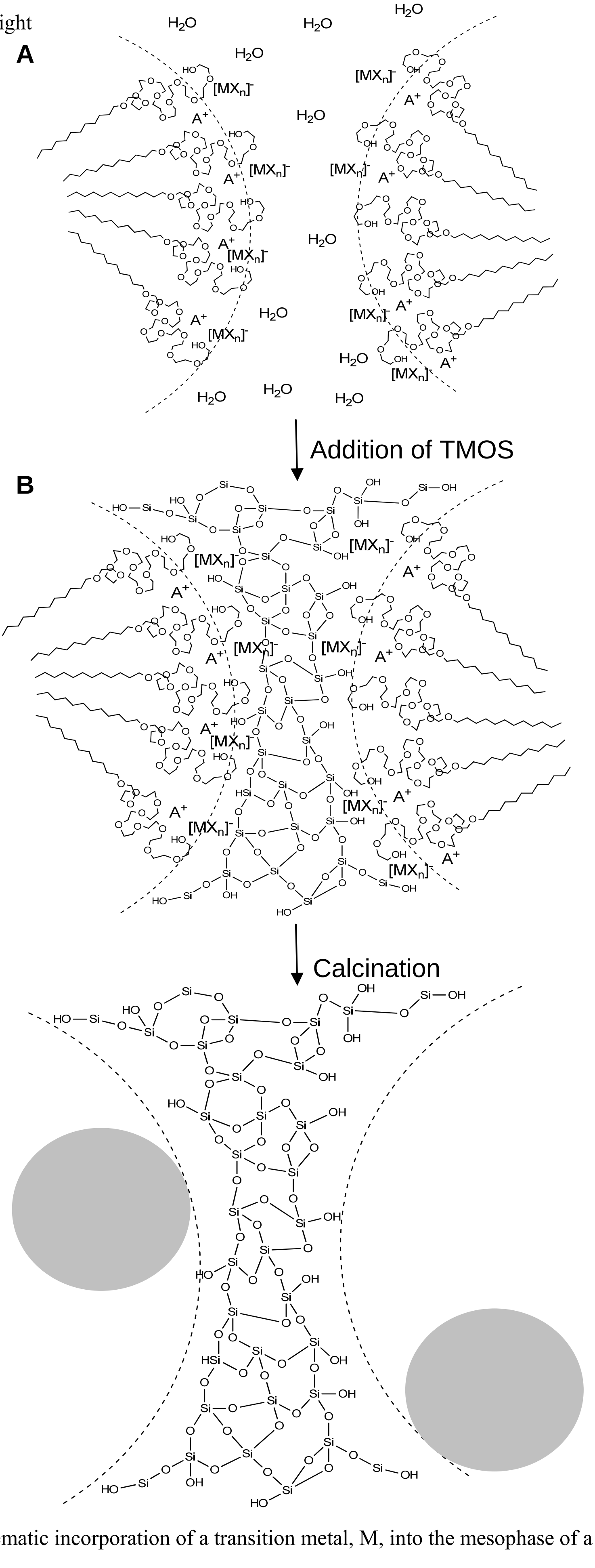

Figure 4.2 Schematic incorporation of a transition metal, M, into the mesophase of a non-ionic surfactant

However, as has clearly been demonstrated, the interaction of the cations with the head group alone are not strong enough to prevent the metal salts from aggregating into larger particles and growing through the silica walls, as suggested in Figure 4.3. Instead, it was suggested in Chapter 2 that the metal precursors could be decomposing at lower temperatures than those required for the hardening of the pores and thereby aggregating freely into the large particles.

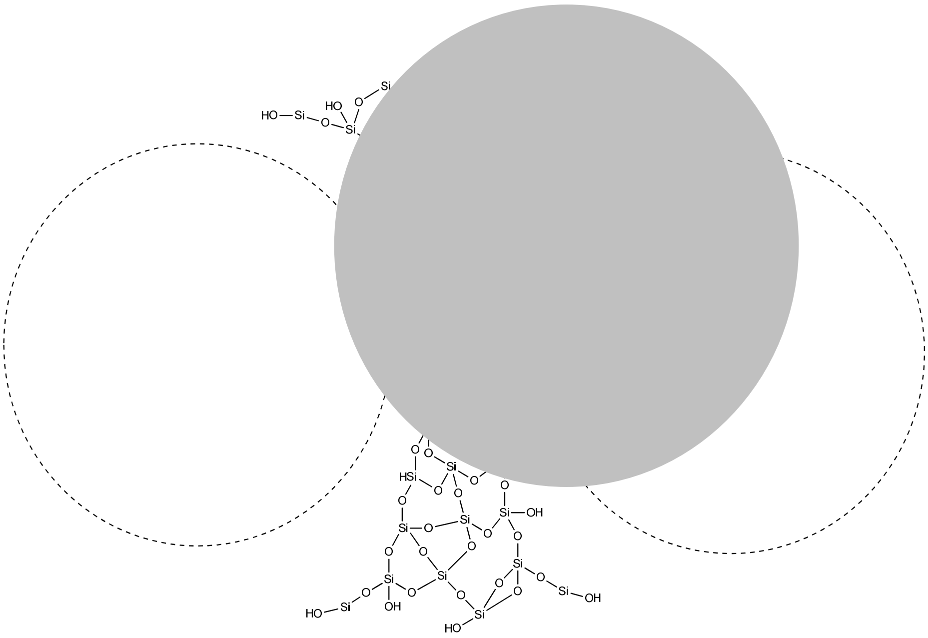

Figure 4.3 Schematic of particle formation within mesoporous silica

This chapter will be concerned with the idea of moving the location of the metal precursor into the micelle *via* control of its solubility. With the metal precursor within the micelle, it will already be in the area that will become the pore; therefore, after hydrolysis and calcination the metal nanoparticles should be well dispersed and, most importantly, contained within the pores.

4.1.1 Organic ligands

In order to position the metal precursor within the micelle, it needs to be soluble within the environment of the centre of the micelle rather than the aqueous phase previously utilised. In the case of polyoxyethylene-10-lauryl ether ($C_{12}EO_{10}$), used for the TLCT of MCM-41, the centre of the micelle is comprised of dodecyl chains, making a very non-polar, hydrophobic environment. Therefore, a metal with a non-polar, organic ligand should be able to dissolve within the micelle. Initially, this was tried with palladium acetate which is known to be soluble in benzene; however, it was found not to be soluble in $C_{12}EO_{10}$, and so the ligand was made more apolar by using a carboxylate with a longer aliphatic chain in an effort to make it more compatible with the hydrophobic environment. Palladium butyrate was tried first but was also found to be insoluble; however, when palladium octanoate (Figure 4.4) was used, it was soluble in $C_{12}EO_{10}$ at a sufficient loading to produce 1 wt% palladium-doped silica. The precise nuclearity of palladium octanoate is not known, but it is certainly found as trimers and tetramers.[4]

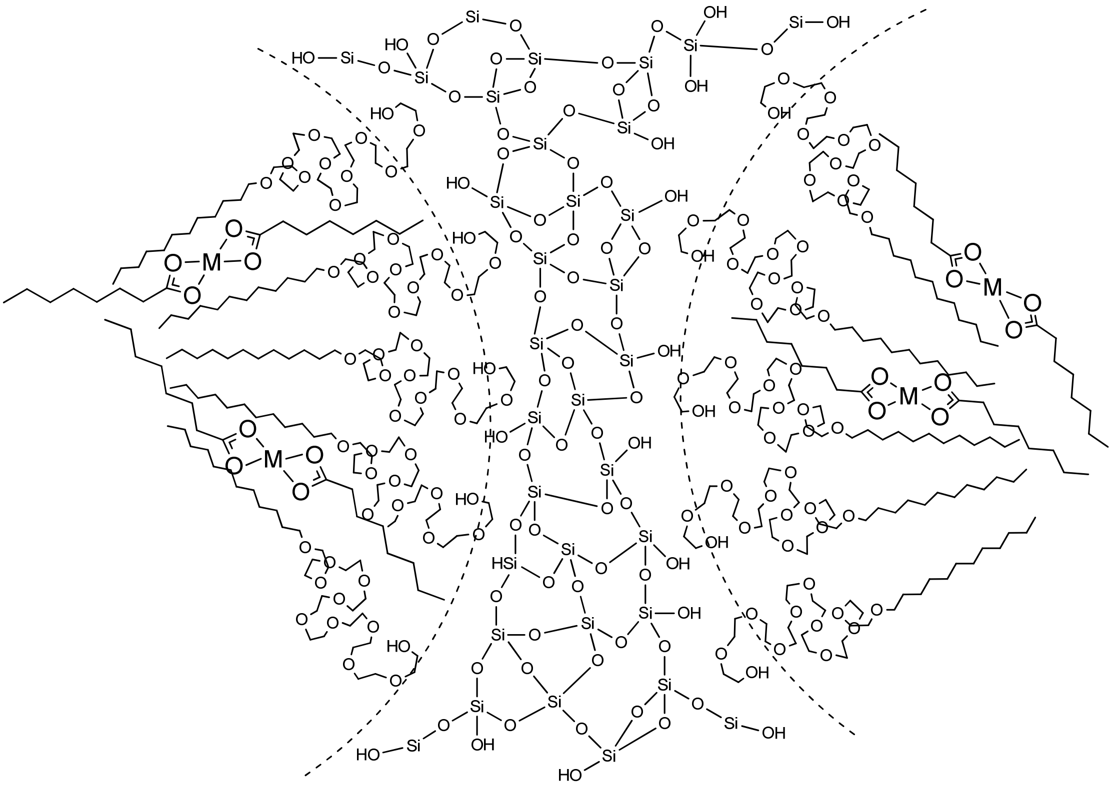

Figure 4.4 Incorporation of a transition metal, M, into the mesophase of a non-ionic surfactant

In addition to palladium, rhodium,[5] copper,[6] ruthenium,[7] chromium, molybdenum[8] and tungsten[9] form well-defined carboxylates in the +II oxidation state and all share the so-called ‘lantern-like’ structure in which a dimeric core is held together by four bridging carboxylates (Figures 4.5).

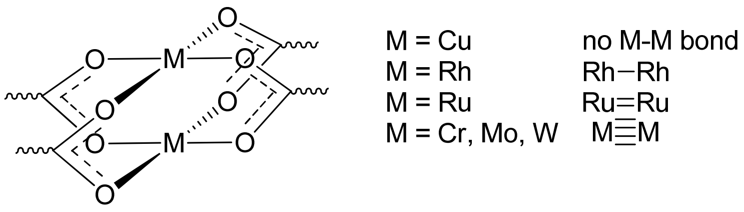

Figure 4.5 Bridging metal-carboxylates

Depending on the metal, there may be a metal-metal bond as indicated in Figure 4.5, and all of the above have been studied as liquid crystals,[10] although the complexes of Ru^{II} are very air sensitive, while those of the group 6 metals are also unstable in air although less so. Encouragingly, some of the long-chain rhodium complexes are known to be soluble in alkanes.

4.1.2 Metal carbonyls

In addition to palladium octanoate, a number of metal carbonyls were tested for solubility. Molybdenum hexacarbonyl and tungsten hexacarbonyl were both found to be soluble in the MCM-41 surfactant by mixing 10 mg of carbonyl with 0.6 g $C_{12}EO_{10}$ and warming to 40 °C. However once water was added to the mixture the complex precipitated, thus they were not suitable complexes for templating. Neither dirhenium decacarbonyl nor triruthenium dodecacabonyl was found to be soluble in $C_{12}EO_{10}$ and, therefore, this type of precursor was abandoned and focus remained on the metal carboxylates.

4.2 Metal octanoates in MCM-41

4.2.1 Palladium

Palladium(II) octanoate was synthesised from commercially available palladium(II) acetate dissolved in benzene under a flow of nitrogen and six molar equivalents of octanoic acid were slowly added to the solution and the mixture heated under reflux for 12 hours. The solvent and unreacted octanoic acid was removed by azeotropic distillation with the use of a Dean-Stark trap, followed by rotary evaporation. The product was then extracted from the crude mixture in diethyl ether and washed with sodium carbonate solution before the solvent was removed and the product dried under vacuum. Unfortunately, despite best efforts to purify, the prepared palladium octanoate appeared to contain a small amount of unreacted octanoic acid. CHN analysis found a deviation of 5 % from the calculated values. While this was not expected to affect its use as a precursor, it would cause inaccuracies in the palladium loading calculation, as such ICP analysis should be performed to determine the amount of palladium present in the doped-silica.

The synthesised palladium octanoate was dissolved in the $C_{12}EO_{10}$ surfactant used for the TLCT preparation of MCM-41 at 40 °C, to bring the $C_{12}EO_{10}$ to the liquid stated. The mixture appeared to be homogeneous and did not separate on cooling back to room temperature. Acidified (pH 2) water was then added to create a surfactant to water ratio of 3:2 by weight. The presence of the hexagonal mesophase was confirmed by polarising optical microscopy (Figure 4.6). Tetramethoxylsilane was then added to the gel and mixed thoroughly to yield a free-flowing liquid. This was placed under a light vacuum at 40 °C to reform the mesophase and remove the evolving methanol. The viscous gel was then left for 24 hours at room temperature on the open bench to complete condensation before it was calcined at 400 °C for 1 hour under nitrogen followed by 5 hours under air.

Both the sol-gel and calcined materials appeared to be a uniform brown in colour, as with previous palladium-doped MCM-41 materials prepared, suggesting the metal precursor was well dispersed throughout the silica as intended.

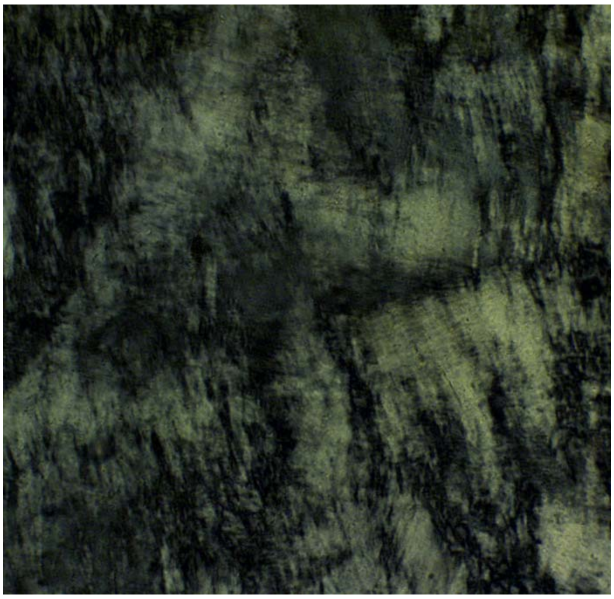

Figure 4.6 H_1 mesophase of the $C_{12}EO_{10}$ surfactant in water mixed with 1 wt% palladium octanoate displaying a typical non-geometric texture

The resulting silica was characterised by porosimetry and low-angle X-ray diffraction (Table 4.1). The BET isotherm (Figure 4.7) and low-angle XRD pattern (Figure 4.8) obtained were both typical of MCM-41 materials synthesised by TLCT, the XRD pattern being indicative of a two-dimensional, hexagonal unit cell. The palladium-doped material shows similar porosity (surface area and pore diameter) to undoped MCM-41 suggesting that the introduction of the palladium octanoate had no adverse effect on the micelle formation, thus the silica had templated around the micelles as expected. However, a decrease in surface area would be expected after doping with palladium as the metal nanoparticles would block pores, preventing them from being measured by porosimetry. Within the accuracy of the experiment, there would appear to be little or no decrease in surface area, but this is not inconsistent with the low palladium loading calculated to be 1.24 wt% based on the amount of palladium(II) octanoate used in the preparation (confirmed by ICP analysis, which gave a value of 1.23 wt%). This is significantly lower than the ~5 wt% used in preparations described in Chapter 2 and 3, where significant decreases in surface area were found.

Table 4.1 Structural data for Pd-doped MCM-41-like silica prepared by TLCT

Precursor	Surface Area / $m^2 g^{-1}$	Pore Diameter / Å	d-spacing *d* / Å	Lattice Parameter, *a* / Å	Pore Wall Thickness / Å
Undoped	1103	34.6	41.9	48.4	13.7
Pd octanoate	1052	34.4	44.0	50.8	16.4

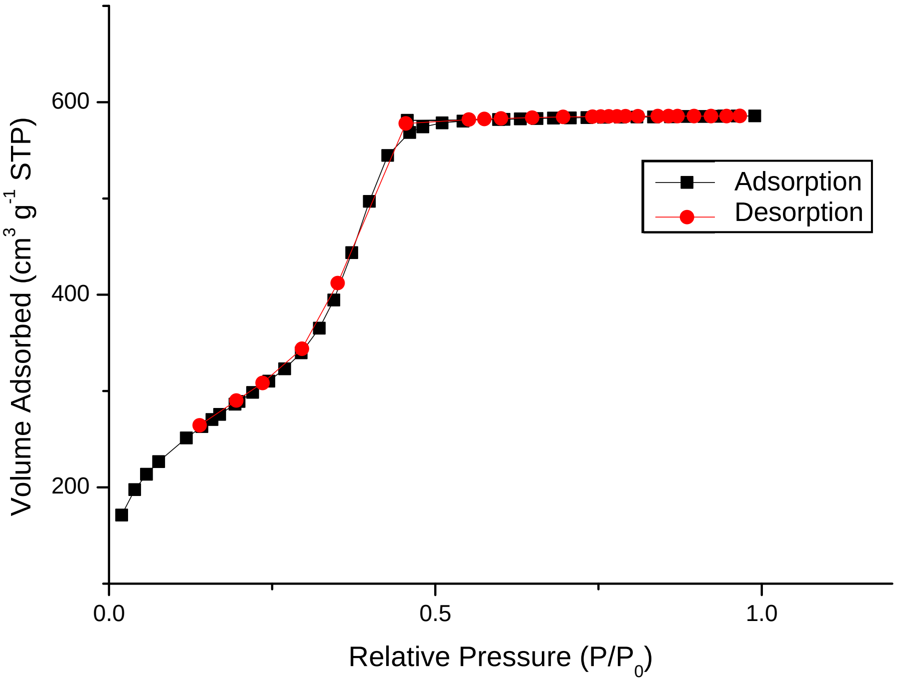

Figure 4.7 Adsorption-desorption isotherm of Pd -doped MCM-41-like silica prepared by TLCT

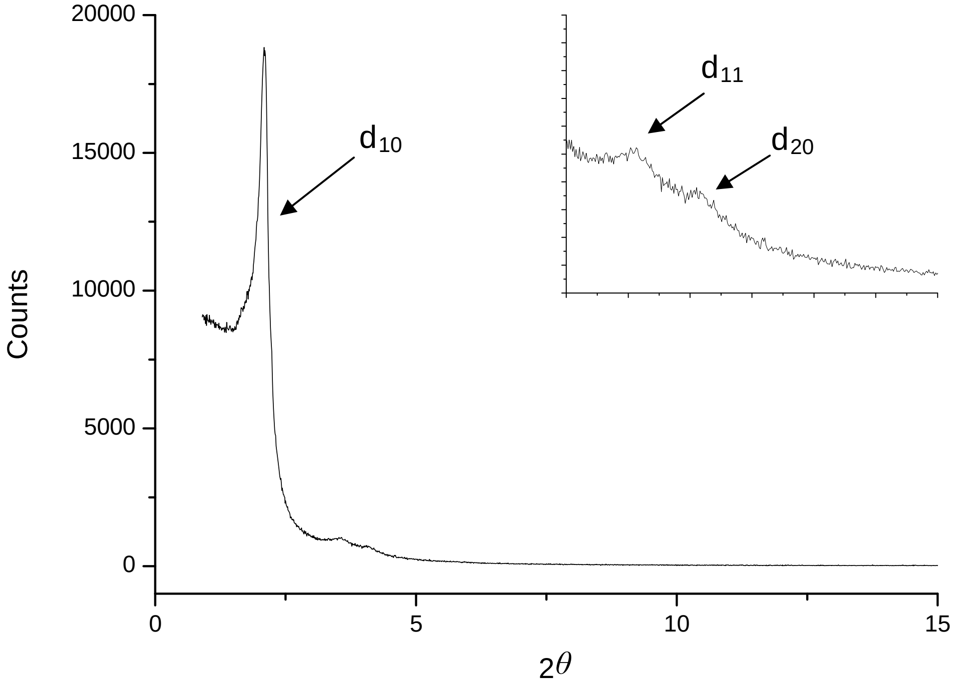

Figure 4.8 X-ray diffraction pattern of Pd-doped MCM-41-like silica prepared by TLCT

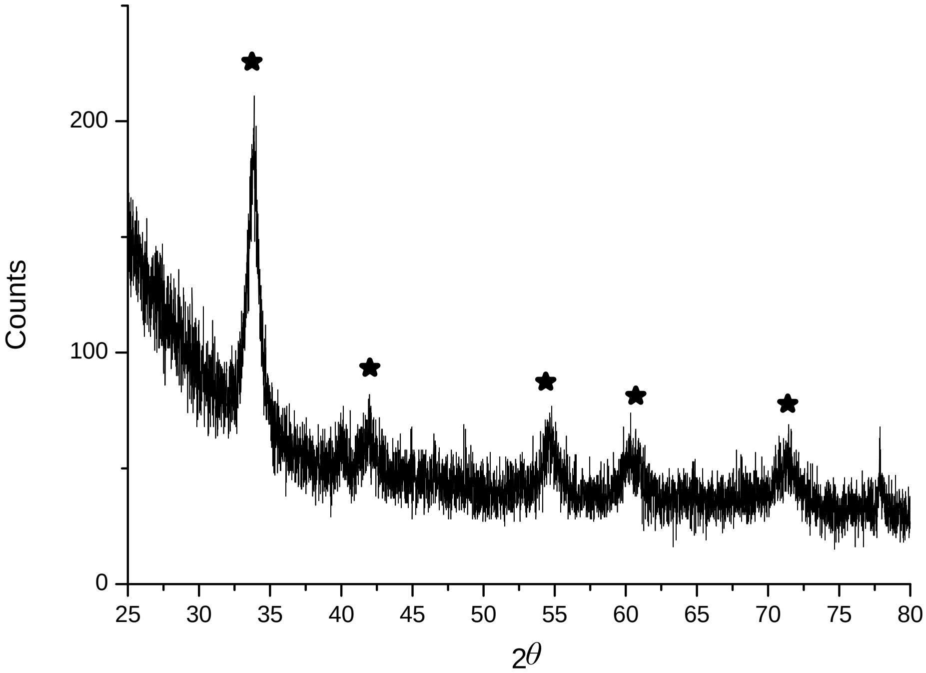

Figure 4.9 Wide-angle X-ray diffraction pattern of Pd-doped MCM-41-like silica prepared by TLCT, (★) peak positions of PdO

Wide-angle XRD allows the oxidation state of the palladium particles to be identified by comparing the peak positions to known materials, the particles detected from palladium(II) octanoate-doped MCM-41 were identified as palladium(II) oxide (Figure 4.9), identical to the materials prepared using the $(NH_4)_2[PdCl_4]$ precursor.

Examining the prepared materials by TEM (Figure 4.10) allowed the particle size to be determined as well as providing a clear image of the pores and the particle position. The palladium oxide particles were seen as small, with a diameter of 4.1 nm, well-dispersed particles that appear to be located within the pores. There is a slight bending of the pores around the particles (Figure 4.10) which suggests that the particles are located within the pores, which has caused a distortion in the silica walls.

The average particle size could also be calculated by use of the wide-angle XRD data (Figure 4.9) in conjunction with the Scherrer equation, which found the particles to be 9.8 nm in diameter, which would suggest that not all the palladium formed the small particles observed in the TEM images. To support this, CO chemisorption was performed and found the average crystallite size was found to be 10.8 nm.

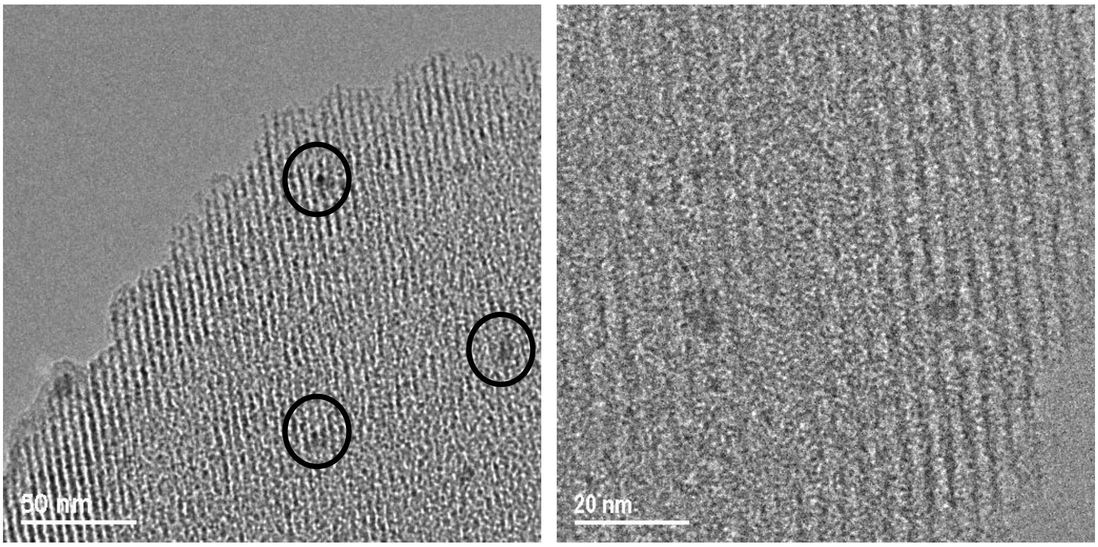

Figure 4.10 TEM images of Pd-doped MCM-41-like silica prepared by TLCT

Palladium octanoate shows a significant improvement as a metal precursor with regards to particle size obtained, yielding the smallest palladium particles observed thus far during this study. As such, it is expected that this material would be very active catalytically as a good portion of the palladium surface would be available for reaction, rather than the bulk being inaccessible as was seen previously. Catalytic activity will be described in Chapter 5.

4.2.2 Rhodium

Rhodium in catalysis

Rhodium is widely investigated as a catalyst for a range of reactions and while no rhodium catalysis was performed during this work, rhodium-doped silicas were prepared and characterised. The following pages detail some of the existing interest in rhodium-doped MCM-41 and SBA-15 for catalysis.

Zha *et al.*[11] reported the use of a rhodium complex anchored within MCM-41 silica as a heterogenised homogeneous catalyst for the hydrosilylation of alkenes. They introduced rhodium to MCM-41 by firstly modifying the silica with 3-(2-cyanoethylsulfanyl)propyltriethoxysilane (Figure 4.11) to introduce sulfur onto the surface in order to anchor $RhCl_3$. Using low-angle XRD, Zha *et al.* determined that the modification and anchoring did not affect the structure of the MCM-41. Catalytic testing of the prepared material found that it was active at 120 °C, with yields in excess of 68%, increasing to 91% over 110 minutes. They also found that the catalyst could be recycled and reused, a significant advantage over homogeneous catalysis.

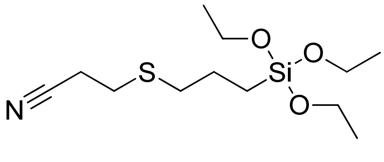

Figure 4.11 3-(2-cyanoethylsulfanyl)propyltriethoxysilane

In comparison, Lang *et al.*[12] introduced a rhodium complex to MCM-41 by modifying the silica with an organoamine which was used to anchor the $[RhH(CO)(PPh_3)_3]$ complex. Low-angle XRD was used to identify the hexagonal structure of the MCM-41 as well as the modified and doped material (Figure 4.12). The d_{11} and d_{20} peaks were not well defined, suggesting that the incorporation of the organoamine onto MCM-41 disrupted some of the long-range ordering.

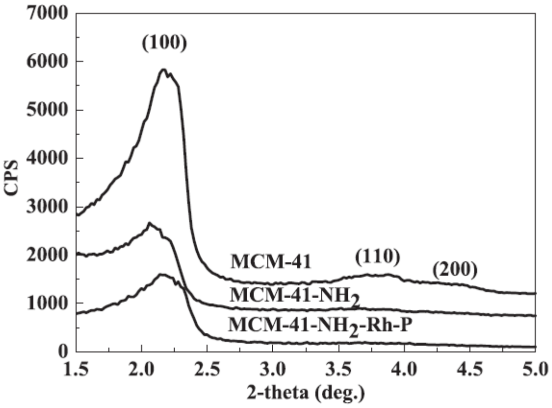

Figure 4.12 Low-angle XRD spectra of MCM-41, MCM-41-NH_2 and MCM-41-NH_2-Rh-P

The modification also has an effect on the surface area of the MCM-41, reducing it from 830 m^2 g^{-1} in the parent material to 530 m^2 g^{-1} after the organoamine has been added. Despite these changes in structure, the material is shown to be an effective catalyst in the synthesis of 2-ethylhexenal from propene, reaching a yield of 77% in a one-pot synthesis.

Rhodium has long been used as a catalyst for the Fischer-Tropsch reaction,[13] in the synthesis of hydrocarbons from synthesis gas (syngas, or carbon monoxide and hydrogen)[14], while more recently, rhodium-doped SBA-15 was studied as a catalyst for the synthesis of ethanol from syngas (carbon monoxide and hydrogen) by Chen *et al.*[15] They used incipient wetness impregnation to introduce rhodium into the pore structure of SBA-15 using aqueous $RhCl_3$. They identified the hexagonal pore structure typical of SBA-15 using low-angle XRD, observing the d_{10}, d_{11} and d_{20} reflections; however, with increased metal loadings, these reflections became less defined and only metal loadings greater than ~7.5 wt% exhibited the d_{10} reflection clearly. As the d_{10} reflection was still visible and pores could be identified by TEM images, this was dismissed as unimportant; however, it could be an indication that higher loadings of metal can disrupt the long-range two-dimensional order and weaken the physical strength of the material, which would be disadvantageous in large scale catalysis.

In contrast to Chen's work with incipient wetness, Marras *et al.*[16] introduced rhodium into SBA-15 by anchoring a rhodium-diphosphine complex to the silica surface (Figure 4.13). The prepared catalyst was tested with the hydroformylation of 1-octene and the activity was compared with the same complex anchored onto a silica gel.[17] Comparatively, rhodium on silica gel was found to be fifteen times less active than the homogeneous analogue, whereas the rhodium on SBA-15 showed activities of almost twice that of the homogeneous analogue, demonstrating the advantages of the high surface area and ordered porosity.

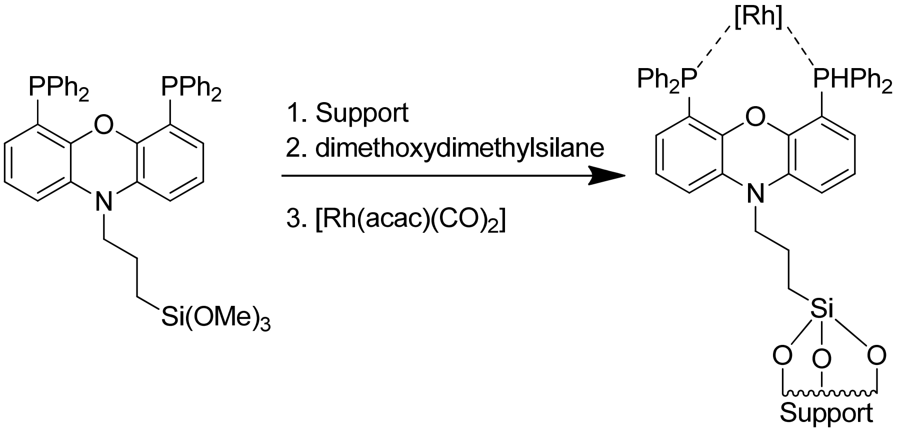

Figure 4.13 Schematic of rhodium-diphosphine complex anchored onto silica support

In 2008, Du *et al.*[18] prepared rhodium catalysts to study the catalysis of N_2O decomposition. The catalytic testing was carried out using an automated eight flow reactor system where the catalyst granules were packed into a tubular quartz reactor and a series of catalysts were prepared and tested using both impregnation (Figure 4.14) and grafting of the rhodium onto SBA-15, using $ClRh(PPh_3)_3$ and $[(CO)_2RhCl]_2$ dissolved in chloroform before the SBA-15 was introduced into the solution.[19] Du *et al.* found that, with both methods, particle dispersion was dependent on the precursor, noting that when grafting a small precursor, such as $[RhCl(CO)_2]_2$, the high mobility allowed the metal to diffuse into the micropore areas of the SBA-15. They observed that better particle dispersion resulted in higher catalytic activity.

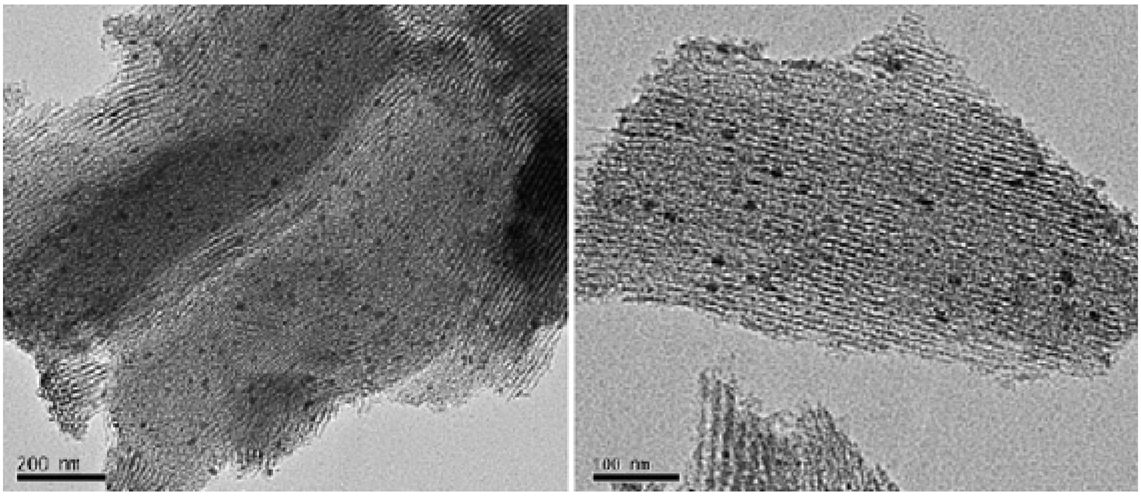

Figure 4.14 TEM images of Du's rhodium-SBA-15 catalysts prepared by impregnation

Preparation of rhodium-doped silica

Rhodium(II) octanoate was prepared using the same method as palladium octanoate, using rhodium(II) acetate as the starting material. Rhodium acetate was first synthesised from a solution of rhodium trichloride, sodium acetate and glacial acetic acid in ethanol, and heated gently under reflux and a flow of nitrogen for an hour, before the product was collected by filtration and recrystallized in boiling methanol.[20] Rhodium(II) octanoate was prepared from the rhodium acetate using the same method described previously for palladium(II) octanoate.

The synthesised rhodium(II) octanoate was dissolved in the $C_{12}EO_{10}$ surfactant in the same way as palladium(II) octanoate, using rhodium octanoate dissolved in $C_{12}EO_{10}$ and heating to 40 °C to assist in the mixing. The mixture was left overnight before it appeared to have fully mixed and appeared to still be homogeneous after cooling to room temperature and the addition of water, followed by TMOS to complete templating.

As for the palladium-doped MCM-41, there is very little difference between the structural properties of the rhodium-doped MCM-41 and the undoped parent material (Table 4.2). A difference in surface area might be expected, but, again, the low metal loading (1.09 wt%) of rhodium likely explains why no experimentally significant decrease is observed. The reflections which identify the hexagonal pore structure are clearly observed by low-angle XRD (Figure 4.15).

Table 4.2 Structural data for Rh-doped MCM-41-like silica prepared by TLCT

Precursor	Surface Area / $m^2 g^{-1}$	Pore Diameter / Å	d-spacing *d* / Å	Lattice Parameter a / Å	Pore Wall Thickness / Å
Undoped	1103	34.6	41.9	48.4	13.7
Rh octanoate	1071	30.6	43.0	49.7	19.0

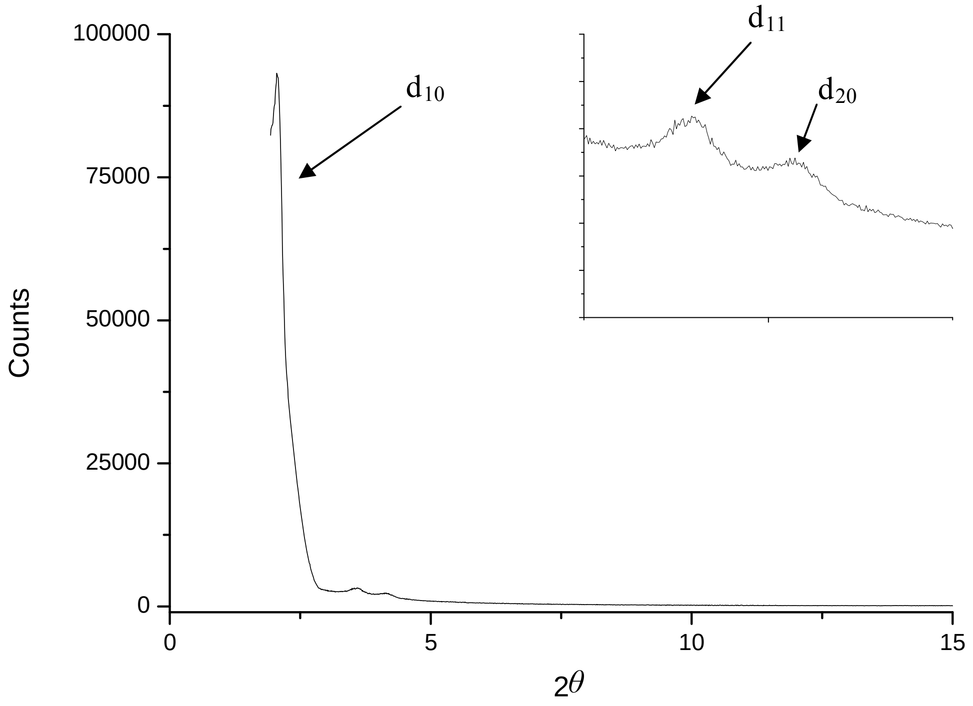

Figure 4.15 X-ray diffraction pattern of Rh-doped MCM-41-like silica prepared by TLCT

Unfortunately, no reflections were observed by wide-angle XRD so it was not possible to determine the nature of the species of the rhodium particles or calculate the average particle size by the Scherrer equation. The absence of wide-angle reflections is either due to the particles being small and with a loading too low to be identified by XRD, or that they are amorphous rather than crystalline, which would also prevent them from being identified by XRD.

To overcome the lack of wide-angle XRD, TEM images (Figure 4.16) were collected which clearly displayed the long, straight pores containing the rhodium particles of a size of 5.4 nm. High-resolution TEM could be used to determine the crystallinity of the particles; however, time restraints prevented this.

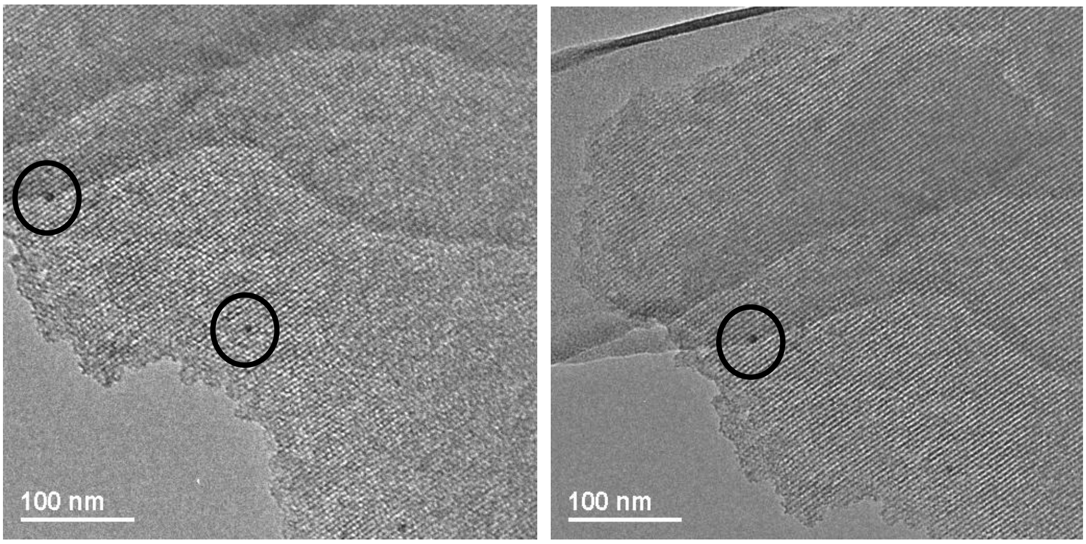

Figure 4.16 TEM images of Rh-doped MCM-41-like silica prepared by TLCT with rhodium particles circled

With both palladium octanoate and rhodium octanoate being suitable precursors for preparing metal nanoparticle-doped MCM-41, yielding nanoparticles that appear to be contained within the pores it has been shown that micelle soluble precursors can be used to dope, regardless of the metal, providing they are soluble within the surfactant in the presence of water. This is a significant advantage over the off-the-shelf precursors used in Chapters 2 and 3 as particle size control has been realised.

4.3 Metal alkanoates in SBA-15

Having shown that metal octanoates lead to nanoparticle-doped silicas using $C_{12}EO_{10}$, attempts were then made to use them in templates employing P123 as surfactant. The same methodology was followed, namely attempting to dissolve the metal octanoate (palladium and rhodium) in the P123 prior to mesophase formation, sol-gel condensation and finally calcination. Unfortunately, however, this did not seem to work very well. Thus, while porosimetry data appeared to be consistent with undoped TLCT-SBA-15 (Table 4.3), low-angle XRD and TEM did not support this, indicating that the hexagonal structure was not well formed. This failure is attributed to the low solubility of the metal octanoates in the PPO part of P123, and indeed the precursor required warming and sonication for over 24 hours before it appeared to have mixed fully.

Table 4.3 Structural data for M-doped SBA-15-like silica prepared by TLCT

Precursor	Surface Area / $m^2 g^{-1}$	Pore Diameter / Å	d-spacing *d* / Å	Lattice Parameter a / Å	Pore Wall Thickness / Å
Undoped	600	51.5	77.4	89.4	37.9
Pd octanoate	638	51.8	88.1	101.7	49.9
Rh octanoate	611	46.2	88.9	102.7	56.4

It is likely that the different micellar environment created by the PPO groups of P123 (Figure 4.17) compared to the $C_{12}EO_{10}$ hydrocarbon chain (Figure 4.18) has resulted in the metal octanoates being less soluble and less compatible with the more polar micelles thereby not allowing the precursors to be used effectively in the TLCT method. That is to say that the micellar core in P123, the PPO fragment, is much less hydrophobic than the alkyl environment provided by the dodecyl chain in $C_{12}EO_8$.

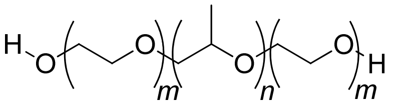

Figure 4.17 P123 surfactant *m* = 20, *n* = 70

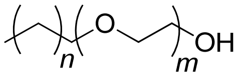

Figure 4.18 $C_{12}EO_{10}$ surfactant; *n* = 11, *m* = 10

Therefore, a new complex was clearly required which would be more compatible with the PPO part of P123. Initially, a step backwards was taken and palladium acetate itself was used (Table 4.4 and Figure 4.19). This appeared to be an improvement compared with palladium octanoate as the pore structure was not disrupted, but palladium particles did not appear to be contained within the pore structure.

Table 4.4 Structural data for Pd-doped SBA-15-like silica prepared by TLCT

Precursor	Surface Area / m^2 g^{-1}	Pore Diameter / Å	d-spacing *d* / Å	Lattice Parameter a / Å	Pore Wall Thickness / Å
$[Pd_3(OAc)_6]$	748	39.4	94.1	101.7	62.3

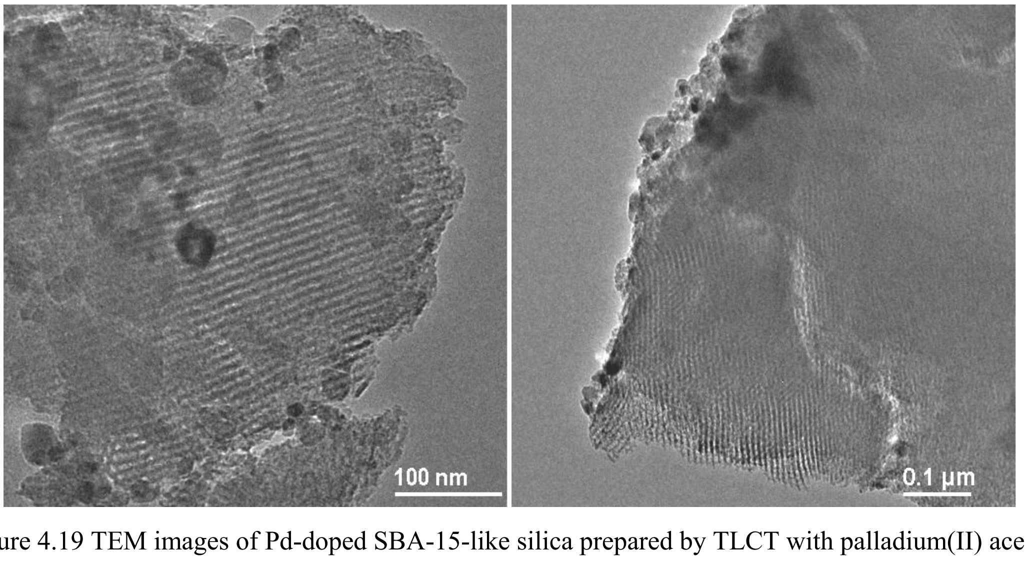

Figure 4.19 TEM images of Pd-doped SBA-15-like silica prepared by TLCT with palladium(II) acetate

The change in ligand assisted in the solubility within the surfactant; however, the larger particle size suggests that this did not result in the intended effect of the metal precursor being located within the micelle during the synthesis of the silica. Therefore, a complex with a branched side chain was proposed, as branched-chain materials have a generally greater organic solubility, which might enhance solubility within the micelle. This was achieved by simply replacing the octanoate ligand for 2-ethyl hexanoate (Figure 4.20). The results of this ligand and complexes with it are detailed in the following pages.

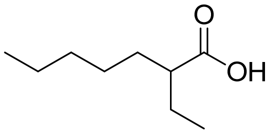

Figure 4.20 Proposed 2-ethyl hexanoic acid precursor

4.3.1 Rhodium

Rhodium(II) 2-ethyl hexanoate was synthesised from rhodium(II) acetate as described above for the octanoate.

The synthesised rhodium 2-ethyl hexanoate was used to prepare rhodium-doped MCM-41 as well as SBA-15. In both cases the precursor was dissolved in the surfactant in the same way as described previously. It was found to be soluble in both $C_{12}EO_{12}$ and P123 surfactants as intended; however, it should be noted that the complex required heating and sonication to assist the complex in dissolving fully in the P123 surfactant.

Table 4.5 Structural data for Rh-doped silica prepared by TLCT

Precursor/Silica	Surface Area / $m^2 g^{-1}$	Pore Diameter / Å	Lattice Parameter / Å	Pore Wall Thickness / Å
Undoped MCM-41	1103	34.6	48.4	13.7
Rh 2-ethyl hexanoate/MCM-41	1056	37.2	55.7	18.4

The rhodium 2-ethyl hexanoate precursor was used to prepare Rh-MCM-41 and was characterised by porosimetry, low-angle XRD and TEM (Table 4.5). The low-angle XRD pattern (Figure 4.21) shows a clear d_{10} peak signalling the hexagonal pore structure; however, the weak d_{11} and d_{20} peaks signify a poor long-range order within the material.

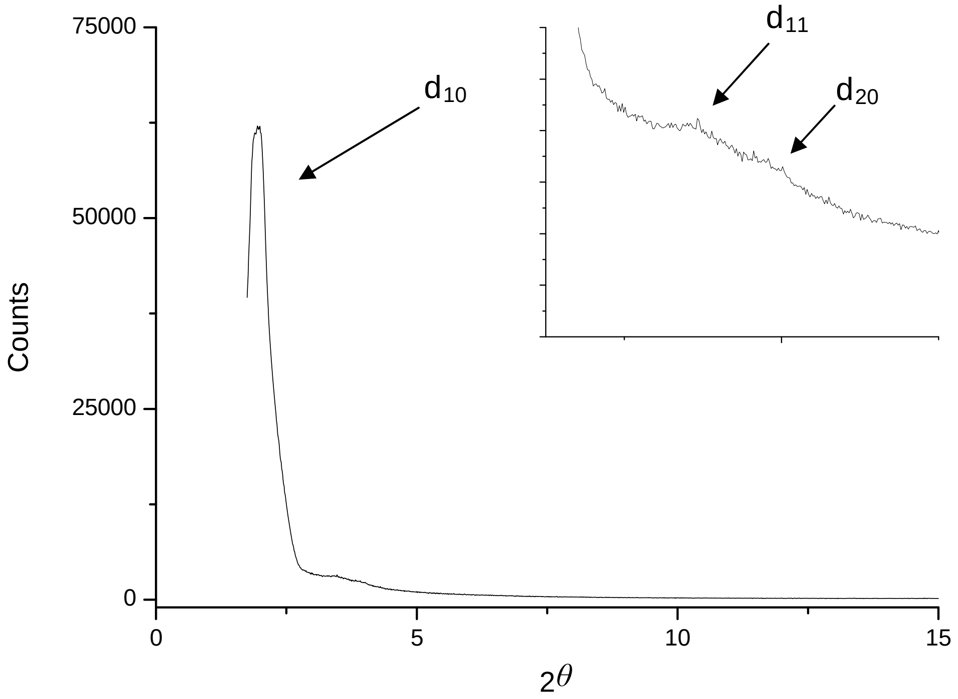

Figure 4.21 X-ray diffraction pattern of Rh-doped MCM-41-like silica prepared by TLCT

The BET isotherm (Figure 4.22) is typical of the mesoporous silica of MCM-41 materials, with the narrow hysteresis showing the narrow pore-size distribution within the material. TEM images (Figure 4.23) clearly show the long, straight pores with well dispersed rhodium particles contained within them. The particles appear to be located within the pores and do not break through the pore walls to occupy multiple pores. The addition of the side chain within the metal precursor appears not to have hindered the templating of the MCM-41 materials and has continued to exhibit the desired properties, with the precursor dissolving within the micelle to control the rhodium particle size.

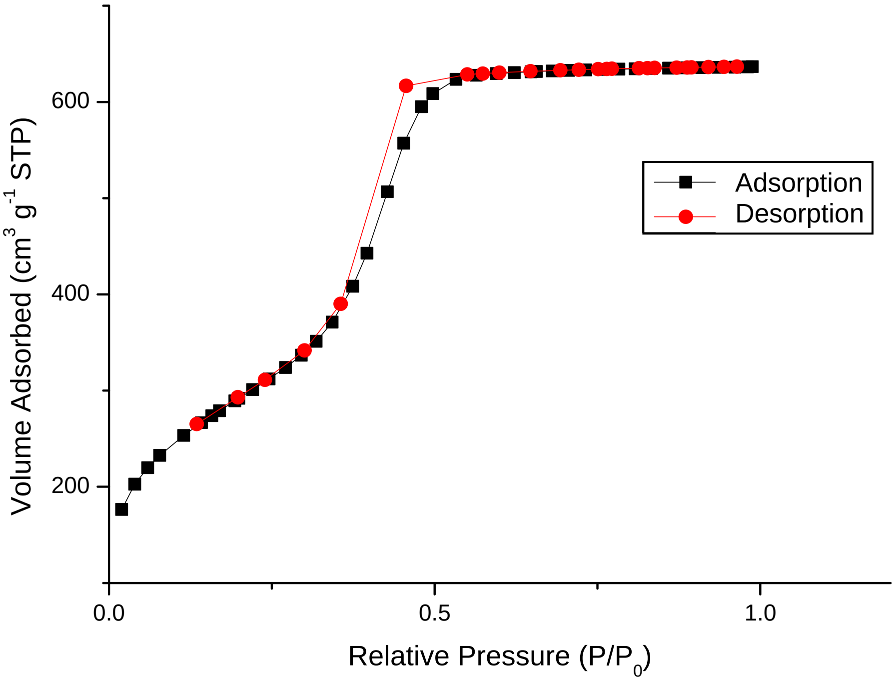

Figure 4.22 Adsorption-desorption isotherm of Rh-doped MCM-41-like silica prepared by TLCT

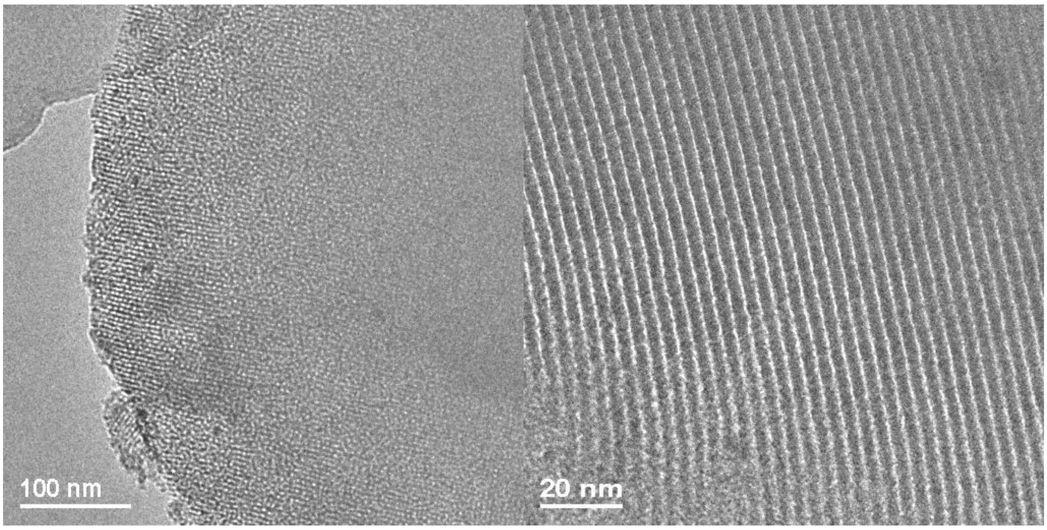

Figure 4.23 TEM images of Rh-doped MCM-41-like silica prepared by TLCT

More significantly, the rhodium-doped SBA-15 prepared using rhodium 2-ethyl hexanoate as precursor was characterised by BET porosimetry, XRD and TEM (Table 4.6). The BET isotherm (Figure 4.24) was typical of SBA-15 type mesoporous silica including the characteristic hysteresis and revealed a surface area similar to that of the undoped SBA-15 and, typical with doped materials, a reduced pore diameter coupled with an increase in pore wall thickness.

Table 4.6 Structural data for Rh-doped silica prepared by TLCT

Precursor/Silica	Surface Area / $m^2\ g^{-1}$	Pore Diameter / Å	Lattice Parameter / Å	Pore Wall Thickness / Å
Undoped SBA-15	600	51.5	89.4	37.9
Rh 2-ethyl hexanoate/SBA-15	585	42.9	93.2	50.2

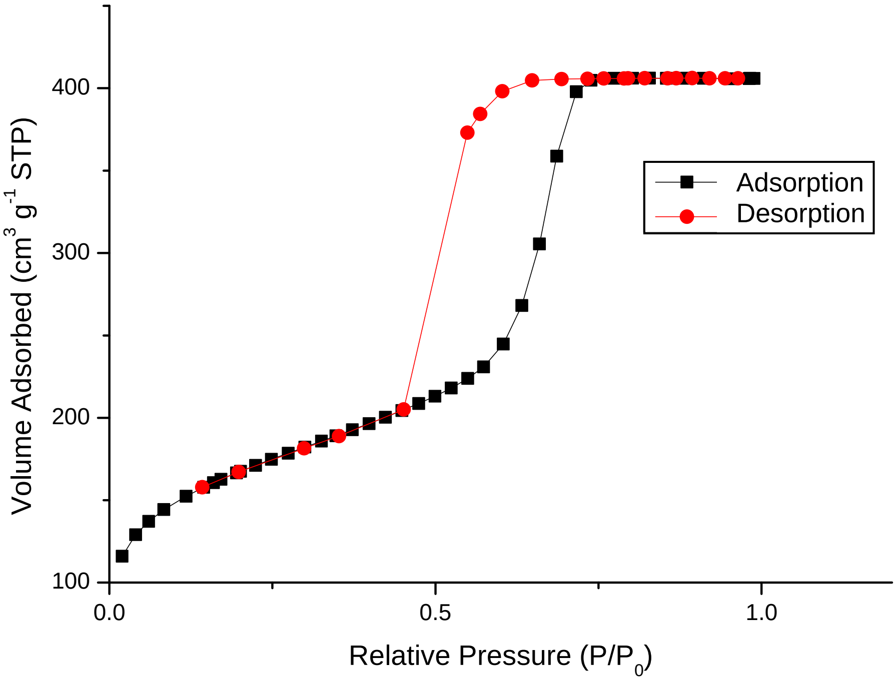

Figure 4.24 Adsorption-desorption isotherm of Rh-doped SBA-15-like silica prepared by TLCT

The collected TEM images (Figure 4.25) are very promising with very clear and well-defined pore structures containing well distributed rhodium nanoparticles contained within the pores. One of the images (Figure 4.25, bottom right) shows an end-on view of the pore structure where the hexagonal pore structure is unmistakable. The particles can be measured from the TEM images to be 7.7 nm in diameter; while this is larger than the pore diameter of 4.3 nm, it is less than the lattice parameter or repeat distance of 9.3 nm suggesting that the particles are filling the whole pore and pushing out into the silica walls anchoring them into position. Unfortunately, wide-angle XRD of these materials did not exhibit any peaks which could be used to identify the particles or calculate the average particle size using the Scherrer equation, suggesting the particles were either too small for detection or were amorphous in nature.

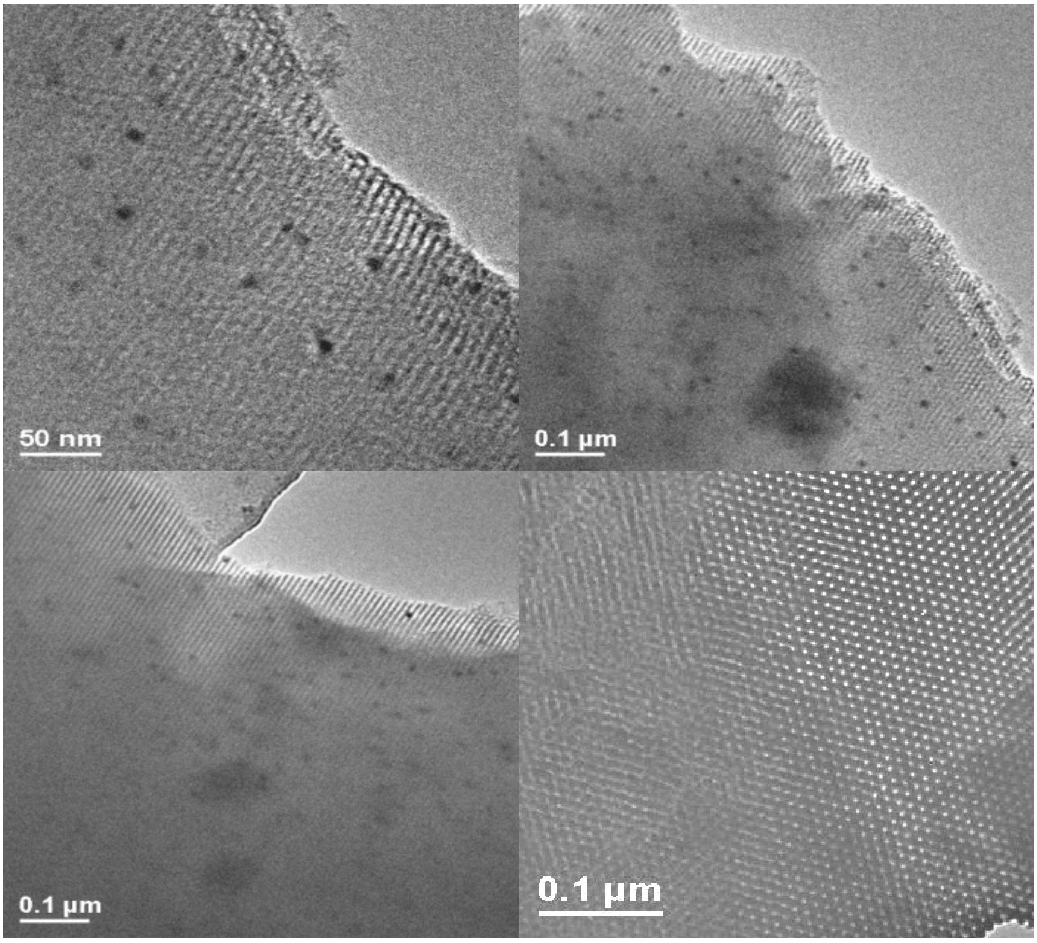

Figure 4.25 TEM images of Rh-doped SBA-15-like silica prepared by TLCT

By simply modifying the organic ligand from octanoate to 2-ethylhexanoate, it has proven possible to prepare a metal complex that is soluble in both the $C_{12}EO_{10}$ surfactant used for MCM-41 and the P123 surfactant used for SBA-15. This allows a great deal of versatility, providing the complex can be prepared to include the desired metal, be that rhodium, palladium or otherwise.

4.3.2 Copper

In an effort to expand the range of available metals that can be successfully doped into the pore structures of MCM-41 and SBA-15, copper was examined as a potential candidate. In the context of this project, this was significant as the group had not previously been able to incorporate copper using a one-pot methodology.

Copper has been of interest to others and has previously been introduced into SBA-15 and the catalytic decomposition of methanol studied by Tsoncheva *et al.*[21] They impregnated the SBA-15 using incipient wetness technique with copper acetylacetonate in toluene to produce 10 wt% of copper oxide in SBA-15. Low-angle XRD was used to confirm that the hexagonal structure of the SBA-15 was not compromised. Studying the catalytic reaction by ^{11}C-radiolabelling techniques, they determined that the primary product of the decomposition varied, depending on the overall coverage of methanol over the surface, with products ranging from CO_2 to methyl formate.

Rico *et al.*[22] also impregnated copper into SBA-15 using the incipient wetness technique with an aqueous solution of copper(II) nitrate at a range of loadings between 1 and 12 wt%. They did this for use in the selective catalytic reduction of NO_x using propane or ammonia as reducing agent. Porosimetry analysis of the materials prepared showed a slight reduction in surface area on increasing copper oxide loading; however, their undoped SBA-15 only had a surface area of 333 m^2 g^{-1}, which is much lower than would be expected using the standard methodology. They report using a procedure described by Gómez-Cazalilla;[23] however, this should have yielded an SBA-15 with a surface area of around 550 m^2 g^{-1}, although no mention of it was made by Rico, a lack of micropores within the SBA-15 could account for the reduced surface area. Rico observed that metal particle size increased with increased loading, from 1.9 nm diameter at 1 wt% to 10.9 nm at 6 wt%, while the pores were observed to have a diameter of 3.1 nm, suggesting that the particles were either forming on the surface or filling the pores as rods, rather than small, spherical particles. Unfortunately, no TEM images were collected of these materials to determine the particle sizes or shapes.

Preparation of copper-doped silica

Copper 2-ethyl-hexanoate was prepared using a different method to the rhodium analogue. A solution of copper(II) acetate in ethanol was added to 2-ethyl hexanoic acid dissolved in ethanol and stirred. On the addition of distilled water to the mixture, copper 2-ethyl-hexanoate precipitated and was collected by filtration.[24]

The copper 2-ethyl-hexanoate was used as precursor for Cu-SBA-15 and 6 mg was found to be soluble in 0.5 g of P123 once heated to 40 °C. The synthesised silica was fully characterised (Table 4.7) and found to exhibit similar structural properties to the undoped SBA-15 prepared previously with the BET isotherm (Figure 4.26) exhibiting the typical SBA-15 hysteresis and the low-angle XRD (Figure 4.27) showing the d_{10} reflection as expected; however, the d_{11} and d_{20} which would signify the long-range ordering of the hexagonal structure are not detected.

Table 4.7 Structural data for Cu-doped SBA-15 prepared by TLCT

Precursor/Silica	Surface Area / $m^2\ g^{-1}$	Pore Diameter / Å	Lattice Parameter / Å	Pore Wall Thickness / Å
Undoped	600	51.5	89.4	37.9
Cu 2-ethyl hexanoate	585	45.9	88.0	42.0

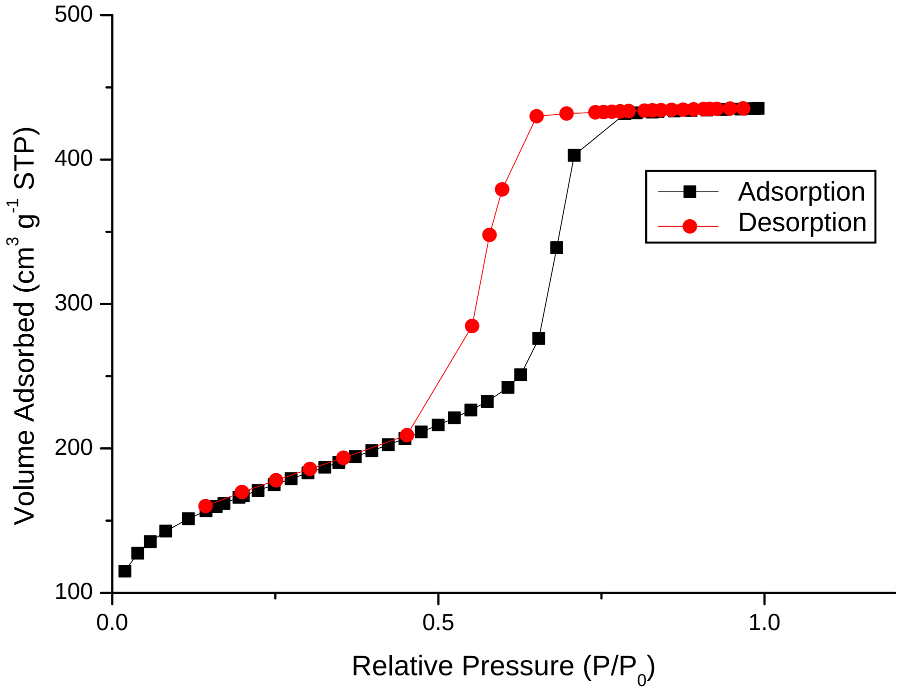

Figure 4.26 Adsorption-desorption isotherm of Cu-doped SBA-15-like silica prepared by TLCT

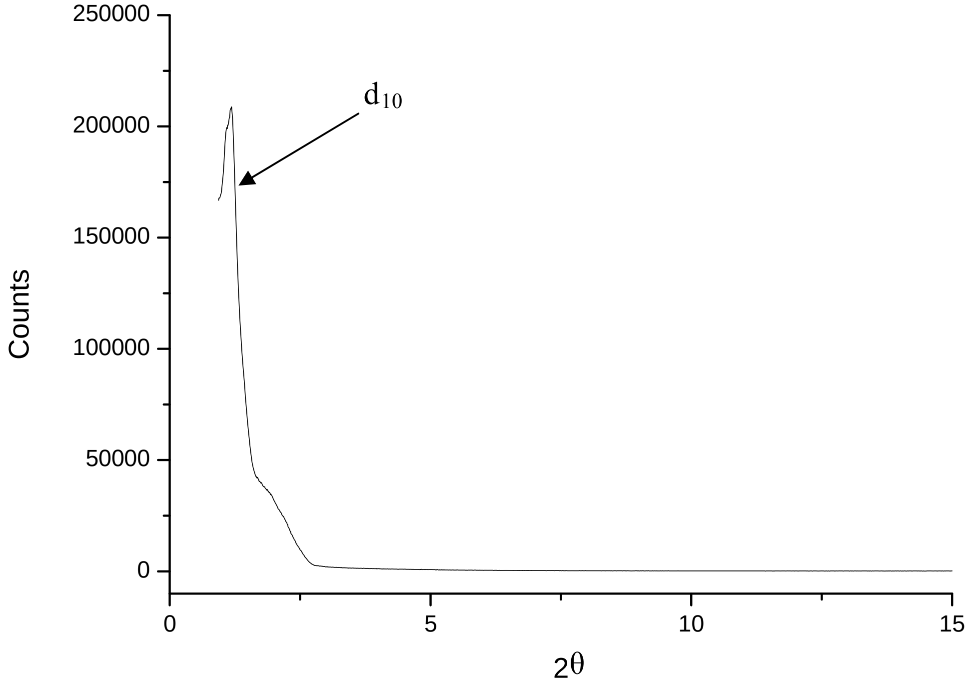

Figure 4.27 X-ray diffraction pattern of Cu-doped SBA-15-like silica prepared by TLCT

TEM images (Figure 4.28) were collected and showed the characteristic long, straight pores; however, no images of the copper particles could be found and wide-angle XRD scans were also unable to identify any particles. It could be assumed that the particles are small and well dispersed within the sample; however, without evidence it is equally possible the particles are large and outside of the pore structure. Particle size distribution could be analysed by N_2O chemisorption to determine the size of the copper particles. Alternatively, the copper could have migrated into the bulk silica during the synthesis, in the same way as was proposed for the lanthanide-doped MCM-41 materials discussed in Chapter 2. If this is the case, the copper would not be accessible to N_2O chemisorption and would need to be identified using EXAFS analysis. The calcined material was pale blue in colour which could indicate that the copper has been incorporated into the silica framework rather than forming particles.

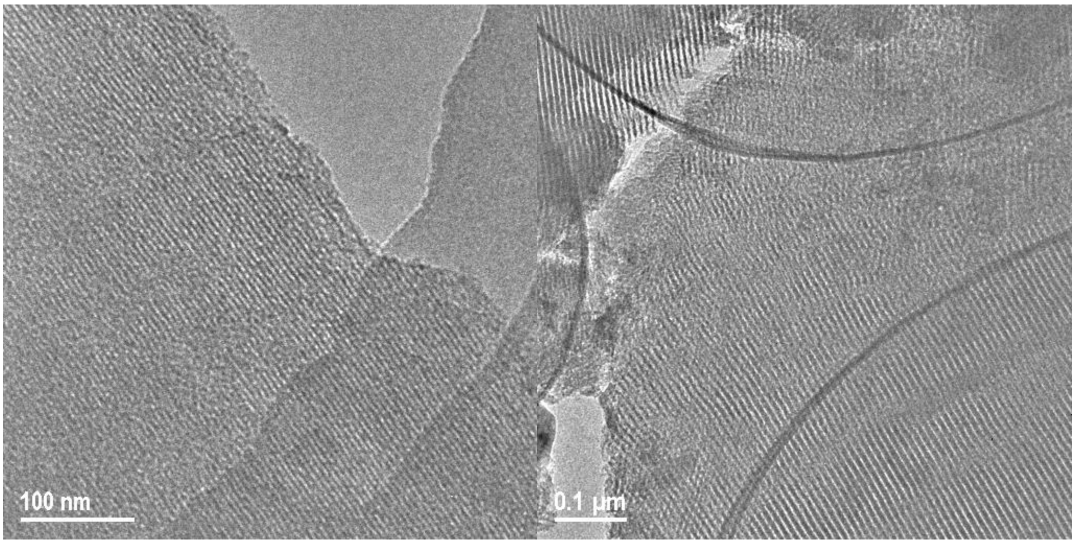

Figure 4.28 TEM images of Cu-doped SBA-15-like silica prepared by TLCT

4.3.3 Palladium

Palladium-doped mesoporous silica has been of interest throughout this study and, therefore, in the interest of completeness, palladium 2-ethyl hexanoate was synthesised and used as the precursor in the doping of both MCM-41 and SBA-15-like silicas using the TLCT method. Porosimetry (Figure 4.29) and XRD analysis (Table 4.8) shows that the physical structure of the silica hasn't been much affected by the inclusion of the palladium precursor, which is consistent with previous materials prepared. The decrease in surface area is indicative of the metal particles occupying some of the pores, reducing the surface area available during the analysis; there is a notable reduction in the case of Pd-SBA-15 with a 25% reduction in surface area after doping, which can be used as an indication that the palladium particles are forming within the pore structure, blocking the pores from porosimetry analysis.

Table 4.8 Structural data for Pd-doped silica prepared by TLCT

Precursor/Silica	Surface Area / m^2 g^{-1}	Pore Diameter / Å	Lattice Parameter / Å	Pore Wall Thickness / Å
Undoped MCM-41	1103	34.6	48.4	13.7
Pd 2-ethyl hexanoate/MCM-41	1012	40.4	51.1	10.7
Undoped SBA-15	600	51.5	89.4	37.9
Pd 2-ethyl hexanoate/SBA-15	457	46.3	98.2	51.9

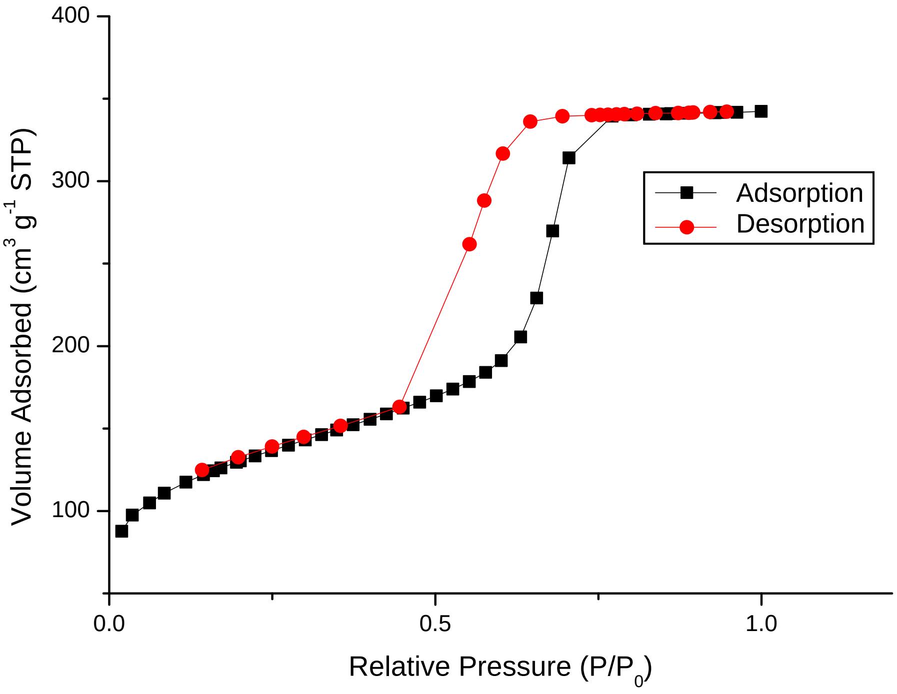

Figure 4.29 Adsorption-desorption isotherm of Pd-doped SBA-15-like silica prepared by TLCT

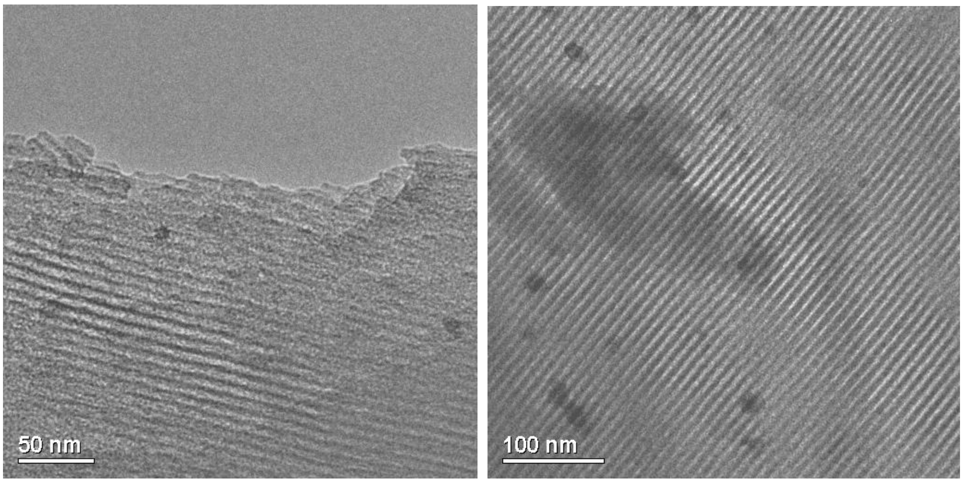

Figure 4.30 TEM images of Pd-doped MCM-41-like silica prepared by TLCT

TEM images collected of both materials (Figures 4.30 and 4.31) show the well-formed pore structure and, more importantly, the palladium nanoparticles. In the case of the palladium doped MCM-41, the nanoparticles are well dispersed and appear to all be of uniform size, each centralised within a pore channel. The particles (10.5 nm by the Scherrer equation and 15.0 nm measured from the TEM images) are larger than the individual pore (4.0 nm); however, examining the image closely it appears that the walls are disrupted around the pores, suggesting that the particles are located within two pores, rather than on the surface.

Considering the TEM images collected for the palladium doped SBA-15 (Figure 4.31) it is possible to identify particles of two distinctly different sizes. The first, larger, particles (A) appear to completely fill the pore and are calculated by the Scherrer equation to have an average size of 11.0 nm and measured from the images to be 7.3 nm. The second, smaller particles (B) are well dispersed throughout the material and are measured to be 1.9 nm in size; the smallest by far to be identified in a material prepared using one-pot synthesis with TLCT. This suggests that the palladium precursor is dissolved and fully contained within the micelles while the silica walls form around them in the aqueous region allowing the particles to remain small, as desired.

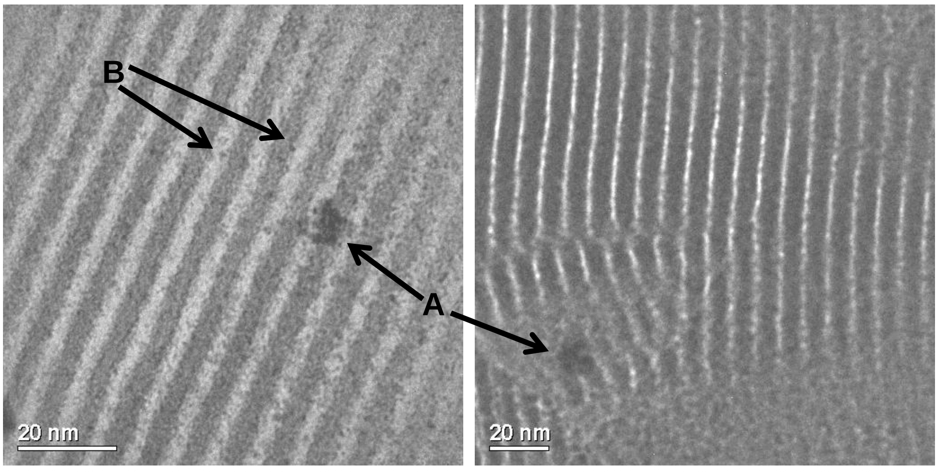

Figure 4.31 TEM images of Pd-doped SBA-15-like silica prepared by TLCT

4.3.4 Gold

In order to explore other organic ligands for preparing metal precursors, a relatively simple synthesis was found for *t*-butylisocyanogold(I) chloride[25] (Figure 4.32), where readily available chloro(tetrahydrothiophene)gold(I) [AuCl(tht)] was dissolved in dichloromethane and mixed with one equivalent of *tert*-butyl isocyanide before the solvent was removed under vacuum.

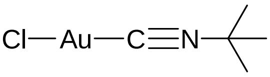

Figure 4.32 *t*-Butylisocyanogold(I) chloride

The synthesised *t*-butylisocyanogold(I) chloride was tested for solubility in both surfactants ($C_{12}EO_{10}$ and P123) by introducing 10 mg of the complex to the surfactant (0.6 g of $C_{12}EO_{10}$ or 0.5 g of P123) before warming to 40 °C to aid in mixing. Observing that both mixtures appeared to mix fully into a homogeneous gel, each mixture was then used in the preparation of the relevant TLCT silica; Au-MCM-41 and Au-SBA-15. Using 10 mg of *t*-butylisocyanogold(I) chloride would result in gold loadings of 3.6 and 2.6 wt%, respectively.

Table 4.9 Structural data for Au-doped silica prepared by TLCT

Precursor/Silica	Surface Area / $m^2\ g^{-1}$	Pore Diameter / Å	Lattice Parameter / Å	Pore Wall Thickness / Å
Undoped MCM-41	1103	34.6	48.4	13.7
Au/MCM-41	1024	34.1	52.8	18.6
Undoped SBA-15	600	51.5	89.4	37.9
Au/SBA-15	497	37.7	90.9	53.1

Characterisation of the prepared silicas (Table 4.9) appears consistent with previously prepared doped silicas, with a reduction in surface area and pore diameter as a result of the metal particles occupying the pores. BET isotherms for both materials (Figures 4.33 and 4.34) are each typical of the mesoporous materials prepared and comparable with previous materials, with Au-SBA-15 showing the characteristic hysteresis.

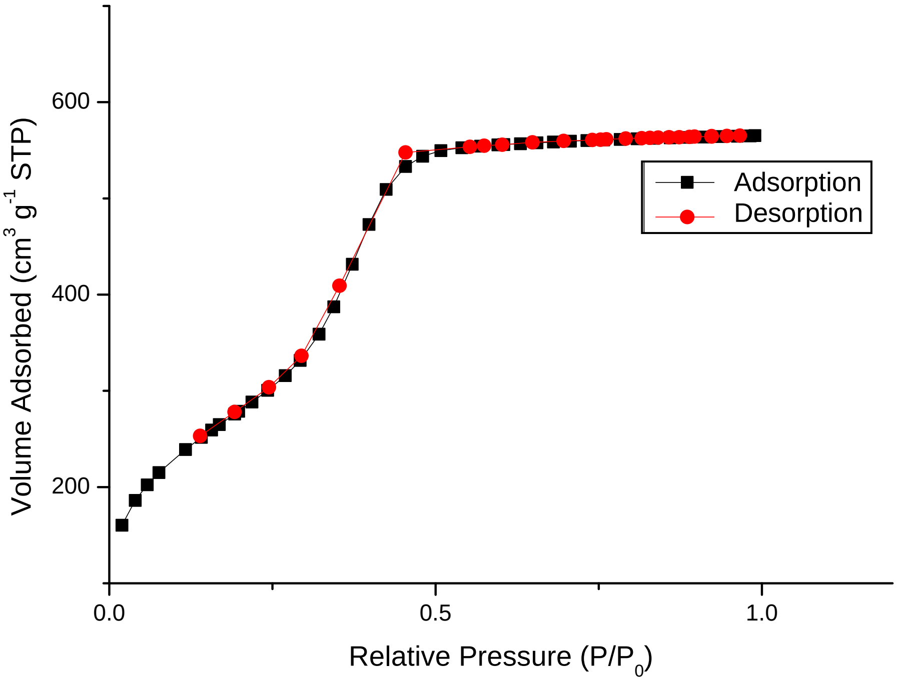

Figure 4.33 Adsorption-desorption isotherm of Au-doped MCM-41-like silica prepared by TLCT

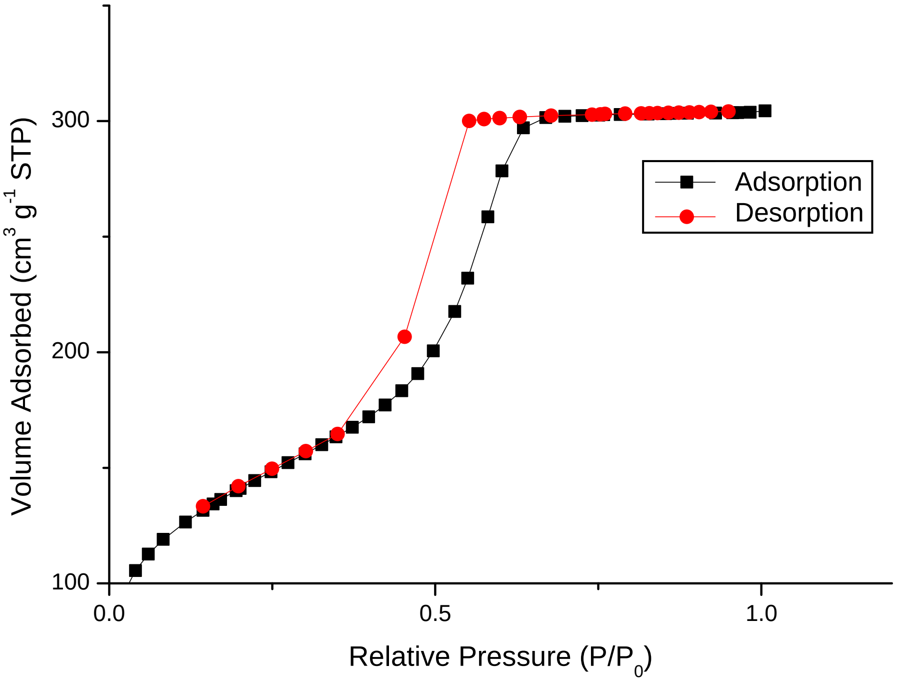

Figure 4.34 Adsorption-desorption isotherm of Au-doped SBA-15-like silica prepared by TLCT

Low-angle XRD of Au-MCM-41 (Figure 4.35) shows the characteristic reflections observed for hexagonal pore structures, although the d_{11} and d_{20} reflections are very weak suggesting limited long-range order. However, TEM images (Figure 4.36) show very clear, long, straight pores are present. Unfortunately, these pores do not appear to contain gold particles. However, it is possible to detect the particles with wide-angle XRD (Figure 4.37) which identifies them as metallic gold and, using the Scherrer equation to calculate the average particle size, the particles are found to be 34.6 nm, much larger than the 3.4 nm pore diameter.

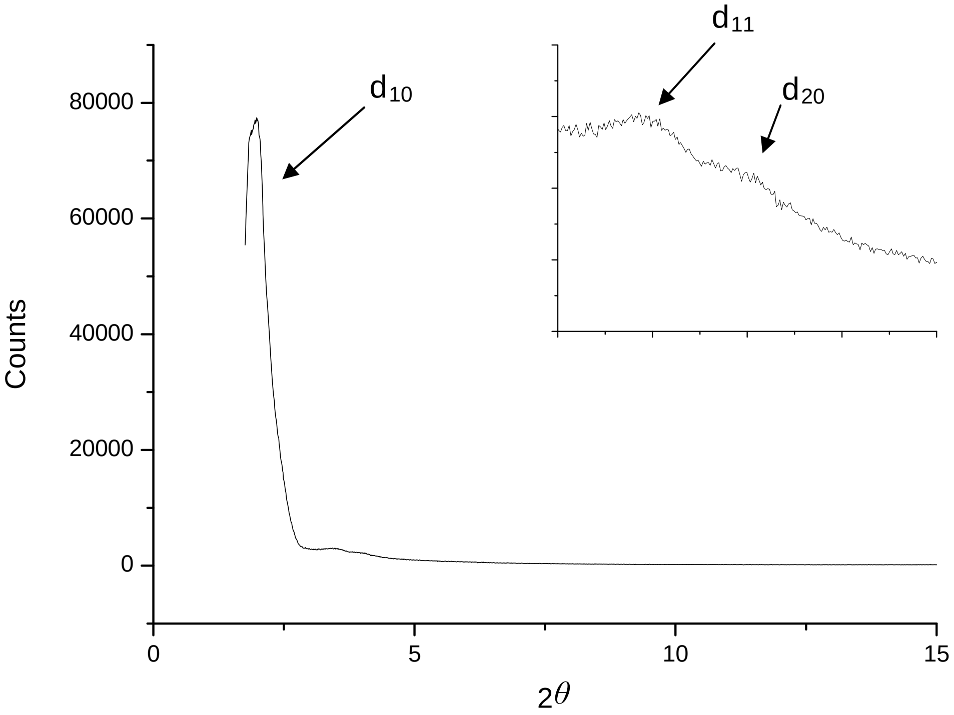

Figure 4.35 X-ray diffraction pattern of Au-doped MCM-41-like silica prepared by TLCT

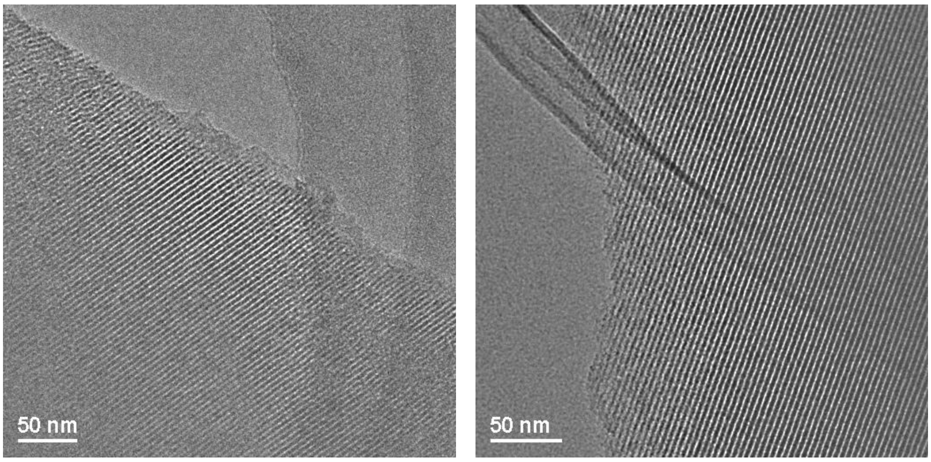

Figure 4.36 TEM images of Au-doped MCM-41-like silica prepared by TLCT

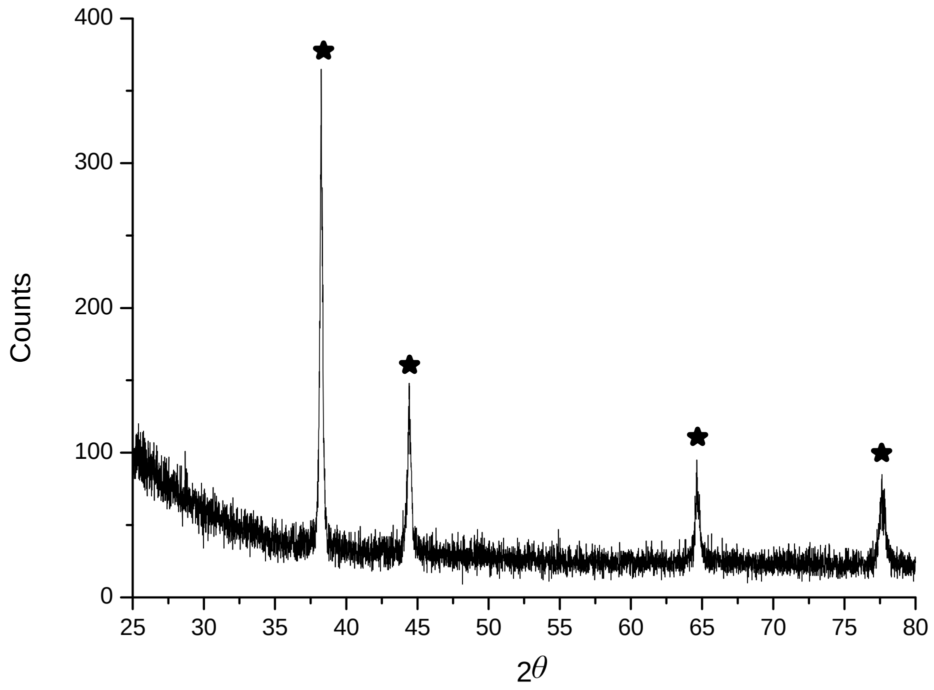

Figure 4.37 Wide-angle X-ray diffraction pattern of Au-doped MCM-41-like silica prepared by TLCT, (★) peak positions of Au metal

Unfortunately, it appears that using *t*-butylisocyanogold(I) chloride as a precursor for gold-doped SBA-15 was also unsuccessful in yielding small gold particles. Calculations using the Scherrer equation found an average particle size of 40.5 nm and in this case, the particle size can clearly be confirmed by the TEM image collected (Figure 4.38).

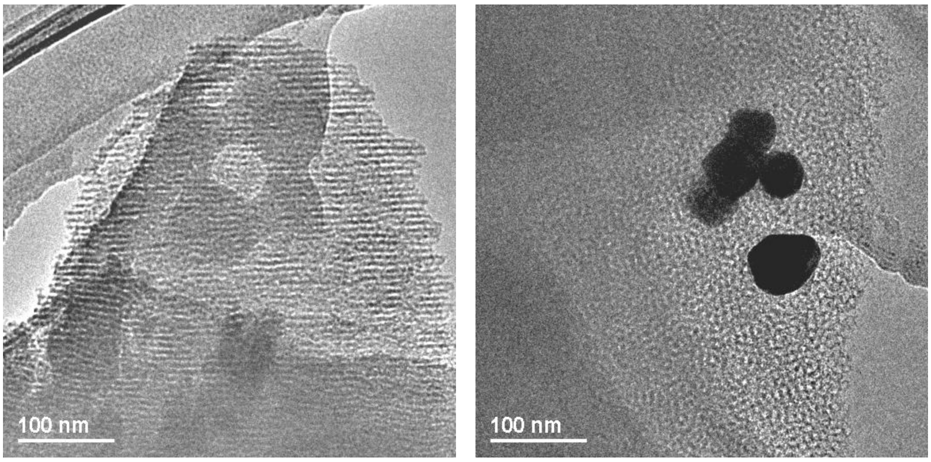

Figure 4.38 TEM images of Au-doped SBA-15-like silica prepared by TLCT

While it is possible to use *t*-butylisocyanogold(I) chloride as a precursor for gold-doped silicas of both MCM-41 and SBA-15 due to its suitable solubility, it is clear that controlling the particle size for gold is still very problematic. Throughout this work gold has aggregated into particles of around 40 nm in size regardless of the precursor or surfactant used. This is likely due to the low temperature at which the gold precursors decomposes (TGA finds that *t*-butylisocyanogold(I) chloride decomposes at 162.8 °C) resulting in the aggregation of large particles during the calcination process while the silica walls are being formed.

4.4 Summary

This chapter describes a significant change to the precursor in an effort to control the metal particle size to generate metal nanoparticles that would be small enough to be contained within the pores of the silica. This is done by changing the location of the metal precursor from the aqueous phase to the micelle centre. The use of these metal alkanoate precursors has proven to be extremely beneficial with palladium and rhodium nanoparticles being successfully doped into both MCM-41 and SBA-15 silicas, with particles observed to be clearly within the pores and of a desirable size.

Introducing gold nanoparticles into the mesoporous silica, it has once again proven difficult to control the particle size. Despite finding an apparently suitable gold precursor, which was shown to be soluble within the micelles as well as proving to be compatible with the templating process, the gold nanoparticles were still observed to be in excess of 40 nm in diameter. Small particles (> 5 nm) are vital if gold is to be used as an effective catalyst and so further work is required to determine a new gold precursor that will produce nanoparticles of the requisite size.

Regrettably, not all precursors used are compatible with this methodology and it was not possible to prepare copped-doped silicas using the precursors described in this Chapter. Further work, in the form of N_2O chemisorption and EXAFS, would be necessary to determine whether the copper introduced has migrated within the silica framework or has simply aggregated into large particles on the surface.

4.5 Experimental

4.5.1 General Experimental

ICP analysis was performed at MEDAC Ltd, Surrey.

4.5.2 Synthesis

Rhodium(II) Acetate

A solution of rhodium trichloride hydrate (1.09 g, 5.21 mmol, assumed trihydrate) and sodium acetate (2.05 g, 24.99 mmol) in glacial acetic acid (20 ml) and absolute ethanol (30 ml) was heated gently under reflux under nitrogen for an hour. The initial red solution rapidly became green, and a green solid deposited. After cooling to room temperature the green solid was collected by filtration through a Buchner funnel. The crude product is dissolved in boiled methanol (100 ml), filtered and then concentrated to about 70 ml. The solution was then cooled in a refrigerator for 24 h before crystals were collected and dried *in vacuo* at 45 ºC for 20 hours to yield emerald-green crystals.

Analysis found (calculated) for Rh acetate; C, 20.70 (21.74); H, 2.97 (2.74).

Palladium(II) Octanoate[26]

Under a flow of nitrogen, palladium(II) acetate (0.51 g, 2.3 mmol) was dissolved in dry benzene (250 ml) and octanoic acid (1.95 g, 13.5 mmol, 6 mol equiv.) were added slowly through a rubber septum. After heating the dark red solution under reflux for 12 h, the apparatus was fitted with a Dean-Stark trap and 150 ml of solvent was removed by azeotropic distillation; the remaining solvent was removed *in vacuo*. The brownish residue was taken up into diethyl ether (150 ml), extracted with 10% Na_2CO_3 solution (3 x 50 ml) and washed with water (pH 7). After drying over $MgSO_4$ the solvent was evaporated and residue dried under vacuum.

Rhodium(II) octanoate (Rh acetate (0.36 g, 1.6 mmol)) was prepared by the same method as was rhodium(II) 2-ethyl hexanoate and palladium(II) 2-ethyl hexanoate using 6 equivalents of 2-ethyl hexanoic acid.

Analysis found (calculated) for palladium(II) octanoate; C, 51.32 (49.05); H, 7.25 (7.72).
Analysis found (calculated) for rhodium(II) octanoate; C, 48.95 (49.36); H, 7.54 (7.77).
Analysis found (calculated) for palladium(II) 2-ethyl hexanoate; C, 53.92 (49.05); H, 8.16 (7.72).
Analysis found (calculated) for rhodium(II) 2-ethyl hexanoate; C, 51.04 (49.36); H, 8.03 (7.77).

Copper(II) 2-ethyl hexanoate

A solution of copper(II) acetate (0.45 g, 2.5 mmol) was dissolved in ethanol (100 m) was slowly added to 2-ethyl hexanoic acid (2 ml, 12.6 mmol) dissolved in ethanol (100 ml) and the mixture was stirred for 1 h. On addition of distilled water (100 ml) a precipitate formed which, after filtration, was washed thoroughly with water (50 ml) and ethanol (50 ml) and dried *in vacuo*.

Analysis found (calculated) for Cu 2-ethyl hexanoate; C, 54.64 (54.91); H, 8.51 (8.64).

t-Butylisocyanogold(I) chloride[25,27]

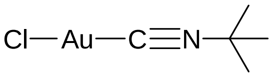

t-Butylisocyanide (0.16 g, 2.0 mmol) was added to Au(tht)Cl (0.64 g, 2.0 mmol) dissolved in dichloromethane (40 ml). The solution was mixed well for 15 minutes at room temperature before evaporating to dryness.

Analysis found (calculated) for t-Butylisocyanogold(I) chloride; C, 18.99 (19.03); H, 2.81 (2.87); N, 4.17 (4.44).

4.5.3 Preparation of Silica

$C_{12}EO_{10}$ templated silicas[28,29,30,31]

Palladium(II) octanoate (0.01 g, 2 wt% with respect to surfactant) was dissolved in polyoxyethylene-10-lauryl ether ($C_{12}EO_{10}$, 0.60 g). Added to this was water (0.40 g) acidified with HCl to pH 2 and the mixture sonicated to aid mixing until a homogeneous, viscous gel was formed. The hexagonal, H_1, phase formed was identified by polarised optical microscopy. Tetramethoxylsilane (0.8 cm^3, 5.35 mmol) was added to the gel and mixed thoroughly to yield a free-flowing liquid. This was placed under a light vacuum (120 mbar) at 40 °C to remove the evolved methanol. When the gel became viscous and the hexagonal mesophase could be identified by polarised optical microscopy, it was left on the open bench for 24 h to complete condensation. A portion (0.91 g) of the as-synthesised material was placed in the tube furnace for calcination to yield a dark brown coloured silicate (0.33 g).

Table 4.10 Range of silicas prepared using $C_{12}EO_{10}$

Metal	Metal Precursor	Mass of Precursor / g	Mass of Metal / g	Wt% of Metal in calcined material$^+$
Pd	Pd octanoate	0.013	0.004	1.25
Pd	Pd 2-ethyl hexanoate	0.011	0.003	0.93
Rh	Rh octanoate	0.011	0.003	1.09
Rh	Rh 2-ethyl hexanoate	0.010	0.003	0.87
Au	t-ButylisocyanoAu(I)Cl	0.016	0.010	3.66

$^+$Calculated wt % of metal within the whole sample after calcination

P123 templated silicas

Palladium(II) octanoate (0.01 g, 2 wt% with respect to surfactant) was dissolved in Pluronic® polymer P123 (0.50 g). Added to this was water (0.50 g) acidified with HCl to pH 2 and the mixture sonicated at 40 °C to aid mixing until a homogeneous, viscous liquid was formed. Templating proceeded in the same method as described above for the $C_{12}EO_{10}$ surfactant. A portion (0.78 g) of the as-synthesised material was placed in the tube furnace for calcination to yield a dark brown coloured silicate (0.31 g)

Table 4.11 Range of silicas prepared using P123

Metal	Metal Precursor	Mass of Precursor / g	Mass of Metal / g	Wt% of Metal in calcined material+
Pd	Pd octanoate	0.024	0.006	1.48
Pd	Pd 2-ethyl hexanoate	0.016	0.004	1.63
Rh	Rh octanoate	0.005	0.001	0.37
Rh	Rh 2-ethyl hexanoate	0.012	0.003	0.87
Cu	Cu 2-ethyl hexanoate	0.006	0.001	0.33
Au	t-ButylisocyanoAu(I)Cl	0.015	0.009	2.61

+Calculated wt % of metal within the whole sample after calcination

4.6 References

1. R. Gounder and E. Iglesia, *J. Am. Chem. Soc.,* 2009, **131,** 1958.
2. Ö. Dag, O. Samarskaya, N. Coombs and G. A. Ozin, *J. Mater. Chem.,* 2003, **13,** 328.
3. N. C. King, *PhD Thesis,* University of Exeter, 2005.
4. N. J. S. Salt, *PhD Thesis,* University of Sheffield, 1989.
5. M. Rusjan, B. Donnio, D. Guillon and F. D. Cukiernik, *Chem. Mater.,* 2002, **14**, 1564.
6. M. A. Castro, M. Rusjan, D. Vega, O. Pena, T. Weyhermüller, F. D. Cukiernik and L. D. Slep, *Inorg. Chim. Acta,* 2011, **374,** 499.
7. M. Rusjan, E. E. Sileo and F. D. Cukiernik, *Solid State Ionics,* 2003, **159,** 389.
8. R. H. Cayton, M. H. Chisholm, J. C. Huffman and E. B. Lobkovsky, *J. Am. Chem. Soc.,* 1991, **113,** 8709.
9. B. G. Alberding, M. H. Chisholm, T. L. Gustafson, Y. Liu, C. R. Reed and C. Turro, *J. Phys. Chem. A,* 2010, **114,** 12675
10. S. Coco, C. Cordovilla, C. Dominguez, B. Donnio, P. Espinet and D. Guillon, *Chem. Mater.,* 2009, **21,** 3282.
11. L. F. Zha, W. S. Yang, W. Y. Hao and M. Z. Cai, *Chin. Chem. Lett.,* 2010, **21,** 1310.
12. W. -Z. Lang, X. -W. Liu, Y. –J. Guo, B. Su, L. –F. Chu and C. –X Guo, *Micro. Meso. Mater.,* 2011, **142,** 7.
13. F. Fischer and H. Tropsch, *Ber.,* 1926, **59,** 830.
14. C. Masters, *Adv. Organometallic Chem.,* 1979, **17,** 61.
15. G. Chen, C. –Y. Guo, Z. Huang and G. Yuan, *Chem. Eng. Res. Design.,* 2011, **89,** 249.
16. F. Marras, J. Wang, M. –O. Coppens and J. N. H. Reek, *Chem. Commun.,* 2010, **46,** 6587.
17. A. J. Sandee, L. A. van der Veen, J. N. H. Reek, P. C. J. Kamer, M. Lutz, A. L. Spek and P. W. N. M. van Leeuwen, *Angew. Chem., Int. Ed.,* 1999, **38,** 3231.
18. J. Du, W. Kuang, H. Xu, W. Shen and D. Zhao, *Appl. Catal. B: Environ.,* 2008, **84,** 490.
19. G. Calleja, R. van Grieken, R. Garcia, J. A. Melero and J. Iglesias, *J. Mol. Catal. A: Chem.,* 2002, **181,** 215.

---

20. G. A. Rempel, P. Legzdins, H. Smith and G. Wilkinson, *Inorg. Syntheses,* 1972, **13,** 90.
21. T. Tsoncheva and E. Sarkadi-Priboczki, *Appl. Surf. Sci.,* 2011, **257,** 6661.
22. M. J. O. Rico, R. Moreno-Tost, A. Jiménez-López, E. Rodríquez-Castellón, R. Pereňíguez, A. Caballero and J. P. Holgado, *Catal. Today,* 2010, **158,** 78.
23. M. Gómez-Cazaliila, J. M. Mérida-Robles, A. Gurbani, E. Rodríguez-Castellón and A. Jiménez-López, *J. Solid State Chem.,* 2007, **180,** 1130.
24. J. A. Wood and A. B. Seddon, *Transition Met. Chem.,* 1985, **10,** 212.
25. A. S. K. Hashmi, T. Hengst, C. Lothschütz and F. Rominger, *Adv. Synth. Catal.,* 2010, **352,** 1315.
26. C. P. Roll, *PhD Thesis,* Friedrich-Schiller-Universitat Jena, 2003.
27. R.Usón, A. Laguna, J. Vicente, J. García, B. Bergareche and P. Brun, *Inorg. Chim. Acta,* 1978, **28,** 237.
28. Y. Huang, W. Qin, X. Huo, Y. Dai, *Coll. Surf. A: Physicochem. Eng. Aspects,* 2006, **276,** 228.
29. K. S. Sharma and A. K. Rakshit, *Bull. Chem. Soc. Jap.,* 2005, **78,** 771.
30. S. B. Sulthana, P. V. C. Rao, S. G. T. Bhat, T. Y. Nakano, G. Sugihara and A. K. Rakshit, *Langmuir,* 2000, **16,** 980.
31. D. J. Mitchell, *J. Chem. Soc., Faraday Trans. I,* 1983, **79,** 975.

CHAPTER FIVE

SELECTIVE OXIDATION REACTIONS

5.1 Introduction

The discovery of MCM-41 in 1992 by Beck *et al.*[1] began a surge of interest into using mesoporous silica in catalysis. By merit of their high surface areas, narrow pore size distributions, well defined chemical properties of the surface and the number of reactions, studies over mesoporous silica constantly increased. A recent review[2] described the range of reactions studied to include the conversion of synthesis gas,[3] oxidative dehydrogenation of light alkanes[4] or ethylbenzene,[5] Knoevenagel and Henry reactions or Claisen-Schmidt condensation,[6] acetalisation and synthesis of acetals/ketals,[7] biomass transformation[8] and acylation reactions.[9]

It has been described previously that unmodified mesoporous silica is inactive catalytically and requires the incorporation of active sites for catalysis. These active sites can be in the form of single atoms,[10] metal complexes[11] or metal oxides.[12] The primary focus of this work is palladium nanoparticles supported on different mesoporous silicas, namely MCM-41 and SBA-15.

Palladium-doped onto MCM-41 has been used as an efficient catalyst in a variety of forms; palladium complexes grafted onto the silica to prepare heterogenised homogeneous catalysts as well as nanoparticles of palladium anchored within the pore structure for true heterogeneous catalysts. In 2007, Xu *et al.*[13] immobilised a palladium complex (poly{γ-mercaptopropylsiloxane} palladium(0)) onto MCM-41 and used the prepared catalyst to test the Heck arylation reaction (Figure 5.1) of styrene with aryl halides. They found that the immobilised complex was an efficient, stable and recyclable catalyst, taking advantage of an easy to prepare material.

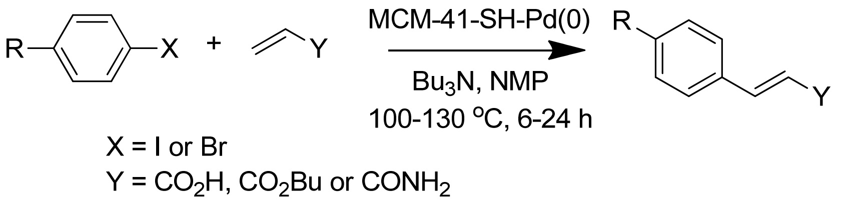

Figure 5.1 Scheme for Heck arylation reaction

An immobilised palladium complex on MCM-41 was also used in the allyation of aldehydes and ketones with allylic chlorides by Zhao *et al.*[14] Modifying MCM-41 with 3-(2-aminoethylamino)propyltrimethoxysilane allowed palladium to be introduced by heating the functionalised silica under reflux with $PdCl_2$ in acetone. This yielded an MCM-41 material with immobilised palladium(II). This was tested catalytically with a range of aldehydes and ketones (Figure 5.2) which successfully reacted to form the intended product with yields in excess of 80%. By utilising a heterogeneous catalyst, it was possible to recover the palladium catalyst by simple filtration and recycle it. Reusing the same catalyst in five reactions did not result in a loss of activity, with yields remaining constant and, with a loss of only 3% of the palladium from the support, leaching was minimal.

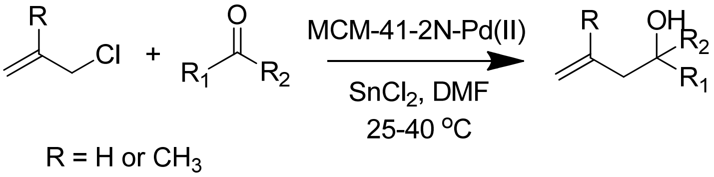

Figure 5.2 Scheme for allyation of aldehydes and ketones

The materials described in this work are palladium nanoparticles supported on silica, rather than palladium complexes. Demel *et al.*[15] prepared a series of catalysts by grafting palladium nanoparticles onto MCM-41 by ion-exchange with cesium cations. They washed the MCM-41 with $CsNO_3$ at room temperature before introducing the palladium, by refluxing the ion exchanged MCM-41 with palladium(II) acetate and tetrabutylammonium acetate in dry THF, a method they had previously reported.[16] They used these catalysts to study the Heck reaction between bromobenzene and *n*-butyl acrylate to give butyl cinnamate. Specifically, they studied the reaction under microwave irradiation rather than the traditional thermal activation;[17] they found that activity was around 10 times higher under microwave conditions, although this led to increased particle aggregation and thereby catalyst deactivation.

Elsewhere, Demel *et al.*[18] reported the synthesis of palladium-grafted MCM-41 for the use in the catalytic reaction for formation of an *N*-substituted pyrrole. They prepared palladium nanoparticles by dissolving palladium(II) acetate in propylene carbonate and heating to 110 °C for 3 hours, the nanoparticles in solution were then introduced into MCM-41 and the mixture stirred overnight before washing with diethyl ether. The catalyst was tested alongside 10% Pd/C, to act as a reference, in the condensation reaction of 2-hydroxyethylamine with *cis*-butene-1,4-diol to give *N*-(2-hydroxyethyl)pyrrole (Figure 5.3). The palladium-nanoparticles grafted onto MCM-41 showed significantly higher activity compared with the Pd/C. However, it should be noted that leaching of the palladium was observed after each reaction with Pd-MCM-41, signified by a reduction in activity when recycled.

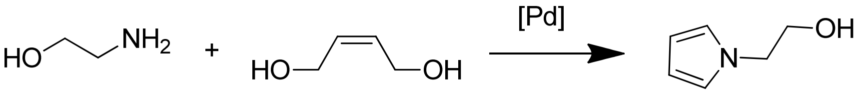

Figure 5.3 Scheme for the formation of *N*-substituted pyrrol

Li *et al.*[19] prepared a palladium-nanoparticle-doped SBA-15 for the catalytic oxidation of benzene. Palladium was introducing into SBA-15 *via* the incipient wetness impregnation of palladium chloride. TEM images of the doped silicas exhibited large palladium particles, larger than the individual pores, suggesting that the palladium had aggregated during synthesis. This led to poor catalytic activity compared with other palladium-doped silicas tested, emphasising the importance of particle size control within the catalysts.

5.1.1 Selective oxidation of crotyl alcohol

With the benefit of previous experience within the group,[20] the intention was to test the materials prepared within this work with the selective oxidation of crotyl alcohol to crotonaldehyde (Figure 5.4) to test for activity and compare with similar materials prepared in the traditional manner.

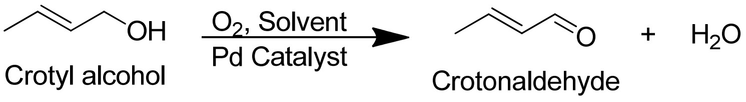

Figure 5.4 Selective oxidation of crotyl alcohol

Crotonaldehyde is one of a number of chemicals of interest as a valuable intermediate with applications within the fine chemical and food industries produced from the selective oxidation of allylic alcohols. Traditionally this reaction had been carried out with stoichiometric oxidations using chromates and peroxides;[21] however, these reactions offered poor yields and interest has increased in replacing them with homogeneous or heterogeneous catalysts.

There are two proposed mechanisms for the homogeneous reaction (Figure 5.5). Route 1 involves the reduction of palladium(II) to palladium(0) as a result of the alcohol producing two protons and the aldehyde product. Route 2, on the other hand, involves the binding of the alcohol as an alkoxide which then undergoes β hydride elimination to leave a hydride complex.

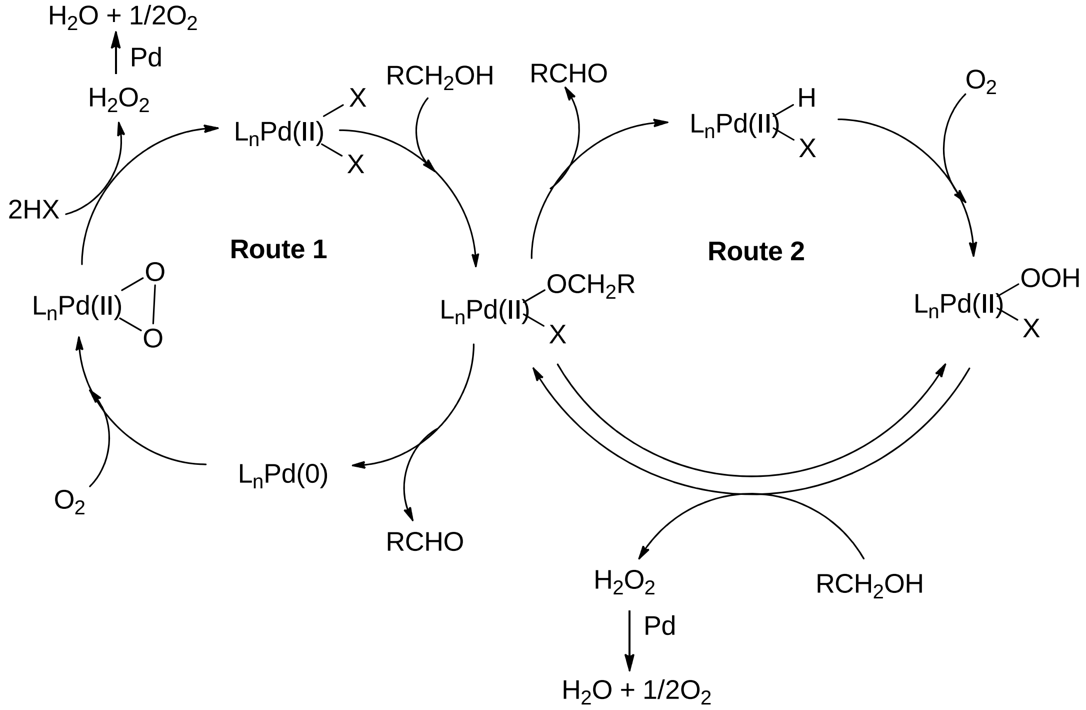

Figure 5.5 Proposed mechanisms for the Pd-catalysed oxidation of alcohols

The mechanism for the selective oxidation of alcohols using heterogeneous methods is thought to occur by oxidative dehydrogenation on the surface of the catalyst with the surface being regenerated by oxygen absorbing dissociatively to remove the hydrogen as water. Rottenberg *et al.*[22] investigated this mechanism by the use of ^{18}O-labelled oxygen and observed the formation of $H_2{}^{18}O$. Examining the organic products by mass spectrometry, none of the heavy isotope was present in the aldehyde, confirming the proposed mechanism. This also shows the requirement for oxygen to be present to facilitate the reaction and push it towards completion.

Lee *et al.*[23] investigated the selective oxidation of crotyl alcohol by use of a Pd model catalyst, *i.e.* a single crystal Pd(111). In addition to the desired product, crotonaldehyde, they observed alcohol dehydration to yield butene and water. They also noted that catalysis over the Pd(111) plane required temperature control as below 380 K; the reaction was hindered by CO being bound reversibly to the surface, and above 400 K the catalyst was deactivated by irreversibly bound carbonaceous residues. In previous studies, the same group identified the importance of the palladium oxidation state[24] as well as particle dispersion[25] with regards to the activity of the catalyst. They determined that it is essential for the palladium particles to consist of a surface layer of palladium oxide over a bulk of palladium metal for highly selective oxidation activity. Additionally, they showed that there is a strong link between catalyst activity and palladium loading, with a higher turnover frequency at lower loadings. Lower metal loadings are related to increased dispersion which leads to an increased proportion of exposed surface palladium oxide.

This chapter will report on the investigations carried out into the catalytic activity, with respect to selective oxidation reactions of the palladium-doped mesoporous silicas whose preparation was described in the previous chapters.

5.2 Material treatment pre-reaction

Before the true activity of the materials prepared during this work can be tested in the catalytic selective oxidation of crotyl alcohol, it is important to examine the reaction conditions and any required catalyst pre-treatment to ensure reliable and repeatable results, which can be compared with other materials. These pages detail that work.

From the wide-angle XRD data presented in Chapters 2-4, we know that after calcination the palladium in the silica pores is palladium oxide, whereas, as shown by Lee *et al.* previously, for effective catalysis it is required to be palladium metal in the bulk with a shell of palladium oxide. Therefore, the catalyst will need to be reduced before use. Thus, each material was reduced under hydrogen for 2 hours at 500 °C and wide-angle XRD confirmed the formation of palladium metal (Figure 5.6). It is assumed that the surface of the palladium particles will oxidise in air to generate the required palladium oxide shell.

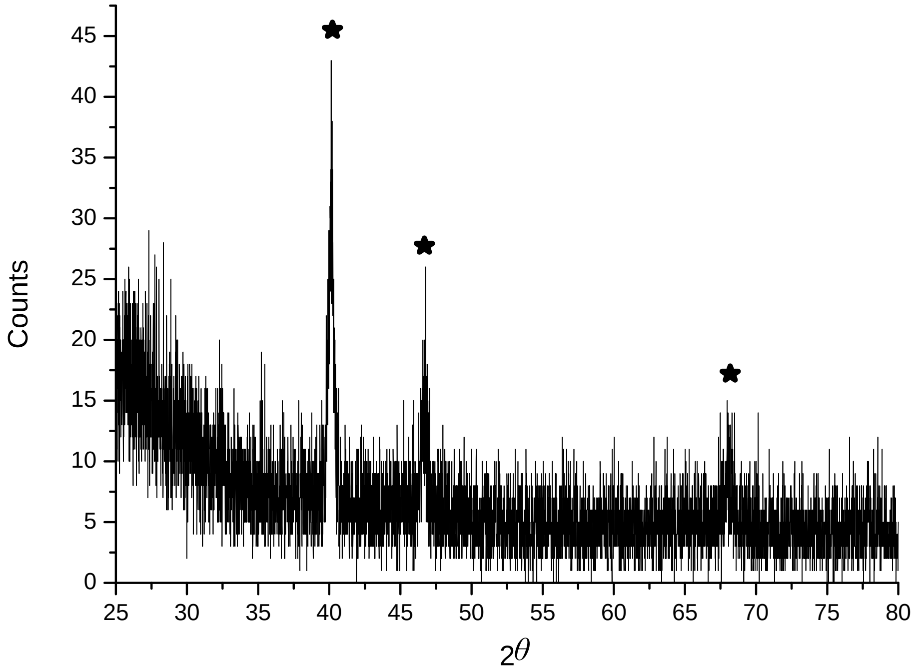

Figure 5.6 Wide-angle X-ray diffraction pattern of Pd-doped MCM-41-like silica prepared by TLCT, (★) peak positions of Pd metal

Each reaction studied used a dilute solution of crotyl alcohol in toluene containing a mesitylene standard and was carried out in a Radley's reaction vessel at 90 °C and with a stirring at 600 rpm; a cooling jacket prevented evaporation. Once the temperature was stabilised, an aliquot of the solution was removed at T_0 (time = 0), and then the dried catalyst prepared by heating at 100 °C for an hour was added to the vessel to start the reaction. Samples were removed at 10, 20, 30, 40, 60, 180 and 300 minutes and after 24 hours, and were analysed by gas chromatography (GC) to monitor the reaction progress.

The primary method for monitoring the progress of the reactions and assessing the activity of the catalysts is by observing the amount of starting material, crotyl alcohol, consumed during the reaction. By virtue of the internal standard and how the peak area of the crotyl alcohol changes in comparison, GC analysis of the reaction mixture allows crotyl alcohol loss (hereafter considered as consumption) to be tracked (Figure 5.7). GC analysis also allows the formation of products to be monitored and for the mass balance of the reaction to be calculated, to determine if any of the reaction mixture has been lost through evaporation.

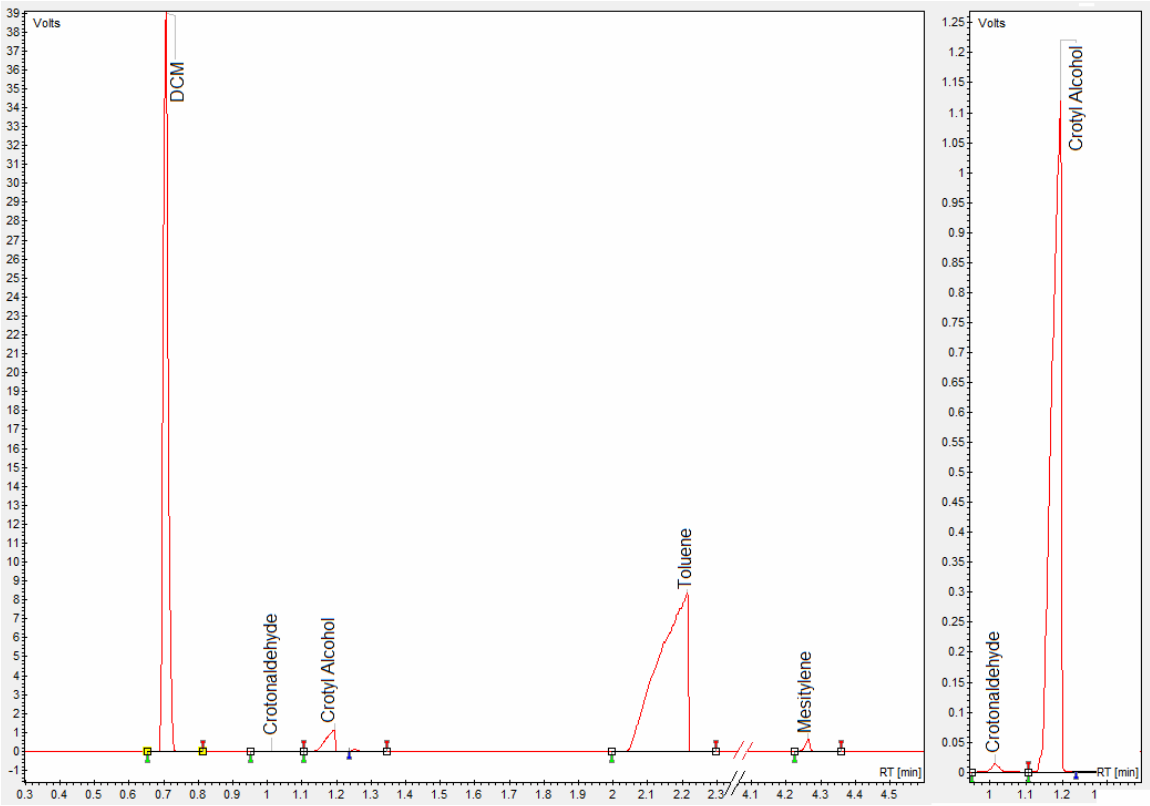

Figure 5.7 GC trace of reaction mixture showing separate peaks

Early testing of these catalysts gave erratic results that were found not to be repeatable. The catalysts were being used directly from calcination without any further treatment, resulting in a wide range of silica particle sizes. This would have significant mass transport limitations as long pores would need to be travelled to access active sites for one material where only short pores would be present in another. In an effort to introduce uniformity into the catalysts before testing, each was ground with pestle and mortar to a fine powder. SEM images were taken of 4.4 wt% palladium-doped MCM-41 prepared by TLCT with the $(NH_4)_2[PdCl_4]$ precursor, prepared and characterised in Chapter 2, (2-Pd-MCM-41) and of a 2.9 wt% palladium-doped SBA-15 prepared by TLCT with the $(NH_4)_2[PdCl_4]$ precursor, prepared and characterised in Chapter 3, (3-Pd-SBA-15), before and after grinding, to demonstrate the difference in particle sizes within the materials (Figure 5.8 and 5.9). Aside from particulate size and distribution, SEM did not reveal any other useful information regarding the structure, although palladium particles were not observed, which suggests that they are within the pore structure rather than on the surface. The pores themselves were not visible at the resolution used.

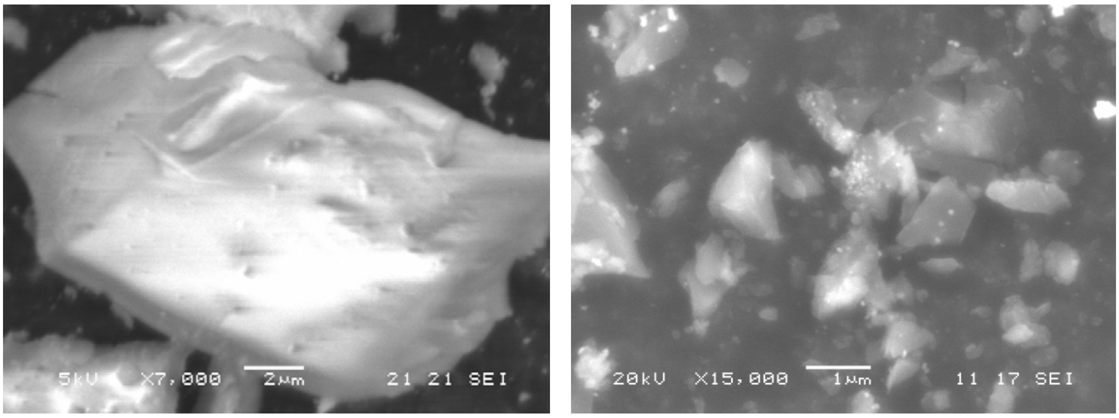

Figure 5.8 SEM images of 2-Pd-MCM-41; Left) before grinding and Right) after grinding

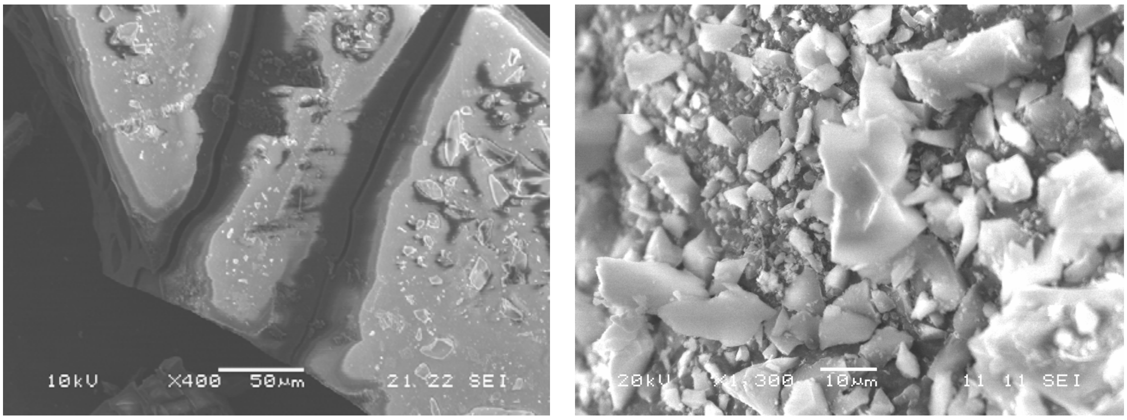

Figure 5.9 SEM images of 3-Pd-SBA-15; Left) before grinding and Right) after grinding

To observe the importance of this pre-treatment on the activity of the catalyst, a single batch of 2-Pd-MCM-41 was split into four, with each being treated differently before introducing them into the reaction as normal. The first was left as-synthesised after calcination while the second was simply ground to a fine powder. The third and fourth samples were reduced under hydrogen, and the fourth was ground to a fine powder the same as sample 2. It can clearly be observed (Figure 5.10) that simply grinding the catalyst allowed an increase of ~30% to the conversion of crotyl alcohol after 24 hours coupled with a ~20% increase as a result of reducing the catalyst beforehand. From this point on, all catalysts were pre-treated by reducing under hydrogen and grinding into a fine powder before use in the reaction.

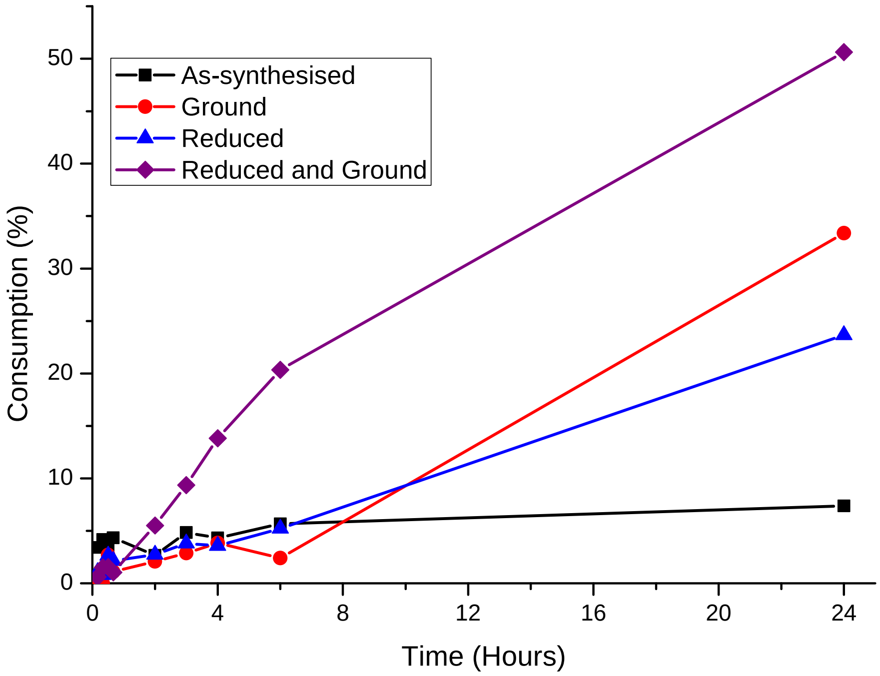

Figure 5.10 Reaction profiles of 2-Pd-MCM-41 showing different pre-treatments

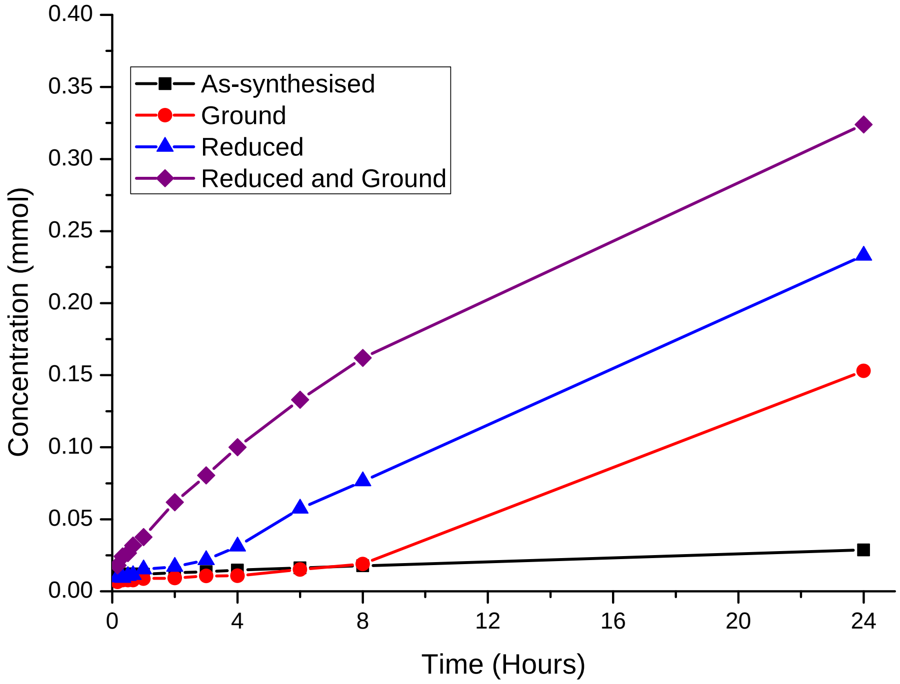

Figure 5.11 Reaction profiles of 2-Pd-MCM-41 showing the formation of crotonaldehyde

GC analysis of the reaction samples will also allow the concentration of products formed during the reaction to be calculated. Plotting the concentration of crotonaldehyde, the primary product, produced during the reaction against time (Figure 5.11) confirms that the desired reaction is indeed occurring and the improvement in the consumption of starting material is mirrored with an increased concentration of crotonaldehyde being produced. It is important to note that for the reduced and ground sample, 4.2 mmol of crotyl alcohol was consumed during the reaction, however only 0.32 mmol of crotonaldehyde was produced. This is a significant difference and will be discussed in more detail later.

To ensure the repeatability and reliability of the reaction profile, reactions were often carried out in duplicate with the same conditions and catalyst used in each reaction. Figure 5.12 shows one such example, 4 wt% $(NH_4)_2[PdCl_4]$ doped onto MCM-41 (2-Pd-MCM-41) where two batches of the same catalyst were used in concert with very similar reaction profiles. In any case where the reaction profiles did not match, the reaction was repeated further to achieve consistency.

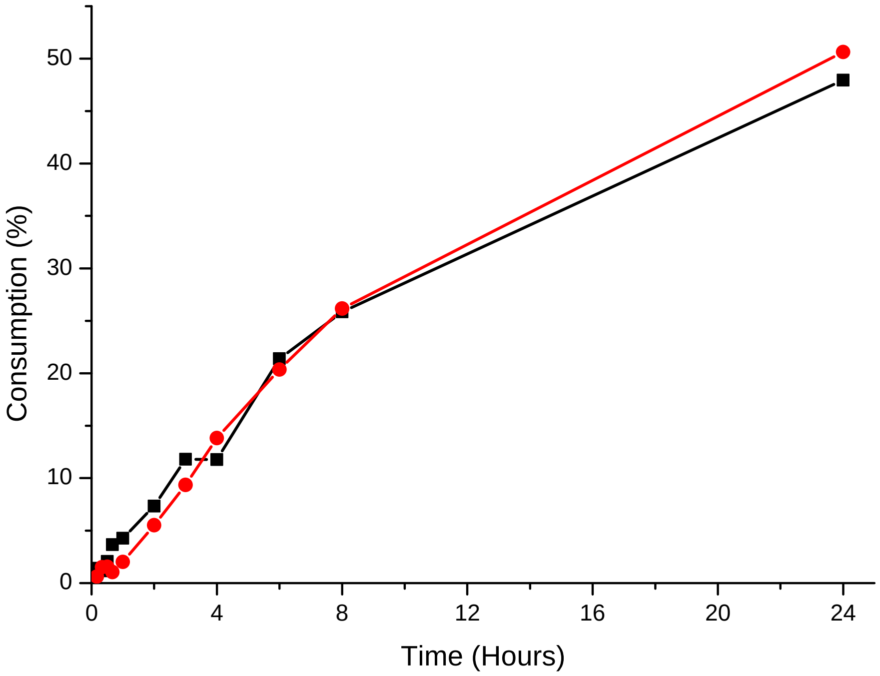

Figure 5.12 Reaction profiles of repeated runs of 2-Pd-MCM-41

5.3 Selective oxidation reaction of Pd-MCM-41

Each of the subsequent reactions were carried out following the procedure established previously (Chapter 5.2) including reducing and grinding the catalyst prior to the reaction. Of initial interest to this work is the palladium-doped MCM-41 materials prepared by TLCT, the catalytic activity of these materials will be described in the following pages.

During this work palladium-doped MCM-41 has been prepared for catalysis using different precursors; the two of interest here are $(NH_4)_2[PdCl_4]$, (2-Pd-MCM-41), described in Chapter 2 and palladium(II) octanoate which was used to prepare 1 wt% palladium-doped MCM-41, described in Chapter 4, (4-Pd-MCM-41). Both were tested for activity with the selective oxidation reaction and while both materials showed similar structural properties with regards to the silica support, the palladium particle sizes were dramatically different, which will likely result in different activities. The reaction profile of these catalysts over 24 hours is displayed below in Figure 5.13.

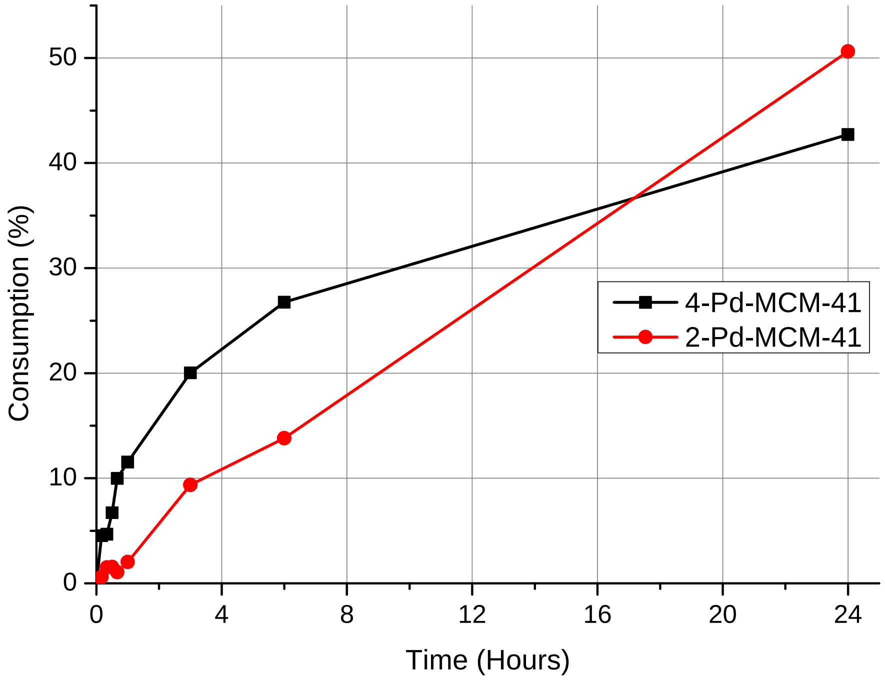

Figure 5.13 Reaction profile of palladium-doped MCM-41 for the selective oxidation of crotyl alcohol

As predicted, due to the smaller particle size generated by the palladium octanoate precursor, initial activity for the 4-Pd-MCM-41 catalyst was much higher than 2-Pd-MCM-41. The initial rate of each catalyst can be calculated from the reaction profile and normalised to one gram of palladium based on the quantity of palladium found within the catalyst. The initial rate is the amount of reagent consumed after one hour of reaction which is then adjusted to calculate the amount that would be consumed if one gram of palladium had been used. Thus, the initial rate normalised to one gram of palladium is 106 mmol h^{-1} for the $(NH_4)_2[PdCl_4]$ doped MCM-41 (2-Pd-MCM-41) and 1545 mmol h^{-1} for palladium octanoate (4-Pd-MCM-41); a significant improvement.

While observing the loss of starting material, crotyl alcohol, ought to give a simple conversion activity of the catalyst, it is more useful to know the formation of products so as to calculate the selectivity of the catalyst towards the desired product, crotonaldehyde. If the catalyst is not selective towards crotonaldehyde as intended, there are a number of possible side products to consider; after crotonaldehyde, butanal is most likely to be observed. Despite a promising apparent conversion of crotyl alcohol, 2-Pd-MCM-41 showed very little formation of either crotonaldehyde or butanal (Figure 5.14) with almost 80% of the crotyl alcohol loss being unaccounted for.

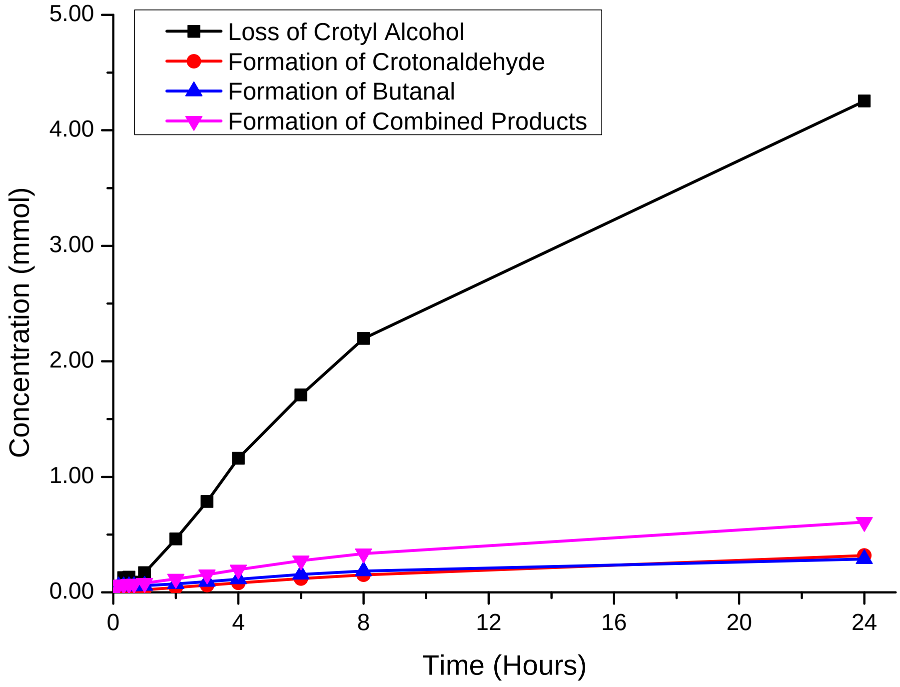

Figure 5.14 Reagent loss and product formation of 2-Pd-MCM-41

4-Pd-MCM-41 fared better with a significant increase in the formation of crotonaldehyde and butanal, with crotonaldehyde as the primary product. However, the combined totals still only account for ~ 60% of the consumed crotyl alcohol (Figure 5.15).

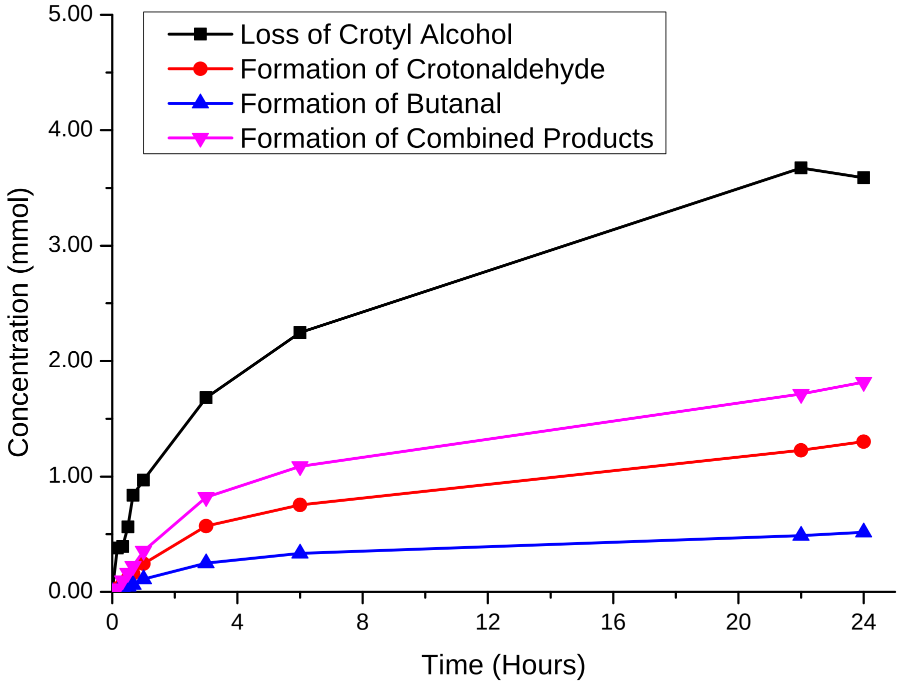

Figure 5.15 Reagent loss and product formation of 4-Pd-MCM-41

Part of the unaccounted loss would likely be due to evaporation of the crotyl alcohol during the reaction. As a measure of this, a blank experiment was performed where the reaction mixture was heated and stirred as normal over the 24 hour period with samples withdrawn at the usual intervals; however, no catalyst was used (Figure 5.16). Where 2-Pd-MCM-41 observed a 50% conversion or loss of crotyl alcohol over this time, the blank reaction only observed 4% lost through evaporation.

There are a number of other potential products (Figure 5.17) which could be produced by an unselective catalyst, and which could account for the discrepancy in mass balance; however, if the amounts produced were too small to be detected, they could not account for much of the crotyl alcohol consumed. Products such as butanal could be produced from either the hydrogenation of crotonaldehyde which would reduce the amount of observed product or via the hydrogenation of butanol from crotyl alcohol.

Alternatively, further oxidation of crotonaldehyde could occur which would result in butyric acid or hydrogenation of crotyl alcohol could produce butanol, butene or butane.

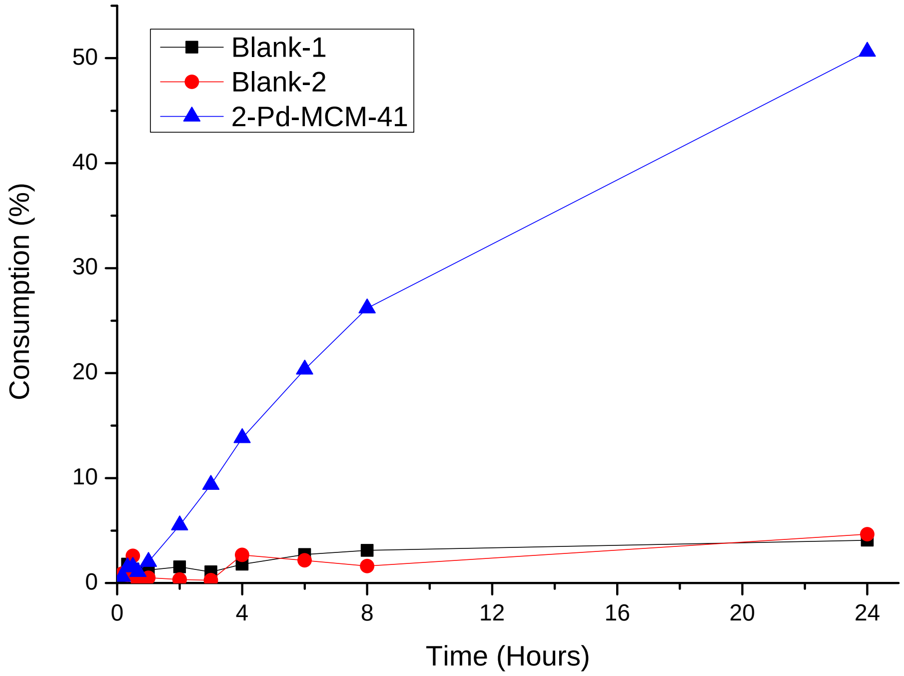

Figure 5.16 Reaction profile of blank reaction compared with 2-Pd-MCM-41

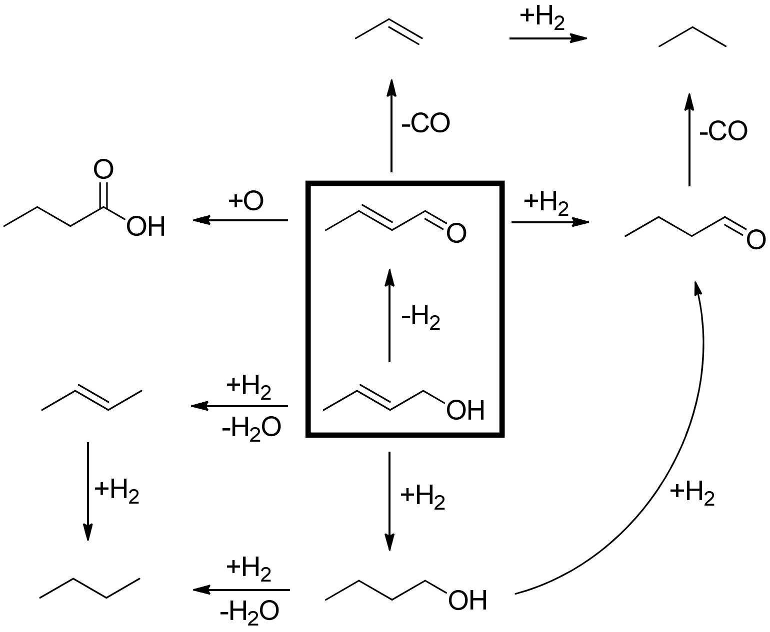

Figure 5.17 Schematic of possible side reaction during oxidation of crotyl alcohol

In an effort to account for the lost crotyl alcohol, a reaction was carried out using an undoped MCM-41 to monitor any reaction taking place on the silica surface. The reaction profile (Figure 5.18) suggests that around 25% of the crotyl alcohol has been consumed in the reaction. However, no products were detected by GC and we know that only ~5% would be lost due to evaporation, which would imply that ~20% of the crotyl alcohol has been taken up by the silica, either absorbed on the surface or within the pores. This would account for the remaining loss of reactant.

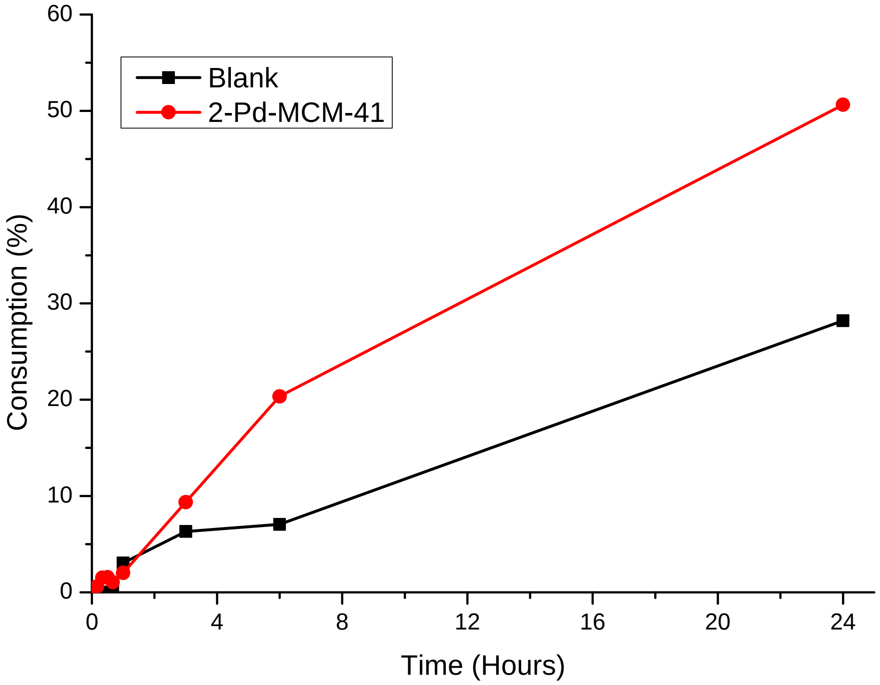

Figure 5.18 Reaction profile of MCM-41 (blank) compared with 2-Pd-MCM-41

Combining the reagents observed to be lost through evaporation or absorption onto silica with the formation of products, crotonaldehyde and butanal, shows the combined mass balance is not dissimilar to the overall reaction profile of consumed crotyl alcohol (Figure 5.19).

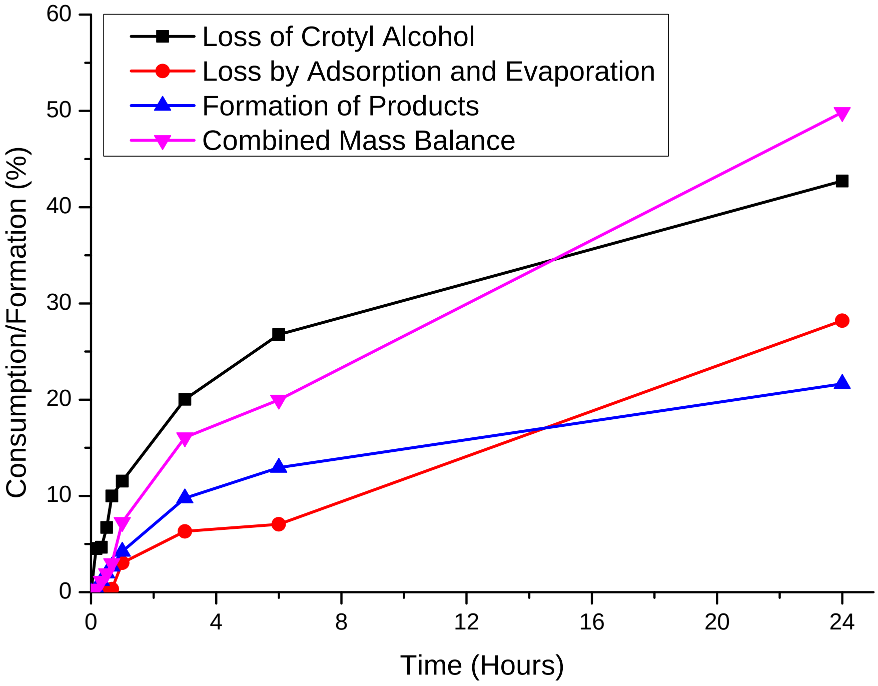

Figure 5.19 Mass balance of 2-Pd-MCM-41

Effect of metal loading on activity

In Chapter 2, the preparation of a series of palladium-doped materials with differing metal loadings (0.01, 0.05, 0.1, 0.5, 1.0 and 2.5 wt%) was described, to examine the effect the amount of palladium has on the activity. Each catalyst was reduced under hydrogen before use in the reaction. The initial rate, normalised for one gram of palladium, was calculated for each reaction and plotted against the palladium loading (Figure 5.20). Just as Lee *et al.* observed, lower loadings lead to a much higher initial rates due to the formation of smaller, more-disperse, particles within the catalyst leading to more of the palladium oxide surface being available for catalysis rather than as bulk metal within the particle.

Determining the palladium metal dispersion by CO chemisorption would allow the turnover frequency of the catalysts to be calculated, although the trend shown by the initial rates (Figure 5.20) is likely to be the same for the turnover frequencies. Further to this, normalising the turnover frequencies to either the number of palladium metal surface atoms, determined from CO chemisorption, or the number of Pd^{II} (PdO) surface atoms, determined from XPS, would allow the dependency of the PdO surface layer to the activity of the catalyst.

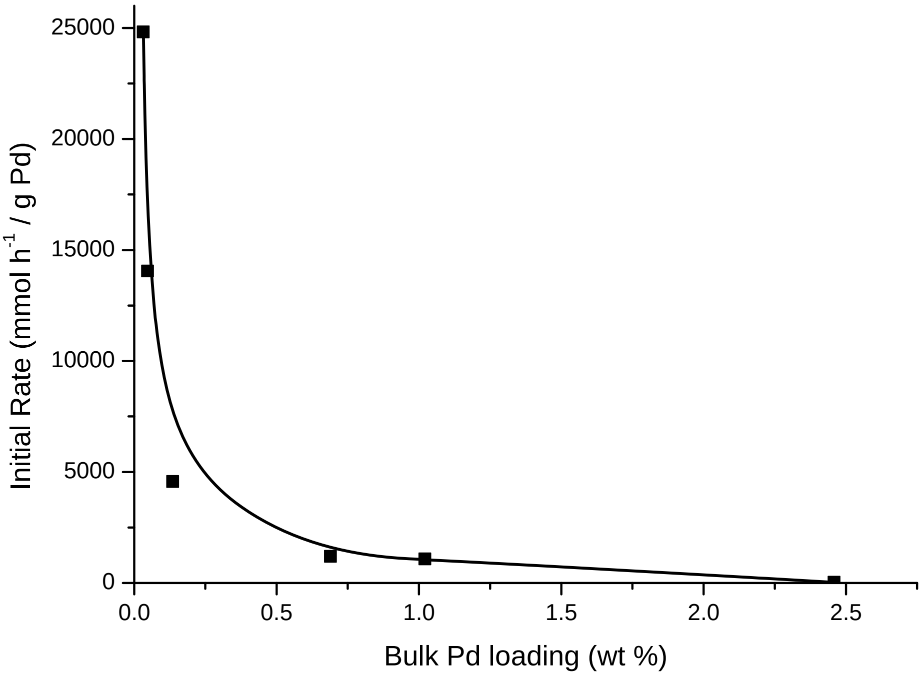

Figure 5.20 Loading-dependent activity of 2-Pd-MCM-41 in crotyl alcohol oxidation

5.4 Selective oxidation reaction of Pd-SBA-15

Palladium-doped SBA-15 catalysts were prepared, characterised and tested for the oxidation of alcohols by Li *et al.*[26] SBA-15 was prepared in the traditional manner[27] and then impregnated with palladium by adsorption of $[Pd(NH_3)_4]^{2+}$ into the pores followed by calcination and reduction under hydrogen. This method resulted in palladium nanoparticles of 3-4 nm in size, located within the mesoporous structure, which were shown to be active in the solvent-free aerobic oxidation of benzyl alcohol, showing improved activity over palladium-doped SBA-15 prepared by incipient wetness impregnation.

SBA-15-like materials are thought likely to show higher activity, compared with MCM-41-like materials, due to their larger pores allowing materials easier access to the active sites within, reducing the effect of any mass transport limitations. The structural properties of palladium-doped SBA-15 was presented in Chapter 3 with the use of $(NH_4)_2[PdCl_4]$, hereafter referred to as 3-Pd-SBA-15.

3-Pd-SBA-15 was tested in the same manner as the Pd-MCM-41 catalysts described previously with the selective oxidation of crotyl alcohol to crotonaldehyde. The reaction profile (Figure 5.21) is more comparable to that of 4-Pd-MCM-41 rather than 2-Pd-MCM-41, which is indicative of the smaller particles with improved access for the reagents.

The initial rate was calculated from the reaction profile, as crotyl alcohol is consumed, and found to be 654 mmol h^{-1} normalised to one gram of palladium. This is found to be about a third of that of palladium-doped SBA-15 synthesised by incipient wetness impregnation. For comparison, Partlett *et al.*[28] prepared a catalyst of 2.5 wt% palladium-doped SBA-15 (IMP-Pd-SBA-15) and tested it in the selective oxidation of crotyl alcohol using the same conditions as this work and found the initial rate to be 1832 mmol h^{-1} g_{Pd}^{-1} (Figure 5.21). While the impregnated Pd-SBA-15 showed a higher initial activity, the reaction profiles for the two materials are not dissimilar, with overall conversion being very close. Crucially, Parlett observed the importance of the palladium oxide surface layer over the palladium metal particles, providing evidence that the palladium oxide is the active site for the reaction.

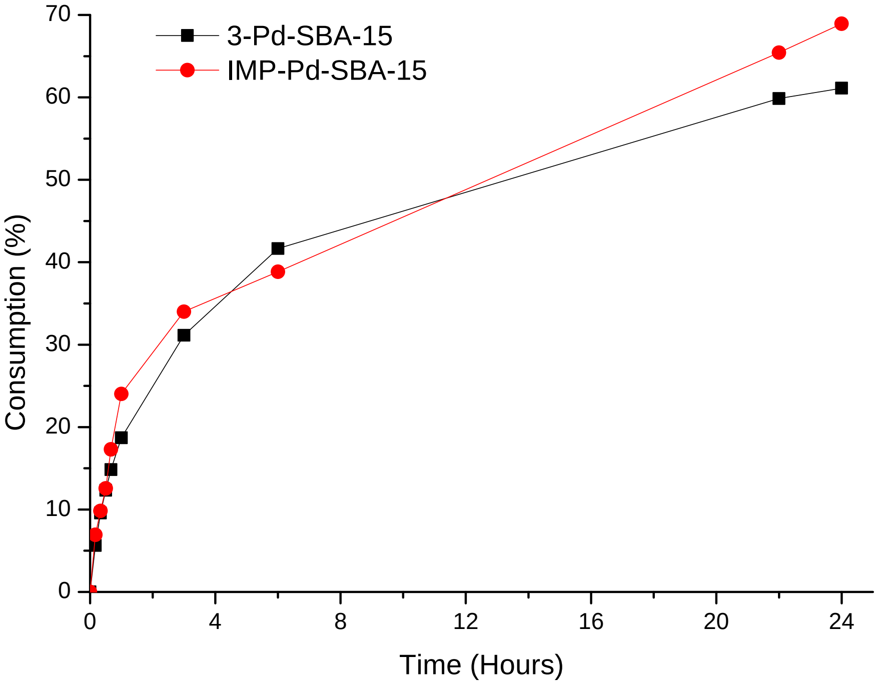

Figure 5.21 Reaction profile of (■) 3-Pd-SBA-15 and (●) IMP-Pd-SBA-15

Examining the products formed during the selective oxidation reaction (Figure 5.22) we observe that butanal is the primary product with 29.8% selectivity over the 6.7% crotonaldehyde, the preferred product. One possible mechanism is for crotonaldehyde to be produced initially before double bond hydrogenation takes place to yield butanal; suggesting that while the catalyst is quite active it is not very selective. Uraz *et al.*[29] investigated the hydrogenation of crotonaldehyde to butanal over a palladium catalyst, using reaction conditions not dissimilar to those employed here for oxidation of crotyl alcohol to crotonaldehyde; 30 – 50 °C, atmospheric pressure and a hydrogen/crotonaldehyde molar ratio of 2:1. Presuming that the hydrogen generated during the oxidation of crotyl alcohol was not removed as water it is possible that hydrogenation of crotonaldehyde could occur proceeding the oxidation of crotyl alcohol. Palladium-doped SBA-15 prepared *via* the TLCT method yields an active catalyst, however further study is still required before it is both active and selective towards the desired product crotonaldehyde.

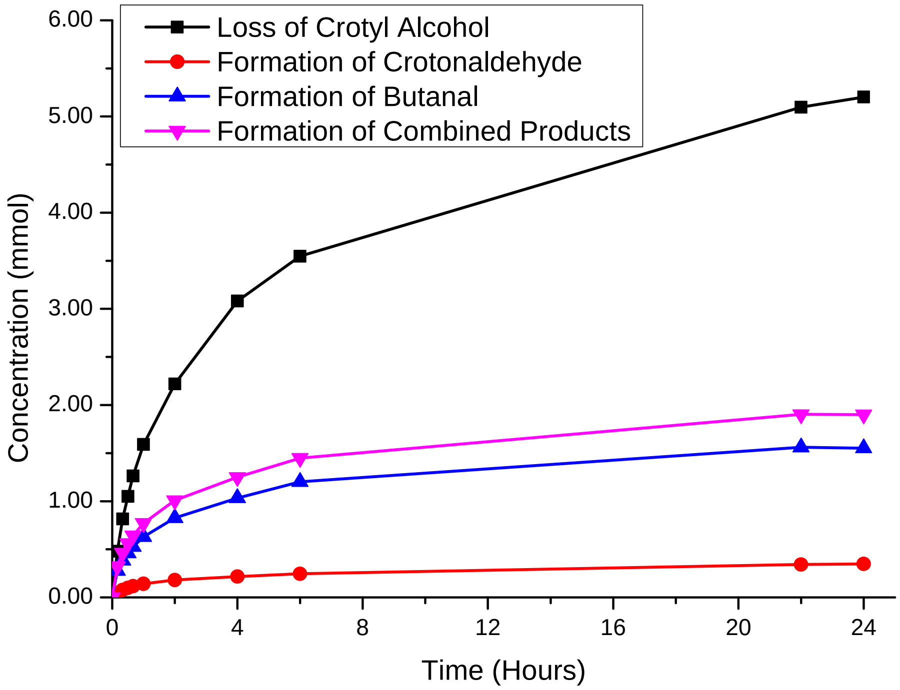

Figure 5.22 Reagent loss and product formation of 3-Pd-SBA-15

5.5 Selective oxidation reaction of gold-doped TLCT materials

Yang *et al.*[30] used SBA-15 as a support for a gold catalyst for the CO oxidation reaction. They introduced gold nanoparticles into the SBA-15 by post-impregnation with $[AuCl_4]^-$ followed by reduction, resulting in a material with a surface area of 360 $m^2\ g^{-1}$, a pore size of 5.7 nm and gold particles measured to be 4.5 nm at a loading of 4.8 wt%. Yang reported that the gold catalysts show reasonable activity and the simple preparation method is favourable, although the gold particles begin to sinter at higher temperatures (above 100 °C) which reduces catalytic activity. This supports the observations made in Chapter 2 that control over the particle size is essential with respect to gold catalysis.

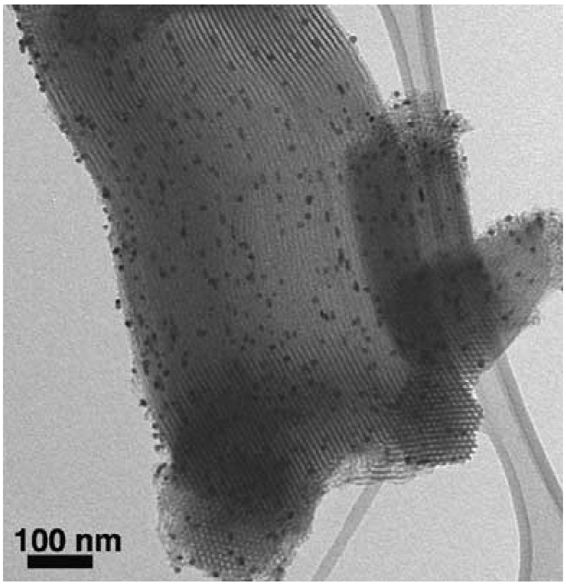

Figure 5.23 TEM image of Yang's Au-SBA-15

More recently, Hu *et al.*[31] prepared a gold catalyst by utilizing a novel technique which involved the co-condensation of TEOS with 1,4-bis(triethoxysily)propane tetrasulfide bound to Au^{3+} (Figure 5.23); the material was calcined yielding a mesoporous silica with gold nanoparticles anchored within the walls. The catalytic activity was tested with the oxidation reaction of benzyl alcohol with high selectivity towards benzaldehyde. It should be noted that while the catalysts showed 43% conversion and 95% selectivity towards benzaldehyde after 5 hours, continuing the reaction for a further 15 hours (20 hours total) resulted in only 53% conversion with a reduction in selectivity to 51% benzaldehyde, with benzoic acid and benzyl benzoate being produced in significant quantities; 38% and 11% respectively.

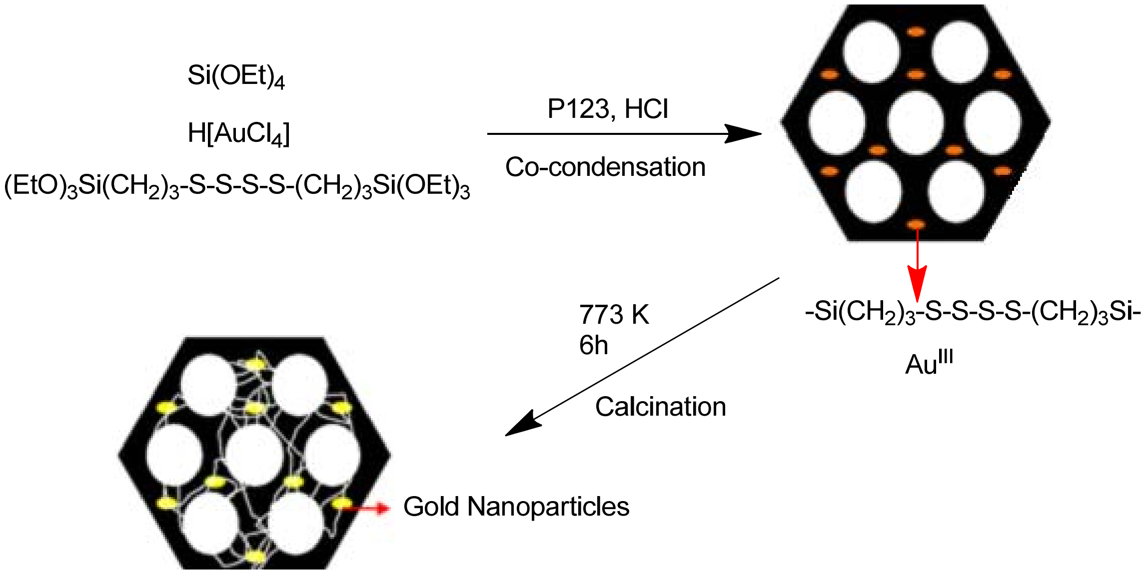

Figure 5.24 Schematic representation of the preparations of Hu’s gold catalysts

Gold has been shown by Lee *et al.*[32] to promote the selective oxidation of crotyl alcohol to croton aldehyde as a bimetallic catalyst with palladium, and a recent review has described the selective oxidation of alcohols using gold catalysts.[33] The review states that of the available metals suitable for selective oxidation of alcohols, ruthenium, platinum, palladium and gold, gold catalysts are the most promising in terms of selectivity and activity.

Gold-doped MCM-41 was prepared at a range of metal loadings, as described in Chapter 2, referred to as 2-Au-MCM-41, and tested for catalytic activity in the selective oxidation reaction of crotyl alcohol to crotonaldehyde. The catalysts were all ground before use and tested as both calcined and reduced materials; however, in all cases activity was found to be negligible (Figure 5.25), showing little difference in reaction profile to that of undoped MCM-41 (blank). This is most likely due to the large size of the gold nanoparticles within the MCM-41, measured to be as large as 40 nm in the higher-loaded catalyst. It has been discussed previously that small particle size, ideally less than 5 nm in diameter, is essential for activity in gold catalysts, it is, therefore, vital that particle size be controlled during the preparation of gold-doped MCM-41 prepared with the TLCT method. While it is clear that none of the gold precursors utilised during this study are suitable in synthesising a gold-doped silica containing nanoparticles contained within the pore structure *via* the TLCT method, it is still feasible that a suitable precursor could be found, allowing an active catalyst to be prepared. The precursor would need to be soluble within the micelles of the templating surfactant and remain stable, decomposing at a higher temperature, during the hydrolysis and hardening of the silica, without aggregating into larger particles.

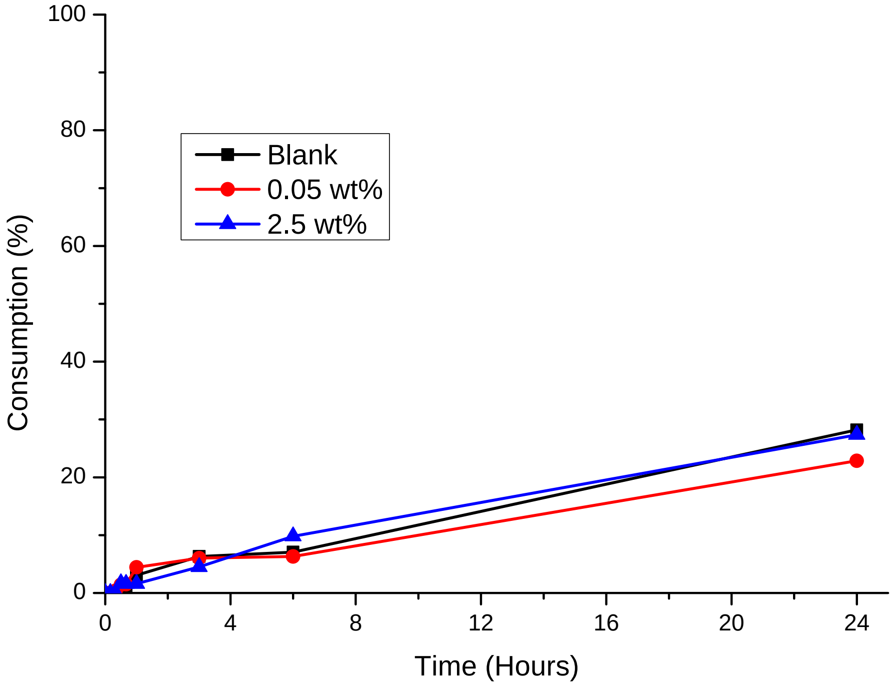

Figure 5.25 Reaction profiles of 2-Au-MCM-41 compared with undoped-MCM-41

5.6 Summary

This chapter has shown that activity and selectivity towards crotonaldehyde in the oxidation of crotyl alcohol and proven the success of preparing catalysts in a one-pot true liquid crystal templating methodology. The exception to the selectivity towards crotonaldehyde seems to be where 3-Pd-SBA-15 is concerned, which produced butanal as the primary product.

The importance of particle size control has been brought to light. It can clearly be seen that small nanoparticles are required for higher activity (Table 5.1) which reinforces the significance of the work described in Chapter 4, producing materials with metal particles well contained within the pore structure.

Table 5.1 Summary of catalytic activity and particle size

Catalyst	Initial rate, normalised to one gram Pd / mmol h^{-1}	Particle Size / nm
2.5 wt% 2-Au-MCM-41	-	40.6
2.5 wt% 2-Pd-MCM-41	28	12.3
2.9 wt% 3-Pd-SBA-15	654	9.8
1.2 wt% 4-Pd-MCM-41	1545	4.1

2.5 wt% palladium-doped SBA-15 prepared by incipient wetness impregnation was found to have an initial rate of 1832 mmol h^{-1} g_{Pd}^{-1} by Parlett *et al.*, whereas the 2.9 wt% 3-Pd-SBA-15 prepared in this work had an initial rate of 654 mmol h^{-1} g_{Pd}^{-1}. Incipient wetness impregnation, while being a two-step method may appear to be beneficial in preparing an active catalyst, it is reasonable to predict that the activity of Pd-SBA-15 prepared with the palladium(II) 2-ethyl hexanoate precursor would show a significant improvement due to the smaller particle size.

The time spent investigating the optimum conditions for the catalyst was highly beneficial, observing a 50% increase in conversion by simply reducing and grinding the catalyst into a powder. It is thought that the mass transport limitation caused by the long pores could be reduced, should it be possible to prepare a bicontinuous material, such as

SBA-16, by true liquid crystal templating as described in Chapter 3. Parlett *et al.* also showed a substantial improvement in activity by changing the support from SBA-15 to SBA-16 (Figure 5.26); although he noted that the narrower pore opening of the support may hinder the diffusion of bulkier alcohols.

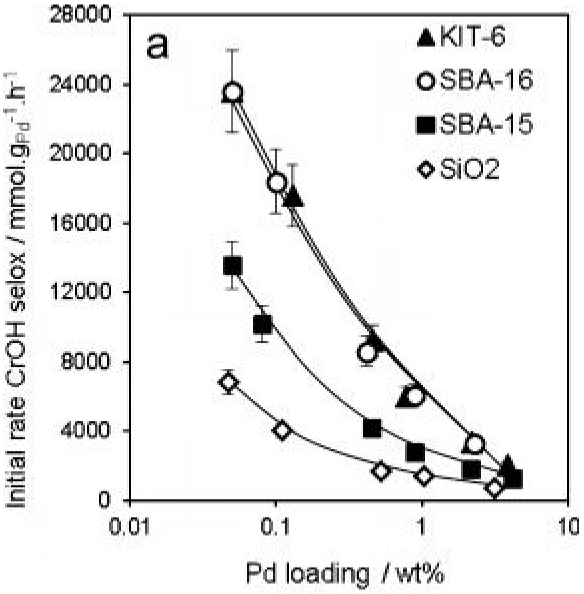

Figure 5.26 Loading-dependent activity of palladium-doped silicas in crotyl alcohol oxidation

5.7 Conclusion

The work described in Chapters 2, 3 and 4 has demonstrated that the aims of the research have been achieved. That is: a range of mesoporous silicas doped with metal nanoparticles were prepared in a one-pot synthesis using true liquid crystal templating and were subject to catalytic testing as described in Chapter 5.

It has proven possible to introduce several different metals, including palladium, platinum and gold, into the mesoporous silica, MCM-41, by utilising 'off-the-shelf' precursors, $(NH_4)_x[MCl_4]$, without having to alter the methodology, resulting in reliable and predictable products. However, control of the particle size using these reagents was not achieved. With particles appearing ten times larger, in the case of gold, than the pores they were supposed to be contained within, it was clear that an improvement had to be made.

Altering the surfactant from $C_{12}EO_{10}$ to P123 to yield an SBA-15-like material resulted in larger pores allowing the nanoparticles to be better confined. The particle size of palladium oxide was observed to be 21.2 nm in MCM-41 (Figure 5.27A) reducing to 14.8 nm when the same precursor was used with P123 to prepare SBA-15 (Figure 5.27B); still larger than the pores, but much closer to the target.

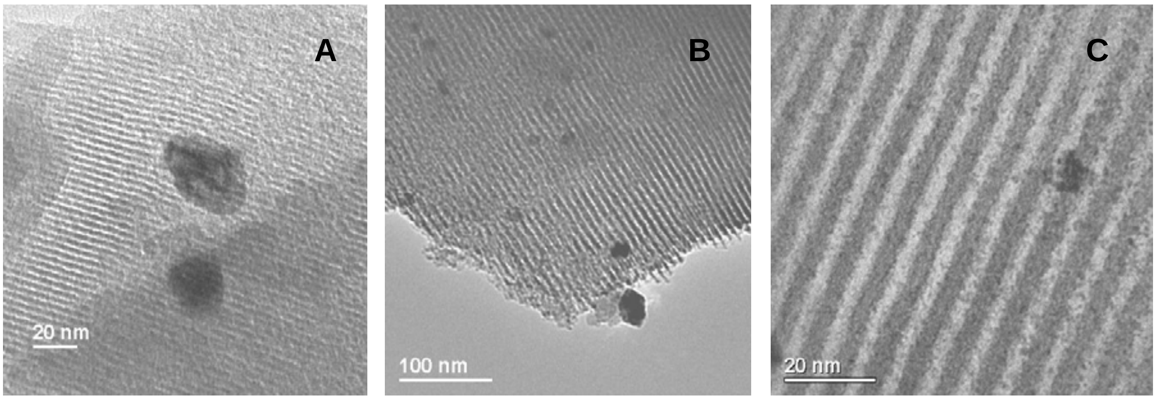

Figure 5.27 TEM images of Pd-doped silica prepared by TLCT; A) MCM-41 prepared using $(NH_4)_2[PdCl_4]$; B) SBA-15 prepared using $(NH_4)_2[PdCl_4]$; C) SBA-15 prepared using palladium(II) 2-ethyl hexanoate

The inability to control particle size led to a different approach to the synthesis. Thus, it was recognised that the ammonium salts were water-soluble and so would reside in the space that would, in due course, become the silica framework, whereas the final 'destination' of the nanoparticle would be in the voids. During the synthesis, the area that will become the voids will be occupied by the surfactant alkyl chains and so represent a very hydrophobic environment. Thus, by identifying and using hydrophobic metal complexes, it should be possible to locate them in the correct place from the beginning. Long- and/or branched-chain metal alkanoates were identified as suitably hydrophobic complexes.

This move away from the ‘off-the-shelf’ precursors to the metal alkanoates detailed in Chapter 4, allowed the particle size to be reduced further. Palladium oxide particles with a diameter of 4.1 nm were observed in MCM-41, while SBA-15 exhibited particles as small as 1.9 nm (Figure 5.27C), displaying particles which appear to be contained within an individual pore.

Unfortunately, while the same trend was observed with gold-doped mesoporous silicas, the reduction in size was not nearly enough. MCM-41 silica doped with the $(NH_4)[AuCl_4]$ precursor yielded gold particles of 49.8 nm, reducing to 36.4 nm with SBA-15 and finally the micelle soluble complex of gold yielded particles of 34.6 nm in MCM-41. This does not rule out the possibility of discovering a suitable gold precursor which will be stable within the micellar environment and produce particles of the desired size; potentially gold octanoate could be synthesised and tested for suitability.

Particle size control is critical in order to prepare effective catalysts and examples of the dependency of particle size with gold and palladium catalysis have been discussed. Further, the work described in Chapter 4 demonstrated a vast improvement in introducing nanoparticles within the silica pores with the one-step TLCT methodology. However, particle size control was not the only hurdle to be overcome. While preparing the template, difficulties in preparing a homogeneous mixture of the surfactant, water and TMOS prevented the mesophase from being formed which resulted in a non-porous silica. If all of the produced methanol was not removed during hydrolosis the mesophase would be disrupted, which would also result in a non-porous silica. Additionally, dissolved precursors would precipitate out of the mixture if the concentration was too high or they were found to be insoluble, which would result in large metal particles forming on the surface of the silica rather than within the pores. Despite these difficulties, a range of nanoparticle-doped silicas have been prepared and tested catalytically in Chapter 5. The range of metals investigated is not comprehensive and still allows for further work to exploit the adaptability of the TLCT method.

The catalytic results detailed in Chapter 5 confirmed the importance of particle size control and its relation to activity, with material containing the smallest palladium particles showing the highest activity. In addition, other key factors have also been discussed in order to isolate an active catalyst. The catalyst with the highest activity was shown to be 1 wt% palladium-doped MCM-41 prepared using a palladium(II) octanoate precursor. The catalyst was reduced under hydrogen for 2 hours to generate palladium metal particles with a palladium oxide shell, and then ground into a fine powder to shorten the pores to allow the reagents readily access to the active site. It is expected that Pd-SBA-15 prepared with palladium(II) 2-ethylhexanoate would show even higher activity due to the larger pores and smaller particles.

In a like-for-like comparison, TLCT palladium-doped silica is similar in catalytic activity to materials prepared in a two-step process, such as incipient wetness impregnation (Figure 5.28). While activity is not improved, TLCT is advantageous by being a one-step process. It should be noted that this comparison has not been made using the palladium(II) 2-ethylhexanoate-doped SBA-15, which if the trend follows, should prove more active than the two-step catalyst.

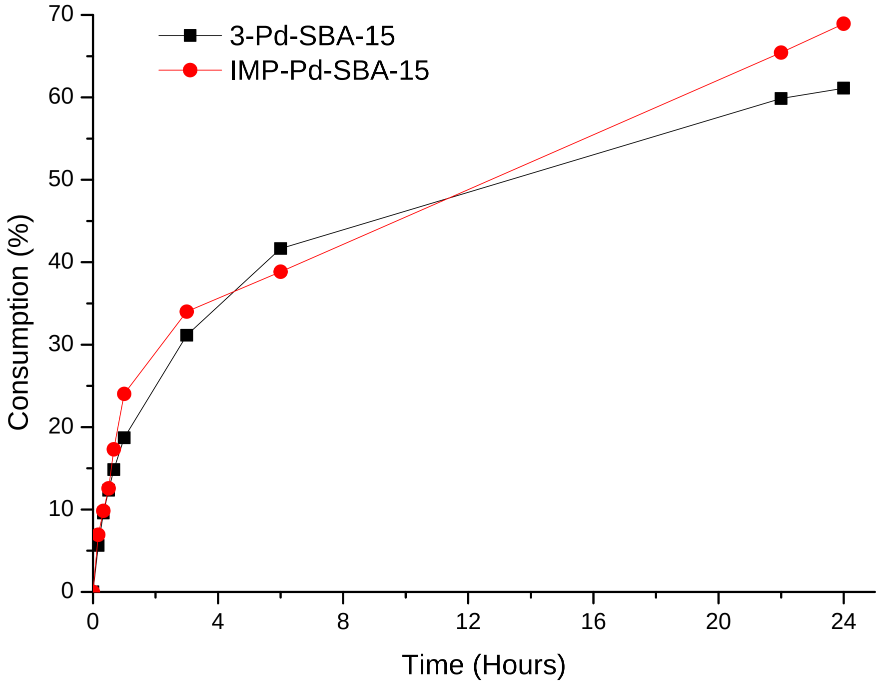

Figure 5.28 Reaction profile of (■) 3-Pd-SBA-15 and (●) IMP-Pd-SBA-15

5.8 Experimental

5.8.1 General Experimental

All reagents and solvents were used as received.

Alcohol oxidation was performed using a Radleys Carousel Reaction Station equipped with 25 ml reactor tubes. Reactors were charged with crotyl alcohol (8.4 mmol, 6.04 g) in toluene (100 cm^3), with 1% mesitylene as an internal standard. Reactions were performed at 90 ºC with 50 mg of catalyst. Samples were periodically withdrawn for analysis using a Varian CP3800 GC equipped with CP-8400 Autosampler and DB5 capillary column (film thickness 0.25 µm, id 0.32 mm, length 30 m). Crotonaldehyde and butanal were the principle reaction products. There were no side products attributable to toluene oxidation. Reactions were run for up to 24 hours with initial rates determined from the linear portion of the reaction profile.

5.9 References

1. J. S. Beck, J. C. Vartuli, W. J. Roth, M. E. Leonowicz, C. T. Kresge, K. D. Schmitt, C. T. W. Chu, D. H. Olson, E. W. Sheppard, S. B. McCullen, J. B. Higgins and J. L. Schlenker, *J. Am. Chem. Soc.,* 1992, **114,** 10834.
2. R. M. Martín-Aranda and J. Čejka, *Top. Catal.,* 2010, **53,** 141.
3. A. Martínez and G. Prieto, *Top. Catal.,* 2009, **52,** 75.
4. L. Čapek, J. Adam, T. Grygar, R. Bulánek, L. Vradman, G. Košova-Kučerová, P. Čičmanec and P. Knotek, *Appl. Catal. A: General,* 2008, **342,** 99.
5. Sujandi, E. A. Prasetyanto, D.-S. Han, S.-C. Lee and S.-E. Park, *Catal. Today,* 2009, **141,** 374.
6. S.-E. Park and E. A. Prasetyanto, *Top. Catal.,* 2009, **52,** 91.
7. E. Pérez-Mayoral, R. M. Martín-Aranda, A. J. López-Peinado, P. Ballesteros, A. Zukal and J. Čejka, *Top. Catal.,* 2009, **52,** 148.
8. M. Stöcker, *Angew. Chem. Int. Ed.,* 2008, **47,** 9200.
9. D. P. Sawant, V. V. Balasubramanian, J. Justus, S. B. Halligudi, A. C. Bose, K. Ariga, T. Mori and A. Vinu, *Top. Catal.,* 2009, **52,** 111.
10. I. Nowak, A. Feliczak, I. Nekoksová and J. Čejka, *Appl. Catal. A: General,* 2007, **321,** 40.
11. J. A. Melero, R. van Grieken and G. Morales, *Chem. Rev.,* 2006, **106,** 3790.
12. J. Aguado, J. M. Escola, M. C. Castro and B. Paredes, *Appl. Catal. A: General,* 2005, **284,** 47.
13. Q. Xu and M. Cai, *React. Funct. Polym.,* 2007, **67,** 515.
14. H. Zhao, J. Peng, R. Xiao, W. Hao and M.-Z. Cai, *J. Organomet. Chem.,* 2011, **696,** 2030
15. J. Demel, S.-E. Park, J. Čejka and P. Štěpnička, *Catal. Today,* 2008, **132,** 63.
16. M. T. Reetz and J. G. de Vries, *Chem. Commun.,* 2004, 1559.
17. J. Demel, J. Čejka and P. Štěpnička, *J. Mol. Catal. A: Chem.,* 2007, **274,** 127.
18. J. Demel, J. Čejka, S. Bakardjieva and P. Štěpnička, *J. Mol. Catal. A: Chem.,* 2007, **263,** 259.
19. J.-J. Li, X.-Y. Xu, Z. Jiang, Z.-P. Hao and C. Hu, *Environ. Sci. Technol.,* 2005, **39,** 1319.
20. S. F. J. Hackett, *PhD Thesis,* University of York, 2008.

21. G. Cainelli and G. Cardillo, *Chromium oxidations in organic chemistry, Springer, Berlin,* **1984.**
22. M. Rottenberg and P. Baertschi, *Helv. Chim. Acta,* 1956, **39,** 1973.
23. A. F. Lee, Z. Chang, P. Ellis, S. F. J. Hackett and K. Wilson, *J. Phys. Chem. C,* 2007, **111,** 18844.
24. A. F. Lee and K. Wilson, *Green Chem.,* 2004, **6,** 37.
25. A. F. Lee, S. F. J. Hackett, J. S. J. Hargreaves and K. Wilson, *Green Chem.,* 2006, **8,** 549.
26. C. Li, Q. Zhang, Y. Wang and H. Wan, *Catal. Lett.,* 2008, **120,** 126.
27. D. Zhao, J. Feng, Q. Huo, N. Melosh, G.H. Frederickson, B.F. Chmelka and G. D. Stucky, *Science*, 1998, **279**, 548.
28. C. M. A. Parlett, D. W. Bruce, N. S. Hondow, A. F. Lee and K. Wilson, *ACS Catal.,* 2011, **1,** 636.
29. C. Uraz, F. S. Atalay and S. Atalay, *Chem. Biochem. Eng. Q.,* 2004, **18,** 373.
30. C. Yang, M. Kalwei, F. Schüth and K. Chao, *Appl. Catal. A: Gen.,* 2003, **254,** 289.
31. J. Hu, L. Chen, K. Zhu, A. Suchopar and R. Richards, *Catal. Today,* 2007, **122,** 277.
32. J. Naughton, A. F. Lee, S. Thompson, C. P. Vinod and K. Wilson, *Phys. Chem. Chem. Phys.,* 2010, **12,** 2670.
33. C. D. Pina, E. Falletta, L. Prati and M. Rossi, *Chem. Soc. Rev.,* 2008, **37,** 2077.